frontiers | Research Topics

Advances in development and utilization of underground space, volume II

Edited by
Yuwei Zhang, Zhanping Song, Liang Cui,
Ping Zhang and Naifei Liu

Published in
Frontiers in Earth Science
Frontiers in Ecology and Evolution
Frontiers in Environmental Science

ISSN 1664-8714
ISBN 978-2-8325-5685-6
DOI 10.3389/978-2-8325-5685-6

About Frontiers

Frontiers is more than just an open access publisher of scholarly articles: it is a pioneering approach to the world of academia, radically improving the way scholarly research is managed. The grand vision of Frontiers is a world where all people have an equal opportunity to seek, share and generate knowledge. Frontiers provides immediate and permanent online open access to all its publications, but this alone is not enough to realize our grand goals.

Frontiers journal series

The Frontiers journal series is a multi-tier and interdisciplinary set of open-access, online journals, promising a paradigm shift from the current review, selection and dissemination processes in academic publishing. All Frontiers journals are driven by researchers for researchers; therefore, they constitute a service to the scholarly community. At the same time, the *Frontiers journal series* operates on a revolutionary invention, the tiered publishing system, initially addressing specific communities of scholars, and gradually climbing up to broader public understanding, thus serving the interests of the lay society, too.

Dedication to quality

Each Frontiers article is a landmark of the highest quality, thanks to genuinely collaborative interactions between authors and review editors, who include some of the world's best academicians. Research must be certified by peers before entering a stream of knowledge that may eventually reach the public - and shape society; therefore, Frontiers only applies the most rigorous and unbiased reviews. Frontiers revolutionizes research publishing by freely delivering the most outstanding research, evaluated with no bias from both the academic and social point of view. By applying the most advanced information technologies, Frontiers is catapulting scholarly publishing into a new generation.

What are Frontiers Research Topics?

Frontiers Research Topics are very popular trademarks of the *Frontiers journals series*: they are collections of at least ten articles, all centered on a particular subject. With their unique mix of varied contributions from Original Research to Review Articles, Frontiers Research Topics unify the most influential researchers, the latest key findings and historical advances in a hot research area.

Find out more on how to host your own Frontiers Research Topic or contribute to one as an author by contacting the Frontiers editorial office: frontiersin.org/about/contact

Advances in development and utilization of underground space, volume II

Topic editors

Yuwei Zhang — Xi'an University of Architecture and Technology, China
Zhanping Song — Xi'an University of Architecture and Technology, China
Liang Cui — Lakehead University, Canada
Ping Zhang — Luleå University of Technology, Sweden
Naifei Liu — Xi'an University of Architecture and Technology, China

Citation

Zhang, Y., Song, Z., Cui, L., Zhang, P., Liu, N., eds. (2024). *Advances in development and utilization of underground space, volume II*. Lausanne: Frontiers Media SA.
doi: 10.3389/978-2-8325-5685-6

Table of contents

frontiers | Frontiers in Earth Science

TYPE Original Research
PUBLISHED 15 February 2023
DOI 10.3389/feart.2023.1143003

OPEN ACCESS

EDITED BY
Zhanping Song,
Xi'an University of Architecture and Technology, China

REVIEWED BY
Cheng Lyu,
Sichuan University, China
Shengzhi Wu,
Shandong Jianzhu University, China
Xiao Zhang,
Southwest Jiaotong University, China

*CORRESPONDENCE
Yongquan Zhu,
yongquan_zhu2022@163.com

SPECIALTY SECTION
This article was submitted to Environmental Informatics and Remote Sensing, a section of the journal Frontiers in Earth Science

RECEIVED 12 January 2023
ACCEPTED 31 January 2023
PUBLISHED 15 February 2023

CITATION
Dong Y, Zhang H, Wang M, Yu L and Zhu Y (2023), Variable model for mechanical parameters of soft rock and elastoplastic solutions for tunnels considering the influence of confining pressure. *Front. Earth Sci.* 11:1143003. doi: 10.3389/feart.2023.1143003

Variable model for mechanical parameters of soft rock and elastoplastic solutions for tunnels considering the influence of confining pressure

Yucang Dong[1], Hai Zhang[1], Mingnian Wang[2], Li Yu[2] and Yongquan Zhu[3]*

[1]Hebei Technology Innovation Center for Intelligent Development and Control of Underground Built Environment, School of Urban and Geology Engineering, Hebei GEO University, Shijiazhuang, China, [2]School of Civil Engineering, Southwest Jiaotong University, Chengdu, China, [3]State Key Laboratory of Mechanical Behavior and System Safety of Traffic Engineering Structures, Shijiazhuang, China

The accurate understanding of the influence of confining pressure on the mechanical characteristics of soft rock and how to comprehensively consider this influence in the elastoplastic analysis of tunnels are the fundamental premises for the effective evaluation of the deformation control and stability of soft rock tunnels. Therefore, this paper firstly investigates the effect of confining pressure on the deformation and strength characteristics of phyllite and slate, using triaxial experiment results and proposed variable models for the mechanical parameters (E, v, c, φ) of soft rock with confining pressure variation. Secondly, according to the second stress state around tunnels and these variable models for the mechanical parameters of soft rock, a new elastoplastic solution for tunnels is devised, which simultaneously considers the effect of confining pressure on the deformation and strength characteristics of the surrounding rock. Finally, with the proposed elastoplastic solution, the effect of multiple factors (initial pressure, supporting force, and tunnel radius) on the stress and displacement of tunnel surrounding rock is analyzed.

KEYWORDS

soft rock, circular tunnel, mechanical parameter, variable model, elastoplastic solution

1 Introduction

In recent years, increasing numbers of tunnels have been constructed in soft rock stratum. However, major deformation of tunnels occurs frequently when tunnels pass through soft rock with high geo-stress, which often leads to the destruction of the tunnel support structure and brings about significant potential safety hazards for constructors (Chen et al., 2020; Li et al., 2020). Essentially, the fundamental reason why the problem of tunnel deformation occurs frequently is that the influence of confining pressure on the mechanical characteristics of soft rock has not yet been completely ascertained, resulting in the existing elastoplastic solution not being accurately analyzed and evaluated for stress and displacement around tunnels (Li F et al., 2021; Luo et al., 2021). Therefore, the influence of confining pressure on the mechanical characteristics of soft rock and more accurate elastoplastic solutions for tunnels are current research hotspots (Wu et al., 2022).

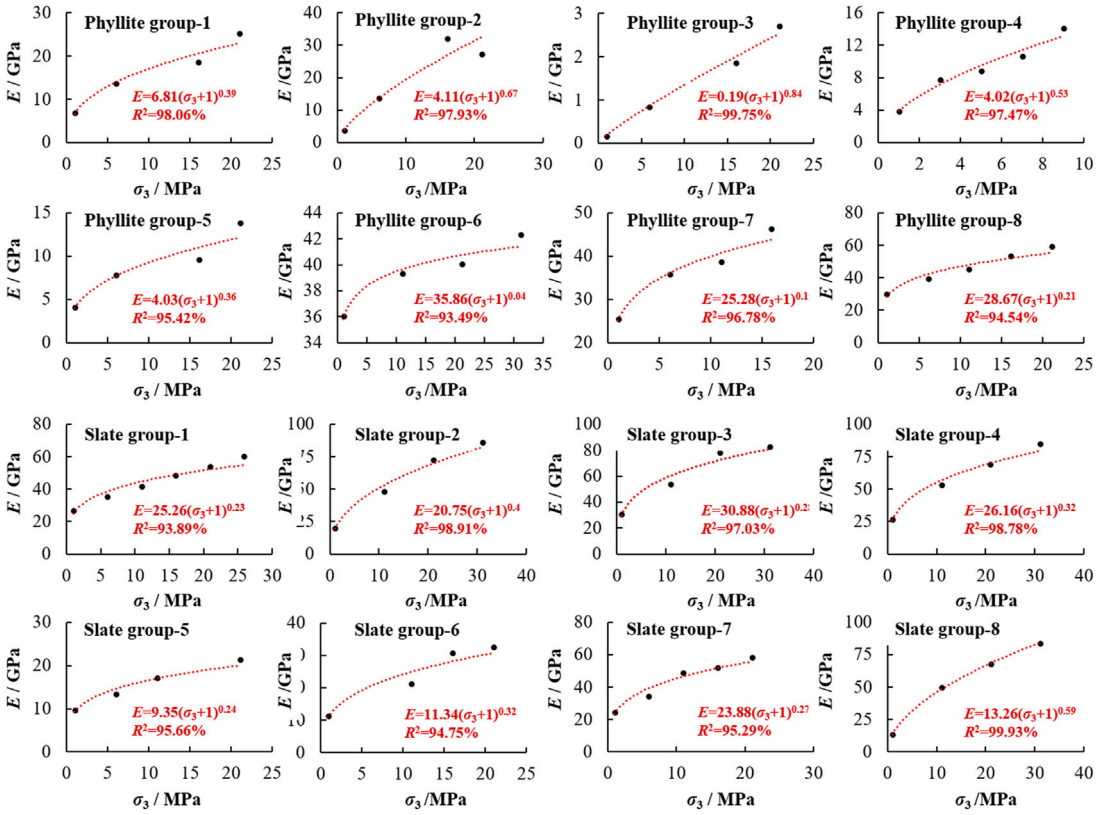

FIGURE 1
Variation of elasticity modulus with the influence of confining pressure of slate and phyllite.

Regarding the influence of confining pressure on the mechanical characteristics of soft rock, the achievements of numerous scholars in the past decades can be divided into three categories. Firstly, the influence of confining pressure on the stress-strain curves of soft rock was discovered by (Alam et al., 2008; Debecker and Vervoort, 2009; Chen et al., 2016; Fu et al., 2018) through triaxial experiments. The results of these experiments show that the lithology of soft rock is usually slate and phyllite, and the range of confining pressure is 0MPa–40 MPa (Gholami and Rasouli, 2013; Hu et al., 2016; Hao et al., 2019). Secondly, based on the above-mentioned experiment results, the evolution of mechanical characteristics with the influence of confining pressure was analyzed, for example, the effect of confining pressure on failure patterns, peak strength, *etc.* (Xu et al., 2018). Thirdly, a series of new strength criteria and a constitutive model, which considers the influence of confining pressure, was proposed, for example, the GZZ strength criterion, the uniform strength criterion, and the elastoplastic damage constitutive model, *etc.* (Saeidi et al., 2013; Singh et al., 2015). In addition, several scholars devoted to the influence of confining pressure on the creep mechanical behavior and gas tightness characteristics of soft rock, such as Lyu and Liu, have investigated the creep gas tightness characteristics through experiments and proposed a corresponding creep-damage constitutive model (Lyu et al., 2021; Lyu et al., 2022). However, the majority of existing studies only focus on the influence of confining pressure on the strength parameters of soft rock but neglect the influence of confining pressure on the deformation parameters of soft rock. Therefore, a new, universal variable model for the mechanical parameters (including strength and deformation parameters) of soft rock considering the influence of confining pressure is urgently needed, which is one of the main purposes of this paper.

In terms of elastoplastic solutions for soft rock tunnels, the influence of confining pressure on the strength of soft rock and the strain-softening behavior of soft rock are the current research focuses. For instance, Kang et al. (Yi et al., 2020) and Chen et al. (Chen et al., 2022) devised a series of new solutions, which consider the influence of confining pressure on the strength of soft rock. In developing these solutions, they considered that it introduces many new strength criteria, such as GZZ, improved M-C, and D-P strength criteria to elastoplastic solutions. Many other scholars (Cui et al., 2015) have devised a series of new solutions for the strain-softening behavior of soft rock. In developing these solutions, they defined the plastic softening parameters (η) and assumed that η linearly controls the strength parameter variation in the post-failure stage. However, the effect of confining pressure is not considered in these solutions. Most existing solutions only consider the effect of confining pressure or the strain-softening behavior of soft rock on strength characteristics but ignore the influence of confining pressure on deformation characteristics, which leads to these solutions not calculating and evaluating stress and displacement around soft rock tunnels. Therefore, it is necessary to propose a new elastoplastic solution for soft rock tunnels, which simultaneously considers the effect of confining pressure on the

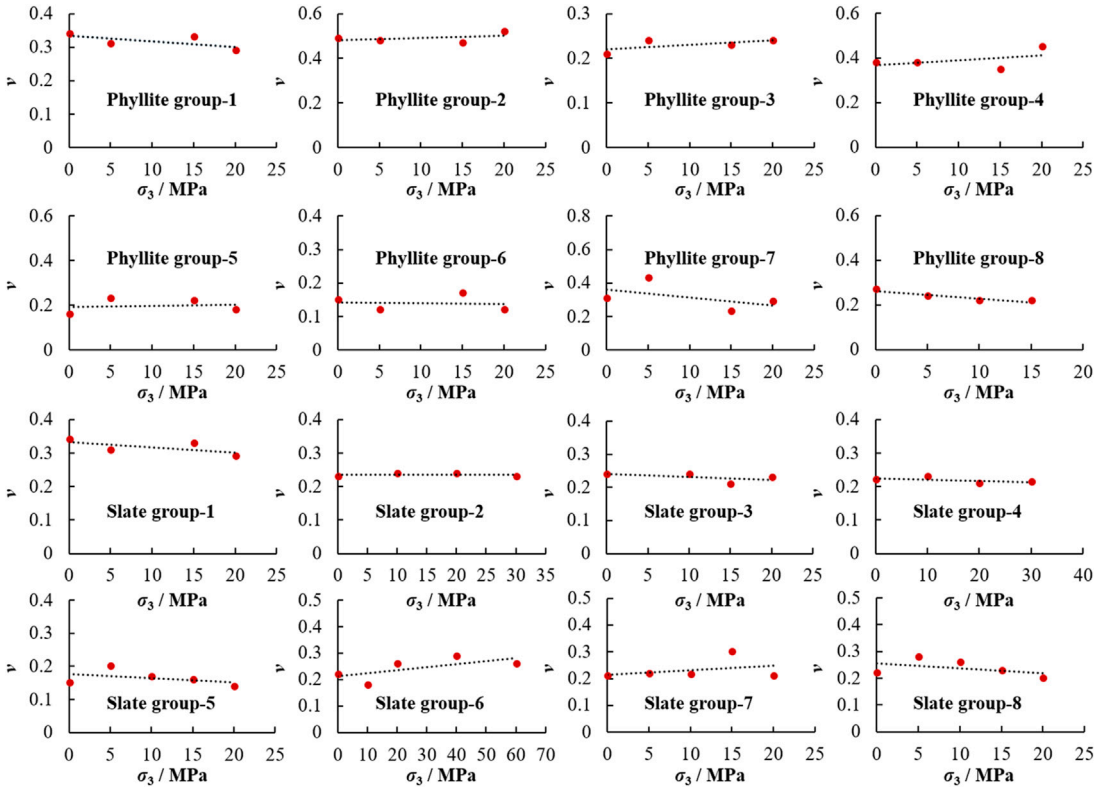

FIGURE 2
Variation of Poisson ratio with the influence of confining pressure influence for slate and phyllite.

deformation and strength of soft rock, which is another of the main purposes of this paper.

Therefore, this paper firstly investigates the effect of confining pressure on the mechanical characteristics of soft rock using triaxial experiment results and proposes variable models for the mechanical parameters (E, ν, c, φ) of soft rock considering the influence of confining pressure. Secondly, a new elastoplastic solution for tunnels was devised, which simultaneously considers the mechanical characteristic variation of the surrounding rock due to the influence of confining pressure. Finally, the effect of multiple factors (initial pressure, supporting force, and tunnel radius) on the stress and displacement of tunnel surrounding rock is analyzed.

2 Variable model for mechanical parameters of soft rock with the influence of confining pressure

2.1 Variable model for elasticity modulus (E) with the influence of confining pressure

Based on the triaxial experiment results of 69 samples (35 samples of slate and 34 samples of phyllite from eight regions), the variation of the elasticity modulus under the influence of confining pressure for slate and phyllite, respectively, is revealed in Figure 1. Experimental result sources can be found in Supplementary Appendix SA.

As shown in Figure 1, the elasticity modulus of phyllite and slate gradually increases with increasing confining pressure, not constant. Further, using the universal global optimization method, it has been found that the power function can represent this variation with the influence of confining pressure, and the correlation coefficient of fitting results of all sample groups are more than 90%. Therefore, the variable model for the elasticity modulus of soft rock with the influence of confining pressure is proposed in Figure 5, and the undetermined parameters of variable models can be obtained by means of triaxial compression experiments.

2.2 Variable model for Poisson ratio (ν) with the influence of confining pressure

Based on the triaxial experiment results of 67 samples (35 samples of slate and 32 samples of phyllite from nine regions), the variation of the Poisson ratio with the influence of confining pressure for slate and phyllite, respectively, is revealed in Figure 2. Experimental result sources can be found in Supplementary Appendix SA.

As shown in Figure 2, the variation trend for the Poisson ratio of soft rock with variable confining pressure is almost linear, and the value of the Poisson ratio under different confining pressure conditions is practically equal to that under the 0 MPa confining pressure condition, which means the confining pressure does not

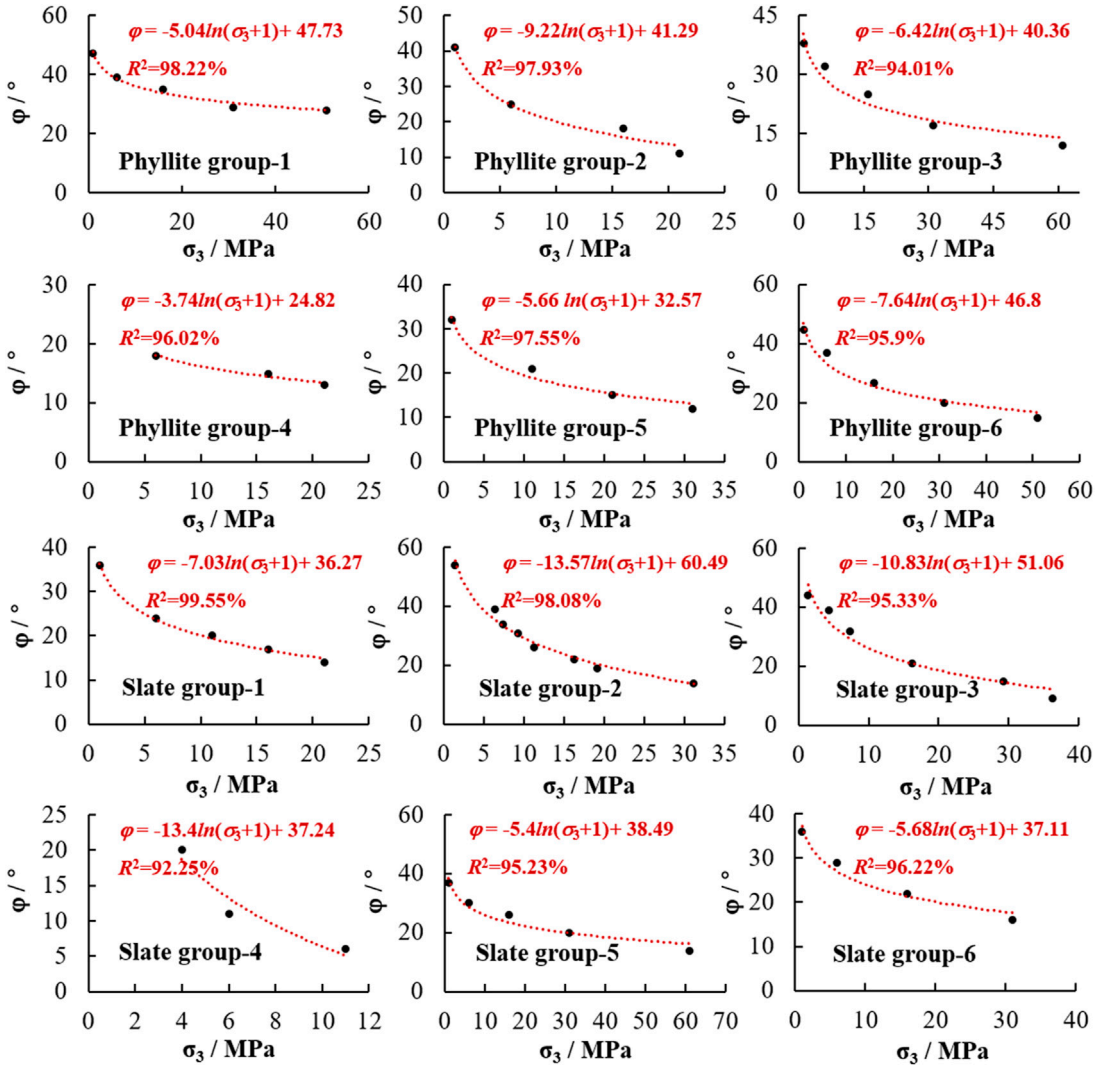

FIGURE 3
Variation of friction angle with the influence of confining pressure influence for slate and phyllite.

have a significant influence on the Poisson ratio of soft rock. Therefore, the variable model for the Poisson ratio of soft rock with the influence of confining pressure is proposed in Figure 5.

2.3 Variable model for friction angle (φ) with the influence of confining pressure

Based on the triaxial experiment results of 57 samples (31 samples of slate and 26 samples of phyllite from six regions), the variation of the friction angle with the influence of confining pressure for slate and phyllite, respectively, is revealed in Figure 3. Experimental result sources can be found in Supplementary Appendix SA.

As shown in Figure 4, the friction angle of soft rock gradually decreases with increasing confining pressure. Further, using the universal global optimization method, it is found that the logarithmic function can represent this variation with the influence of confining pressure, and the correlation coefficient of fitting results of all sample groups are more than 90%. Therefore, the variable model for the friction angle of soft rock with the influence of confining pressure is proposed in Figure 5, and the undetermined parameters of the variable model can be obtained by means of triaxial compression experiments.

2.4 Variable model for cohesion (c) with the influence of confining pressure

Based on the triaxial experiment results of 57 samples (31 samples of slate and 26 samples of phyllite from six regions), the variation of cohesion with the influence of confining pressure for slate and phyllite is revealed in Figure 4. Experimental result sources can be found in Supplementary Appendix SA.

As shown in Figure 4, the cohesion of soft rock gradually decreases with increasing confining pressure. Further, using the universal global optimization method, it has been found that the power function can represent this variation with the influence of

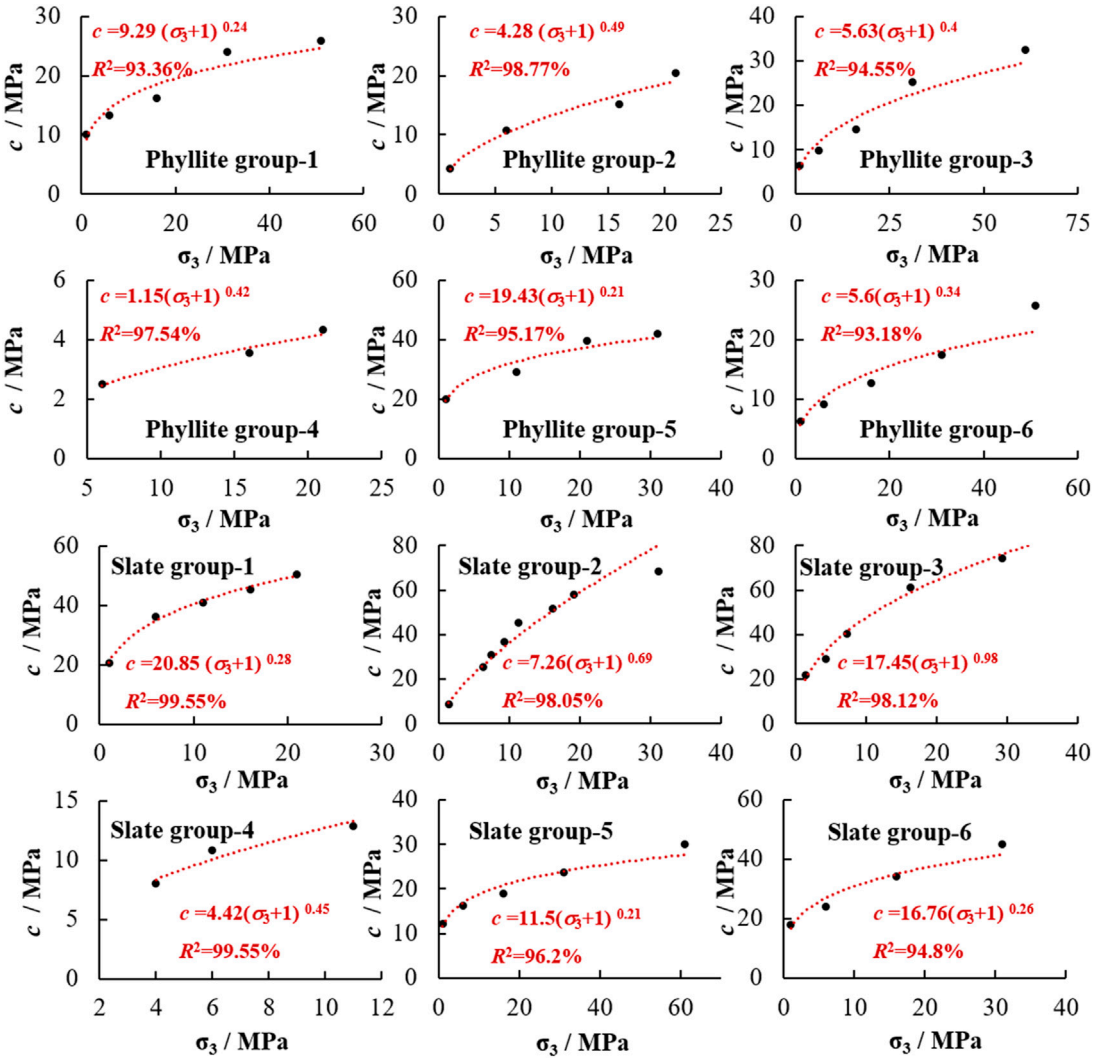

FIGURE 4
Variation of cohesion with the influence of confining pressure influence for slate and phyllite.

confining pressure, and the correlation coefficient of fitting results of all sample groups are more than 90%. Therefore, the variable model for the cohesion of soft rock with the influence of confining pressure is proposed in Figure 5, and the undetermined parameters of variable models can be obtained by means of triaxial compression experiments. In variable models for the mechanical parameters of soft rock, the units of confining pressure and cohesion are both MPa, the unit of the elasticity modulus is GPa, and the unit of the friction angle is degree.

3 Elastoplastic solution for tunnels considering the influence of confining pressure

After the circular tunnel excavation, the secondary stress state of the surrounding rock is shown in Figure 6 (Fang et al., 2021). Radial stress increases with increasing radial distance, which means confining pressure on the surrounding rock increases with increasing radial distance, not constant. Meanwhile, by combining the variable model for the mechanical parameters of soft rock with the influence of confining pressure, it can be concluded that the mechanical parameters of surrounding rock vary with radial stress variation, not constant.

Therefore, in order to derive an elastoplastic solution for tunnels considering the influence of confining pressure, the stress field of the rock surrounding the tunnel is divided and the stress partition of the surrounding rock is: surrounding rock are divided into numerous concentric circle rings, the center of which is the center of the tunnel in polar coordinates, as shown in Figure 7. The mechanical parameters of each concentric circle ring are controlled by radial stress, which can be calculated using a variable model for the mechanical parameters of soft rock, and the mechanical parameters at different angles are the same in each ring.

The derivation process of elastoplastic solutions for tunnels considering the influence of confining pressure is subject to the

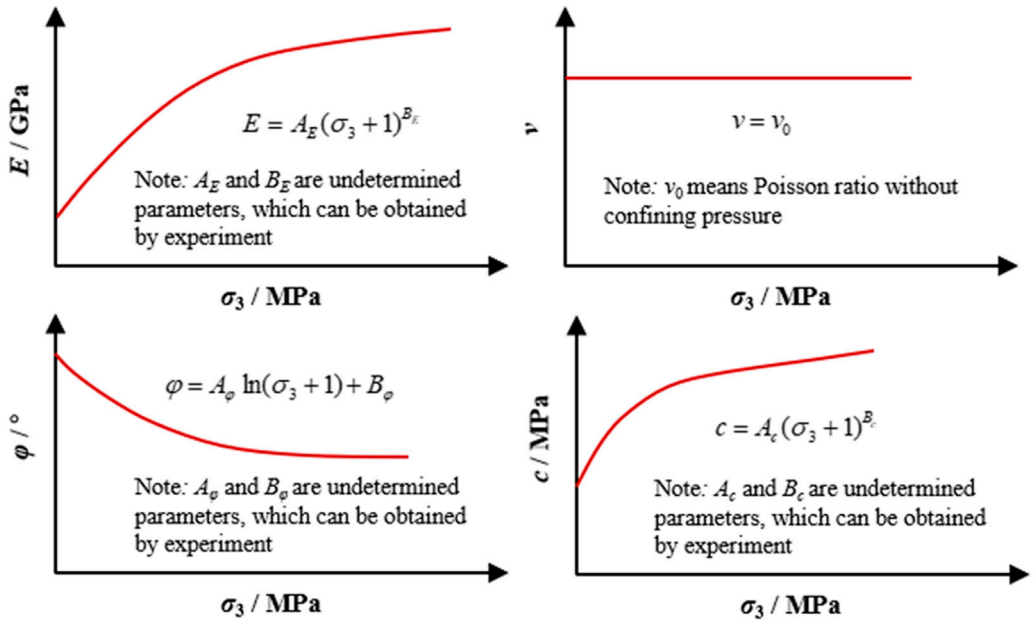

FIGURE 5
Variable models for mechanical parameters of soft rock with the influence of confining pressure.

following basic assumptions: (1) Surrounding rock is homogeneously isotropic. (2) The tunnel excavation disturbance process is considered a plane strain problem. (3) Surrounding rock is in a hydrostatic stress field without considering the influence of gravity before tunnel excavation, and the hydrostatic stress is P_0. (4) After tunnel excavation, σ_θ is considered σ_1, σ_z is considered σ_2, and σ_r is considered σ_3.

3.1 Yield function and plastic potential function

The yielding function controls the yielding process of the surrounding rock:

$$f = \frac{3\sin\varphi_{(\sigma_r)} - 1}{1 - \sin\varphi_{(\sigma_r)}}\sigma_r + \sigma_\theta + \frac{2c_{(\sigma_r)}\cos\varphi_{(\sigma_r)}}{1 - \sin\varphi_{(\sigma_r)}} \tag{1}$$

In Eq. 1, $\varphi_{(\sigma_r)}$ is friction angle and $c_{(\sigma_r)}$ is cohesion, and both are controlled by radial stress (σ_r).

Based on the non-associative plastic flow rule (Chen et al., 2022), the plastic potential function is:

$$g(\sigma_\theta, \sigma_r) = \sigma_\theta + \frac{3\sin\phi - 1}{1 - \sin\phi}\sigma_r + \frac{2c\cos\phi}{1 - \sin\phi} \tag{2}$$

ϕ is dilation angle in Eq. 2. Then

$$d\varepsilon_r^p = \frac{3\sin\phi - 1}{1 - \sin\phi}d\varepsilon_\theta^p \tag{3}$$

and, if $K_\phi = (1 - 3\sin\phi)/(1 - \sin\phi)$, Eq. 8 can be transformed into:

$$d\varepsilon_r^p = -K_\phi d\varepsilon_\theta^p \tag{4}$$

3.2 Critical supporting pressure (P_{ic})

When the tunnel radius is equal to that of the plastic zone, P_i is equal to P_{ic}. Therefore, σ_r and σ_θ at the radius of the tunnel satisfy the stress condition:

$$\begin{cases} \sigma_r + \sigma_\theta = 2P_0 \\ f(\sigma_r, \sigma_\theta) = 0 \\ \sigma_r = P_{ic} \end{cases} \tag{5}$$

Then, the expression of P_{ic} is:

$$2P_0 - 2P_{ic} + \left(\frac{\left(1 + \sin\varphi_{(P_{ic})}\right)}{\left(1 - \sin\varphi_{(P_{ic})}\right)} - 1\right)P_{ic} + \frac{2c_{(P_{ic})}\cos\varphi_{(P_{ic})}}{1 - \sin\varphi_{(P_{ic})}} = 0 \tag{6}$$

So, P_{ic} can be obtained by solving the above-mentioned expression.

3.3 Elastoplastic solution for plastic zone of surrounding rock

As shown in Figure 8, the plastic zone is divided into n concentric annuli and the boundary of i th is in Eq. 7:

$$\rho_{(i)} = r_{(i)}/R_p \tag{7}$$

R_p is the plastic zone radius and it is assumed that each annulus has the same thickness, which can be expressed as below:

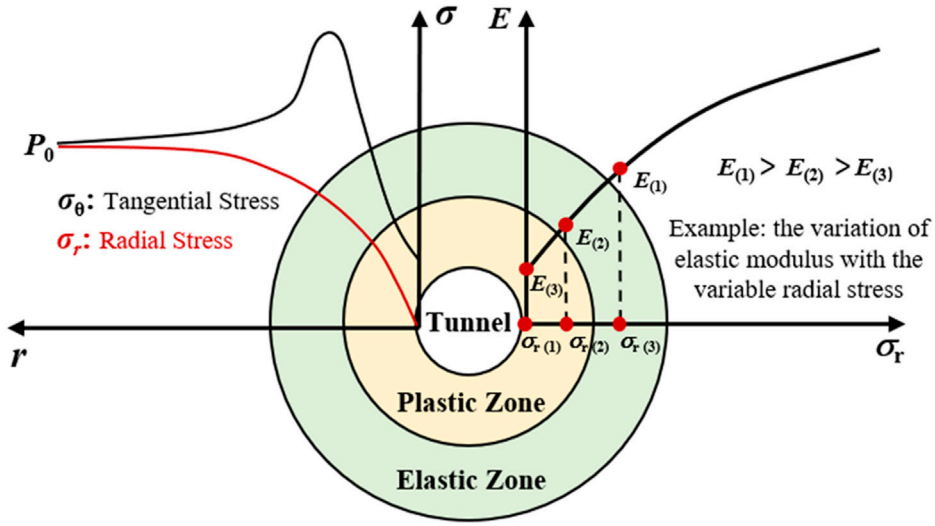

FIGURE 6
Secondary stress state of surrounding rock and variation of mechanical parameters of surrounding rock.

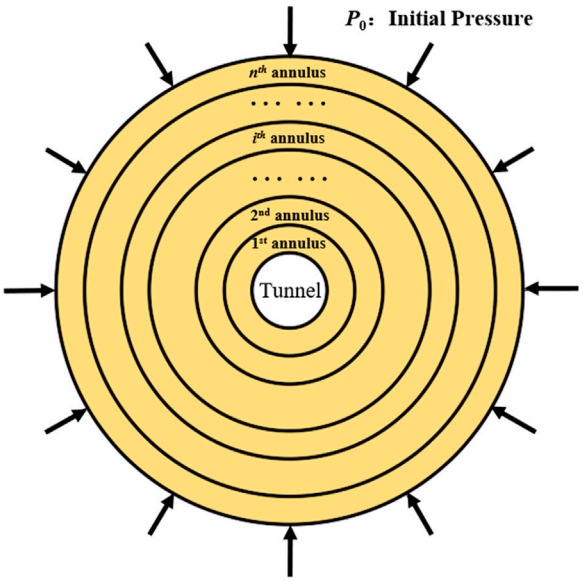

FIGURE 7
Stress partition of tunnel surrounding rock.

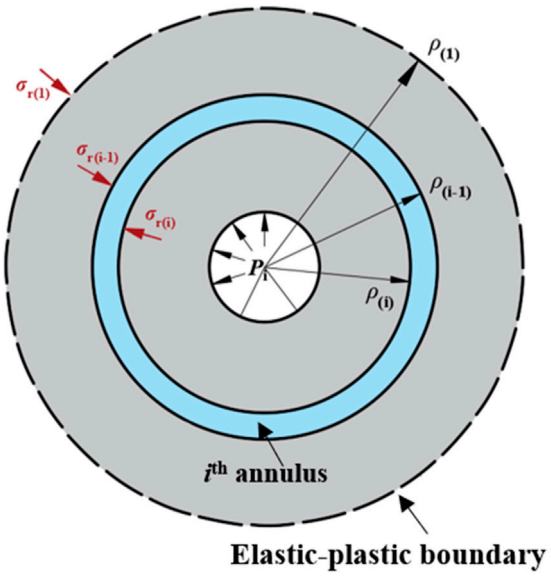

FIGURE 8
Plastic zone of tunnel surrounding rock.

$$\Delta\rho = \rho_{(i)} - \rho_{(i-1)} \tag{8}$$

The outer stress boundary condition ($\rho_{(1)} = 1$) in the plastic zone is:

$$\begin{cases} \sigma_{r(1)} + \sigma_{\theta(1)} = 2P_0 \\ f\left(\sigma_{r(1)}, \sigma_{\theta(1)}\right) = 0 \end{cases} \tag{9}$$

Eq. 9 can be solved using MATLAB software, then $\sigma_{r(1)}$ and $\sigma_{\theta(1)}$ can be obtained.

Then, the strain in the first ring is:

$$\begin{cases} \varepsilon^e_{r(1)} = (1+\nu_{(1)})(\sigma_{r(1)} - P_0)/E_{(\sigma_{r(1)})} \\ \varepsilon^e_{\theta(1)} = (P_0 - \sigma_{r(1)})(1+\nu_{(1)})/E_{(\sigma_{r(1)})} \end{cases} \tag{10}$$

$\sigma_{r(i)}$ and $\sigma_{\theta(i)}$ of any ring (i th ring) is obeyed by the yield criterion. So, the yield criterion is:

$$f\left(\sigma_{r(i)}, \sigma_{\theta(i)}\right) = \frac{3\sin\varphi_{(\sigma_{r(i)})} - 1}{1 - \sin\varphi_{(\sigma_{r(i)})}}\sigma_{r(i)} + \sigma_{\theta(i)} + \frac{2c_{(\sigma_{r(i)})}\cos\varphi_{(\sigma_{r(i)})}}{1 - \sin\varphi_{(\sigma_{r(i)})}} \tag{11}$$

Meanwhile, $\sigma_{r(i)}$ and $\sigma_{\theta(i)}$ satisfy the equilibrium equation:

$$d\sigma_{r(i)}/d\rho_{(i)} + \left(\sigma_{r(i)} - \sigma_{\theta(i)}\right)/\rho_{(i)} = 0 \tag{12}$$

Eq. 12 could be transformed as:

$$\frac{\sigma_{r(i)} - \sigma_{r(i-1)}}{\Delta\rho} + \frac{2\sin\varphi_{(\overline{\sigma_r})}\left(\sigma_{r(i)} + \sigma_{r(i-1)}\right) + \frac{4c_{(\overline{\sigma_r})}\cos\varphi_{(\overline{\sigma_r})}}{1-\sin\varphi_{(\overline{\sigma_r})}}}{\rho_{r(i)} + \rho_{r(i-1)}} = 0 \tag{13}$$

Where:

$$\bar{\sigma}_{r(i)} = \frac{\left(\sigma_{r(i)} + \sigma_{r(i-1)}\right)}{2}$$

Then, $\sigma_{r(i)}$ and $\sigma_{\theta(i)}$ are expressed as:

$$\sigma_{r(i)} = \frac{\frac{2c_{(\sigma_{r(i)})}\cos\varphi_{(\sigma_{r(i)})}}{\left(1-\sin\varphi_{(\sigma_{r(i)})}\right)\left(\rho_{r(i)}+\rho_{r(i-1)}\right)} + \left(\frac{1}{\Delta\rho} - \frac{1-\sin\varphi_{(\sigma_{r(i)})}}{\left(1-\sin\varphi_{(\sigma_{r(i)})}\right)\left(\rho_{r(i)}+\rho_{r(i-1)}\right)}\right)\sigma_{r(i-1)}}{\frac{1}{\Delta\rho} + \frac{1+\sin\varphi_{(\sigma_{r(i)})}}{\left(1-\sin\varphi_{(\sigma_{r(i)})}\right)\left(\rho_{r(i)}+\rho_{r(i-1)}\right)}} \tag{14}$$

$$\sigma_{\theta(i)} = \frac{2c_{(\sigma_{r(i)})}\cos\varphi_{(\sigma_{r(i)})}}{1-\sin\varphi_{(\sigma_{r(i)})}} - 2\sin\varphi_{(\sigma_{r(i)})}\sigma_{r(i)} \tag{15}$$

And stress increment is:

$$\Delta\sigma_{r(i)} = \sigma_{r(i)} - \sigma_{r(i-1)} \tag{16}$$

$$\Delta\sigma_{\theta(i)} = \sigma_{\theta(i)} - \sigma_{\theta(i-1)} \tag{17}$$

Total strains can be separated into two parts:

$$\begin{Bmatrix}\varepsilon_r\\ \varepsilon_\theta\end{Bmatrix} = \begin{Bmatrix}\varepsilon_r^e\\ \varepsilon_\theta^e\end{Bmatrix} + \begin{Bmatrix}\varepsilon_r^p\\ \varepsilon_\theta^p\end{Bmatrix} \tag{18}$$

So that Eq. 18 can be reformulated as:

$$\begin{Bmatrix}\varepsilon_{r(i)}\\ \varepsilon_{\theta(i)}\end{Bmatrix} = \begin{Bmatrix}\varepsilon^e_{r(i-1)} + \Delta\varepsilon^e_{r(i)}\\ \varepsilon^e_{\theta(i-1)} + \Delta\varepsilon^e_{\theta(i)}\end{Bmatrix} + \begin{Bmatrix}\varepsilon^p_{r(i-1)} + \Delta\varepsilon^p_{r(i)}\\ \varepsilon^p_{\theta(i-1)} + \Delta\varepsilon^p_{\theta(i)}\end{Bmatrix} \tag{19}$$

Combined with Eqs 16, 17, the elastic strain increments are:

$$\Delta\varepsilon^e_{r(i)} = \frac{\left(1+\nu_{(i)}\right)\left(\left(1-\nu_{(i)}\right)\Delta\sigma_{r(i)} - \nu_{(i)}\Delta\sigma_{\theta(i)}\right)}{E_{(i)}} \tag{20}$$

$$\Delta\varepsilon^e_{\theta(i)} = \frac{\left(1+\nu_{(i)}\right)\left(\left(1-\nu_{(i)}\right)\Delta\sigma_{\theta(i)} - \nu_{(i)}\Delta\sigma_{r(i)}\right)}{E_{(i)}} \tag{21}$$

Combined with Eqs 19–21, the compatibility equation (Eq. 12) can be approximated as:

$$\frac{1+\nu_{(i)}}{E_{(i)}}\frac{2\sin\varphi_{(\overline{\sigma_r})}\left(\sigma_{r(i)} + \sigma_{r(i-1)}\right) + \frac{4c_{(\overline{\sigma_r})}\cos\varphi_{(\overline{\sigma_r})}}{1-\sin\varphi_{(\overline{\sigma_r})}}}{\rho_{r(i)} + \rho_{r(i-1)}} - \frac{d\varepsilon^e_{\theta(i)} + d\varepsilon^p_{\theta(i)}}{d\rho} + 2\frac{\varepsilon^p_{\theta(i)} - \varepsilon^p_{r(i)}}{\rho_{r(i)} + \rho_{r(i-1)}} = 0 \tag{22}$$

Approximating Eq. 22 with regard to ρ and rearranging $\Delta\varepsilon^p_{\theta(i)}$ gives:

$$\Delta\varepsilon^p_{\theta(i)} = \frac{\left[\frac{\left(1+\nu_{(i)}\right)\left(2\sin\varphi_{(\overline{\sigma_r})}\left(\sigma_{r(i)}+\sigma_{r(i-1)}\right) + \frac{4c_{(\overline{\sigma_r})}\cos\varphi_{(\overline{\sigma_r})}}{1-\sin\varphi_{(\overline{\sigma_r})}}\right)}{\left(\rho_{r(i)}+\rho_{r(i-1)}\right)E_{(i)}} - \frac{2\left(\varepsilon^p_{\theta(i-1)} - \varepsilon^p_{r(i-1)}\right)}{\rho_{r(i)}+\rho_{r(i-1)}} - \frac{\Delta\varepsilon^e_{\theta(i)}}{\Delta\rho_{(i)}}\right]}{\left[\frac{2+2K_\varphi}{\rho_{r(i)}+\rho_{r(i-1)}} + \frac{1}{\Delta\rho_{(i)}}\right]} \tag{23}$$

$\Delta\varepsilon^p_{r(i)}$ is given as below:

$$\Delta\varepsilon^p_{r(i)} = -K_\varphi\Delta\varepsilon^p_{\theta(i)} \tag{24}$$

Total strain is:

$$\begin{Bmatrix}\varepsilon_{r(i)}\\ \varepsilon_{\theta(i)}\end{Bmatrix} = \begin{Bmatrix}\varepsilon_{r(i-1)}\\ \varepsilon_{\theta(i-1)}\end{Bmatrix} + \begin{Bmatrix}\Delta\varepsilon^e_{r(i)}\\ \Delta\varepsilon^e_{\theta(i)}\end{Bmatrix} + \begin{Bmatrix}\Delta\varepsilon^p_{r(i)}\\ \Delta\varepsilon^p_{\theta(i)}\end{Bmatrix} \tag{25}$$

For a sufficiently large n, mechanical parameters of the $(i+1)$ ring can be replaced by those of the i ring and the stop condition of finite difference iterative process is:

$$\sigma_{r(n)} = P_i \tag{26}$$

R_p can be calculated in accordance with $\rho_{(n)}$ and the displacement at the tunnel can be obtained using the following expression:

$$R_p = r_0/\rho_{(n)} \tag{27}$$

$$u_{(n)} = \varepsilon_{\theta(n)} \cdot r_0 \tag{28}$$

3.4 Elastoplastic solution for elastic zone of surrounding rock

After tunnel excavation, the elastic zone can be regarded as a thick-walled cylinder. The stress conditions at inner and outer boundaries are:

$$\begin{cases}\sigma_{r(outer)} = P_0, \sigma_{\theta(outer)} = P_0\\ \sigma_{r(inner)} = \sigma_{r(1)}, \sigma_{\theta(inner)} = \sigma_{\theta(1)}\end{cases} \tag{29}$$

Lame solution (Yi et al., 2020) can calculate radial and tangential stresses at any radius. So, the stress expressions at any radius in the elastic zone are listed below:

$$\sigma_{r(i)-elastic} = P_0\frac{r^2_{(i-elastic)} - R^2_p}{r^2_{(i-elastic)}} + \sigma_{r(1)}\frac{R^2_P}{r^2_{(i-elastic)}} \tag{30}$$

$$\sigma_{\theta(i)-elastic} = P_0\frac{r^2_{(i-elastic)} + R^2_p}{r^2_{(i-elastic)}} - \sigma_{r(1)}\frac{R^2_P}{r^2_{(i-elastic)}} \tag{31}$$

Further, combined with the mechanical parameter expression of the surrounding rock, the strain expressions at any radius in the elastic zone are as follows, and the subscript "elastic" is applied in the expression to represent the elastic zone of the surrounding rock.

$$\varepsilon_{r(i)-elastic} = \frac{1+\nu_{(i)}}{E_{(i)}}\left[\left(1-\nu_{(i)}\right)\sigma_{r(i)-elastic} - \nu_{(i)}\sigma_{\theta(i)-elastic}\right] \tag{32}$$

$$\varepsilon_{\theta(i)-elastic} = \frac{1+\nu_{(i)}}{E_{(i)}}\left[\left(1-\nu_{(i)}\right)\sigma_{\theta(i)-elastic} - \nu_{(i)}\sigma_{r(i)-elastic}\right] \tag{33}$$

3.5 Finite difference calculation process

The above-mentioned expressions were compiled by MATLAB software for automatic solution operation. The finite difference calculation process is shown in Figure 9.

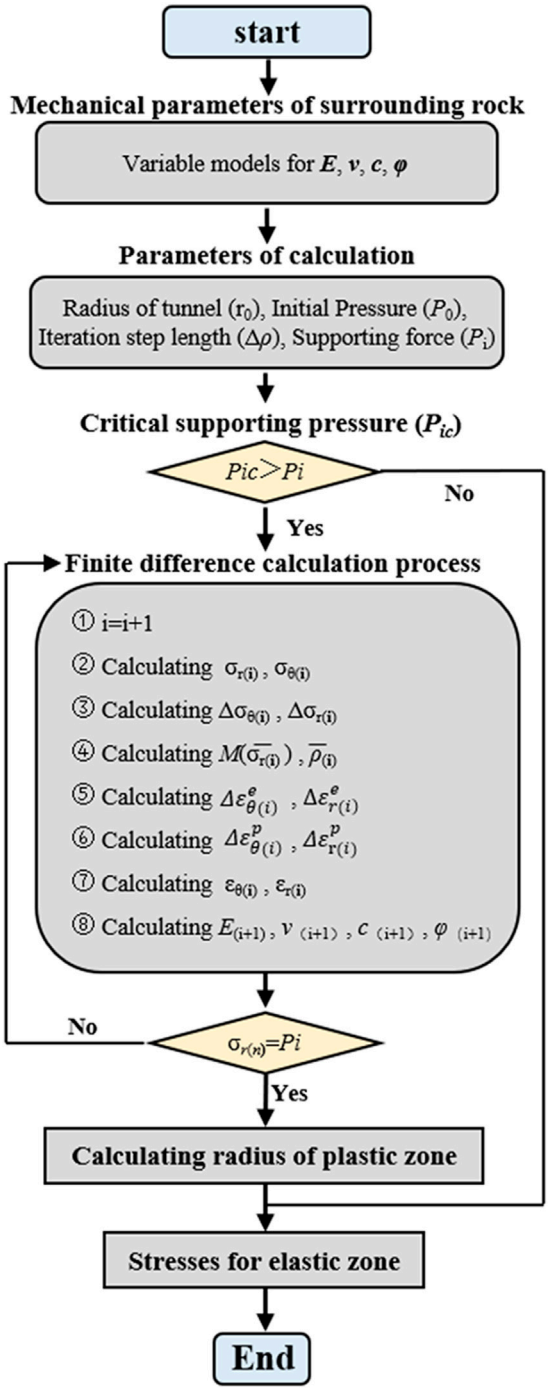

FIGURE 9
Finite difference calculation process.

3.6 Verification example

If the undetermined coefficient of the confining pressure term is equal to zero in every variable model for the mechanical parameters of surrounding rock, the finite difference process can be reduced to the classic elastoplastic solution.

Therefore, in order to validate this new solution, the results of two methods (new solution and classic solution) are compared with each other. Parameters of verification examples are listed in Table 1. Expressions of classic solutions are obtained from (Fang et al., 2021).

TABLE 1 Parameters of verification example.

Name	Parameter	Value
tunnel	initial pressure	25 MPa
	radius	3 m
	supporting force	0 kPa
classic solution	elasticity modulus	12.49 GPa
	Poisson ratio	0.249
	cohesion	2 MPa
	friction angle	30°
proposed solution	variable model for elasticity modulus	A_E=12.49, B_E=0
	variable model for Poisson ratio	v_0=0.249
	variable model for cohesion	A_c=2, B_c=0
	variable model for friction angle	A_φ=0, B_φ=30°

As shown in Figure 10, the plastic zone radius and radial stress distribution results of the proposed solution agree with those of the classic solutions, and displacement around the tunnel resulting from the proposed method is slightly greater than that of the classic solution, but the deviation does not affect the accuracy of the proposed method. The reason for the deviation in the displacement of tunnel surrounding rock is that the classic solution ignores the small quantity of higher order in the derivation process, so the calculated result is smaller than that obtained by the proposed solution. However, the deviation cannot affect the accuracy of the proposed method; therefore, the above result validates the proposed solution as accurate and correct.

4 Analysis of influencing factors

The influence of initial pressure, supporting force of the tunnel, and radius of the tunnel on stress and displacement around the tunnel is analyzed by the proposed solution. Taking the Muzhailin tunnel as an example, variable models for the mechanical parameters of surrounding rock are based on experimental results from the Muzhailin tunnel in Table 2 (Li Z et al., 2021). The Muzhailing tunnel is a typical soft rock tunnel under high geo-stress conditions and belongs to the Lanzhou-Chongqing Railway in China. The longitudinal length of the Muzhailing tunnel is 19020m, and the height and width of the tunnel section are 11.98 m and 10.48m, respectively. The maximum geo-stress of the Muzhailing tunnel is 27.5 MPa and the surrounding rock of the Muzhailing tunnel is carbonaceous slate.

4.1 Influence analysis of initial pressure factor

In the influence analysis of the initial pressure (P_0) factor, the tunnel radius (r_0) is 5m, and the supporting force (P_i) is 0 kPa.

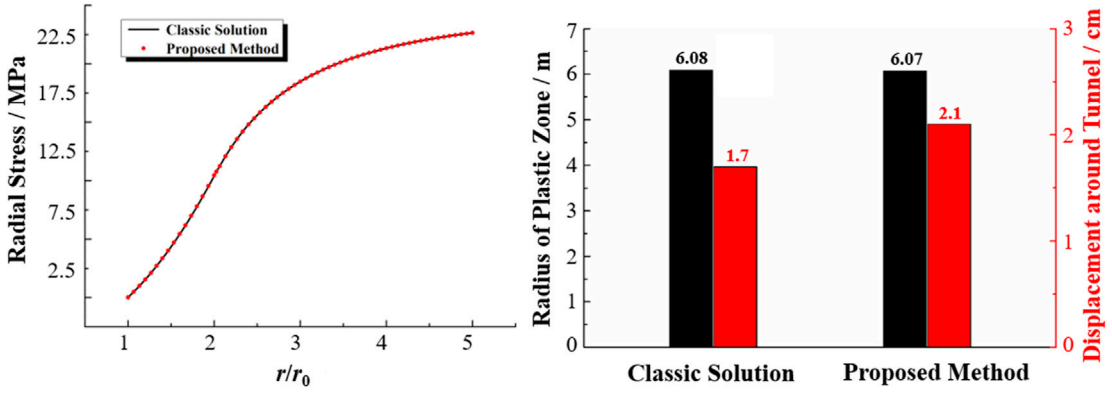

FIGURE 10
Comparison results between classic solution and proposed method.

TABLE 2 Variable models for the mechanical parameters of surrounding rock.

Name	Variable model	Note
elasticity modulus/GPa	$E = 2.51\,(\sigma_r + 1)^{0.33}$	The unit of radial stress is MPa
Poisson ratio	$\nu_0 = 0.33$	
friction angle/°	$\varphi = -1.98\ln(\sigma_r + 1) + 31.19$	
cohesion/MPa	$c = 0.34\,(\sigma_r + 1)^{0.26}$	

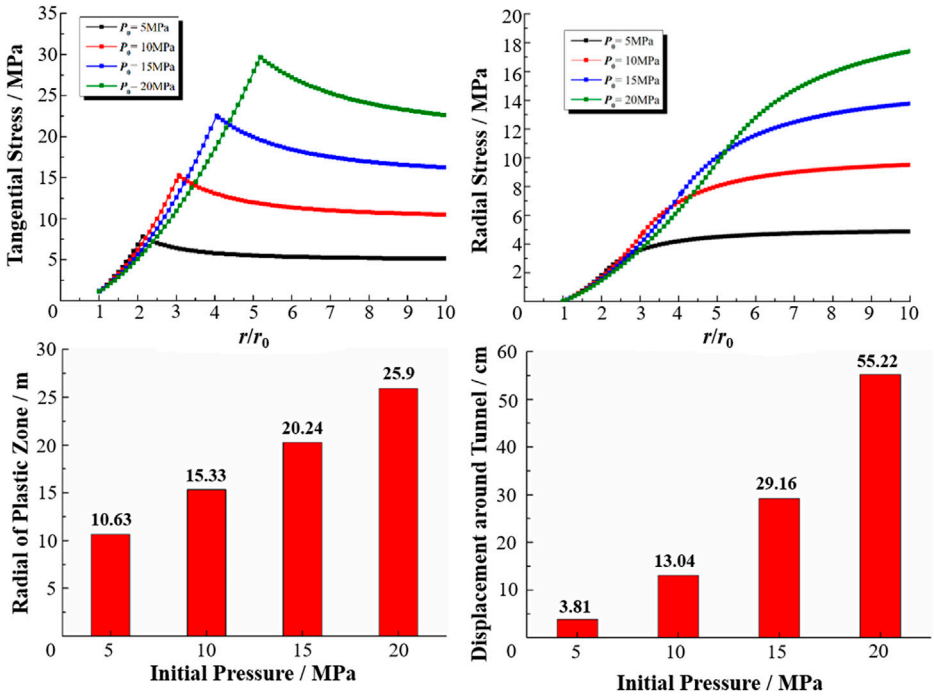

FIGURE 11
Influence analysis results of initial pressure factor.

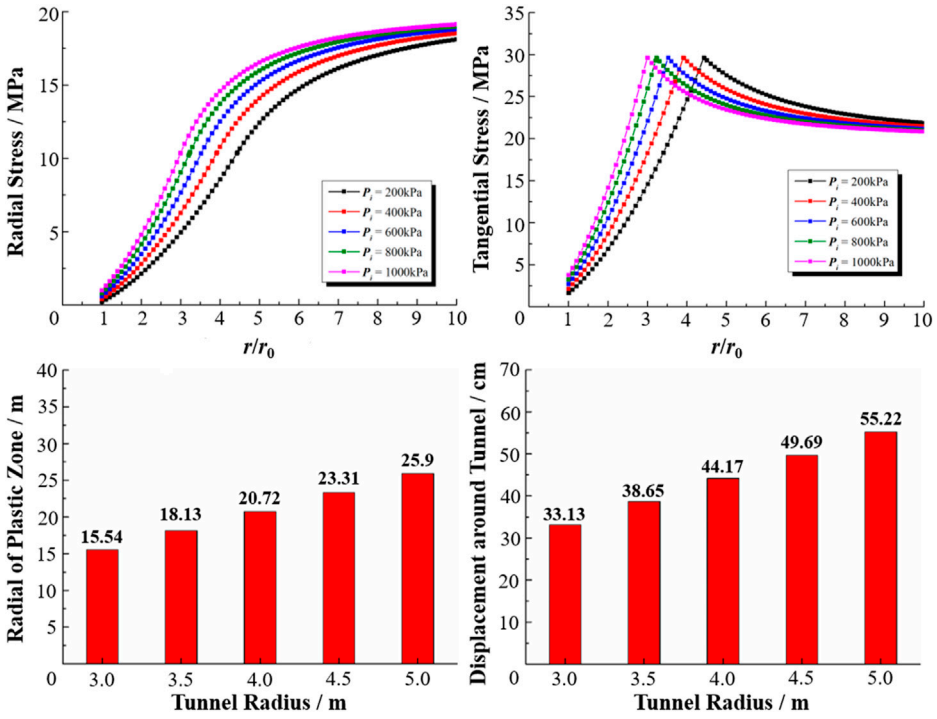

FIGURE 12
Influence analysis results of supporting force factor.

Figure 11 shows the influence analysis results of the initial pressure factor.

As shown in Figure 11, the stress level of tunnel surrounding rock significantly increases with increasing initial pressure. Moreover, the distance from the tunnel center to the appearance location of peak tangential stress of the surrounding rock increases gradually. When the initial pressure is 5 MPa, the peak tangential stress is 7.84 MPa, and its location is 2.16 times the tunnel radius. However, the peak tangential stress is 29.66 MPa, and its location is 5.2 times the tunnel radius when the initial pressure increases to 20 MPa. Displacement around the tunnel and the plastic zone radius of the surrounding rock increase with the increasing initial pressure. When initial pressure is 5 MPa, the plastic zone radius and displacement around the tunnel are 10.63 m and 3.81cm, but they increase to 25.9m and 55.22 cm (increasing by 143% and 1,349%) when initial stress is 20 MPa.

4.2 Influence analysis of supporting force factor

In the influence analysis of the supporting force (P_i) factor, the radius of the tunnel (r_0) is 5 m and the initial pressure (P_0) is 20 MPa. Figure 12 shows the influence analysis results of the supporting force factor.

As shown in Figure 12, the stress state of tunnel surrounding rock gradually changes to a three-dimensional state from a two-dimensional plane state with increasing supporting force. When supporting force increases, the stress level of tunnel surrounding rock increases, but the distance from the tunnel center to the appearance location of peak tangential stress of the surrounding rock gradually decreases. When the supporting force is 200kPa, the distance is 4.42 times the tunnel radius; however, the distance decreases to 2.99 times the tunnel radius (decreasing by 32.35%) when the supporting force increases to 1000 kPa. The peak stresses (including radial and tangential stress) of tunnel surrounding rock are determined only by the strength parameters of the surrounding rock; therefore, the supporting force only affects the appearance location of the peak stresses, not their values. Displacement around the tunnel and the plastic zone radius of the surrounding rock both decrease with increasing supporting force. The plastic zone radius of the surrounding rock and displacement around the tunnel are 22.12 m and 40cm, respectively, when the supporting force is 200 kPa. However, the radius and the displacement decrease to 14.97 m (decreasing by 32.32%) and 17.9 cm (decreasing by 61.96%), respectively, when the supporting force increases to 1000 kPa.

4.3 Influence analysis of tunnel radius factor

In the influence analysis of the tunnel radius (r_0) factor, the initial pressure (P_0) is 20 MPa and the supporting force (P_i) is 0 kPa. Figure 13 shows the influence analysis results of the tunnel radius factor.

As shown in Figure 13, the stress level of tunnel surrounding rock gradually decreases, but the stress disturbance range of the surrounding rock increases as the tunnel radius increases. The

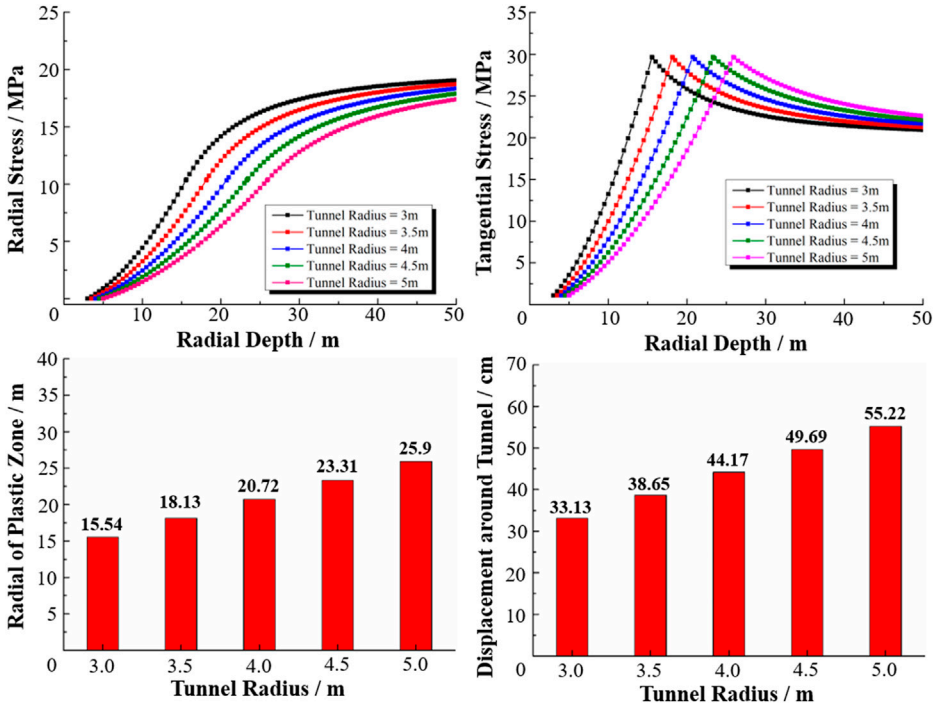

FIGURE 13
Influence analysis results of tunnel radius factor.

distance from the tunnel center to the appearance location of peak tangential stress of the surrounding rock gradually increases as the tunnel radius increases. When the radius of the tunnel is 3 m, the distance is 15.54m; however, the distance increases to 25.9 m (increasing by 66.67%) when the tunnel radius increases to 5 m. The tunnel radius only affects the appearance location of peak tangential stress of the surrounding rock, not its values. With the increasing tunnel radius, displacement around the tunnel and the plastic zone radius of the surrounding rock both increase. The plastic zone radius of the surrounding rock and displacement around the tunnel are 15.54 m and 33.13 cm, respectively, when the tunnel radius is 3 m. However, the radius and the displacement respectively increase to 25.9 m (increasing by 66.67%) and 55.22 cm (increasing by 66.68%) when the tunnel radius increases to 5 m.

5 Conclusion

This paper firstly investigates the effect of confining pressure on the deformation and strength characteristics of soft rock (slate and phyllite) using triaxial experiment results and proposed variable models for the mechanical parameters (E, ν, c, φ) of soft rock with confining pressure variation. Secondly, according to the second stress state around tunnels and these variable models for the mechanical parameters of soft rock, a new elastoplastic solution for tunnels was devised, which simultaneously considers the effect of confining pressure on the deformation and strength characteristics of the surrounding rock. Moreover, this new solution is validated by classical solutions. Finally, the effect of multiple factors (initial pressure, supporting force, and tunnel radius) on the stress and displacement of tunnel surrounding rock are analyzed. Several main conclusions can be summarized as follows.

1. Regarding the influence of confining pressure on the deformation parameters (E, ν) of soft rock, confining pressure has a significant influence on the elasticity modulus but does not significantly affect the Poisson ratio of soft rock. With increasing confining pressure, the elasticity modulus significantly increases, but the Poisson ratio is practically constant. Variable parameter models for the elasticity modulus (its form being power function) and the Poisson ratio (its form being constant function) were established, respectively, with the influence of confining pressure.
2. Regarding the influence of confining pressure on the strength parameters (c, φ) of soft rock, confining pressure has a significant influence on the friction angle and cohesion of soft rock. With increasing confining pressure, the friction angle decreases and cohesion increases gradually. Variable parameter models for the friction angle (its form being logarithmic function) and cohesion (its form being power function) were established, respectively, with the influence of confining pressure.
3. After soft rock tunnel excavation, with the variable radial stress of the surrounding rock, the mechanical parameters (E, ν, c, φ) of the surrounding rock vary and are controlled by radial stress, not constant. Based on the secondary stress state of surrounding rock and variable models for the mechanical parameters of soft rock, a new elastoplastic solution was devised, which simultaneously considers the effect of confining pressure on the deformation and

strength characteristics of the surrounding rock. Meanwhile, this new solution can be reduced to the classical solution, and its correctness and accuracy are validated by the classical solution.

4. The influence of multiple factors (initial pressure, supporting force, and tunnel radius) on the stress and displacement of tunnel surrounding rock are analyzed. With increasing initial pressure, the displacement around the tunnel and the plastic zone radius of the surrounding rock both gradually increase. With the increasing supporting force of the tunnel, the distance from the tunnel center to the appearance location of peak tangential stress of the surrounding rock decreases. With increasing supporting force, the plastic zone radius of the surrounding rock and displacement around the tunnel both decrease gradually. With increasing tunnel radius, the distance increases from the tunnel center to the appearance location of peak tangential stress of the surrounding rock. With increasing tunnel radius, the plastic zone radius of the surrounding rock and displacement around the tunnel both increase gradually.

Data availability statement

The original contributions presented in the study are included in the article/Supplementary Material, further inquiries can be directed to the corresponding author.

Author contributions

This study's goals and ideas are offered by YZ and YD derived the formula and wrote the first manuscript, HZ analyzed the original data, and MW and LY revised and polished the manuscript. All the listed authors contributed substantially to the research and approved the paper's publication.

Acknowledgments

State Key Laboratory of Mechanical Behavior and System Safety of Traffic Engineering Structures, Major Science and Technology project (2019-A05) of China Railway Construction Co. LTD, Hebei Technology Innovation Center for Intelligent Development and Control of Underground Built Environment, opening research project (KF2021-09) and research project (QN202203) supported this paper.

Conflict of interest

The authors declare that the research was conducted in the absence of any commercial or financial relationships that could be construed as a potential conflict of interest.

The reviewer XZ declared a shared affiliation with the authors MW, YL to the handling editor at time of review.

Publisher's note

All claims expressed in this article are solely those of the authors and do not necessarily represent those of their affiliated organizations, or those of the publisher, the editors and the reviewers. Any product that may be evaluated in this article, or claim that may be made by its manufacturer, is not guaranteed or endorsed by the publisher.

Supplementary material

The Supplementary Material for this article can be found online at: https://www.frontiersin.org/articles/10.3389/feart.2023.1143003/full#supplementary-material

References

Alam, M. R., Swamidas, A. S. J., Gale, J., and Munaswamy, K. (2008). Mechanical and physical properties of slate from britannia cove, newfoundland. *Can. J. Civ. Eng.* 35 (7), 751–755. doi:10.1139/l08-042

Chen, J., Liu, W., Chen, L., Luo, Y., Li, Y., Gao, H., et al. (2020). Failure mechanisms and modes of tunnels in monoclinic and soft-hard interbedded rocks: A case study. *KSCE J. Civ. Eng.* 24 (4), 1357–1373. doi:10.1007/s12205-020-1324-3

Chen, W., Zhang, D., Fang, Q., Chen, X., and Xu, T. (2022). A new numerical finite strain procedure for a circular tunnel excavated in strain-softening rock masses and its engineering application. *Appl. Sci.* 12 (5), 2706. doi:10.3390/app12052706

Chen, Y.-F., Wei, K., Liu, W., Hu, S.-H., Hu, R., and Zhou, C.-B. (2016). Experimental characterization and micromechanical modelling of anisotropic slates. *Rock Mech. Rock Eng.* 49 (9), 3541–3557. doi:10.1007/s00603-016-1009-x

Cui, L., Zheng, J.-J., Zhang, R.-J., and Dong, Y.-K. (2015). Elasto-plastic analysis of a circular opening in rock mass with confining stress-dependent strain-softening behaviour. *Tunn. Undergr. Space Technol.* 50, 94–108. doi:10.1016/j.tust.2015.07.001

Debecker, B., and Vervoort, A. (2009). Experimental observation of fracture patterns in layered slate. *Int. J. Fract.* 159 (1), 51–62. doi:10.1007/s10704-009-9382-z

Fang, H., Zhang, D., Fang, Q., and Wen, M. (2021). A generalized complex variable method for multiple tunnels at great depth considering the interaction between linings and surrounding rock. *Comput. Geotechnics* 129, 103891. doi:10.1016/j.compgeo.2020.103891

Fu, H., Zhang, J., Huang, Z., Shi, Y., and Chen, W. (2018). A statistical model for predicting the triaxial compressive strength of transversely isotropic rocks subjected to freeze–thaw cycling. *Cold Regions Sci. Technol.* 145, 237–248. doi:10.1016/j.coldregions.2017.11.003

Gholami, R., and Rasouli, V. (2013). Mechanical and elastic properties of transversely isotropic slate. *Rock Mech. Rock Eng.* 47 (5), 1763–1773. doi:10.1007/s00603-013-0488-2

Hao, X., Xu, Q., Yang, D., Wang, S., and Wei, Y. (2019). Effect of bedding angle and confining pressure on the brittleness of geomaterials: A case study on slate. *Adv. Mater. Sci. Eng.* 2019, 1–17. doi:10.1155/2019/1650170

Hu, K., Feng, Q., and Wang, X. (2016). Experimental research on mechanical property of phyllite tunnel surrounding rock under different moisture state. *Geotechnical Geol. Eng.* 35 (1), 303–311. doi:10.1007/s10706-016-0107-6

Li, F., Jiang, A., and Zheng, S. (2021). Anchoring parameters optimization of tunnel surrounding rock based on particle swarm optimization. *Geotechnical Geol. Eng.* 39 (6), 4533–4543. doi:10.1007/s10706-021-01782-3

Li, Y., Yang, S., Tang, X., Ding, Y., and Zhang, Q. (2020). Experimental investigation of the deformation and failure behavior of a tunnel excavated in mixed strata using transparent soft rock. *KSCE J. Civ. Eng.* 24 (3), 962–974. doi:10.1007/s12205-020-0072-8

Li, Z., Li, Z., Huang, W., Xu, Z., Zhang, W., and Chen, K. (2021). Tunnel bottom cavity laws of heavy-haul Railway tunnel under train load and groundwater in weak surrounding rock condition. *KSCE J. Civ. Eng.* 26 (3), 1451–1464. doi:10.1007/s12205-021-5953-y

Luo, Y., Wu, Y., Chen, J., Dong, F., Liu, W., Chen, L., et al. (2021). Back-calculation method of rock mass pressure in a shallow-buried super large-span tunnel using upper-bench CD method. *KSCE J. Civ. Eng.* 26 (1), 433–447. doi:10.1007/s12205-021-0312-6

Lyu, C., Liu, J., Ren, Y., Liang, C., and Liao, Y. (2021). Study on very long-term creep tests and nonlinear creep-damage constitutive model of salt rock. *Int. J. Rock Mech. Min. Sci.* 146, 104873. doi:10.1016/j.ijrmms.2021.104873

Lyu, C., Liu, J., Ren, Y., Liang, C., and Zeng, Y. (2022). Mechanical characteristics and permeability evolution of salt rock under thermal-hydro-mechanical (THM) coupling condition. *Eng. Geol.* 302, 106633. doi:10.1016/j.enggeo.2022.106633

Saeidi, O., Vaneghi, R. G., Rasouli, V., and Gholami, R. (2013). A modified empirical criterion for strength of transversely anisotropic rocks with metamorphic origin. *Bull. Eng. Geol. Environ.* 72 (2), 257–269. doi:10.1007/s10064-013-0472-9

Singh, M., Samadhiya, N. K., Kumar, A., Kumar, V., and Singh, B. (2015). A nonlinear criterion for triaxial strength of inherently anisotropic rocks. *Rock Mech. Rock Eng.* 48 (4), 1387–1405. doi:10.1007/s00603-015-0708-z

Wu, F., He, C., Kou, H., Wang, B., Meng, W., Meng, H., et al. (2022). Discussion on reasonable clear spacing of twin-tunnels in weak surrounding rock: Analytical solution and numerical analysis. *KSCE J. Civ. Eng.* 26 (5), 2428–2442. doi:10.1007/s12205-022-0898-3

Xu, G., He, C., Su, A., and Chen, Z. (2018). Experimental investigation of the anisotropic mechanical behavior of phyllite under triaxial compression. *Int. J. Rock Mech. Min. Sci.* 104, 100–112. doi:10.1016/j.ijrmms.2018.02.017

Yi, K., Kang, H., Ju, W., Liu, Y., and Lu, Z. (2020). Synergistic effect of strain softening and dilatancy in deep tunnel analysis. *Tunn. Undergr. Space Technol.* 97, 103280. doi:10.1016/j.tust.2020.103280

frontiers | Frontiers in Earth Science

TYPE Original Research
PUBLISHED 20 February 2023
DOI 10.3389/feart.2023.1140038

OPEN ACCESS

EDITED BY
Yuwei Zhang,
Xi'an University of Architecture and Technology, China

REVIEWED BY
Kai Wei,
Southwest Jiaotong University, China
Yongjun Ni,
Beijing Jiaotong University, China

*CORRESPONDENCE
Chenglong Ge,
893261710@qq.com

SPECIALTY SECTION
This article was submitted to Environmental Informatics and Remote Sensing, a section of the journal Frontiers in Earth Science

RECEIVED 08 January 2023
ACCEPTED 08 February 2023
PUBLISHED 20 February 2023

CITATION
Zhou H, Ge C, Chen Y and Song X (2023), Study on performance and fractal characteristics of high-strength manufactured sand concrete with different MB values.
Front. Earth Sci. 11:1140038.
doi: 10.3389/feart.2023.1140038

Study on performance and fractal characteristics of high-strength manufactured sand concrete with different MB values

Hailong Zhou[1], Chenglong Ge[1]*, Yan Chen[1] and Xingfang Song[2]

[1]College of Water Resources and Civil Engineering, Inner Mongolia Agricultural University, Hohhot, China, [2]Inner Mongolia Road and Bridge Group Co., Ltd., Hohhot, China

The mud powder in the manufactured sand will have an influence on the indicators of the manufactured sand concrete (MSC), and the methylene blue value can quantitatively indicate the mud powder content. To demonstrate the impact of MB values on the performance and microstructural characteristics of the manufactured sand concrete, the paper designed five high-strength MSC proportions at five MB values by controlling the clay powder content. On this basis, the workability, chloride migration coefficient, relative dynamic modulus of elasticity (P), mass loss rate (η), and dry shrinkage rate of MSC concrete were tested under five mix ratios, and the relationship between concrete microstructure, fractal characteristics, and compressive strength (f_{cc}) was analyzed by combining SEM technology and fractal theory. The experiment showed that: the higher the MB, the lower the fluidity of the MSC, and the cohesiveness gradually increases, while the water retention remains basically unchanged. In addition, the chloride migration coefficient gradually increases, the P after 300 freeze-thaw cycles first increases and then gradually decreases, while the η and drying shrinkage first decreases and then gradually increases, and the MB value corresponding to the turning point of these three changes are all 1.10. With MB values of 0.85 and 1.10, the degree of hydration of MSC is higher and the overall structural compactness is better. The higher the MB value, the more inadequate the hydration of concrete, and the mineral components such as fly ash that have not been hydrated inside gradually increase, which leads to the gradual decrease of the overall structure compactness. In addition, when the MB value is small, the SEM image texture of concrete is relatively simple, the fractal dimension value is small, and the corresponding f_{cc} is large. When the MB value is large, the texture of the SEM image is complex, the fractal dimension is large, and the corresponding f_{cc} is small.

KEYWORDS

MB value, manufactured sand concrete, working performance, durability, fractal characteristics

1 Introduction

The MS will produce mud powder in the mining and processing process, and the fine powder particles below 75 μm are composed of stone powder MS. It has been shown that the right amount of stone powder has an improving effect on the performance of MSC (Wang et al., 2021; Zheng et al., 2021; Elik and Marar, 1996). However, unlike stone powder, mud powder will adversely affect the working performance, mechanical properties, and durability

of concrete due to its characteristics, which is also an important reason for controlling the content of mud powder in MS in engineering applications (Xiao et al., 2020; Che et al., 2021).

At present, the relevant scholars mainly use methylene blue (MB) value to characterize the silt content in MC, and systematically study the working performance and mechanical properties of MSC under different MB values. Wang et al. (2009) investigated the workability and mechanical properties of MSC with different MB values. Research indicates that the MSC compatibility, flexural strength, and 7 d f_{cc} all gradually decreased with the MB increase, but the 28d f_{cc} remained the same. Gui et al. (2011) investigated the compatibility of MSC with different stone dust contents and MB values in MS. Research indicates that when the MB value < 1, the appropriate amount of stone powder in the MS helps to improve the compatibility of MSC; MB value ≥ 1, the stone powder content should be controlled < 5% to ensure the workability of MSC. Deng et al. (2021) investigated the f_{cc} of MSC at different MB values and pointed out that the highest point of 3d f_{cc} of MSC occurs at MB value 0.75 and the highest point of 7d f_{cc} of MSC occurs at MB value 1.5. Zhou et al. (2016) investigated the freezing resistance and strength of MSC with different MB values, and the results showed that increasing the MB value would not have a negative effect on the f_{cc} of C30 MSC, but would reduce the f_{cc} and freezing resistance of C60 MSC. Sun et al. (2021) discussed the f_{cc} and carbonation of MSC at different MB values, and the results showed that the f_{cc} of MSC shows a trend of slowly increasing and then rapidly decreasing with the MB value, the modulus of elasticity decreased gradually, and the carbonation depth became deeper gradually. Xia et al. (2021) found that as the MB value increased, MSC indicators such as electrical flux rate and chloride ion diffusion coefficient showed a tendency to increase first and then decrease. The research shows that there are large differences in the performance of different strength grades of MSC at different MB values (Wang et al., 2012). At present, there are fewer systematic studies on the effect of MB value on the performance of MSC, especially for high-strength MSC.

In addition, the deterioration of MSC properties is the macroscopic manifestation of the internal microstructure change. Therefore, it is of significance to study the internal structure changes of concrete from a micro perspective for understanding the deterioration mechanism of concrete during service. At present, related scholars commonly use the SEM method to investigate the hydration products and internal structure change pattern of concrete from a microscopic perspective (Mouret et al., 1999; Diamond and Huang, 2001). Shen et al. (2021) used the SEM technique to analyze the evolution of internal concrete defects under external load. Yang et al. (2012) used the SEM technique to photograph the transition zone at the concrete interface and observed the evolution of the hydration reaction of aggregates and pastes at various ages. Wang et al. (2005) studied the micro-crack characteristics of concrete at different temperatures using SEM technology. Li et al. (2022) revealed the mechanism of salt and frost deterioration of wind-cured sand concrete using the SEM technique. Patil et al. (2018) studied the microstructure of bagasse ash concrete with SEM technology. Khonsari et al. (2018) revealed the effect of swollen perlite aggregates on the number, shape, and distribution of concrete pores by SEM images. From the existing results, most studies are mainly based on the qualitative description of the apparent morphology characteristics of concrete by SEM, which fails to quantitatively characterize the change characteristics and trends of internal structure. With the development of digital image processing technology, combined with SEM images and fractal theory, establishing quantitative relationships between internal pores and macroscopic mechanical properties of concrete from the microscopic point of view, to realize the purpose of microscopic service to the macroscopic (Zhang et al., 2021; Han et al., 2022).

To explore the influence of MB value on the performance and microstructure characteristics of MSC, the mix proportion of high strength MSC under five MB values was designed by controlling the content of mud powder. On this basis, the effects of MB value on the working performance, chloride penetration resistance, salt freezing resistance, and dry shrinkage of MSC were studied through the working performance test of fresh concrete, chloride penetration resistance test, salt freezing resistance test, and shrinkage test of hardened concrete under five mixing ratios. Secondly, combined with SEM technology and the differential box dimension method, the fractal dimension of the surface of concrete hydration products was quantitatively calculated, the variation law of fractal dimension with MB value was analyzed, and the relationship between fractal dimension and f_{cc} of concrete was established.

2 Experiment

2.1 Testing material

Test materials mainly include the following:

(1) The cement is Jidong P·O42.5 grade cement, 28 d f_{cc} is 54.2 MPa, density is 3,030 kg/m^2, and volume stability is qualified.
(2) Metakaolin was produced by Inner Mongolia Super Brand Building Materials Co., Ltd., with a density of 2.67 g/cm^3.
(3) The fineness of fly ash is 9.1% and the water requirement ratio is 92%.
(4) The coarse and fine aggregates are all produced by Inner Mongolia Lutong Stone Co., Ltd. The parent rock is basalt. The MS is sieved and washed by a 75 μm square-hole sieve. The fineness modulus is 3.5, the bulk density is 1,582 kg/m^3, the crushing index is 16.3%, and the stone powder content is 1.6%.
(5) Mud powder used in Zhuozi Mountain gravel field local soil, through 75 μm square hole sieve, liquid limit W_L=40%, plastic limit W_P=19%.
(6) Additives used in Inner Mongolia Hengzhong Engineering Materials Co., Ltd. Polycarboxylate superplasticizer, water reduction rate of 30%.
(7) The mass fraction of methylene blue ($C_{16}H_{18}ClN_3S{\cdot}3H_2O$) was greater than 95%.

2.2 Test scheme

Experiment to explore the effect of clay powder content on the performance and fractal characteristics of MSC, five different concrete proportions of MSC with different clay powder content

TABLE 1 Proportion of MSC.

Group name	MP content (%)	MB value	C ($kg·m^{-3}$)	FA ($kg·m^{-3}$)	MK ($kg·m^{-3}$)	MP ($kg·m^{-3}$)	MS ($kg·m^{-3}$)	CS ($kg·m^{-3}$)	Water ($kg·m^{-3}$)	WR ($kg·m^{-3}$)	f_{cc} (MPa)	f_{ts} (MPa)
MP0	0	0.85	410	50	40	0	777	1,073	150	6	96.6	5.92
MP0.5	0.5	1.10	410	50	40	3.89	773.11	1,073	150	6	97.4	6.06
MP1	1.0	1.35	410	50	40	7.77	769.23	1,073	150	6	95.3	5.98
MP1.5	1.5	1.70	410	50	40	11.66	765.34	1,073	150	6	93.5	5.75
MP2	2.0	2.00	410	50	40	15.54	761.46	1,073	150	6	92	5.57

Note. MP, is mud powder; C is cement; FA, is fly ash; MK, is metakaolin; MS, is manufactured sand; CS, is crushed stone; WR, is water reducer.

TABLE 2 Test results of workability of MSC under different MB values.

Group name	MB value (g/kg)	Slump (mm)	Expansion degree (mm)	Working performance		
				Cohesiveness	Moisture retention	Liquidity
MP0	0.85	220	500	good	excellent	excellent
MP0.5	1.10	210	500	good	excellent	good
MP1	1.35	200	480	excellent	excellent	good
MP1.5	1.70	185	460	cxcellent	cxcellent	fair
MP2	2.00	165	420	excellent	excellent	poor

were designed as shown in Table 1 Proportion of MSC The mud powder contents selected in the experiment were 0%, 0.5%, 1.0%, 1.5%, and 2.0%, respectively. The MB values under the corresponding conditions were 0.85, 1.10, 1.35, 1.70, and 2.00, respectively, measured by the methylene blue test. In addition, Table 1 Proportion of MSC also shows the f_{cc} and tensile strength (f_{ts}) of MSC at 28 d age under the above five mixing ratios.

Based on this, this paper carried out macro tests such as chloride ion penetration test, salt freezing test, and drying shrinkage test of MSC under the above mix ratio, and used SEM technology to test the microstructure of MSC at 28 d. Among them:

(1) Anti-chlorine ion penetration test using rapid chloride migration coefficient method (or RCM method). The specimen was a cylinder of Φ100 mm × 50 mm. Under standard maintenance conditions for 84 d, the anti-chlorine ion permeation grade is set to RCM-V. The voltage selected during the test was 60V, and the test lasted for 96 h.
(2) Fast freezing method was used in the salt-freezing test, and the specimen was a prism of 100 mm × 100 mm × 400 mm. The salt-freeze test was carried out after curing for 28 days under standard curing conditions. The freezing and thawing medium was 3% NaCl solution, and the freezing resistance grade was F300. The η and P were measured every 25 times.
(3) Shrinkage test using contact method, the specimen is 100 mm × 100 mm × 515 mm prism. The length of specimens was measured at 3 d, 7 d, 14 d, 28 d, 60 d, 90 d, and 120 d.
(4) For microstructure tests, field emission scanning electron microscopy was used to observe the microscopic morphology of hydration products in concrete specimens with five groups of MB values at 28 d age.

3 Test result analysis

3.1 Workability

Table 2 Test results of workability of MSC under different MB values. Indicates the fresh concrete workability at different MB values. Table 2 test results of workability of MSC under different MB values. Indicates that both the slump and extension of fresh concrete mixes show an overall trend of gradual decrease with the MB value. When the MB value increased from 0.85 to 2.00, the slump decreased by 25% from 220 mm to 165 mm. The expansion is reduced by 16% from 500 mm to 420 mm. Hence, the higher the MB value, the worse the flowability of the fresh concrete mix. Table 2 test results of workability of MSC under different MB values. Reveals that the higher the MB value, the greater the cohesiveness of the fresh concrete mix increases, while the water retention remains largely unchanged.

The main reasons for this phenomenon are: Firstly, the mud powder itself has strong water absorption; Secondly, the mud powder can adsorb the molecules of the polycarboxylate superplasticizer into its interlayer structure, reducing the molecular weight of the superplasticizer, which weakens the water-reducing efficiency of the water-reducing agent. In the case of unchanged water consumption and water-reducing agent dosage, with the increase of mud powder content, the free water inside the

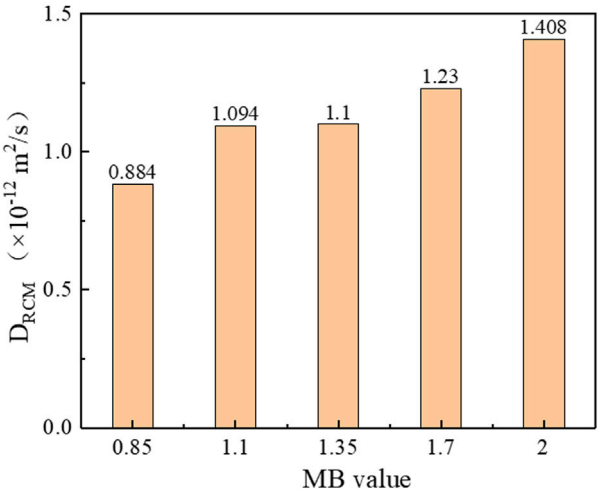

FIGURE 1
Test results of chloride permeability coefficient of MSC.

slurry gradually decreases, and the effective water consumption for fresh concrete mixing also decreases accordingly, and the cohesiveness of the mix increases. At this time, the flow resistance between the materials inside the slurry increases, which leads to the deterioration of its fluidity. Therefore, The more the content of mud powder (MB value), the slump and expansion of fresh concrete mixes are gradually reduced.

3.2 Resistance to chloride ion penetration

The impermeability of concrete refers to the difficulty of resisting the diffusion, penetration, or migration of liquids, gases, or ions in concrete by external effects such as pressure, ion concentration differences, and electric fields. Most studies use the concrete chloride migration coefficient to characterize its impermeability, and the chloride migration coefficient is also an important indicator to describe the compactness of concrete. In general, the smaller the chloride migration coefficient, the better the permeability of the concrete and the higher the degree of compactness. The chloride migration coefficient of concrete obtained using the RCM method can be calculated according to Eq. 1.

$$D_{RCM} = \frac{0.0239 \times (273 + T)L}{(U - 2)t}\left(X_d - 0.0238\sqrt{\frac{(273 + T)LX_d}{U - 2}}\right) \quad (1)$$

where D_{RCM} is the chloride permeability coefficient of concrete (m^2/s), U is the absolute voltage (V), T is the average value of the initial temperature and the end temperature of the anode solution (°C), L is the thickness of the specimen (mm), X_d is the chloride penetration depth (mm), t is the test duration (h).

The specific results that can be obtained using Eq. 1 are shown in Figure 1 Test results of chloride permeability coefficient of MSC. After analysis, the chloride migration coefficient increased from 0.884 × 10^{-12} m^2/s to 1.408 × 10^{-12} m^2/s when the MB value increased from 0.85 to 2.00, which increased by 59.28%. That is the chloride migration coefficient of the MSC gradually increases with increasing MB value, which is consistent with the conclusion obtained by Xia et al. (2021).

The above phenomenon shows that the MB value, the more permeable the concrete is, and the less dense it becomes. This is because the mud powder is an expansive clay, the mixing of mud powder will make the concrete wet expand and dry shrinkage, thus affecting the bonding of cementitious materials and aggregates, causing micro-cracks inside the concrete, which in turn makes the concrete less compact and more permeable (Liu et al., 2015).

3.3 Salt freezing resistance

P and η are the main indicators of the frost resistance of concrete. Salt freeze resistance tests were carried out on concrete specimens (age 28 days) at different MB values using the fast freeze method; the P and η of the specimens were measured every 25 cycles, and the results are shown in Figure 2. The P and η can be calculated according to Eqs 2, 3.

$$P = \frac{f_n^2}{f_0^2} \times 100\% \quad (2)$$

where P is the relative dynamic elastic modulus after n cycles of freezing and thawing, f_0 and f_n are the initial transverse fundamental frequency and the transverse fundamental frequency (Hz) after n cycles of freezing and thawing, respectively.

$$\eta = \frac{m_0 - m_n}{m_0} \times 100\% \quad (3)$$

where η is the mass loss rate, m_0 and m_n are initial mass and mass (g) after n cycles of freezing and thawing, respectively.

From Figure 2A, it can be seen that the P can be divided into two stages in general as the number of freeze-thaw cycles n increases. (1) For $n \leq 125$ cycles, the internal pore structure of the specimen is unaffected by the n, and thus the P does not change with the increase in the n. (2) For $n > 125$ cycles, the P decreases gradually with the increase of the n. This indicates that after a certain n (125 cycles), the specimens gradually produce microcracks caused by freeze-thaw action, and the number of microcracks gradually increases with the increase of the n. In addition, after 300 freeze-thaw cycles, the P of the specimens showed an overall increase with the increase of MB value and reached the maximum value at the MB value of 1.10, and then gradually decreased.

From Figure 2B, it can be seen that the η, in general, can be divided into three stages as the n increases. Stage I: negative decreasing stage. $n \leq 125$ times, the η is negative, and its absolute value increases with the increase of the n. From the previous analysis, it can be seen that when $n \leq 125$ times, the internal pore structure of the specimen is basically not affected by the freeze-thaw cycle, so the quality of the specimen does not change with the increase in the n. On the contrary, due to the existence of water absorption of mineral admixture and the initial tiny pores inside the specimen, the specimen continuously absorbs the water in the environment during the freeze-thaw process, and its quality gradually increases with the increase of the n, which

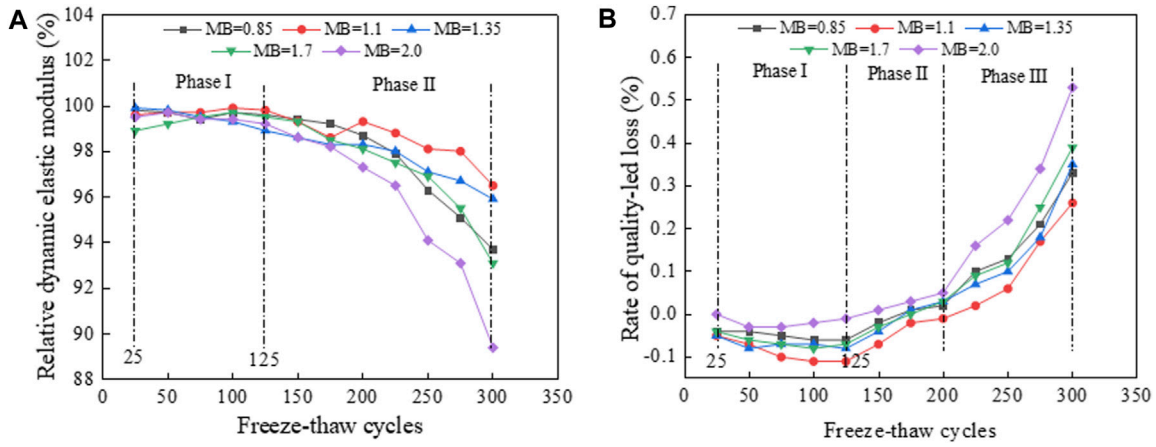

FIGURE 2
Variation of P and η of MSC with freeze-thaw cycles: **(A)** P, **(B)** η.

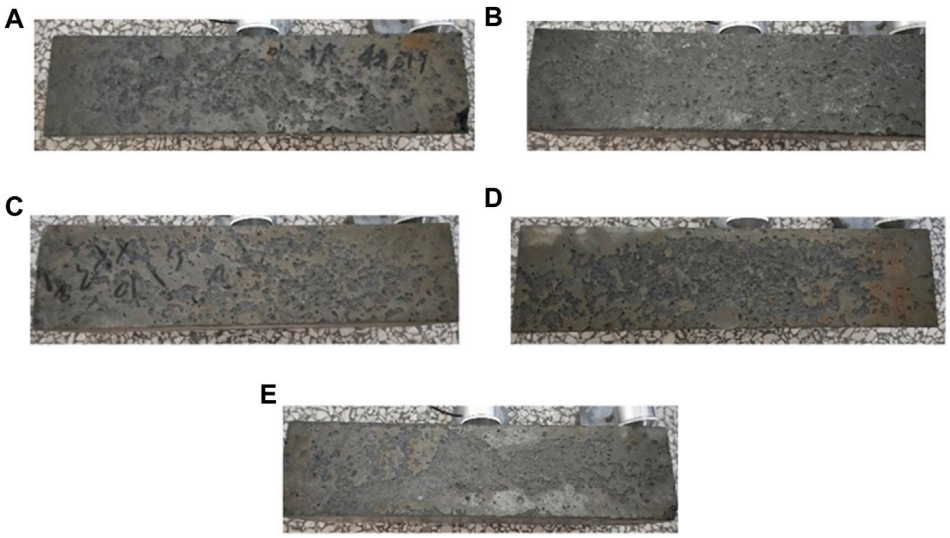

FIGURE 3
Surface morphology of MSC after 300 cycles of salt freezing: **(A)** MB=0.85, **(B)** MB=1.1, **(C)** MB=1.35, **(D)** MB=1.7, **(E)** MB=2.0.

leads to the increasing absolute value of the specimen quality loss rate. Stage II: Negative increase stage. $125 < n < 200$ times, the quality loss rate is still negative, but its absolute value gradually decreases with the increase in the n. This is because after the n exceeds 125, the surface of the specimen starts to shed due to the freeze-thaw action, which leads to the reduction of the specimen quality. However, the mass of the specimen shedding at this stage is relatively small, and the mass after the freeze-thaw cycle is still larger than its initial mass. Therefore, the η in this stage is still negative. Stage III: positive increasing stage. $n \geq 200$ times, the mass of the specimen after freeze-thaw cycles is less than its initial mass, and the total mass shed in this stage increases gradually with the increase of the n. Therefore, the η at this stage is positive and increases gradually with the n. In addition, after 300 freeze-thaw cycles, the η of the specimens showed an overall decrease with the increase of MB value and reached the minimum value at the MB value of 1.10, and then gradually increased again. It indicates that the surface of the MSC at different MB values showed some peeling phenomenon after 300 freeze-thaw cycles, but the surface morphology remained relatively intact, as shown in Figure 3.

The changes in P and η can be seen that the appropriate amount of mud powder can effectively improve the salt freezing resistance of the mechanism sand concrete, but the content of mud powder will reduce the salt freezing resistance of the machine when it exceeds a certain value. From the test results, the best MB value can be determined as 1.10 for the ratio designed in this paper, and the corresponding mud powder content is 0.5%.

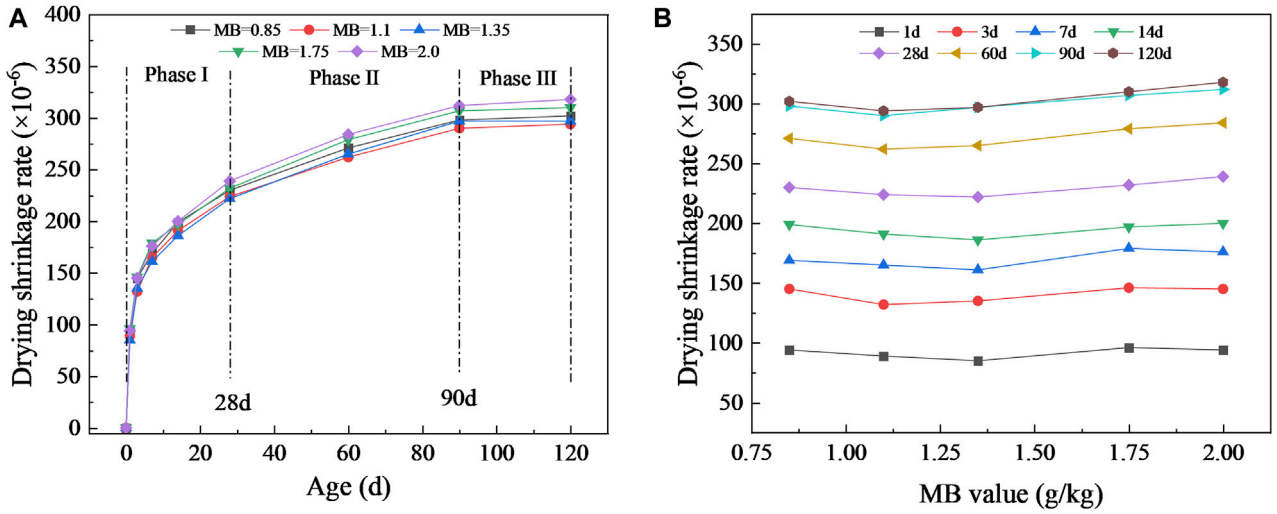

FIGURE 4
Variation of drying shrinkage rate of MSC with age and MB value: **(A)** age, **(B)** MB value.

3.4 Contractility

Concrete is prone to shrinkage during hardening, leading to cracking. Cracking not only accelerates the entry of corrosive substances into the material but also causes the overflow of hydration products within the material. Especially in the northern region, long-term seasonal freeze-thaw cycles will accelerate the development of material microstructure damage, resulting in a decline in the overall stability and durability of concrete. Research on concrete shrinkage mostly revolves around drying shrinkage, and the drying shrinkage rate is commonly used to evaluate its shrinkage.

Figure 4 shows the variation of drying shrinkage of concrete specimens with age under different mixing ratios. As the age increases, the shrinkage evolution process of concrete under different MB values can be divided into three stages: rapid shrinkage, slow shrinkage, and shrinkage balance (Zhao et al., 2018). ① In the rapid shrinkage stage (age ≤ 28 d), the drying shrinkage rate of this stage is relatively large, and the shrinkage amount can account for 75% of the total shrinkage, or even higher. Therefore, the drying shrinkage of concrete mainly occurs in the early stage. ② Slow shrinkage stage (28 d < age < 90 d), the shrinkage deformation rate of this stage is slow, and the shrinkage process lasts longer. ③ Shrinkage balance stage (age ≥ 90 d), the shrinkage process of this stage is close to stability, and the relative humidity inside the concrete and the environment reaches equilibrium. When the ambient humidity is lower than the internal relative humidity of concrete, the shrinkage process will restart until the internal and external relative humidity balance is reached again.

In addition, when the age is the same, the drying shrinkage of concrete decreases first, and reaches the minimum value when the MB value is 1.10 (mud powder content is 0.5%), and then gradually increases. This shows that an appropriate amount of mud powder can inhibit the drying shrinkage process of concrete; on the contrary, when the mud powder content is too high, it will promote the development of the concrete drying shrinkage process. The reasons for this phenomenon can be explained from the following two aspects: 1) an Appropriate amount of mud powder can fill the pores between aggregates, which has played a certain optimization role in the internal porosity, thereby reducing the drying shrinkage of concrete; 2) However, mud powder belongs to clay minerals, which is loose and porous, and has good water absorption performance. The excessive content of mud powder will make cement absorb too much water in the hydration process, and the water content of concrete after hardening is relatively large. When the internal relative humidity of concrete is greater than the environmental humidity, the surface moisture evaporates, the internal moisture diffuses to the surface, and the moisture adsorbed by mud powder is released, increasing the dry shrinkage of concrete.

To study the timeliness of concrete shrinkage deformation, based on a large number of test results, scholars have established many prediction models for calculating the shrinkage strain of concrete under different conditions (An et al., 2001). Among them, the hyperbolic prediction model given by the China Academy of Construction Sciences is the most widely used (Lv et al., 2004), and its expression is:

$$\varepsilon_s(t) = \frac{t}{a + bt} \tag{4}$$

where, $\varepsilon_s(t)$ is the drying shrinkage of concrete at time t; a and b are the material test constants.

Eq. 4 is used to fit the dry shrinkage rate of MSC under different MB values in Figure 4, and the results are shown in Table 3 Analysis results of shrinkage of MSC (hyperbolic function) under different MB values. The predicted results are close to the experimental results, with a large correlation coefficient R and the error is relatively small. It indicates that the relationship between the dry shrinkage rate of

TABLE 3 Analysis results of shrinkage of MSC (hyperbolic function).

Group name	MB value (g/kg)	Regression coefficient		120 d measured value	120 d calculated value	*R*
		a	*b*			
MP0	0.85	0.0132	0.0035	302	277.0083	0.9471
MP0.5	1.10	0.0149	0.0035	294	275.9255	0.9538
MP1	1.35	0.0162	0.0035	297	275.1032	0.9489
MP1.5	1.70	0.0132	0.0034	310	284.9003	0.9423
MP2	2.00	0.0142	0.0033	318	292.5402	0.9487

MSC and age under the condition of mix proportion in this test can be described by the hyperbolic function expressed in Eq. 4.

4 Fractal feature analysis

4.1 Method of fractal dimension theory

Fractal is a method for characterizing or describing irregular, self-similar, and scale-invariant objects or phenomena. The quantitative parameters characterizing the fractal properties of objects or phenomena are generally called fractal dimensions. The spatial distribution of concrete microstructure can be qualitatively seen from SEM images, but it cannot be quantitatively described. Combined with fractal theory, the distribution of concrete microstructure satisfies a certain fractal law, and the fractal analysis can effectively quantify and compare the complexity of the microstructure. Therefore, based on the information contained in SEM images, the spatial distribution of concrete microstructure can be quantitatively characterized by fractal dimension. At present, the methods for calculating fractal dimension mainly include box dimension, Hausdorff dimension, similarity dimension, Brownian motion algorithm, and differential box dimension (Yang et al., 2009). Because differential box dimension DB has good accuracy and applicability and can meet the requirements of computational efficiency and dynamic characteristics, it is often used as a measure of image surface texture roughness.

The digital image obtained by using the scanning electron microscope equipment is a grayscale image, which can be regarded as a three-dimensional space (x, y, z). Where x and y denote the position of the pixel in the image plane and z denotes the grayscale value of the pixel. Therefore, the gray values constitute a concave and convex surface, and the spatial distribution of each pixel color can reflect the texture characteristics of the image. According to the fractal theory, the fractal dimension is an important parameter for the quantitative portrayal of non-smooth, non-regular, broken, and other extremely complex fractals, characterizing the complexity and roughness of the fractals. That is to say, the larger the fractal dimension, the more complex and rough the fractals are; conversely, the smaller the fractal dimension, the simpler and smoother the fractals are. The fractal dimension combines spatial information and color information of images simply and organically, which effectively reflects the complexity of material structure.

When calculating fractal dimension based on a grayscale SEM image, the traditional method is to convert it into a black and white pixel image by binarization. For SEM images, each gray value in the image represents the corresponding information. After binarization processing, the characteristics of cementitious materials, hydration products, holes, and cracks cannot be effectively expressed, which affects the data analysis results. Therefore, this paper directly calculates the fractal dimension by using the difference box dimension based on the gray image of concrete SEM. The main idea of this method is as follows (Sarkar and Chaudhuri, 1994): For an $M \times M$ image, it can be regarded as a surface (x, y, z) in three-dimensional space, where (x, y) represents the position in the surface and z is the gray value at that position. The plane is divided into several grids of $L \times L$, let $r=L/M$, and each grid is a box of $L \times L \times h$. h represents the gray value of each box and satisfies $G/h=M/L$. G represents the total gray level. Assuming that in the (i, j) grid, the maximum and minimum image gray levels are box l and box k respectively, then:

$$n_r(i,j) = l - k + 1 \tag{5}$$

The total number of boxes needed to cover the whole image is:

$$N_r = \sum_{i,j} n_r(i,j) \tag{6}$$

The fractal dimension is:

$$D = \lim \frac{\log N_r}{\log(1/r)} \tag{7}$$

For a series of L, the specific values of $\log N_r$ and $\log(1/r)$ can be obtained, and then the least square method is used for linear regression analysis in the double logarithmic coordinate system. The linear slope obtained by regression is the difference box dimension D_B.

4.2 Fractal characteristics analysis of SEM images

Figure 5 shows the SEM images of MSC under different MB values (5,000 ×) and the difference box dimension D_B calculated by a double logarithmic coordinate system. When the MB value is small, the hydration degree of MP0 and MP0.5 groups is high, and the structure

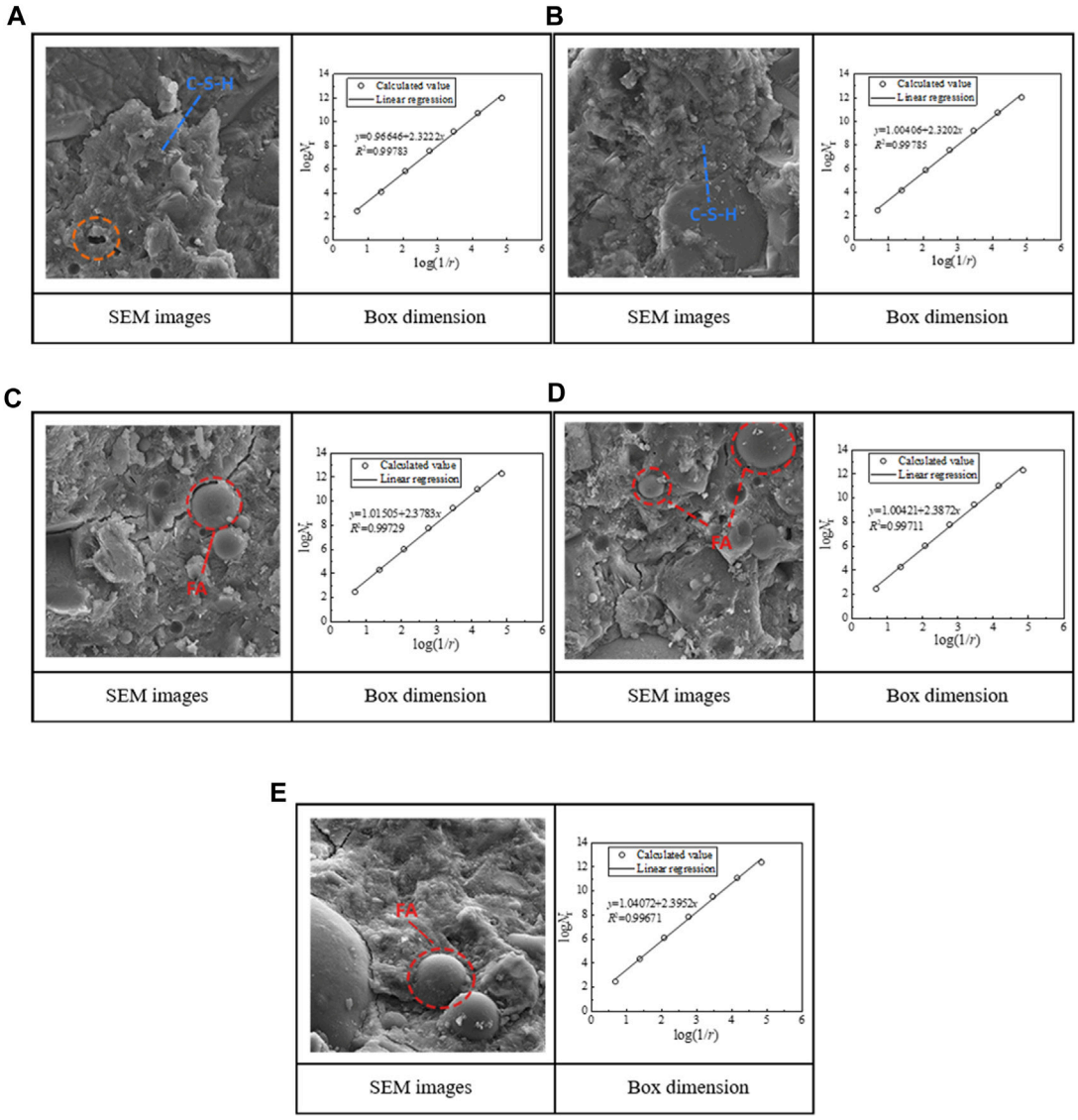

FIGURE 5
SEM images and fractal dimension of MSC: **(A)** MP0, **(B)** MP0.5, **(C)** MP1, **(D)** MP1.5, **(E)** MP2.0.

formed by hydration is close, containing C-S-H gel, which makes the cement particles and other hydration products closely connected to form a dense whole with a strong spatial structure. The degree of hydration of the MP1~MP2 group gradually decreases with the increase of MB value, and the mineral components such as fly ash that have not completed hydration inside gradually increase, and cracks appear on the concrete surface. This is because the clay powder itself is not active, and the addition of too much clay powder has an inhibiting effect on the hydration of the cementitious material, resulting in an increase in unhydrated fly ash particles. Due to the poor bonding effect between fly ash and hydration products, which in turn causes cracks to appear at the junction of the two, affecting the overall structural compactness.

In addition, it can be seen from Figure 5 that the fractal dimensions of MSC under different MB values are between 2.3202 and 2.3952, and the fitting degree of the differential box dimension method to the fractal dimension of the MSC surface is above 0.996, indicating that the surface morphology of MS coagulation under different MB values has good fractal characteristics. When the MB value is 0.85 and 1.10, the hydration degree of the MP0 and MP0.5 groups is higher, the microscopic appearance is relatively flat, and the texture of the SEM image is simple. The fractal dimension of these two groups of images is relatively small and close to 2.3222 and 2.3202, respectively. Then, with the increase of MB value, the hydration degree of the MP1.0 → MP2.0 group decreased gradually, and there were a large number of unhydrated fly ash in the concrete, and the internal began to appear micro cracks. At this time, the SEM image showed complex texture, and the fractal dimension of the image was larger, which were 2.3783, 2.3872, and 2.3952, respectively.

The above analysis shows that the fractal dimension can quantitatively explain the changing trend of MSC structure under different MB values, and can better reflect the influence of mud powder on the hydration degree and structure of concrete. The

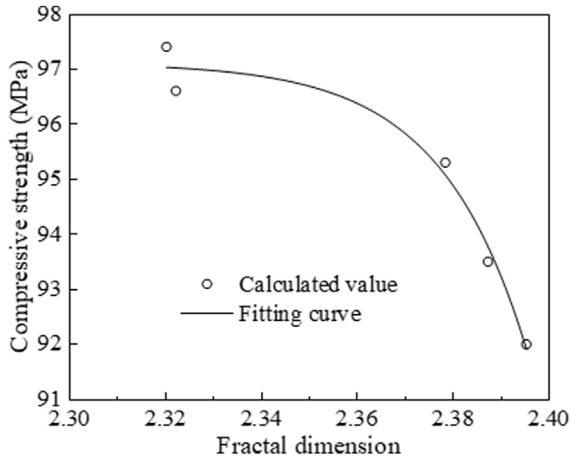

FIGURE 6
Relationship between fractal dimension and compressive strength under different mud powder content.

hydration degree of concrete not only affects the microstructure of concrete but also affects its macroscopic mechanical properties. To quantitatively analyze the influence of the microstructure of concrete on its strength, Figure 6 shows the variation of f_{cc} of MSC with fractal dimension. It can be seen that as an important feature of geometric objects, fractal dimension can not only quantitatively describe the microstructure of concrete hydration products, but also show a good correlation with the variation law of f_{cc}. After fitting, the relationship between the fractal dimension and fcc of concrete can be described by the exponential function represented by Eq. 8, and the correlation coefficient is 0.9772.

$$f_{cc} = 97.1059 - 0.0149 \exp\left(\frac{D_B - 2.2898}{0.018}\right) \quad (8)$$

5 Conclusion

(1) With the increase of MB value, the MSC collapse and extension are gradually decreased, and the cohesiveness is gradually increased, while the water retention is unchanged. In addition, with the increase of MB value, the migration coefficient of chloride ions of MSC increases gradually. After 300 freeze-thaw cycles, the P first increased and then gradually decreased, while the η and drying shrinkage rate first decreased and then gradually increased, and the MB values corresponding to the turning points of the P, η, and drying shrinkage rate were 1.10.

(2) With the increase of n, the change law of P can be divided into two stages basically unchanged and gradually decreased. The change process of η can be divided into three stages: negative value reduction, negative value increase, and positive value increase. At the same time, with the increase of age, the shrinkage evolution process of concrete can be divided into three stages: rapid shrinkage, slow shrinkage, and shrinkage balance, and the drying shrinkage mainly occurs in the rapid shrinkage stage, which accounts for more than 75% of the total shrinkage.

(3) When the MB value is 0.85 and 1.10, the hydration degree of concrete is high, and hydration forms a large number of C-S-H gel, which makes cement particles and other hydration products closely connected to form a solid dense whole of spatial structure. With the increase of MB value, the hydration degree of concrete gradually decreases, and the mineral components such as fly ash that are not hydrated in the interior gradually increase, cracks appeared at the junction of fly ash and hydration products, and the overall structural compactness gradually decreased.

(4) The fractal dimension can quantitatively characterize the effect of MB values on the hydration and structure of concrete and shows a good correlation with the variation pattern of its f_{cc}. When the MB value is small, the SEM image texture of concrete is relatively simple, the fractal dimension value is small, and the corresponding f_{cc} is large. When the MB value is large, the texture of the SEM image is complex, the fractal dimension is large, and the corresponding f_{cc} is small.

Data availability statement

The original contributions presented in the study are included in the article/Supplementary Material, further inquiries can be directed to the corresponding author.

Author contributions

HZ provides guidance for experimental and theoretical research, conceives and designs research methods, and supports the project economically. CG completed data collection, data analysis, and paper drafting. YC assists with data collection. XS provides experimental materials and equipment for this study.

Funding

National Natural Science Foundation of China (51569021), the Natural Science Foundation of Inner Mongolia (2020MS05076), and the Key Project of Scientific Research in Higher Education Institutions of Inner Mongolia Autonomous Region (NJZZ16057).

Conflict of interest

XS was employed by Inner Mongolia Road and Bridge Group Co., Ltd.

The remaining authors declare that the research was conducted in the absence of any commercial or financial relationships that could be construed as a potential conflict of interest.

Publisher's note

All claims expressed in this article are solely those of the authors and do not necessarily represent those of their affiliated organizations, or those of the publisher, the editors and the reviewers. Any product that may be evaluated in this article, or claim that may be made by its manufacturer, is not guaranteed or endorsed by the publisher.

References

An, M. Z., Zhu, J. S., and Qian, W. Z. (2001). Autogenous shrinkage problem of high performance concrete. *J. Build. Mater.* 2001 (2), 159–166. doi:1007-9629(2001)02-0159-08

Che, D. L., Wang, J. J., Ding, Z. W., Ma, B., and Zhang, Y. H. (2021). Research on the performance of manufactured sand concrete with different stone powder content. *E3S Web Conf.* 283, 01044. doi:10.1051/e3sconf/202128301044

Deng, L., Shen, J. R., Lu, S. J., Wang, K. G., and Xie, D. Y. (2021). "Study on how to determine the methylene blue (MB) value of machine-made sand and its effects on admixture dosage and compressive strength of concrete," in *4th international conference on civil, architecture, and environment research* (Zhuhai, China: IOP Publishing). doi:10.1088/1755-1315/676/1/012104

Diamond, S., and Huang, J. (2001). The ITZ in concrete – A different view based on image analysis and SEM observations. *Cem. Concr. Compos.* 23 (2-3), 179–188. doi:10.1016/s0958-9465(00)00065-2

Elik, T., and Marar, K. (1996). Effects of crushed stone dust on some properties of concrete. *Cem. Concr. Res.* 26 (7), 1121–1130. doi:10.1016/0008-8846(96)00078-6

Gui, M. M., Zeng, C. S., Gong, M. Z., and Jun, Z. P. (2011). Effect of stone dust and MB value for manufactured sand on workability of self-compacting concrete and model analysis. *Appl. Mech. Mater.* 1366 (71-78), 3821–3826. doi:10.4028/www.scientific.net/AMM.71-78.3821

Han, X., Wang, B., and Feng, J. J. (2022). Relationship between fractal feature and compressive strength of concrete based on MIP. *MIP* Constr. Build. Mater. 322 (7), 126504. doi:10.1016/J.CONBUILDMAT.2022.126504

Khonsari, S. V., Eslami, E., and Anvari, A. (2018). Fibrous and non-fibrous Perlite concretes experimental and SEM studies. *Eur. J. Environ. Civ. Eng.* 22 (2), 138–164. doi:10.1080/19648189.2016.1182083

Li, Y. G., Zhang, H. M., Chen, S. J., Hu, D. W., and Gao, W. (2022). Multi-scale deterioration mechanism of salt freezing of aeolian sand concrete. *Acta Mater. Compos. Sin.* 40 (0), 1–12. doi:10.13801/j.cnki.fhclxb.20220607.004

Liu, Z. A., Zhou, M. K., and Yao, X. K. (2015). Study on harmfulness and evaluation of fine powder in manufactured sand. *J. Build. Mater.* 18 (1), 150–155. doi:10.3969/j.issn.1007-9629.2015.01.027

Lv, Y. F., Liu, L. X., and Luo, W. H. (2004). Experimental study on shrinkage performance of commercial concrete. *J. Zhengzhou Univ. (Eng. Ed.)* 25 (3), 65–69. doi:1671-6833(2004)03-0065-05

Mouret, M., Bascoul, A., and Escadeillas, G. (1999). Microstructural features of concrete in relation to initial temperature—SEM and ESEM characterization. *Cem. Concr. Res.* 29 (3), 369–375. doi:10.1016/S0008-8846(98)00160-4

Patil, C., Kalburgi, P. B., Patil, M. B., and Prakash, K. B. (2018). An investigation on the micro structural and elemental composition of sugarcane bagasse ash blended concrete using SEM and EDS technique. *Int. J. Eng. Manuf.* 8 (3), 54–66. doi:10.5815/ijem.2018.03.05

Sarkar, N., and Chaudhuri, B. B. (1994). An efficient differential box-counting approach to compute fractal dimension of image. *IEEE Trans. Syst. Man, Cybern.* 24 (1), 115–120. doi:10.1109/21.259692

Shen, J. R., Xu, Q. J., and Liu, M. Y. (2021). Statistical analysis of defects within concrete under elevated temperatures based on SEM image. *Constr. Build. Mater.* 293 (1), 123503. doi:10.1016/J.CONBUILDMAT.2021.123503

Sun, H., You, Y., Guan, Q. F., Wang, J., and Zhou, Y. X. (2021). Study on the influence of MB value of manufactured sand on carbonation performance of concrete. *Concrete* 2021 (11), 89–92. doi:10.3969/j.issn.1002-3550.2021.11.019

Wang, J. G., Zhou, H. L., Ge, C. L., and Chen, Y. (2021). Influence of stone powder on working performance and mechanical properties of high-strength manufactured sand concrete. *Eng. J. Drainage Irrigation Mach.* 39 (8), 804–810. doi:10.3969/j.issn.1674-8530.21.0002

Wang, J. L., Niu, K. M., Tian, B., and Sun, L. Q. (2012). Effect of methylene blue (MB)-value of manufactured sand on the durability of concretes. *J. Wuhan Univ. Technol. Engl. Ed. Mater. Sci.* 27 (6), 1160–1164. doi:10.1007/s11595-012-0622-0

Wang, J. L., Yang, Z. F., Niu, K. M., Ke, G. J., and Zhou, M. K. (2009). Influence of MB-value of manufactured sand on the shrinkage and cracking of high strength concrete. *J. Wuhan Univ. Technology-Mater. Sci. Ed* 24 (2), 321–325. doi:10.1007/s11595-009-2321-z

Wang, X. S., Wu, B. S., and Wang, Q. Y. (2005). Online SEM investigation of microcrack characteristics of concretes at various temperatures. *Cem. Concr. Res.* 35 (7), 1385–1390. doi:10.1016/j.cemconres.2004.07.015

Xia, J. L., Gao, Y. P., Zhang, P. X., Guan, Q. F., Wang, J., and Zhou, Y. X. (2021). Effect of MB value of manufactured sand on electric flux and chloride diffusion coefficient of concrete. *Archit. Sci.* 37 (3), 78–84. doi:10.13614/j.cnki.11-1962/tu.2021.03.013

Xiao, C., Guo, Y. G., Li, B., Zhou, M. K., Li, B. X., Liu, Z., et al. (2020). Coupled effects of the content and methylene blue value (MBV) of microfines on the performance of manufactured sand concrete. *Constr. Build. Mater.* 240, 117953. doi:10.1016/j.conbuildmat.2019.117953

Yang, H. C., Cheng, M. Y., and Wang, J. P. (2012). An investigation on the interfacial transition zone in concrete using SEM. *Adv. Mater. Res.* 1616 (446-449), 166–170. doi:10.4028/www.scientific.net/AMR.446-449.166

Yang, Y. C., Peng, R. D., and Zhou, H. W. (2009). Fractal dimension calculation method of three-dimensional space digital image. *J. China Univ. Min. Technol.* 38 (2), 251–258. doi:1000-1964(2009) 02-0251-08

Zhang, Y. C., Zhang, Z. R., Zhou, J. H., Zhao, L., and Liu, J. X. (2021). Application of fractal theory in concrete research. *J. Phys. Conf. Ser.* 1865 (3), 032014. doi:10.1088/1742-6596/1865/3/032014

Zhao, W. H., Su, Q., Wang, W. B., Niu, L., and Liu, T. (2018). Experimental study on the effect of water on the properties of cast *in situ* foamed concrete. *Adv. Mater. Sci. Eng.* 2018, 1–11. doi:10.1155/2018/7130465

Zheng, S. Y., Liang, J. L., Hu, Y. J., Wei, D. Y., Lan, Y. F., Du, H. L., et al. (2021). An experimental study on compressive properties of concrete with manufactured sand using different stone powder content. *Ferroelectrics* 579 (1), 189–198. doi:10.1080/00150193.2021.1903257

Zhou, M. K., Liu, Z. A., and Chen, X. (2016). Frost durability and strength of concrete prepared with crushed sand of different characteristics. *Adv. Mater. Sci. Eng.* 2016, 1–9. doi:10.1155/2016/2580542

frontiers | Frontiers in Earth Science

TYPE Original Research
PUBLISHED 23 March 2023
DOI 10.3389/feart.2023.1167962

OPEN ACCESS

EDITED BY
Naifei Liu,
Xi'an University of Architecture and Technology, China

REVIEWED BY
Yun Cheng,
Yancheng Institute of Technology, China
Yugen Li,
Yulin University, China

*CORRESPONDENCE
Min Yang,
yangmin0069@126.com

SPECIALTY SECTION
This article was submitted to Environmental Informatics and Remote Sensing, a section of the journal Frontiers in Earth Science

RECEIVED 17 February 2023
ACCEPTED 10 March 2023
PUBLISHED 23 March 2023

CITATION
Li H and Yang M (2023), Study on influencing factors of slope stability and evolution law of safety factor in coal measure strata.
Front. Earth Sci. 11:1167962.
doi: 10.3389/feart.2023.1167962

Study on influencing factors of slope stability and evolution law of safety factor in coal measure strata

Hongru Li[1,2] and Min Yang[1,2]*

[1]Institute of Geotechnical Engineering, Xi'an University of Technology, Xi'an, China, [2]Loess Soil Mechanics and Engineering Key Laboratory of Shaanxi Province, Xi'an, China

Aiming at the influence factors and their action regulation of the slope stability in the coal measure strata of Beijing–Hong Kong & Macao Expressway, the influence characteristics of injection dip angle of rock stratum, thickness and strength parameters of the soft interlayer, slope height and size of slope angle on the slope safety factor are systematically studied by using the limit equilibrium method theory. The influence of slope height, thickness of weak interlayer and shear strength parameters on the stability of slope in coal measure strata with different dip angles is that the safety factor decreases first and then increases with the increase of strata dip angle. The minimum safety factor of slope under the action of each factor is near the strata dip angle of 30°, which indicates that the stability of slope in coal measure strata is poor when the dip angle of rock stratum is about 30°. With the increase of slope angle, the minimum safety factor decreases. However, when the slope angle is less than 40°, the slope is in a stable state and the dip angle of the strata do not affect the stability of the slope. Slopes with different slope angles have the minimum safety factor that is not affected by slope height. The difference between analytical solution and numerical solution is analyzed. The research provides a theoretical basis for the treatment of slopes in coal measure strata and has certain practical significance.

KEYWORDS

coal measure strata, dip angle of rock stratum, slope angle, strength parameter, safety factor

1 Introduction

Coal measures strata are sedimentary rocks containing soft coal seam structure, which are roughly continuous deposition with each other and are closely related in Genesis. The carbonaceous mudstone and shale in the strata are weak, with large carbon content, strong heat absorption, easy weather and disintegrate. It is greatly affected by drying and soaking activation, and this process is irreversible. The typical engineering geological characteristics of the rock-soil mass in coal measures strata are uneven rock formations, poor interlayer cementation, loose structure, fast weathering speed after excavation, easy softening encountering water, easy destruction of structure leading to loss of strength and so on. Under the action of water and other exogenic forces, it is easy to form the weak zone, which is mostly composed of coal measure strata and weathered material, with the characteristics of water insulation, water content and weak strength. Due to the free face of slope and the softening of thin carbonaceous mudstone under the infiltration of water, the slope in the coal measure strata often collapses along the interface of coal measure strata, as shown in Figure 1.

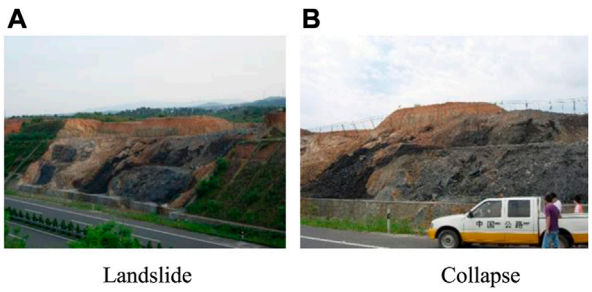

FIGURE 1
Landslide and collapse of coal measure slope on Beijing–Hong Kong & Macao Expressway. **(A)** Landslide **(B)** Collapse.

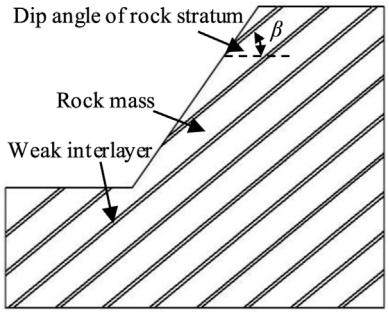

FIGURE 2
The slope model with the dip angle of rock stratum of 30°.

In view of the particularity of coal-bearing soil, domestic and foreign scholars have carried out research on its mechanical properties. Qing and Huang (2005) studied the change process of material composition of piedmont soft soil and slip zone soil on slope in soft areas of coal strata. Li and Li (2006a) analyzed the chemical constituents of slip zone soil of carbonic mudstone in coal measure strata by X-ray method, and explored the relationship between water content, dry density and strength. Li et al. (2006b) measured the permeability characteristics of various rocks in coal measure strata during the whole stress-strain process by experimental method. Xiong et al. (2011) found that the influence of peak strength of coal-bearing soil on confining pressure in saturated state is greater than that in natural state. Hu et al. (2010), Li et al. (2006b), Cao et al. (2008) studied the influence of water content on the shear strength of coal measure soil and the rheological characteristics of weak structural plane in coal measures. Wang et al. (2010) and Yang et al. (2013) studied the conduction characteristics of the rocks in Huainan and Huaibei coalfield under uniaxial compression, and found that there was a correlation between electrical conductivity and stress (strain). Yang et al. (2012), Chai et al. (2013), and Erguler and Ulusay (2009) studied the improvement performance of the rudaceous soil of coal measure strata. Xia et al. (2013) and Liu et al. (2004) conducted a triaxial creep test of soft rock in coal measure strata in deep well, and proposed a non-linear creep constitutive model of soft rock. Cao et al. (2008) studied the rheological properties of weak structural planes in coal measures through laboratory tests. Wu and Wang (1996) preliminarily studied the relationship between rheological properties of coal rock and its microstructure. Zhu and Hong (2009) and Wang and Hong (2014) carried out laboratory tests and theoretical analysis on the physical and mechanical properties of block and powder coal measure soils in Guangwu Expressway. These basic research results provide theoretical knowledge for understanding the physical and mechanical properties of coal-bearing soil, and also provide a basis for scientific utilization and improvement of coal-bearing soil in engineering.

Coal strata often encounter coal strata in the process of road construction and subgrade excavation, which are more common in southwest China. The investigation found that there have been serious collapse and landslide accidents in the coal measure strata slope of some highway projects in Guangdong Province. There are many coal measure strata in the northern section of Beijing–Hong Kong & Macao Expressway in Guangdong Province, and there are many serious landslide accidents in the coal measure strata slope during operation. The special engineering properties of coal measure strata cause the particularity of its slope stability, which is easy to form stress concentration and deformation along the weak interlayer. There are many factors that cause slope instability, mainly including rainfall, earthquake and human activities (Chen, 2005; Wang et al., 2013). Especially in rainfall, the weak interlayer is easy to form a sliding surface, which will lead to slope deformation (Li et al., 2018). The landslide is generally close to the ground surface. Li (2003) analyzed the stability of high slope in coal measure strata from Xiaotang to Gantang section of Beijing-Zhuhai Expressway, and found that the landslides in coal measure strata are mainly shallow sliding. The stability analysis of slope of coal measure strata mostly focuses on the limit analysis method to study the mechanism of slope instability (Xu et al., 2009; Wang et al., 2013). At present, the research on the influence of rainfall on the stability of coal measure strata slope is mainly focused on the specific practical scheme, and it has not carried on the systematic research on the factors affecting the stability and its sensitivity (Yang and Lu, 2006; Cui et al., 2008; Zhu and Hong, 2009). Due to the characteristics of the coal measure strata, it is inevitable that different grading excavation forms and reinforcement measures will be caused by different formation characteristics in the section of the expressway that needs to be grading excavation. Therefore, from the perspective of economy and safety, there are different grading excavation and support forms for different formation characteristics. It is necessary to study the influence of excavation slope angle on its safety and stability.

TABLE 1 Influencing factors settings.

Influencing factors		Specification of variables
Weak interlayer	Inclination angle (°)	10, 20, 30, 40, 50, 60, 70, 80
	Thickness (cm)	40, 60, 100
	Cohesion (kPa)	10,20,30
	Internal friction angle (°)	10,15,25
Slope	Height (m)	20, 30, 40
	Angle (°)	30, 40, 50, 60

TABLE 2 Physical and mechanical parameters of materials.

Material \ Parameter	Soil natural density (kg/m^3)	Cohesive force (kPa)	Internal friction angle (°)
Rock formation	2,200	75	30
Weak interlayer	2,000	30	15

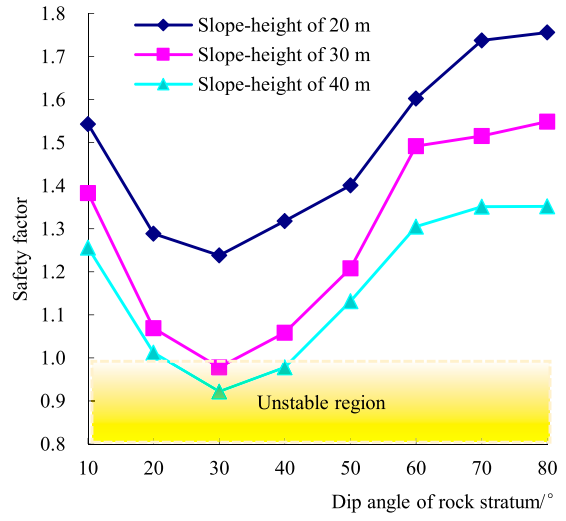

FIGURE 3
The influence of interlayer angle on safety factor at different slope heights.

In view of the shortcomings in the study of slope in coal measure strata, this paper systematically studies the influence of dip angle of rock stratum, thickness and strength index of weak interlayer, slope height and slope angle on safety factor by numerical simulation method. The variation law of safety factor with several influencing factors is explored, and the theoretical formula for calculating the dip angle of the most dangerous rock stratum is deduced mathematically, which provides a theoretical basis for the stability evaluation and treatment measures of practical engineering.

2 Numerical simulation analysis of influencing factors of slope stability in coal measure strata

There are many factors affecting the stability of the slope in coal measures strata, such as the spacing, thickness and strength of weak interlayer in stratum, interlayer angle, groundwater, slope angle and the angle between rock stratum and slope. However, fundamentally, the stability of slope in coal measures strata is mainly depends on the mechanical properties of weak interlayer, which is an important feature of its different from other slopes. In this paper, the slope along the tendency of coal measure strata is taken as the research object. The single factor analysis method is used to study the influence of various factors on the slope stability with the dip angle of rock stratum as the major variable, slope height, thickness and strength of weak interlayer and slope angle as secondary variables based on Slope/W software. It deduces the theoretical formula for calculating the dip angle of the most dangerous rock stratum under different working conditions.

2.1 Numerical calculation model

The slope in coal measure strata with slope angle of 45° and weak interlayer thickness of 60 cm is selected as the basic model. The basic model of calculation is shown in Figure 2. As there are many factors that affect the stability of the slope, and there are mutual influences between them, the problems are complicated. According to the relevant literature (Ha and Zhang, 1994; Li et al., 2018; Shi et al., 2023), it is found that the main factor affecting the landslide is the inclination angle of the weak interlayer in the coal-bearing strata. Therefore, the inclination angle of the weak interlayer is the main factor, and the other is the secondary factor. The selection of influencing factors is shown in Table 1. The calculation parameters are shown in Table 2.

2.2 Calculation analysis

2.2.1 The influence of slope height on slope stability

The basic model of slope angle of 45° and weak interlayer thickness of 60 cm is used to study the influence of slope height on slope stability along the tendency of coal measure strata. Under the condition of constant material parameters of coal measure strata, the slope height is set to 20, 30, and 40 m respectively, to analyze the safety factor of the slope corresponding to the dip angle of interlayer 10°, 20°, 30°, 40°, 50°, 60°, 70°, and 80° respectively. The limit equilibrium method is used to solve the slope safety change law under various working conditions, as shown in Figures 3, 4.

Figure 3 shows that under the condition of a certain height, the safety factor decreases first and then increases with the increase of the inclination angle of the weak interlayer. It is found that each slope height has a minimum safety factor when the dip angle reaches a certain value. When the slope is the minimum safety factor, the slope does not necessarily occur landslide instability, which is only reflected in the minimum safety factor at this dip angle. When the interlayer angle is 30°, the safety factor corresponding to the slope of different heights is the smallest, indicating that the most dangerous dip angle of the interlayer is 30° under the three slope heights. When the interlayer angle is less than 30°, the safety factor decreases rapidly with the increase of the interlayer angle. When the interlayer angle is greater than 30° and less than 60°, the slope safety factor increases rapidly with the increase of the interlayer angle. When the interlayer

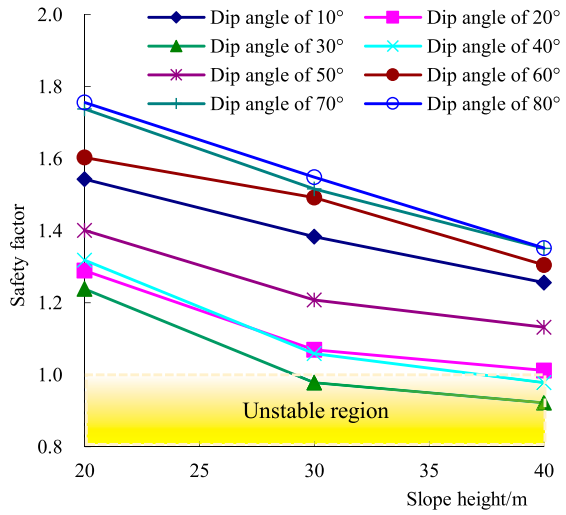

FIGURE 4
Influence of slope heights on safety factor at different interlayer angle.

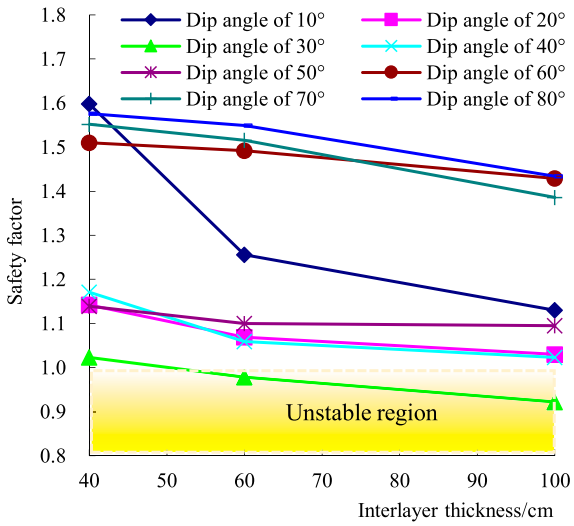

FIGURE 6
Influence of interlayer thickness on safety factor at different interlayer angle.

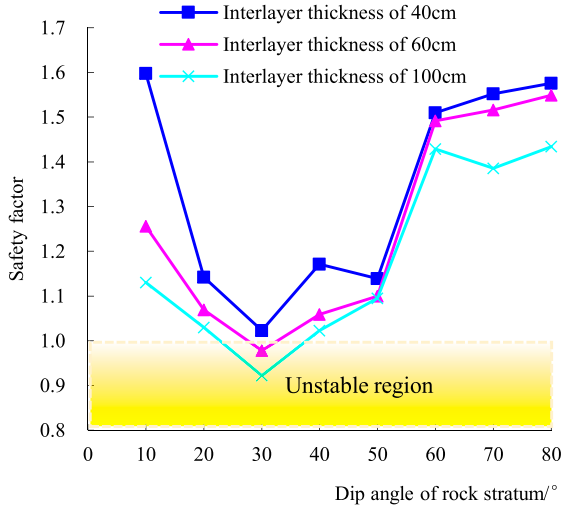

FIGURE 5
Influence of interlayer angle on safety factor at different interlayer thickness.

angle is greater than 60°, the safety factor of the slope increases slowly with the increase of the interlayer angle. When the slope height is 40 m, the variation curve of the safety factor is at the lower part of the other two curves, and the safety factor is the smallest in the case of three slope heights. In the case of the same interlayer angle, the safety factor of the slope decreases with the increase of the slope height. When the slope is 40 m high and the interlayer angle is within the range of 20° and 45°, the slope will undergo landslide instability.

Figure 4 shows that under the same dip angle, the safety factor of the slope basically decreases linearly with the increase of the slope height. When the interlayer angle is within the range of 30° and 60°, the change of the safety factor shows a turning phenomenon. There are differences in the stability of the coal measure with different slope heights. Significant influence is found between the slope height and the dip angle of the interlayer.

2.2.2 The influence of interlayer thickness on slope stability

The basic model of slope angle of 45° and slope height of 50 m is used to study the influence of interlayer thickness on slope stability along the tendency of coal measure strata. The interlayer thickness is set to 40, 60, and 100 cm respectively. Under the condition of a certain thickness of the interlayer, the interlayer dip angles are set to 10°, 20°, 30°, 40°, 50°, 60°, 70°, and 80° respectively. The limit equilibrium method is used to solve the slope safety change law under various working conditions, as shown in Figures 5, 6.

Figure 5 shows that the safety factor decreases first and then increases with the increase of the dip angle of the weak interlayer under the condition of a certain interlayer thickness. When the dip angle of the interlayer is 30°, the safety factor of the slope is the smallest, and the most dangerous dip angle does not change with the thickness of the interlayer. Different interlayer thickness has no effect on the most dangerous dip angle of rock strata, but the safety factor is different. The thicker the interlayer, the smaller the safety factor. When the dip angle of the interlayer is less than 30°, the safety factor decreases rapidly with the increase of the interlayer angle. When the interlayer dip angle is greater than 30°, the safety factor increases with the increase of the dip angle. When the thickness of the weak interlayer is less than 60 cm, and the interlayer dip angle is not about 30°, the slope will not fail.

Figure 6 shows that when the dip angle of the interlayer is constant, the safety factor of the slope decreases with the increase of the thickness of the interlayer. When the dip angle of the interlayer is 10°, the decrease of the safety factor is the largest with the increase of the thickness of the interlayer. When the dip angle of the interlayer is 70° and 80°, the decrease of safety factor is the smallest. When the dip

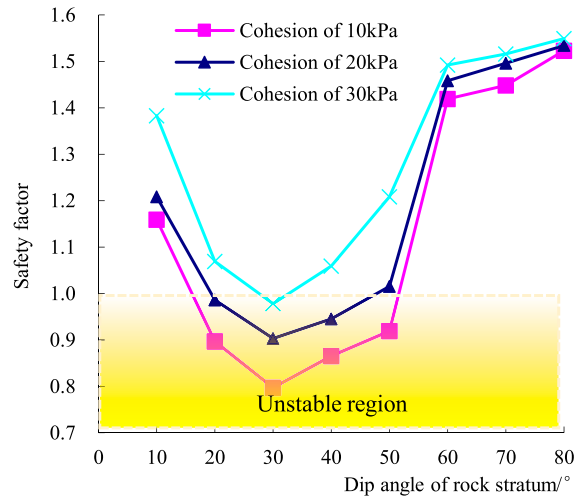

FIGURE 7
Influence of interlayer angle on safety factor at different interlayer cohesive.

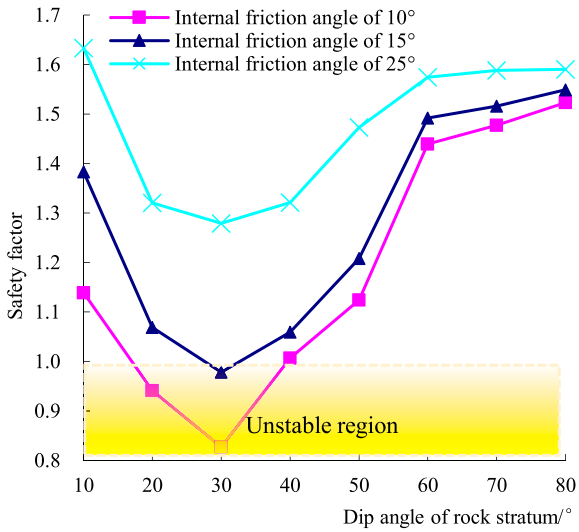

FIGURE 9
Influence of interlayer dip angle on safety factor at different internal friction angle of weak interlayer.

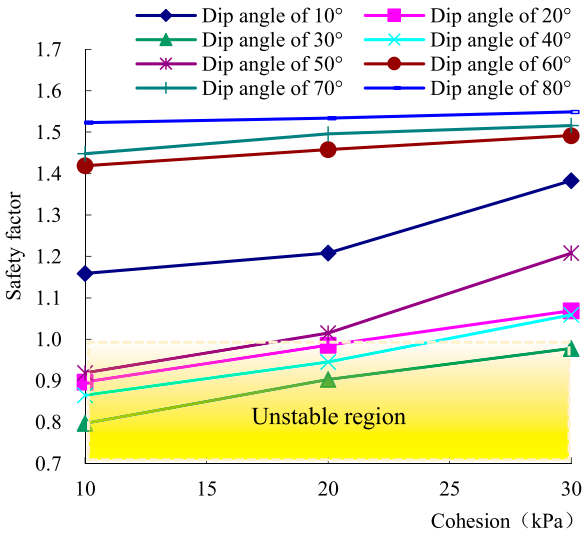

FIGURE 8
Influence of interlayer cohesive on safety factor at different interlayer angle.

angle of the interlayer is greater than 60°, the influence of the increase of the thickness of the interlayer on the slope safety factor gradually decreases.

2.2.3 The influence of cohesion on slope stability

The basic model of slope angle of 45°, slope height of 50 m and weak interlayer thickness of 60 cm is used to study the influence of cohesion of weak interlayer on slope stability along the tendency of coal measure strata. The cohesion of weak interlayer is set to 10, 20, and 30 kPa respectively. Under the condition of a certain cohesive of the interlayer, the interlayer dip angles are set to 10°, 20°, 30°, 40°, 50°, 60°, 70°, and 80° respectively. The limit equilibrium method is used to solve the slope safety change law under various working conditions, as shown in Figures 7, 8.

Figure 7 shows that under the condition of certain interlayer cohesion, the safety factor of the slope decreases first and then increases with the increase of the dip angle of the rock stratum. When the dip angle of the rock stratum is 30°, the safety factor of the slope reaches the minimum value, which means that the most dangerous dip angle of the rock stratum is 30° and this angle does not change with the change of the interlayer cohesion. When the dip angle of the rock stratum is less than 60°, the change amplitude of the slope safety factor is large. When the dip angle of the rock stratum is greater than 60°, the increase rate of the slope safety factor decreases with the increase of the dip angle of the rock stratum, which means that the increase of the dip angle of the rock stratum has little impact on the slope safety factor. When the cohesion is less than 20 kPa and the dip angle of the rock stratum is within the range of 20° and 50°, the slope will fail.

Figure 8 shows that the safety factor of the slope increases gradually with the increase of the cohesion of the interlayer when the dip angle of the rock stratum is fixed. When the dip angle of the rock stratum is 60°, 70° and 80°, the safety factor of the slope does not increase significantly with the increase of the cohesion of the interlayer, which is basically in a horizontal straight line. When the dip angle of the rock stratum is greater than 60°, the increase of the cohesion of the interlayer has less influence on the increase rate of the safety factor of the slope.

2.2.4 The influence of internal friction angle of weak interlay on slope stability

The basic model of slope angle of 45°, slope height of 50 m and weak interlayer thickness of 60 cm is used to study the influence of internal friction angle of weak interlayer on slope stability along the tendency of coal measure strata. The internal friction angle of weak interlayer is set to 10°, 15° and 25° respectively. Under the condition of a certain internal friction angle of the interlayer, the interlayer dip

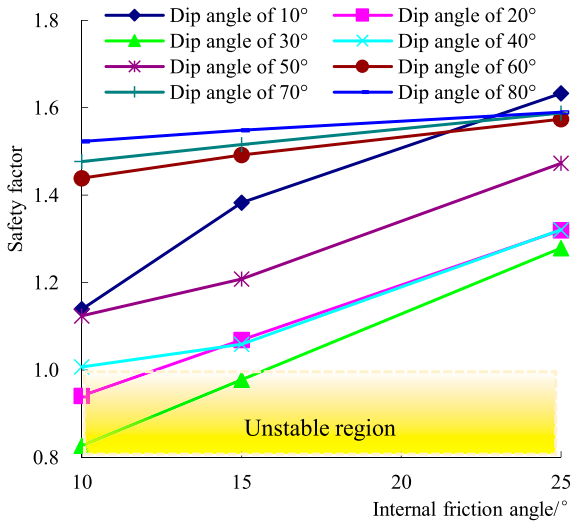

FIGURE 10
Influence of internal friction angle of weak interlayer on safety factor at different interlayer dip angle.

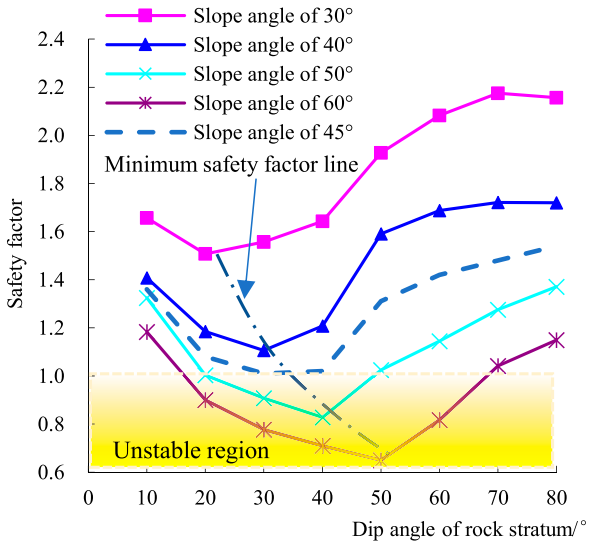

FIGURE 11
Influence of dip angle of rock stratum on safety factor at different slope angle.

angles are set to 10°, 20°, 30°, 40°, 50°, 60°, 70° and 80° respectively. The limit equilibrium method is used to solve the slope safety change law under various working conditions, as shown in Figures 9, 10.

Figure 9 shows that the influence of the internal friction angle of the interlayer on the slope safety factor is similar to that of the cohesion of the interlayer. The most dangerous dip angle of the rock stratum is 30° and this angle does not change with the change of the internal friction angle. When the dip angle of rock stratum is less than 60°, the variation amplitude of slope safety factor with the dip angle of rock stratum is larger. When the dip angle of the rock stratum is greater than 60°, the increase rate of the slope safety factor decreases with the increase of the dip angle of the rock stratum, that is, the increase of the dip angle of the rock stratum has little effect on the slope safety factor. When the dip angle of rock stratum is the most dangerous, the friction angle has a great influence on the slope safety factor. When the friction angle is 25°, the slope safety factor is 1.27. When the friction angle is 15°, the safety factor is only 0.978, and the slope has occurred. When the internal friction angle is less than 10°, the slope with the dip angle of 18° and 42° will have landslide.

Figure 10 shows that the safety factor of the slope increases gradually with the increase of the internal friction angle of the interlayer when the dip angle of the rock stratum is constant. When the dip angle of rock stratum is 60°, 70° and 80°, the increase of slope safety factor decreases with the increase of interlayer cohesion, which indicates that when the dip angle of rock stratum is greater than 60°, the increase of interlayer internal friction angle has less influence on the increase rate of slope safety factor.

2.2.5 The influence of slope angle on slope stability

The basic model of slope height of 50 m and weak interlayer thickness of 60 cm is used to study the influence of slope angle on slope stability along the tendency of coal measure strata.

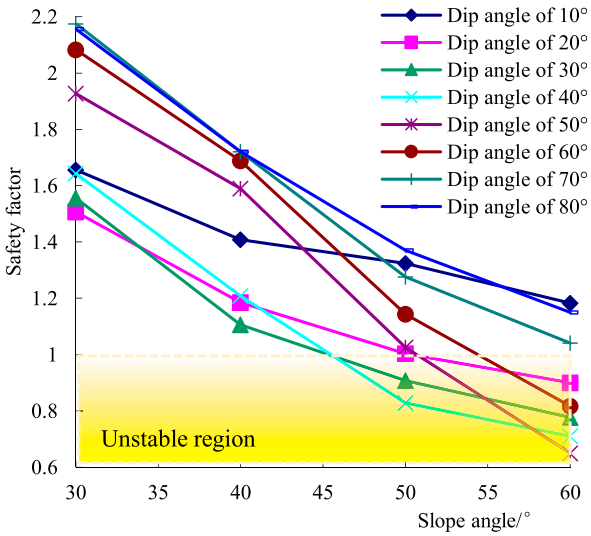

FIGURE 12
Influence of slope angle on safety factor at different dip angle of rock stratum.

The slope angle is set to 30°, 40°, 50° and 60° respectively. Under the condition of a certain slope angle, the interlayer dip angles are set to 10°, 20°, 30°, 40°, 50°, 60°, 70° and 80° respectively. The limit equilibrium method is used to solve the slope safety change law under various working conditions, as shown in Figures 11, 12.

Figure 11 shows that under different slope angles, the safety factor of the slope decreases first and then increases with the increase of the dip angle of the rock stratum, and their safety factor has a minimum value. When the slope angles are 30°, 40°, 50°, and 60°

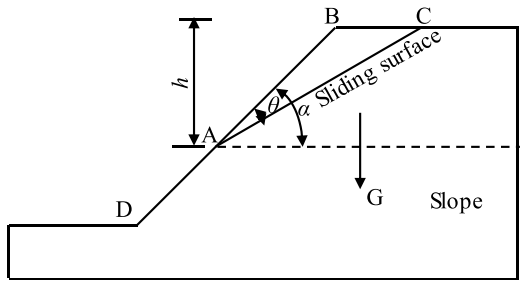

FIGURE 13
Geometric physical diagram of slope.

respectively, the rock stratum inclination corresponding to the minimum safety factor will be 20°, 30°, 40°, and 50° respectively. With the gradual increase of slope angle, the most dangerous dip angle of rock stratum is also gradually increasing, and this angle is smaller than the slope angle. When the slope angle is 50°, and the dip angle of the rock stratum is between 20° and 50°, the instability of the slope occurs. When the slope angle is 60° and the dip angle of the rock stratum is between 18° and 68°, the slope will suffer landslide. In the practical engineering of slope treatment, special attention should be paid to the relationship between slope angle and the dip angle of the rock stratum.

Figure 12 shows that under the condition of a certain dip angle of the rock stratum, the safety factor of the slope decreases with the increase of the slope angle. When the dip angle of the rock stratum is 10°, the safety factor of the slope decreases at the minimum, which shows that when the dip angle of the rock stratum is small, the increase of the slope angle will not significantly reduce the safety factor of the slope.

Analyzing the influence characteristics of slope height, thickness and strength index of weak interlayer, and other factors on slope stability at different dip angles of rock stratum, it is found that when the dip angle of rock stratum is around 30°, safety factors of slope are minimum and the stability of slope is poor, which should be noted. When the dip angle of rock stratum is about 30°, cutting slope and improving the strength index of weak interlayer have little effect on slope stability, which provides a reference for the treatment of slope in coal measure strata.

3 The theoretical of the most dangerous dip angle of slope in coal measures strata

3.1 Fundamental assumption

The sliding surface of soil slope is usually assumed to be a curved surface. The rock slope with weak interlayer is usually regarded as a straight line or a turning curve, which greatly reduces the difficulty of solving the safety factor of slope by analytical method. On the premise of simplifying the sliding surface into a plane straight line, the existence of the most dangerous dip angle of the rock stratum is theoretically proved.

3.2 Theoretical formula derivation

Suppose a slope is shown in Figure 13, h is the height of the slide block, γ is the weight of the slide body, φ is the internal friction angle on the sliding surface, c is the cohesion on the sliding surface, α is the slope angle, θ is the slipping angle, the length of sliding surface AC is l, and the thickness of the slope is taken as the unit thickness.

Assuming that the slope slides along the weak interlayer zone and the sliding surface is AC plane, then ABC is the sliding block. According to the law of sines of triangle and the height h of the sliding block, the weight of the sliding block can be obtained.

$$G = S \cdot \gamma \cdot l = \frac{\gamma h^2}{2 \sin \alpha \cdot \sin \theta} \sin(\alpha - \theta) \tag{1}$$

The calculating formula of the down-sliding force on the sliding surface is shown in Eq. 2.

$$T = G \cdot \sin \theta = S \cdot \gamma \cdot l = \frac{\gamma h^2}{2 \sin \alpha} \sin(\alpha - \theta) \tag{2}$$

The calculation formula of anti-sliding force is shown in Eq. 3.

$$T' = c \cdot l + G \times \cos \theta \tan \varphi = \frac{2ch \sin \alpha + \gamma h^2 \sin(\alpha - \theta) \cos \theta \tan \varphi}{2 \sin \alpha \sin \theta} \tag{3}$$

The calculation formula of safety factor of the slope is shown in Eq. 4.

$$F_s = \frac{T'}{T} = \frac{2c \sin \alpha + \gamma h \sin(\alpha - \theta) \cos \theta \tan \varphi}{\gamma h \sin \theta \cdot \sin(\alpha - \theta)} \tag{4}$$

In order to prove that there is the most dangerous dip angle in the rock mass of the slope under the condition of a certain slope angle, only the solution of Eq. 4 is needed.

In this paper, the calculation is proved when the slope angle is 45°.

The calculation formula of safety factor of the slope is shown in Eq. 5.

$$F_s = \frac{T'}{T} = \frac{2c}{\gamma h(\sin \theta \cos \theta - \sin^2 \theta)} + \frac{\tan \varphi}{\tan \theta} \tag{5}$$

The most dangerous dip angle of the rock strata can be obtained by solving the first-order reciprocal of the angle of the slide crack in Eq. 5 and making it equal to zero.

It can be obtained by a series of simplified calculations on its reciprocal.

$$\frac{dF_s}{d\theta} = \frac{(2c\gamma h - \gamma h \tan \varphi)\tan^2 \theta + (4c\gamma h + 2\gamma h \tan \varphi)\tan \theta - (\gamma h \tan \varphi + 2c\gamma h)}{\gamma h \sin^2 \theta (\cos \theta - \sin \theta)^2 \cdot (1 + \tan^2 \theta)} \tag{6}$$

If Eq. 6 is equal to 0, it is equivalent to let its molecules equal to zero.

$$(2c\gamma h - \gamma h \tan \varphi)\tan^2 \theta + (4c\gamma h + 2\gamma h \tan \varphi)\tan \theta - (\gamma h \tan \varphi + 2c\gamma h) = 0 \tag{7}$$

Taking tan θ as an unknown, solving the quadratic equation of one variable can get Eq. 8.

$$\tan \theta = \frac{-(4c - 2 \tan \varphi) + 4\sqrt{2c^2 + c \tan \varphi}}{2(2c - \tan \varphi)} \tag{8}$$

Eq. 8 is the formula for calculating the most dangerous dip angle of rock mass in the slope when the slope angle α is 45°.

Since the internal friction angle on the sliding surface is small, $\tan\varphi$ is smaller. Compared with the cohesion of the rock mass, it can be ignored, and the simplified calculation formula of the most dangerous dip angle is obtained.

$$\tan\theta = \frac{-4c + 4c\sqrt{2}}{4c} = \sqrt{2} - 1 \tag{9}$$

Through analytical calculation, the most dangerous dip angle of rock strata is 23°. This is 8° different from the result of 31° obtained by interpolation from Figure 11. The reason for the analysis is that the numerical analysis method is to use the arc combined with the broken segment method, and the analytical solution is to use the slider overall balance method. Combined with the actual engineering and the calculation model, the analysis of Eq. 4 shows that the safety factor is not related to the slope height and thickness of the interlayer under the condition of a certain slope angle, which accords with the results of numerical calculation. This proves the correctness of the law found by numerical simulation from the theory of physical model and analytical mathematics, and also shows that there exists the most dangerous dip angle in coal measures strata.

4 Conclusion

This paper analyzes the engineering geological characteristics of coal measure strata, the physical and mechanical properties of coal measure soil, the deformation and failure mode of coal measure strata slope and its stability influencing factors. The influence of various factors on the stability of coal measure strata slope is analyzed by limit equilibrium method. The conclusions are as follows.

(1) The influence of slope height, weak interlayer thickness and its shear strength parameters on the slope stability of coal measures slope with different dip angles is that the safety factor decreases first and then increases with the increase of dip angle. When the dip angle of rock is greater than 60°, the safety factor increases slowly.
(2) The cohesion of the weak interlayer has the greatest influence on the safety factor of the slope, followed by the slope height, the thickness of the weak interlayer and internal friction angle. When the slope height, the thickness of the weak interlayer and the shear strength parameters change respectively, the minimum safety factor of the slope is the rock dip angle of 30° nearby, which indicate that the stability of the coal measure strata slope is poor when the rock dip angle is about 30°.
(3) With the increase of slope angle, the minimum safety factor of slope decreases, and the dip angle of rock corresponding to the minimum safety factor increases. When the slope angle is less than 40°, the change of rock dip angle has little effect on slope stability, and the slope is in a stable state.
(4) The theory of calculating the instability safety factor of block landslide in coal measures are derived based on the analytical theory. It is proved that there is a minimum safety factor unrelated to the slope height for any slope angle. The difference between analytical solutions and numerical solutions is analyzed, and the universality of the law obtained by numerical calculation is verified.

Data availability statement

The original contributions presented in the study are included in the article/supplementary material, further inquiries can be directed to the corresponding author.

Author contributions

HL provided overall guidance on the article and wrote this paper. MY modified the article language.

Funding

This work was supported by Loess Soil Mechanics and Engineering Key Laboratory of Shaanxi Province Foundation (13JS073) and Natural Science Foundation of Shaanxi Province (2017JM5059).

Conflict of interest

The authors declare that the research was conducted in the absence of any commercial or financial relationships that could be construed as a potential conflict of interest.

Publisher's note

All claims expressed in this article are solely those of the authors and do not necessarily represent those of their affiliated organizations, or those of the publisher, the editors and the reviewers. Any product that may be evaluated in this article, or claim that may be made by its manufacturer, is not guaranteed or endorsed by the publisher.

References

Cao, Y., Huang, R., Tang, H., Zheng, H., and Tao, F. (2008). The rheological properties of the weak structural plane of a hydropower station high slope coal experimental study. *Chin. J. rock Mech. Eng.* 27 (2), 3732–3739.

Chai, Z., Guo, W., Kang, T., and Chen, W. (2013). Organic silicon modified shale properties change law study. *J. rock Mech. Eng.* 32 (1), 168–175.

Chen, Z. (2005). *Rock slope stability analysis: The principle, method and application*. Beijing: science press, 157–204.

Cui, Z., Cao, W., and Tang, H. (2008). Stability evaluation of high-cutting coal measure slope a long highway [J]. *J. Chongqing Jiaot. Univ. Nat. Sci.* 27 (6), 1108–1163.

Erguler, Z. A., and Ulusay, R. (2009). Water-induced variations in mechanical properties of clay-bearing rocks. *Int. J. Rock Mech. Min. Sci.* 46 (2), 355–370. doi:10.1016/j.ijrmms.2008.07.002

Ha, Q., and Zhang, Y. (1994). Investigation on the stability of Lianzi cliff dangerous rock body on Changjiang river. *Chin. J. Geol. hazard control* 5 (3), 24–42. doi:10.16031/j.cnki.issn.1003-8035.1994.03.004

Hu, X., Hong, B., Wang, H., and Du, Q. (2010). Comparative study on the water sensitivity of shear strength of high liquid limit soil and coal-bearing soil. *J. Sichuan Univ. Eng. Sci. Ed.* 42 (1), 54–59. doi:10.15961/j.jsuese.2010.01.017

Li, H., Zhang, P., Wang, S., and Zhao, H. (2018). A study of the influence of rainfall on slope stability along the tendency of coal measure strata. *J. geomechanics* 24 (6), 836–848. doi:10.12090/j.issn.1006-6616.2018.24.06.087

Li, J. (2003). Stability analysis and control of cutting high slopes in coal measure strata along Xiaotang-Gantang of Beijing-Zhuhai expressway. *Hydrogeol. Eng. Geol.* (5), 86–88. doi:10.16030/j.cnki.issn.1000-3665.2003.05.020

Li, Y., and Li, T. (2006a). Study on slip band of carbon mudstone landslide in coal measure strata. *Geotech. Eng. Tech.* 20 (2), 88–93.

Li, Y., Ma, Z., He, Y., Wang, B., and Liang, X. (2006b). Experimental study on the strata of rock seepage. *J. Exp. Mech.* 21 (2), 129–134.

Liu, J., Yang, C., Li, X., and Jiang, D. (2004). Wan kai highway through the tunnel surrounding rock creep characteristics of coal measure strata of experimental study. *J. rock Mech. Eng.* 23 (22), 3794–3798.

Qing, S., and Huang, R. (2005). On features of piedmont soft soil on slope in soft areas of coal strata in Southwest China. *Hydrogeol. Eng. Geol.* (2), 53–57. doi:10.16030/j.cnki.issn.1000-3665.2005.02.011

Shi, J., Hu, Q., Luo, Y., Liao, Z., Qi, L., and Wang, X. (2023). Study on evolution law of fault stress field in coal measures at different fault dips. *Min. Saf. Environ. Prot.* 50 (1), 1–8. doi:10.19835/j.issn.1008-4495.2023.01.001

Wang, H., Huang, M., and Liu, Y. (2013). Three-dimensional stability analysis of slope with weak interlayer. *Rock soil Mech.* 34 (2), 156–160. doi:10.16285/j.rsm.2013.s2.026

Wang, H., Ji, H., Cheng, H., and Wang, J. (2010). Huaibei coal measures strata mainly conductive characteristics of rock under the condition of uniaxial compression test study. *J. rock Mech. Eng.* (8), 1631–1638.

Wang, Y., and Hong, B. (2014). Physico-mechanical properties of giant soil of coal measure strata for Guangwu High Way. *Henan Sci.* 32 (11), 2309–2312. doi:10.13537/j.issn.1004-3918.2014.11.028

Wu, L., and Wang, J. (1996). Preliminary exploration to rheology and micro-effect characteristics of coal. *J. rock Mech. Eng.* 15 (4), 328–332.

Xia, H., Bao, Y., and Li, D. (2013). The creep characteristics of deep mine soft rock strata experimental study. *J. Lanzhou Univ.* 49 (4), 564–568. doi:10.13885/j.issn.0455-2059.2013.04.012

Xiong, D., Zhao, Z., Su, C., and Wang, G. (2011). Experimental study of effect of water-saturated state on mechanical properties of rock in coal measure strata. *Chin. J. Rock Mech. Eng.* 30 (5), 998–1006.

Xu, B., Qian, Q., Yan, C., and Xu, H. (2009). Stability and strengthening analyses of slope rock mass containing multi-weak interlayers. *J. rock Mech. Eng.* 28 (2), 3959–3964.

Yang, K., Yuan, L., Qi, L., and Liao, B. (2013). Establishing predictive model for rock uniaxial compressive strength of No.11–2 coal seam roof in Huainan mining area. *J. rock Mech. Eng.* 32 (10), 1991–1998.

Yang, W., Hong, B., Zhou, B., and Kang, L. (2012). Conglomeratic coal can land reform benign test research [J]. *Rock soil Mech.* 33 (1), 96–102. doi:10.16285/j.rsm.2012.01.013

Yang, Y., and Lu, D. (2006). Study on treatment of high-cut carbonaceous shale slope in expressway. *Chin. J. Rock Mech. Eng.* 25 (2), 392–398.

Zhu, L., and Hong, B. (2009). Physico-mechanical characteristics of powdered soil of coal measure strata. *Rock Soil Mech.* 30 (5), 1317–1322. doi:10.16285/j.rsm.2009.05.042

frontiers | Frontiers in Earth Science

TYPE Original Research
PUBLISHED 09 May 2023
DOI 10.3389/feart.2023.1178622

OPEN ACCESS

EDITED BY
Naifei Liu,
Xi'an University of Architecture and Technology, China

REVIEWED BY
Ning Li,
Xi'an University of Architecture and Technology, China
Gaochen Sun,
Xi'an Shiyou University, China

*CORRESPONDENCE
Min Yang,
yangmin0069@126.com

RECEIVED 03 March 2023
ACCEPTED 04 April 2023
PUBLISHED 09 May 2023

CITATION
Li H, Yang M and Yin X (2023), Study on safety assessment methods of gravity anchors based on a simplified mechanical model.
Front. Earth Sci. 11:1178622.
doi: 10.3389/feart.2023.1178622

Study on safety assessment methods of gravity anchors based on a simplified mechanical model

Hongru Li[1,2], Min Yang[1,2]* and Xiaotao Yin[3]

[1]Institute of Geotechnical Engineering, Xi'an University of Technology, Xi'an, China, [2]Loess Soil Mechanics and Engineering Key Laboratory of Shaanxi Province, Xi'an, China, [3]State Key Laboratory of Geomechanics and Geotechnical Engineering, Institute of Rock and Soil Mechanics, Chinese Academy of Sciences, Wuhan, China

Gravity anchor blocks are a common type of ground anchor used for suspension bridges, whose bearing depends on its large body and gravity. As there is no stratum requirement, the safety of the anchor block is important for bridge stability. This study summarizes all available estimation indexes, calculating methods, and evaluation criteria for gravity anchor block safety for the Ruili bank of the Banjin Dam grand suspension bridge. The anti-overturning, anti-sliding, base stress, and deformation safeties were comprehensively evaluated using methods including the suggested specification method (SM), simplified mechanical method (SMM), and finite element method (FEM), the results of which were compared and analyzed. The reasons for errors and improved formulas and working conditions were presented. The main conclusions were as follows. 1) The methods for calculating different evaluation indexes according to specifications lack consistency. Moreover, FEM requires that designers have good computer skills and has low feasibility in practice. 2) The SMM for gravity anchor block safety estimation as described in this study, whose indexes cover systematic and overall, the computational formula is simple and speedy, with relatively conservative results and good practicability. 3) SM, SMM, and FEM were all used for the safety estimation of gravity anchor blocks in Ruili bank. The anti-overturning and anti-sliding stability coefficients must all meet the specification requirements of 2.0. SM cannot be used to estimate the base tensile stress under limited conditions. SMM denoted tensile stress at 2.5 times the main cable design force, compared to 3.2 P for FEM. Deformation calculation methods are not given by SM, but can be suggested by SMM based on the elastic mechanics. The horizontal displacements under design load conditions were 122 mm (SMM), 108 mm (FEM), and 44 mm (composite foundation treated by root piles), with a safety standard of <80 mm. The vertical displacements were 338 mm (SMM), 110 mm (FEM), and 123 mm (composite foundation treated by root piles), with a safety standard of <160 mm. These findings proved the feasibility of SMM for the safety design of gravity anchor blocks in cases lacking regional experience.

KEYWORDS

gravity anchor block, anti-overturning stability coefficient, anti-sliding stability coefficient, base stress, ground bearing capacity, deformation stability

1 Introduction

Gravity anchors are a traditional anchorage type used for both sea and land, including ground-anchored suspension bridges in areas with open terrain and general strata. With increasing construction of long-span suspension bridges, the contradiction between anchorage safety and environmental protection requirements has become increasingly prominent. The accurate evaluation of the safety of gravity anchors is an urgent challenge in the context of the goals of economy and environmental protection.

At present, safety evaluation indexes and methods of gravity anchorage are mainly based on the *Design Specification for Highway Suspension Bridge* (JTG/T D 65-05-2015) and the *Specification for Design of Foundation of Highway Bridges and Culverts* (JTG D63-2007). These indexes mainly consider anti-overturning and anti-sliding stability coefficients, maximum foundation stress, foundation bearing pressure, and deformation control standard determined by the main span. Research has mainly focused on safety evaluation. 1) The design of gravity anchorage mainly relies on the friction provided by the structure–foundation to resist sliding; thus, the friction test of concrete-foundation soil is the basic design parameter to ensure the safety of gravity anchorage (Ran et al., 2018; Tan et al., 2015, Ji et al., 2003; Liu et al., 2011; Liu et al., 2022a). 2) The indoor model test (Li et al., 2005; Li et al., 2018), field scale test (Li, 1995), and numerical experiment (Li et al., 2016; Huang et al., 2014; Liu et al., 2020) are used to determine whether the anti-sliding stability of gravity anchor-foundation, base stress, and deformation meet the design and specification requirements. 3) The parameters obtained from these investigations are inserted into the theoretical formula to estimate the evaluation indexes of the anchorage and evaluate its safety (Yin et al., 2017a; 2017b; Liu and Lin, 2014; Zhu, 2011; Liu, 1999; Liu et al., 2022b).

In this study, according to the specifications for suspension bridges and bridge culverts, the indexes, methods, and evaluation standard of safety evaluation of gravity anchors were systematically summarized. A corresponding simplified mechanical model of the anchorage was established based on the gravity anchor block project of the Ruili bank of the Banjin Dam suspension bridge. The safety of the anchorage was comprehensively evaluated using standard, simplified mechanical, and finite element methods. The physical and mechanical mechanisms of the mechanical model method were identified, and the differences improved. This study aimed to establish a simple and systematic safety evaluation method and index system for gravity anchors.

2 Safety evaluation index and calculation method for gravity anchors

2.1 Anti-overturning stability coefficient

According to the provision of Article 8.4.1 for the *Design Specification for Highway Suspension Bridge* (JTG/T D 65-05-2015), the anti-overturning stability coefficient of the pier foundation is not less than 2.0.

According to the provisions of Article 4.4.1 for the *Specification for Design of Foundation of Highway Bridges and Culverts* (JTG D63-2007), the anti-overturning stability coefficient and eccentricity of the pier foundation are calculated according to the following formula:

$$k_0 = \frac{s}{e_0}, \tag{1}$$

$$e_0 = \frac{\sum P_i e_i + \sum H_i h_i}{\sum P_i}, \tag{2}$$

where k_0 is the anti-overturning stability coefficient of the pier foundation, s is the distance from the center of gravity of the section to the overturning axis (m), e_0 is the eccentricity from the action point of the external force R to the center of gravity axis of the base (m), P_i is the vertical force (kN), e_i is the arm of the vertical force to the center of gravity of the section (m), and h_i is the arm of horizontal force to the center of gravity of the section (m).

2.2 Anti-sliding stability coefficient

According to the provision of Article 8.4.1 for the *Design Specification for Highway Suspension Bridge* (JTG/T D 65-05-2015), the anti-sliding stability coefficient of the pier foundation is not less than 1.6 in the construction stage and not less than 2.0 in the use phase.

According to the provisions of Article 4.4.2 for the *Specification for Design of Foundation of Highway Bridges and Culverts* (JTG D63-2007), the formula to calculate the anti-sliding stability coefficient of the pier foundation is as follows:

$$k_a = \frac{\mu \sum P_i + \sum T_{iP}}{\sum T_{ia}}, \tag{3}$$

where k_a is the anti-sliding safety factor of the pier foundation, $\sum P_i$ is the sum of vertical force, $\sum T_{iP}$ is the sum of anti-sliding horizontal force, $\sum T_{ia}$ is the sum of sliding horizontal force, and μ is the friction coefficient between the base and foundation.

2.3 Safety control standard of base stress and foundation load

According to the provision of Article 8.4.2 for the *Design Specification for Highway Suspension Bridge* (JTG/T D 65-05-2015), tensile stress is not allowed in the anchorage base during construction and operation, and the maximum stress value satisfies the following formula:

$$P_{\max} \le \gamma_R [f_a], \tag{4}$$

where γ_R is the base resistance coefficient and is generally taken as 1.00 in the use stage and 1.25 in the construction stage, referring to Article 3.3.6 of the *Specification for Design of Foundation of Highway Bridges and Culverts* (JTG D63-2007), and $[f_a]$ is the allowable bearing capacity of subsoil, referring to Article 3.3 of the *Specification for Design of Foundation of Highway Bridges and Culverts*.

According to the provisions of Article 4.2 for the *Specification for Design of Foundation of Highway Bridges and Culverts* (JTG D63-2007), the bearing capacity of the foundation satisfies the following formula under the condition of uniaxial eccentric of foundation base:

TABLE 1 Physical and mechanical parameters of rock soil mass and anchor materials in engineering.

Material		Unit weight γ (kN/m^3)	Cohesion c (kPa)	Internal friction angle φ (°)	Elastic modulus E (MPa)	Poisson ratio (μ)
Gravel soil	Natural	17.3	23.6	36.0	30	0.33
	Saturated	18.6	22.3	35.5	25	0.34
Rock mass	Natural	26.0	500.0	38.0	8,000	0.23
	Saturated	26.5	400.0	36.0	7,500	0.22
Anchorage concrete		25.0	1,000.0	45.0	25,500	0.20

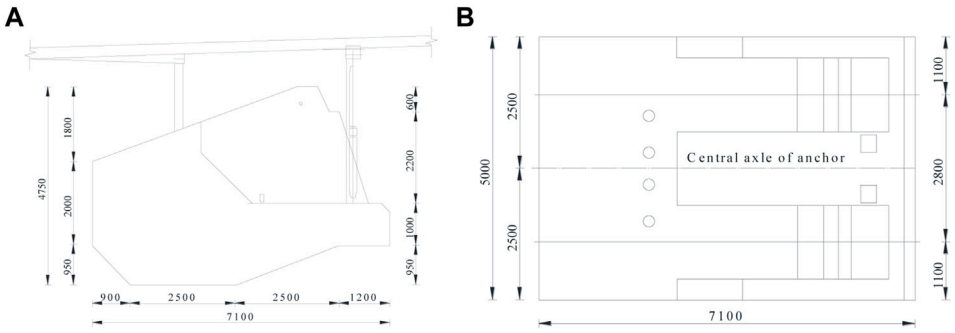

FIGURE 1
Design drawing of gravity anchor blocks in Ruili bank. **(A)** The vertical view of gravity anchor. **(B)** The cross section of gravity anchor.

$$p_{\max} = \frac{\sum P_i}{A} + \frac{M}{W} \le \gamma_R [f_a], \tag{5}$$

$$0 \le p_{\min} = \frac{\sum P_i}{A} - \frac{M}{W} \le \gamma_R [f_a], \tag{6}$$

where A is the base area (m^2), M is the bending moment of horizontal force and vertical force on the center of gravity axis of the base (kN·m), W is the sectional resistance moment in the eccentric direction of the base, and the formula is $BL^2/6$, where B is the transverse width and L is the axial length.

2.4 Deformation control criteria

According to the provision of Article 8.4.1 for the *Design Specification for Highway Suspension Bridge* (JTG/T D 65-05-2015), the allowable horizontal deformation of the anchorage should not be greater than 0.0001 times the main span and the vertical displacement should not be greater than 0.0002 times the main span during the operation stage.

3 Introduction of the super large suspension bridge anchorage and Banjin Dam engineering

The super large suspension bridge anchorage for Banjin Dam is a single-span, double-hinged, steel truss girder, double-tower ground-anchored suspension bridge with a main span of 800 m. The Ruili and Menglian banks both contain embedded gravity anchorages. The foundation of Ruili bank is a loose, slightly dense gravel soil layer. The allowable bearing capacity of the foundation is 250 kPa, and the coefficient of friction on the basis is 0.40. The foundation of the Menglian bank is strongly weathered dolomite. The allowable bearing capacity of the foundation is 500 kPa, and the coefficient of friction on the basis is 0.45. The parameters of the rock soil mass and structural materials are shown in Table 1.

The anchorage of Ruili bank is located on the top of a small hill. Most of the cover soil on the surface is adobe soil of the quaternary system. The soil thickness is 1.40–55.30 m by drilling. The underlying bedrock is limy dolomite of the Middle Triassic Hewanjie Formation with large thickness, which has good mechanical properties. Therefore, it can be used as the bearing strata for anchorage. After construction according to the anchorage design scheme, a temporary slope is formed around the anchorage foundation pit.

Taking the gravity anchor block in Ruili bank with relatively poor stability as an example, the sizes of the left and right anchor blocks are 71 m long × 25 m wide in the horizontal projection. The prestress is applied to the front and rear anchor surfaces at 377,788.7 kN, which is obtained according to the weight of a single abutment and anchor. The design diagram of the gravity anchor block on Ruili bank is shown in Figure 1.

The control elements of the safety evaluation of the gravity anchor block on Ruili bank are as follows:

(1) Structural safety index

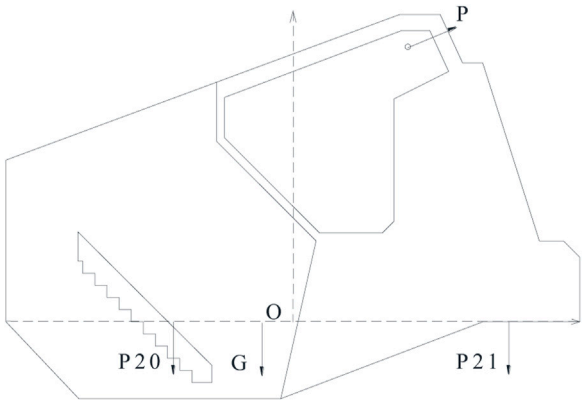

FIGURE 2
Simplified diagram of forces acting on gravity anchor blocks on Ruili bank.

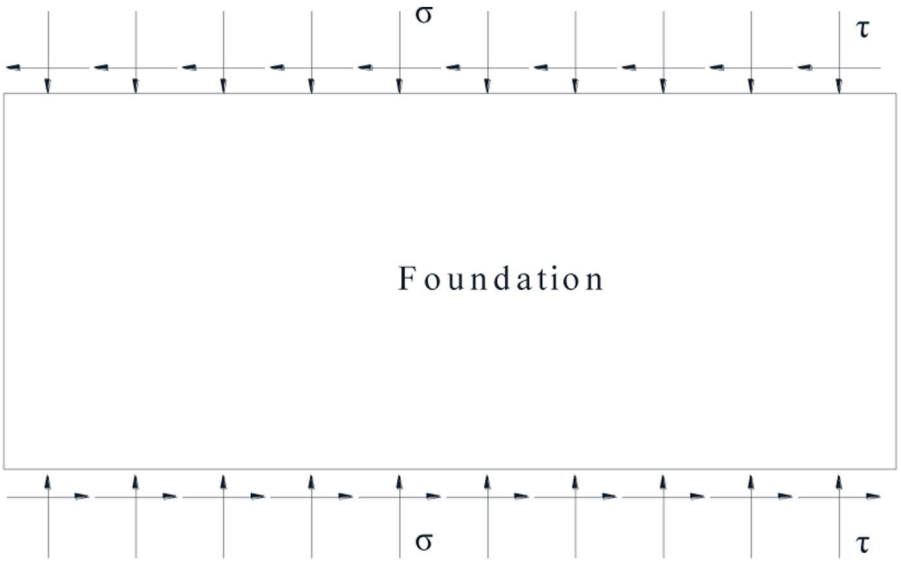

FIGURE 3
Simplified diagram of forces acting on the gravelly soil foundation on Ruili bank.

The anti-sliding stability coefficient K_a of the gravity anchor block is >2.0 and the anti-overturning stability coefficient K_c is >2.0.

(2) Safety of the foundation bearing

The base stresses in the construction and operation stages must be less than the modified allowable bearing capacity of gravel soil foundation, with no tensile stress.

According to the safety evaluation standard for foundation bearings, taking the axis section of Ruili bank as an example, the excavation depth of abutment is approximately 25.0 m from the natural ground to the basement. The anchorage basement is approximately 35.0 m from the natural ground. According to the *Specification for Design of Foundation of Highway Bridges and Culverts* (JTG D63-2007), the correction coefficient of loose-slightly slightly dense gravelly soil is 50% of the correction coefficient of dense gravel soil; thus, k_1 = 3.0/2.0 = 1.5 and k_2 = 5.0/2.0 = 2.5. The natural unit weight γ_1 of basal gravel soil is 17.3 kN/m^3. The unit weight γ_2 of backfilling soil is 16.3 kN/m^3. The correction of the bearing capacity of the gravelly soil foundation is as follows:

$$f_a = f_{a0} + k_1\gamma_1(b-2) + k_2\gamma_2(h-3), \quad (7)$$

where k_1 and k_2 are the correction coefficients of dense gravel soil; b and h are the width and depth of the foundation, respectively; and f_{a0} is the bearing capacity of the gravelly soil foundation.

TABLE 2 Safety estimation results of the gravity anchor blocks on Ruili bank based on simplified mechanical models.

Index	Anti-sliding stability coefficient k_a	Anti-overturning stability		Base stress/kPa				Deformation/mm	
		Eccentricity e_0/m	Coefficient k_0	Construction stage		Operation stage		Horizontal	Vertical
				Center	Off-center	Center	Off-center		
Calculated results	2.1	2.1	16.7	604.1	819.3	577.7	793.0	122.2	337.7
Normative standard	2.0	-	2.0	1,354.0				80.0	160.0

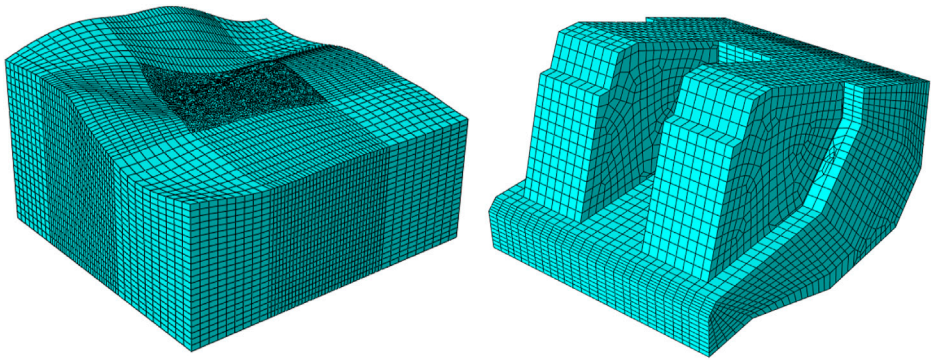

FIGURE 4
Numerical model of the Ruili bank.

The bearing capacity of the gravel soil with depth and width corrections of 1,354 kPa (abutment base) and 1,762 kPa (anchorage base) can be used to determine the bearing safety of the gravel soil foundation under the condition that considers depth and width correction.

(3) Deformation stability

The allowable horizontal deformation of the anchorage should not be greater than 0.0001 times the main span, while the horizontal deformation should not be >80 mm. The vertical deformation should not be greater than 0.0002 times the main span, while the vertical deformation of this project is not >160 mm.

4 Safety evaluation of the anchorage based on the simplified mechanical model

The coordinate system 0 point of the simplified mechanical model is the geometric center of the horizontal projection of the bottom surface. The weight of the anchorage G is approximately 1,072,207.0 kN, and its action point coordinates are (−2.5, 0.0). The design load P of a single cable is 214,000.0 kN. The horizontal angle at the top of the cable abutment is 22.23°, with action point coordinates of (14.2, 34.0). The pile load of the approach bridge P_{20} is 9,777.0 kN, with action point coordinates of (−14.8, 0.0). The pile load of the approach bridge P_{21} is 24,334.0 kN, with action point coordinates of (26.7, 0.0). The simplified diagram of forces acting on the gravity anchor blocks on the Ruili bank is shown in Figure 2.

The forces and their parameters in Figure 2 are inserted into Formula 1, Formula 2, Formula 3, Formula 4, Formula 5, Formula 6. The anti-sliding stability coefficient, anti-overturning stability coefficient, and base stress of the anchorage structure are listed in Table 2. The foundation force analysis is simplified, as shown in Figure 3. The forces and their parameters in Figure 3 are inserted into Formula 8 of the elastic mechanical shear strain and Formula 9 of the compression deformation to simply estimate the horizontal displacement and vertical displacement of the foundation. The calculated displacement is smaller than the actual displacement. The safety estimation results of the gravity anchor blocks on Ruili bank based on simplified mechanical models are shown in Table 2. The thickness of gravel soil is 30.0 m.

$$\gamma = \frac{2(1+\mu)}{E}\tau, \tag{8}$$

$$\varepsilon = \frac{(1-\mu)}{E}\sigma. \tag{9}$$

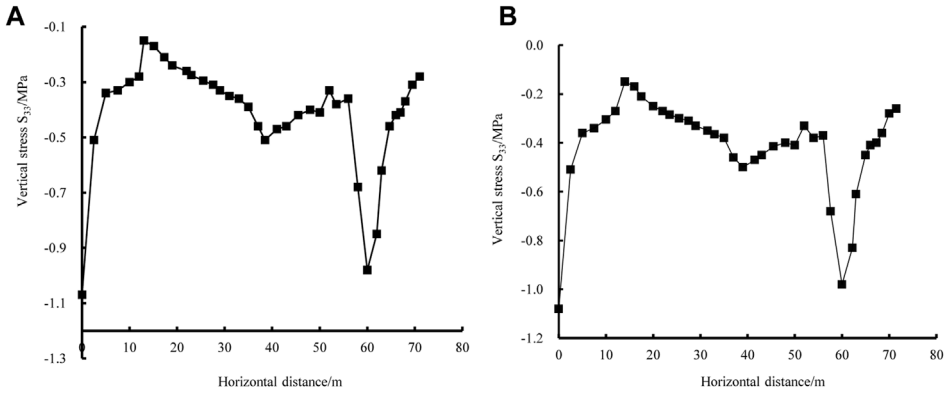

FIGURE 5
Vertical stress curve of the Ruili bank base floor under the one-time design load condition. **(A)** The vertical stress in the natural state. **(B)** The vertical stress in saturated state.

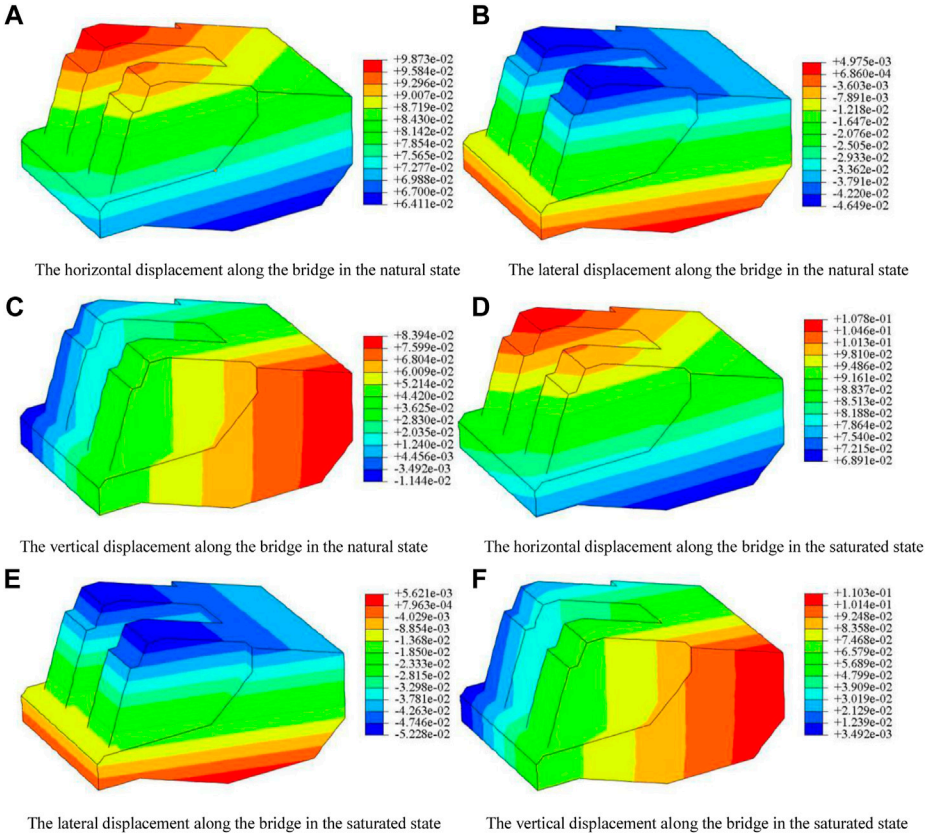

FIGURE 6
Displacement contours of Ruili bank anchors under the one-time design load condition.

The calculation of anti-sliding and anti-overturning stability coefficients considers the weight of anchorage, the pile load of the approach bridge, and the cable force in Table 2. The calculation of the base stress only considers the weight of the anchorage in the construction stage, while the calculation of the eccentric bending moment considers all the forces. The calculation of the base stress and eccentric bending moment considers all the forces in the operation stage. Table 2 shows that the anti-overturning stability of the Ruili bank calculated using the simplified mechanical model meets the normative standard. The anti-sliding stability

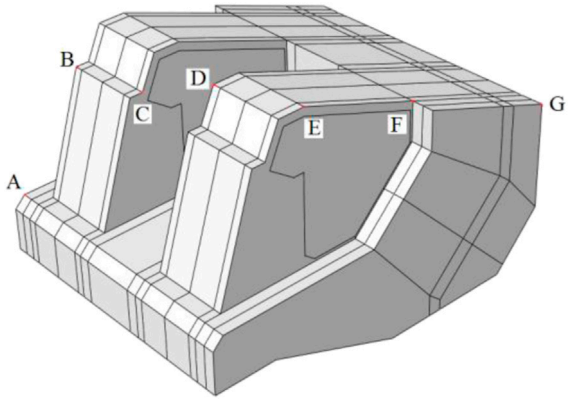

FIGURE 7
Monitoring point diagram.

TABLE 3 Maximum and minimum displacement of Ruili bank anchors under the one-time design load condition.

Stage	State	Displacement/mm					
		Maximum			Minimum		
		Horizontal	Lateral	Vertical	Horizontal	Lateral	Vertical
Construction	Natural	98.7	5.0	83.9	64.1	−46.5	−11.4
Operation	Saturated	107.8	5.6	110.3	68.9	−52.3	3.5

also meets the normative standard. The average and maximum stresses of the base stress are less than the bearing capacity of foundation gravel soil with depth and width correction in the construction and operation stages, and the bearing capacity of the gravel soil foundation is safe. The horizontal and vertical deformations of the anchorage-foundation do not meet the deformation stability standard.

5 Safety evaluation of anchorages based on finite element numerical analysis

According to the terrain survey and anchorage design data, the numerical model size was 200 m from the foundation boundary along the *x* and *y* directions respectively, and the *z* direction is 200 m down from the bottom of the foundation based on the Abaqus calculation software. The numerical model of Ruili bank is shown in Figure 4.

The numerical model was divided into 170,901 elements and 233,400 nodes. The calculation adopted an elastic–plastic constitutive. The calculation parameters are shown in Table 1. The model was surrounded by normal constraints and the bottom was fully constrained.

The simulation of the construction process mainly comprised two parts. 1) The numerical loading test at the full design load, which is the initial geo-stress balance, followed by the excavation of 1–4 layers of soil, application of the anchor and prestress, application of the full large design load, and foundation pit backfill. 2) The numerical overload test, which continues loading at the full design load test until the tensile stress, connectivity of plastic zone, or 20 times the design load appears on the base.

5.1 Design load tests

To evaluate the bearing safety characteristics of gravel soil under the design load, the vertical stress of a single anchor base along the bridge direction axis under natural and saturated parameters is extracted and organized, as shown in Figure 5.

Figure 5 shows that the maximum at the toe of the abutment is 1,072 kPa, which is less than the bearing capacity of foundation gravel soil with a depth and width correction of 1,354 kPa (abutment base) in the natural state. The maximum postmedian anchorage is 970 kPa, which is less than the bearing capacity of foundation gravel soil with a depth and width correction of 1,762 kPa (anchorage base). The maximum at the toe of the abutment is 1,036 kPa, which is less than the bearing capacity of foundation gravel soil with depth and width correction of 1,354 kPa (anchorage base) in the saturated state. The maximum postmedian anchorage is 988 kPa, which is less than the bearing capacity of foundation gravel soil with a depth and width correction of 1,762 kPa (anchorage base). Therefore, the bearing capacity of the foundation gravel soil is safe.

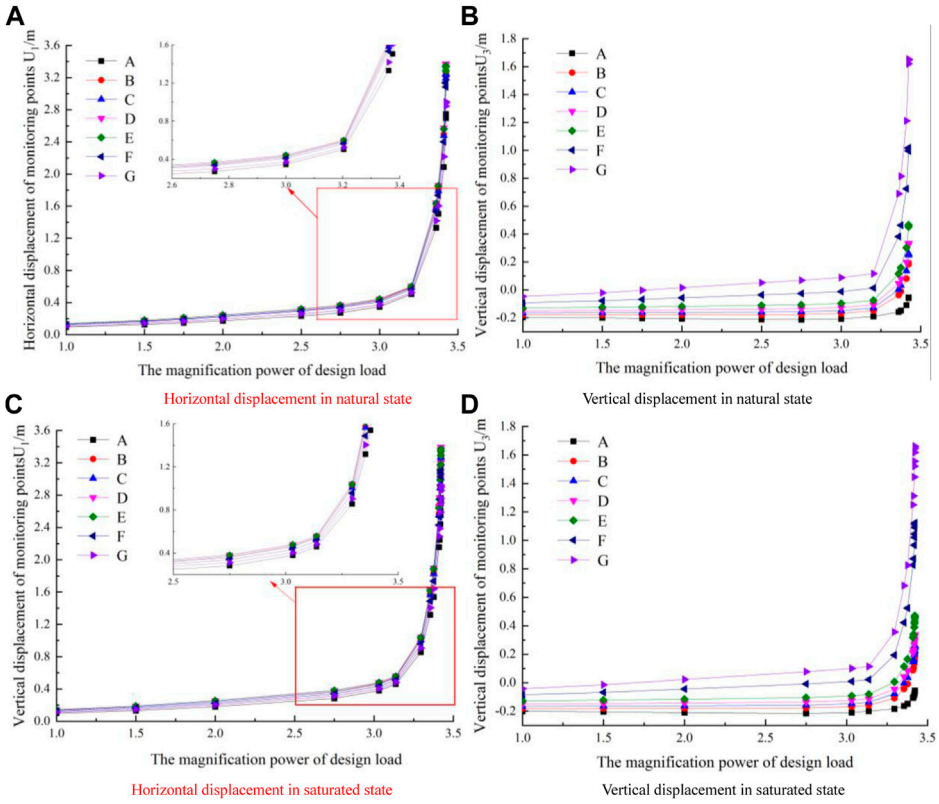

FIGURE 8
Load-settlement curve of the monitoring point of the anchorage under overload on Ruili bank.

To evaluate the corner dislocation characteristics of the anchorage structure under the design load, the displacement calculation results of the anchorage structure under the final force of the foundation pit excavation, anchorage construction completion, cable hanging, prestress application, backfill foundation pit, and normal use are shown in Figure 6. The maximum and minimum displacements of the Ruili bank anchor at the full design load are shown in Table 3.

According to Figure 6 and Table 3, the maximum horizontal displacement along the bridge appears at the top of the abutment, which is 98.7–107.8 mm. The lateral displacement appears on both sides of the top of the abutment, with a maximum displacement of 5.0–52.3 mm. The maximum vertical displacement appears at the top of the abutment, with a maximum settlement of 11.4–110.3 mm. The maximum horizontal displacement of the anchorage structure is 107.8 mm, which is greater than 80.0 mm; thus, it does not meet the safety standard for horizontal displacement of the structure. The maximum vertical displacement of the anchorage structure is 110.3 mm, less than 160.0 mm, which meets the safety standard for the vertical displacement of the structure.

The normal and tangential forces of the anchorage base are, respectively, used by surface integral and multiplied by the designed concrete-gravel soil friction coefficient of 0.40 to obtain the anti-sliding force. The safety factor against sliding is calculated as follows:

$$F_a = \frac{F_{anti-sliding\ force}}{F_{horizontal\ force}}. \tag{10}$$

Natural state:

$$F_s = \frac{0.4 \times 1.603 \times 10^9}{3.136 \times 10^8} = 2.045 > 2.0. \tag{11}$$

Saturated state:

$$F_s = \frac{0.4 \times 1.603 \times 10^9}{3.148 \times 10^8} = 2.037 > 2.0. \tag{12}$$

The anti-sliding stability coefficient of the gravity anchorage of the Ruili bank is 2.05 in the natural state and the anti-sliding stability coefficient is 2.04 in the saturated state under the full design load, which are both greater than the 2.00 in the specification, thus meeting the requirements for anti-sliding stability.

5.2 Overload test

(1) Determination of the ultimate bearing capacity of the anchorage-foundation system

The monitoring point diagram is shown in Figure 7. The ultimate bearing capacity of the anchorage-foundation system was determined by the P–S curve of the load test. The displacement and loading amounts of the different geometric

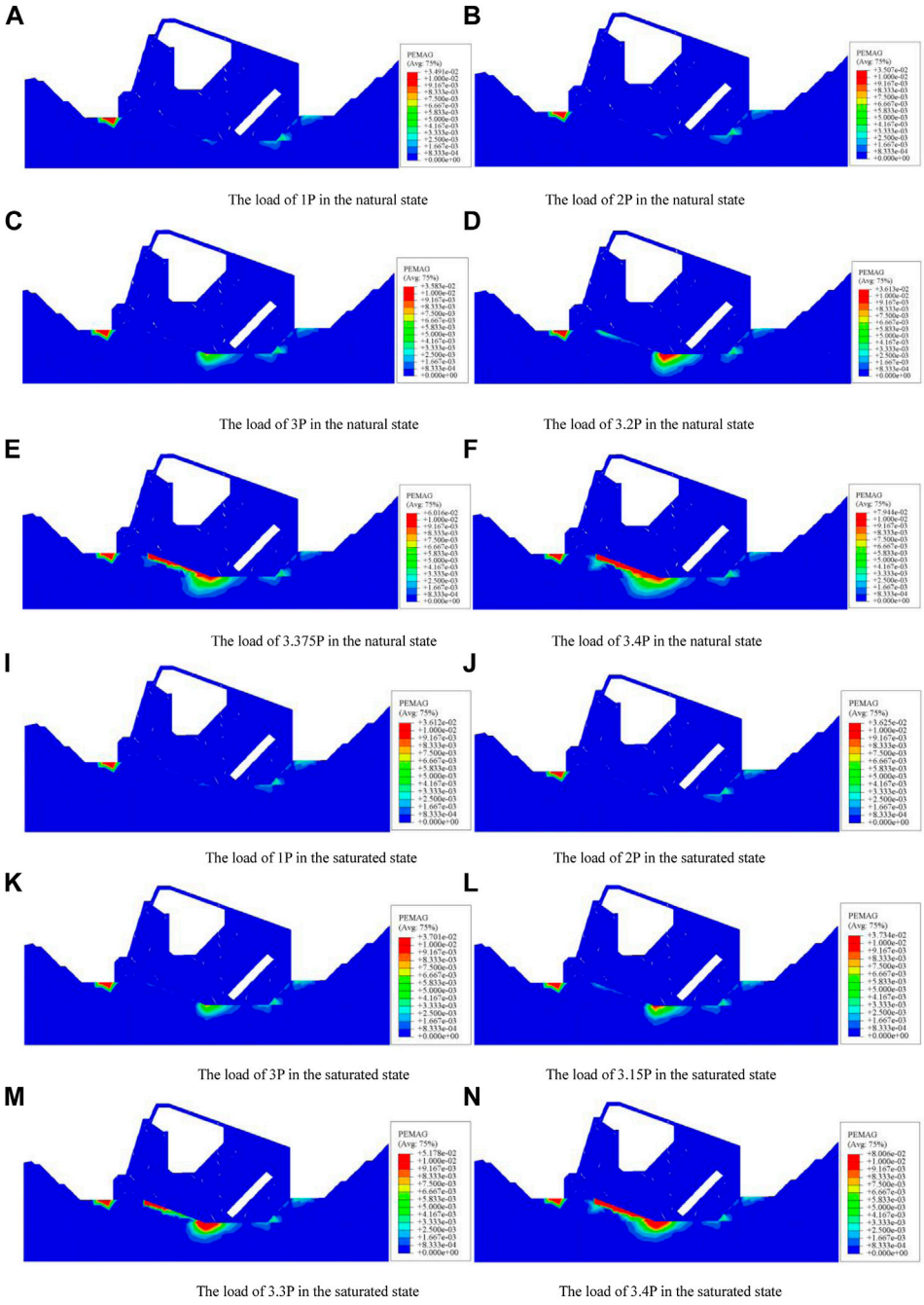

FIGURE 9
Plastic zone cloud diagram of the anchorage axis section of the Ruili bank under overload conditions.

corners of the anchorage structure are drawn in the load–settlement curve as shown in Figure 8. The ultimate bearing capacity at the inflection point of the curve is 3.20 P overload in the natural state and 3.15 P overload in the saturated state, where P is the design load.

The connectivity of the plastic zone was taken as a diagnostic criterion for system instability. The plastic zone cloud diagram on the anchorage-foundation axis section under the overload test is shown in Figure 9. Figure 9 and Table 4 show that the plastic zone is connected at a load of 3.20–3.75 P, and that the maximum plastic strain is multiplied in the natural state. The plastic zone is connected at the load of 3.15 P–3.30 P, and plastic strain increased dramatically in the saturated state. The ultimate bearing capacity obtained by plastic strain is 3.20 P load in the natural state and 3.15 P load in the saturated state.

As an important index of safety evaluation of gravity anchors, the vertical stress of the basement axis under overload is shown in

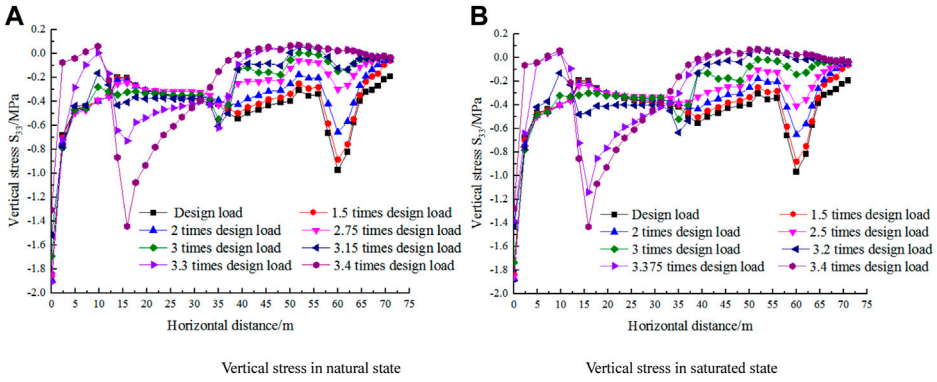

FIGURE 10
Vertical stress curves of the Ruili bank base floor under overload conditions.

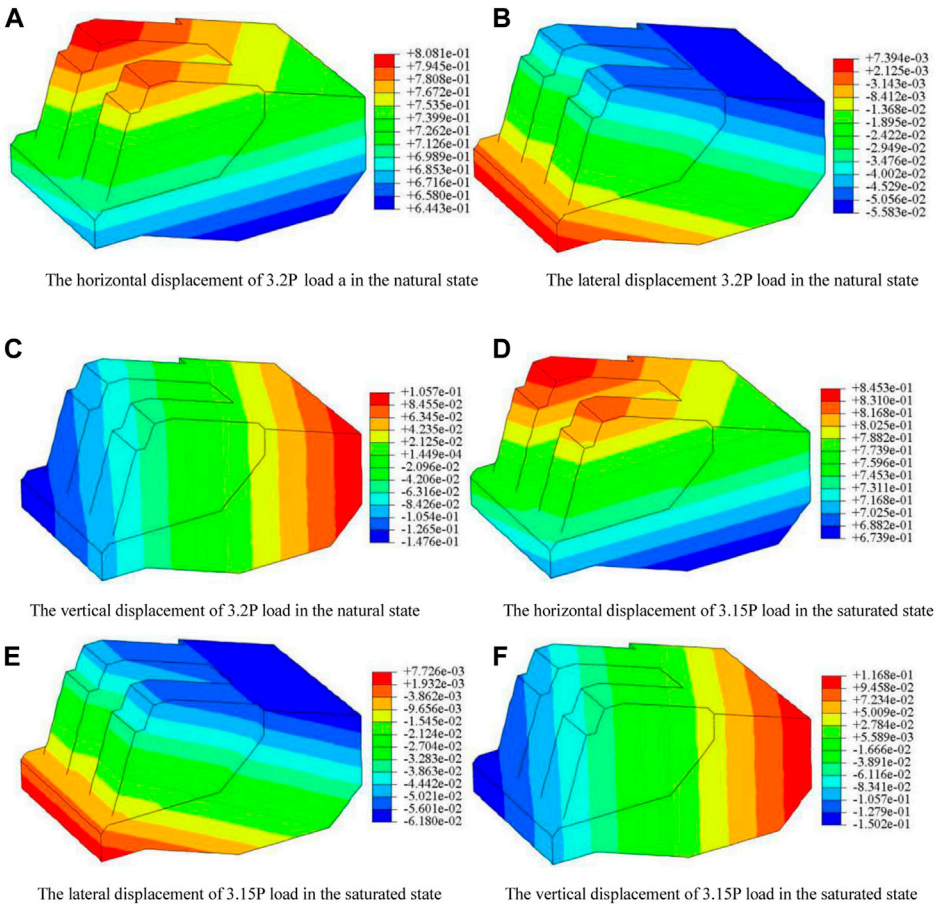

FIGURE 11
Displacement cloud diagram along the bridge of anchor of Ruili bank in the limit state.

Figure 10. Figure 10 shows that most of the base stress is tensile stress under the action of 3.20 P overloading in the natural state. The maximum vertical stress of the abutment base is 1.07 MPa under the action of 1 P overloading, 1.38 MPa under 1.5 P overloading, 1.43 MPa under 2.0 P overloading, and 1.73 MPa under 2.5 P overloading. Most of the base stress is tensile stress under the action of 3.15 P overloading in the natural state. The maximum vertical stress of the abutment base is 1.04 MPa under the action of 1 P overloading, 1.52 MPa under 1.5 P overloading, 1.69 MPa under 2.0 P overloading, and 1.84 MPa under 2.5 P overloading. The

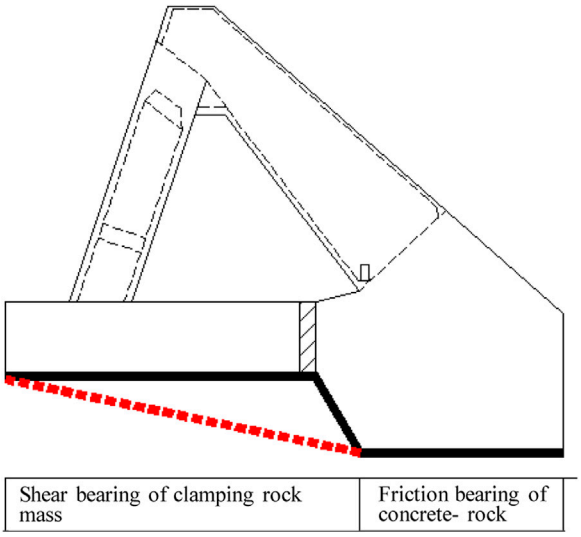

FIGURE 12
Failure mode of gravity anchor-foundation.

TABLE 4 Maximum equivalent plastic strain of the Ruili bank under overload conditions.

State	1.0 P	2.0 P	3.0 P	3.2 P	3.375 P	3.4 P
Natural	0.03491	0.03507	0.03583	0.03613	0.06016	0.07944
State	1.0 P	2.0 P	3.0 P	3.15 P	3.3 P	3.4 P
Saturated	0.03612	0.03625	0.03701	0.03734	0.05178	0.08006

allowable bearing capacity of the gravel soil foundation with modified abutment depth and width is 1,354 kPa. The ultimate overload of the foundation with the maximum stress value of 1,450 kPa exceeding the bearing capacity of 1,354 kPa is 3.5 P, which is larger than the overload of 1.5 P revealed by the finite element based on the bearing capacity. Through the specification calculation, the ultimate overload of the maximum base exceeding the foundation bearing capacity of 1,354 kPa is 3.5 P, which is larger than the load of 1.5 P obtained by the finite element based on the bearing capacity.

The ultimate bearing capacities of the anchor rock systems in the Ruili bank are 3.20 P in the natural state and 3.15 P in the saturation state. When the bearing capacity is less than the critical value, the structure is safe, and the base tensile stress zone can be controlled. According to Formula 6, the tensile stress zone appears on the substrate when the load is 2.0–2.5 P, which is smaller than the finite element results.

(2) Safety evaluation of the gravity anchor block in the limit state

The maximum vertical stress appears at the toe of the abutment, which is also the maximum stress position under eccentric action. When the load exceeds 1.5 P, the maximum vertical stress is greater than the bearing capacity of foundation gravel soil with a depth and width correction, and the remaining parts are safe. The displacement cloud diagram along the bridge anchor of the Ruili bank in the limit state is shown in Figure 11. The maximum and minimum displacements of the anchors of Ruili bank in the limit state are shown in Table 5.

Figure 11 and Table 5 show a maximum horizontal displacement of the anchorage structure along the bridge of 845.3 mm at the top of the abutment in the limit state, which is >80.0 mm; thus, it does not meet the safety standard for the horizontal displacement of the structure. The lateral displacement occurs on both sides of the top of the abutment, with a maximum displacement of 61.8 mm. The maximum vertical displacement was 150.2 mm at the top of the abutment. This value was <160.0 mm, which met the safety standard for vertical displacement of the structure.

TABLE 5 Maximum and minimum displacement of anchors in Ruili bank in the limit state.

Stage	State	Maximum displacement/mm			Minimum displacement/mm		
		Horizontal	Lateral	Vertical	Horizontal	Lateral	Vertical
Overload	Natural	808.1	7.4	105.7	644.3	−55.8	−147.6
	Saturated	845.3	7.7	116.8	673.9	−61.8	−150.2

6 Problems and improvement measures

6.1 Anti-sliding bearing mechanism

The failure mode of the stepped gravity anchorages is shown in Figure 12. The anchorage base is friction bearing. The abutment base is the stepped shear bearing, which differs from the friction bearing alone considered in the traditional design.

$$k_a = \frac{uP_{anchor} + P_{abutment}tg\varphi + CS_{abutment} + \sum T_{ip}}{\sum T_{ia}}, \quad (13)$$

where P_{anchor} and $P_{abutment}$ are the vertical force, which is obtained as uniformly distributed stress multiplied by their respective area (kN), c is the cohesion of rock–soil mass with stepped (kPa), φ is the internal friction angle of rock–soil mass with stepped (°), and $S_{abutment}$ is the undersurface projection area of the abutment. The other parameters are the same as in Formula 3.

6.2 Effect of soil backfilling

After excavation of the anchorage foundation, it is generally backfilled, which causes the upper part of the valve base of the abutment to cover the backfill soil to a certain thickness. The effective weight of the backfill soil $G_{backfilling\ soil}$ can be used as a safety margin.

$$k_a = \frac{\mu P_{anchor} + \left(P_{abutment} + G_{backfilling\ soil}\right)tg\varphi + CS_{abutment} + \sum T_{ip}}{\sum T_{ia}}. \quad (14)$$

The anti-sliding stability coefficient calculated by the formula method was relatively large, while the finite element result was relatively small as the base stress was only larger in the local part, and most parts were less than the average stress. The stress distribution obtained by the finite element method was closer to the real situation. This demonstrated the need to distinguish the safety standards of the two methods.

6.3 Deformation stability

The deformation results obtained by finite element calculation were smaller than those calculated by simplified Formula 8, Formula 9. This difference may be attributed to the fact that the simplified formula did not consider the lateral restraint of the foundation. The formula method can be used as a valuation method for preliminary design and lack of regional experience. The finite element method can be used as a valuation method in the construction organization design stage.

The structural deformation of the gravel soil foundation of the Ruili bank did not meet the safety control standards; thus, foundation reinforcement is required. The composite foundation treatment method mainly aims to improve the density and overall stiffness of the gravel soil. Considering the uneven distribution of the gravel soil layer and the borehole wall stability of the gravel soil in the construction stage, the root pile should be used for foundation reinforcement. The concrete construction method should be determined according to the on-site situation.

Assuming root pile diameter D of 0.3 mm, the pile is arranged in a square, with a pile spacing twice the pile diameter of 0.60 m f_{cu} which is generally taken as the average value of cubic compressive strength of the indoor reinforced soil standard test block following the standard 90 days of curing, which is considered 3.0 MPa. E_p is generally preferred 100–200f_{cu}, which is considered 100f_{cu}.

$$d_e = 1.13s = 0.68, \quad (15)$$

$$m = \frac{d^2}{d_e^2 e} = \frac{0.30^2}{0.68^2} = 0.1946, \quad (16)$$

$$E_p = 100 f_{cu} = 300MPa, \quad (17)$$

$$E_{sp} = mE_p + (1-m)E_s = 0.1946*300 + 0.8054*30 = 82.5MPa. \quad (18)$$

The aforementioned parameters are based on experience, and the specific calculation parameters of the project are based on actual construction. By inserting the modulus of the composite foundation into Formula 8, Formula 9, the horizontal displacement was 44.4 mm (< 80.0 mm), and the vertical deformation was 122.8 mm (<160.0 mm). The bearing capacity and deformation of the gravel soil foundation after composite foundation treatment met the requirements.

The use of the aforementioned improved simplified formula methods conveniently allowed the comprehensive and systematic evaluation of anti-sliding stability and anti-overturning stability coefficients of gravity anchors, in addition to base stress checks, foundation bearing capacity, and deformation stability.

7 Conclusion

This study established a corresponding simplified mechanical model of anchorage based on the gravity anchor block project of the Ruili bank of the Banjin Dam suspension bridge. The safety of the anchorage was comprehensively evaluated using the standard method, simplified mechanical model, and finite element method, with the following conclusions:

1) The specifications comprehensively stipulated all aspects of the safety evaluation of the gravity anchors (anti-overturning stability, anti-sliding stability, foundation bearing safety, and deformation stability) but inconsistent calculation methods and models were applied for each index, especially for horizontal deformation. The evaluation of horizontal deformation only recommends the finite element method; however, the operability of the method is greatly limited.

2) The calculation and evaluation methods of anti-overturning stability, anti-sliding stability, base stress control, and deformation stability were established based on the simplified mechanical model according to the original formula of the specification. Compared with the finite element calculation results, the anti-overturning stability coefficient, anti-sliding stability coefficient, horizontal displacement, and vertical displacement obtained by the simplified mechanical model were larger than those of the finite element calculation results, and the maximum and minimum stresses to the foundation were smaller.

3) The improved gravity anchor block safety evaluation index for the physical and mechanical mechanisms was clear, and the calculation was fast. This formula method can be used for the valuation of gravity anchors during preliminary design and in

cases lacking regional experience, or as a supplementary benchmark for the finite element method.

Data availability statement

The original contributions presented in the study are included in the article/supplementary material. Further inquiries can be directed to the corresponding author.

Author contributions

HL provided overall guidance on the article and wrote this paper. MY and XY modified the article language.

Funding

This work was supported by the Loess Soil Mechanics and Engineering Key Laboratory of Shaanxi Province Foundation (13JS073) and the Natural Science Foundation of Shaanxi Province (2017JM5059).

Conflict of interest

The authors declare that the research was conducted in the absence of any commercial or financial relationships that could be construed as a potential conflict of interest.

Publisher's note

References

Guo, X., Yu, M., Xinze, W., Xue, D. Y., and Han, H. X. (2022). Four new species of *Ditrigona* Moore (Lepidoptera, Drepanidae) in China and an annotated catalogue. *J. Railw. Eng. Soc.* 1091 (11), 57–98. doi:10.3897/zookeys.1091.78986

Huang, N., Li, Y., Cheng, L., Sun, G., and Wang, Z. (2014). Stability calculation and numerical analysis on anchorage of suspension bridge with gravity concrete. *J. Henan Univ. Urban Constr.*, 23(3):5–8. doi:10.14140/j.cnki.hncjxb.2014.03.022

Ji, L., Xu, F., and Wang, B. T. (2003). Testing study on base resistance of the anchors at Runyang bridge. *Chin. J. Rock Mech. Eng.* 23 (2), 256–260.

Li, H., Huang, S., Wang, X., Li, S., and Xu, B. (2016). Finite element analysis on horizontal bear capacity characteristic ofgravity anchor. *China Harb. Eng.* 36 (1), 6–9.

Li, J., Zhang, Z., Huang, H., and Li, Y. (2005). Research on similarity model test of anchorage of qingfeng suspension bridge in ningbo. *J. Tongji Univ. Nat. Sci.* 33 (8), 1011–1016.

Li, S., Zhu, X., Li, H., Huang, S., Wang, X., Hou, Q., et al. (2018). Study design and baseline characteristics of inpatients with diabetes mellitus in a tertiary hospital in China: A database study based on electronic medical records. *China offshore oil gas* 30 (2), 152–157. doi:10.1111/jebm.12291

Li, Y., Lu, Z., Burbank, D. E., Kutish, G. F., Rock, D. L., and Van Etten, J. L. (1995). Analysis of 43 kb of the chlorella virus PBCV-1 330-kb genome: Map positions 45 to 88. *J. Tongji Univ. Nat. Sci.* 20 (20), 134–150. doi:10.1006/viro.1995.1462

Liu, M. (1999). Basic ideas of suspension bridge gravity anchor block design. *Highway* (7), 16–23.

Liu, N., Ning, L., Li, G., Song, Z., and Wang, S. (2022a). Method for evaluating the equivalent thermal conductivity of a freezing rock mass containing systematic fractures. *Rock Mech. Rock Eng.* 55, 7333–7355. doi:10.1007/s00603-022-03038-9

Liu, N., Ning, L., Wang, S., Li, G., and Song, Z. (2022b). A fully coupled thermo-hydro-mechanical model for fractured rock masses in cold regions. *Cold Regions Sci. Technol.* 205, 103707. doi:10.1016/j.coldregions.2022.103707

Liu, N., Ning, L., Xu, C., Li, G., Song, Z., and Yang, M. (2020). Mechanism of secondary lining cracking and its simulation for the dugongling tunnel. *Rock Mech. Rock Eng.* 53, 4539–4558. doi:10.1007/s00603-020-02183-3

Liu, W., and Lin, Z. (2014). Test study on the friction resistance of the north concrete anchor of qingcaobei yangtze river bridge. *Highway* 10, 124–128.

Liu, Y., Jun, F., Li, X., Gong, Z., and Chen, H. (2022c). Bearing mechanism of new type combined gravity anchor of suspension bridge. *Chin. J. Undergr. Space Eng.* 18 (S1), 187–193.

Liu, Y., Zhao, M., and Zheng, S. (2011). Test study on the friction resistance of the north concrete anchor of qingcaobei yangtze river bridge. *J. Chongqing Normal Univ. Nat. Sci. Ed.* (5), 911–915.

Ran, T., Mao, J. N., Mei, S. H., Wang, W. W., and Tan, L. H. (2018). Sensitivity analysis of rock-soil parameters of a gravity anchor excavation based on orthogonal experiment method. *J. Yangtze River Sci. Res. Inst.* 35 (2), 101–106. doi:10.11988/ckyyb.20160804

Tan, X., Xu, H., and Peng, W. (2015). The test and calculating method for gravity anchorage's frictional coefficient of suspension bridge. *Chin. J. Undergr. Space Eng.* 11 (2), 549–552+584.

Yin, X., Fei, Y., Zhou, L., Wang, D., and Deng, Q. (2017a). Exploration on the horizontal limit bearing capacity formula of gravity anchorage. *J. Railw. Eng. Soc.* (1), 41–46.

Yin, X., Fei, Y., Zhou, L., Wang, D., and Deng, Q. (2017b). Joint bearing mechanism of structure and foundation for gravity anchor blockblock of suspension bridge. *J. Traffic Transp. Eng.* 17 (2), 1–11.

Zhu, S. (2011). Suggestion on partial safety factor used in anchorage design of suspension bridge. *Xi'nan Highw.* (4), 19–21.

frontiers | Frontiers in Earth Science

TYPE Original Research
PUBLISHED 23 June 2023
DOI 10.3389/feart.2023.1212726

OPEN ACCESS

EDITED BY
Yuwei Zhang,
Xi'an University of Architecture and Technology, China

REVIEWED BY
Jin-Shuai Zhao,
Jiangsu University, China
Shengzhi Wu,
Shandong Jianzhu University, China

*CORRESPONDENCE
Ying Zhao,
zhaoying856@126.com

RECEIVED 26 April 2023
ACCEPTED 01 June 2023
PUBLISHED 23 June 2023

CITATION
Li X, Zhao Y, Xue H, Zhang L and Gong X (2023), Stability analysis of tunnel in sandy cobble strata under different pre-reinforcement techniques.
Front. Earth Sci. 11:1212726.
doi: 10.3389/feart.2023.1212726

Stability analysis of tunnel in sandy cobble strata under different pre-reinforcement techniques

Xiaobin Li[1,2], Ying Zhao[3]*, Haifang Xue[2], Lei Zhang[2] and Xiaoqin Gong[2]

[1]School of Civil Engineering, Chongqing University, Chongqing, China, [2]Qinghai Xihu Expressway Management Co., Ltd., Xining, China, [3]School of Highway, Chang'an University, Xi'an, China

Excavating tunnels in sandy cobble strata carries a high risk of ground collapse caused by instability of the tunnel face. In order to prevent instability at the tunnel face during excavation, this paper focuses on studying the effects of various pre-reinforcement method on the stability of tunnel in the sand-cobble strata. Firstly, pre-reinforcement projects suitable for these tunnels are proposed. Then, using FLAC3D to established numerical models, then simulate the excavation process under six different working conditions: non-reinforced, pre-reinforcement with advance small pipes, pre-reinforcement with pipe-roof, pre-reinforcement with GFRP bolts, pre-reinforcement with advance small pipes and GFRP bolts, and pre-reinforcement with pipe-roof and GFRP blots. The displacement and stress fields of the soil behind and in front of the tunnel face under each condition are obtained. The results show that the use of GFRP bolts for pre-reinforcement can effectively control the deformation of the surrounding rock in front and behind the tunnel face, and pre-reinforcement with advance small pipes or pipe-roof can reduce the settlement of the tunnel crown. Pre-reinforcement by the combination of GFRP bolts with advance small pipes or pipe-roof can better ensure the stability of the tunnel during the excavation process.

KEYWORDS

sandy cobble strata, numerical simulation-, pre-reinforcement techniques, face stability, stone content

1 Introduction

The sandy cobble stratum is a typical mechanically unstable geological formation (Martí et al., 2008), mainly composed of pebbles, gravels, sands, and a small amount of clay, which are widely distributed in cities such as Beijing, Lanzhou, Chengdu, and Shenyang in China. Tunnels passing through sand-cobble stratum are highly susceptible to disrupting the initial equilibrium state of the formation during excavation, and ground collapse accidents caused by tunnel instability frequently occur in the engineering practice. Without reinforcement measures, existing tunnels in sand-cobble stratum will experience more severe disturbances than those in other geological formations (Liang et al., 2017; Jin et al., 2018; Lin et al., 2021). Therefore, when conducting underground engineering construction in sandy cobble stratum, auxiliary measures such as pre-support or pre-reinforcement should be taken to ensure the stability of the formation and the safety of existing tunnels.

To ensure the stability of the tunnel during excavation, various auxiliary methods have been proposed and applied by many scholars in the industry, including pre-grouting, drift face anchoring, vertical pre-reinforcement technology, pre-grouting, and ground freezing

(Lunardi, 2008). Among them, ground pre-grouting and ground freezing methods have been frequently applied to reinforce sandy cobble stratum in recent years and have been proven to be particularly useful in improving the stability of tunnels in sandy cobble stratum during construction (Kang et al., 2021; Mei et al., 2021). Although methods such as ground grouting reinforcement and ground freezing can ensure the stability of the formation during excavation, the construction process is complicated, material waste is serious, and the excavation efficiency is low, which cannot improve the mechanization level of tunnel construction and cannot achieve safe, economic, rapid and efficient construction of tunnels. In this case, a common and economical pre-reinforcement measure is tunnel advance support technology, which can prevent excessive strain during tunnel excavation and maintain the original support capacity of the ground (Shin et al., 2008). Many scholars have conducted research through large-scale field studies (Ocak, 2008; Wang et al., 2016), centrifuge model tests (Hisatake and Ohno, 2008; Juneja et al., 2010; Wong et al., 2012), and numerical simulations (Aksoy and Onargan, 2010; Zhang et al., 2014; Li et al., 2015) to find that the application of pre-support technology greatly improves the stability of the tunnel face.

Although the study of pre-reinforcement technology for tunnels in the sandy cobble stratum is relatively mature, most researchers focus on studying individual reinforcement measures based on the disturbance characteristics of the surrounding rock of existing tunnels (Li et al., 2020; Cao et al., 2021). By analyzing the optimized parameters for various support conditions and conducting numerical simulations of pre-reinforcement methods, they evaluate the reinforcement effect based on the stress and deformation of the surrounding rock and the ground settlement of the tunnel (Yoo and Shin, 2003; Bin et al., 2012; Zhao et al., 2019). However, few researchers have designed multiple pre-reinforcement plans based on engineering geological conditions and project construction characteristics, and compared the comprehensive effects of multiple pre-reinforcement plans. Therefore, various pre-reinforcement measures and their combined comprehensive effects still need further research during the excavation of tunnels in sand-cobble mixed strata.

Based on the complexity of the sand-cobble strata, experimental methods can only provide insights into the mechanical properties of localized sand-cobble mixture. Numerical simulation methods not only enable the establishment of a numerical model for heterogeneous sand-cobble strata, but also allow for the repetition of large-scale numerical experiments. Therefore, numerical simulation methods are better suited for investigating the mechanical properties, deformation characteristics, and stability of sand-cobble strata tunnels (Du et al., 2019). The FLAC3D finite difference software, developed by Itasca, is a continuum mechanics analysis program that can simulate the mechanical properties of various materials such as rock and soil masses, lining, anchor rods, geogrids, etc. It has unique advantages in material elastic-plastic analysis, large deformation analysis, and simulation of construction processes. Some scholars have already used FLAC3D to analyze the stability of tunnels in the sand-cobble mixed strata and obtained good results (Zhang et al., 2019; Cui et al., 2020; Di et al., 2023).

In summary, this study is based on the Da Zhuang tunnel project in Qinghai Province, and designs a pre-reinforcement scheme suitable for tunnel in the sand-cobble mixed stratum based on the geological conditions and construction characteristics of the project. Using the FLAC3D finite difference software, a three-dimensional numerical model is established to investigate the displacement and stress changes of the surrounding rock in front and behind the tunnel face under different working conditions, evaluate the pre-reinforcement effects of different working conditions comprehensively, and propose the optimal pre-reinforcement scheme for the surrounding rock of tunnels in sandy cobble strata. The results can provide valuable experience for similar engineering projects.

FIGURE 1
Sandy cobble stratum.

2 Design of pre-reinforcement technology

2.1 Project overview

The Da Zhuang Tunnel is a separated middle tunnel located in Xi Shan gen Village, Dong Gou Township, Hu Thu Tu Autonomous County, Qinghai Province. The left line starts at ZK40+366 and ends at ZK40+960, with a length of 594 m. The right line starts at YK40+454 and ends at YK41+126, with a length of 672 m. Both tunnels have a 2.5% one-way slope. The left tunnel has a burial depth of 45.2 m, and the maximum burial depth of the right tunnel is approximately 44.7 m. The entrance and exit adopt end-wall and cut-bamboo style doors respectively, and there is one pedestrian cross passage in the tunnel. The tunnel is illuminated by electric lighting, naturally ventilated, and equipped with self-retaining drainage system.

The geological conditions of the project mainly consist of sand-cobble stratum, with the cobble strata appearing as gray-yellow soil, moderately dense, and mainly composed of cobble, followed by pebbles. Sand particles and powdery clay are used for filling, and the cobble particle size is uneven with irregular shapes, which has a significant impact on the tunnel. The rock mass of the tunnel body is mostly Quaternary Upper Pleistocene alluvial gravel (slightly muddy cemented), with poor surrounding rock stability and a surrounding rock grade of level V. During construction, arches without support

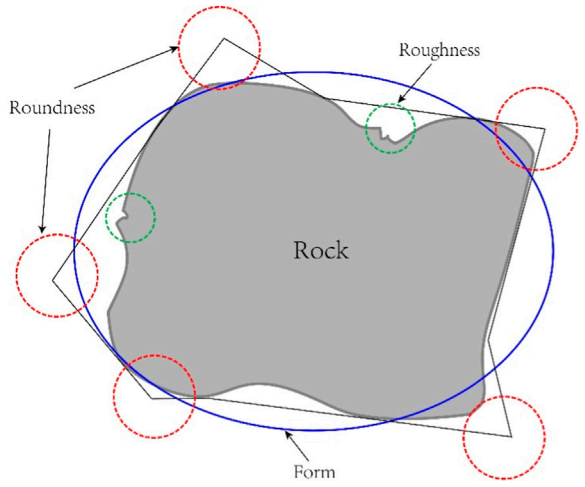

FIGURE 2
Block-shaped information representation symbolization.

are prone to large-scale collapse, and the stability of the side walls is poor. The geological conditions have an extremely unfavorable impact on the blind excavation construction, and the specific situation is shown in Figure 1.

2.2 Summary of pre-reinforcement technology

The pre-reinforcement technology originated from the application of the New Austrian Tunneling Method in mountainous tunnels (Han, 1987). It is difficult to ensure the stability of the excavation face solely through initial support in mountainous tunnels with poor geological conditions and at the entrance and exit sections with sandy cobble mixed strata. To ensure the stability of the excavation face in weak geological layers, appropriate pre-reinforcement techniques need to be applied to the strata. Pre-reinforcement measures can be classified into strata improvement and pre-support methods based on their reinforcement mechanisms on the surrounding soil. Strata improvement refers to improving the mechanical properties of the excavation face and the surrounding strata by grouting, drainage consolidation, or freezing (Kang et al., 2021; Mei et al., 2021). Pre-support method is based on the surrounding rock conditions, construction methods, progress requirements, mechanical support, and the environment in which the project is located before tunnel excavation. It chooses simpler or integrated auxiliary construction methods to strengthen the strength of tunnel surrounding rock to ensure that the excavation face remains stable during tunnel excavation, and the surrounding rock does not collapse. Due to the complex construction process and high cost of strata improvement, and its difficulty in implementation, most projects tend to choose pre-support methods to reinforce the soil around the tunnel.

The necessity and degree of advanced pre-support and support should be determined according to the stability of the surrounding rock. The instability of the surrounding rock is caused by the inability of the support structure to provide sufficient support force, which cannot effectively constrain and control the plastic deformation, resulting in the instability of the excavation face. Reasonable excavation face support measures and scientifically reasonable tunnel construction methods can limit the excessive deformation of the surrounding rock of the excavation face. Conversely, it can promote large deformations, even in better geological conditions. Therefore, selecting appropriate pre-reinforcement methods is critical to the stability of the tunnel construction process.

2.3 Design of pre-reinforcement methods

Based on the geological conditions where the engineering project is located, the geological environment is relatively complex due to the presence of sand-cobble strata. The self-bearing capacity of the tunnel in sandy cobble mixed strata is relatively low, and during the tunnel excavation process, the soil within a certain range in front of the face will undergo plastic deformation due to disturbance, significantly increasing the risk of rock instability. Therefore, it is necessary to perform pre-reinforcement of the surrounding rock of the tunnel to change its initial state and enhance its self-bearing capacity, thereby improving the stability of the face. Currently, the main pre-reinforcement methods for tunnel in sandy cobble mixed strata include the use of advance small pipes, pipe-roof and GFRP bolt (Peila, 1994; Yoo, 2002; Funatsu et al., 2008). Advance small pipes, as the main technical means of pre-reinforcement, have been widely used in China. The small pipes, made of steel, typically have a diameter of about $\phi 32 \sim \phi 60mm$, and a length of 2–6 m, and are mainly arranged longitudinally along the tunnel. They are inclined forward and upward at a certain angle outside the contour line of the excavation profile on the arch top, and the exposed end of the pipe body is usually supported on the steel frame behind the excavation face. The pipes must penetrate into the stable soil ahead to form the pre-reinforcement system. The pipe-roof pre-reinforcement method has a similar structural and layout form to the advance small pipes, with the difference being that larger diameter steel pipes are used, typically around $\phi 100 \sim \phi 600mm$, and with a length of 5–20 m. The pipe-roof method is implemented by driving steel pipes into the upper area of tunnel within a certain range and then injecting grout or pouring concrete into these pipes, thus forming a pre-support structure with higher rigidity in the soil layer, enhancing the bearing capacity of weak surrounding rock, and effectively controlling rock deformation. The anchor rod is the most widely used technology for pre-reinforcement and initial support in rock tunnel construction. It has simple operation, convenient construction, and fast results. Glass fiber bars (DFRP) are commonly used as the material for face anchor rods, which are easy to cut, meet the requirements for pre-reinforcement of the advance core soil, and meet the needs of excavation equipment to excavate soil (Tonon, 2010). In addition, the use of glass fiber reinforced plastic (GFRP) bolts reinforcement can effectively control the deformation of the stratum, significantly improve the overall stability of the tunnel during excavation (Mitarashi et al., 2003), and when combined with the pipe-roof method, it can greatly reduce surrounding rock displacement (Shin et al., 2008).

In summary, based on the engineering background of the Da Zhuang Tunnel in Qinghai Province, this study aims to address the issue of advanced support technology for tunnel in the sand-cobble mixed strata. A three-dimensional numerical model will be established using the finite difference software FLAC3D to

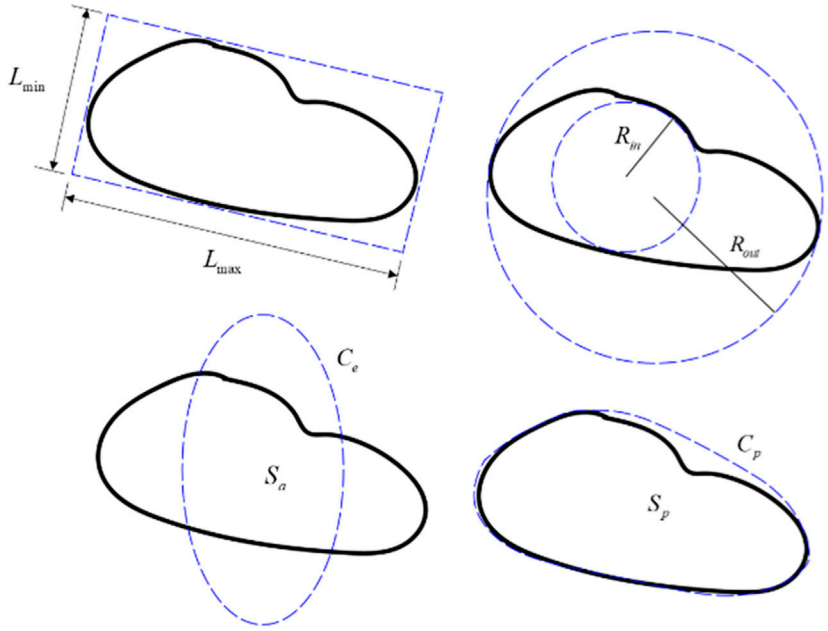

FIGURE 3
Block-shaped information representation symbolization.

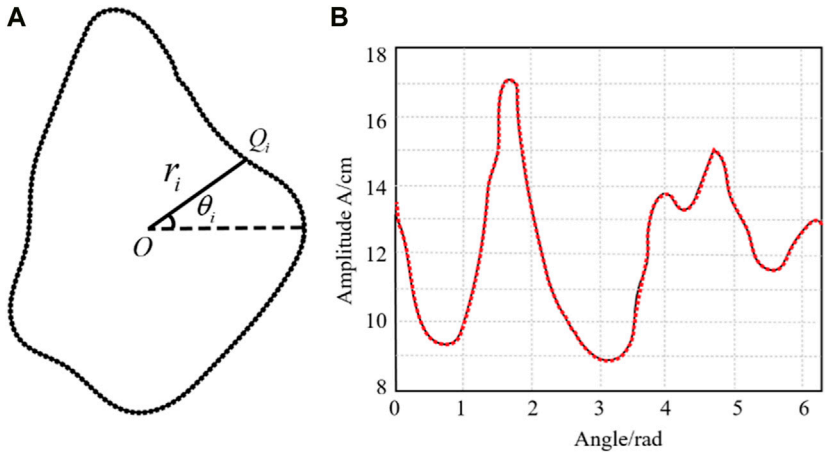

FIGURE 4
Transformation of **(A)** block outlines and **(B)** discrete signals.

simulate the effects of six different pre-reinforcement methods on construction stability, including non-reinforced, pre-reinforcement with advance small pipes, pre-reinforcement with pipe-roof, pre-reinforcement with GFRP bolt, pre-reinforcement with advance small pipes and GFRP bolt, and pre-reinforcement with pipe-roof and GFRP blot. Considering the difficulties in drilling and the risk of collapse during construction in sandy cobble mixed strata, reasonable advanced support measures and their parameters will be determined. By comparing and analyzing the displacement and stress changes of the surrounding rock and the tunnel face under the six working conditions during the construction process, the best pre-reinforcement method for this engineering project will be determined, providing valuable reference for similar projects.

3 Numerical modelling of the tunnel

3.1 Methodology for establishing a cobble database

In numerical simulation studies of tunnels in the sand-cobble strata, it is common practice to treat the strata as homogeneous

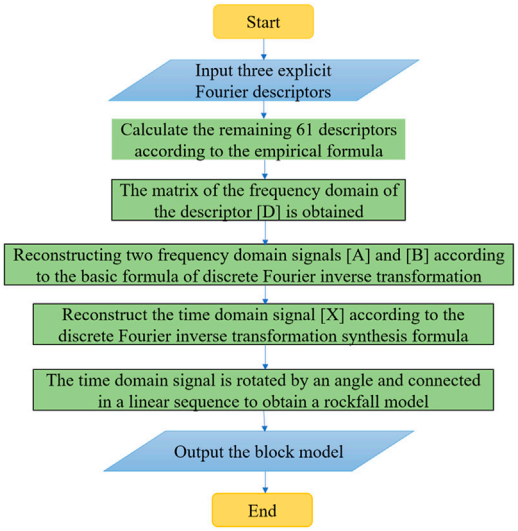

FIGURE 5
The process of reconstructing the block model.

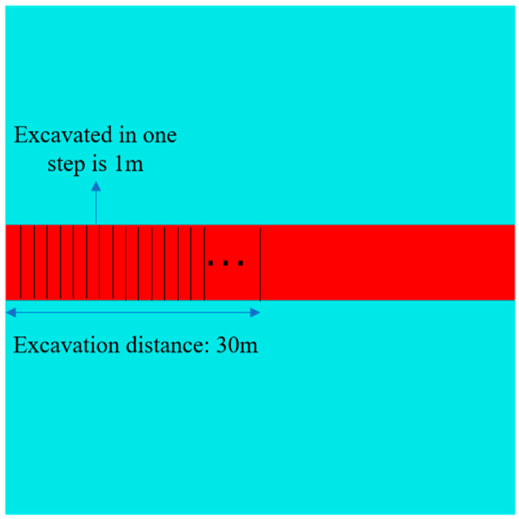

FIGURE 7
Details of excavation.

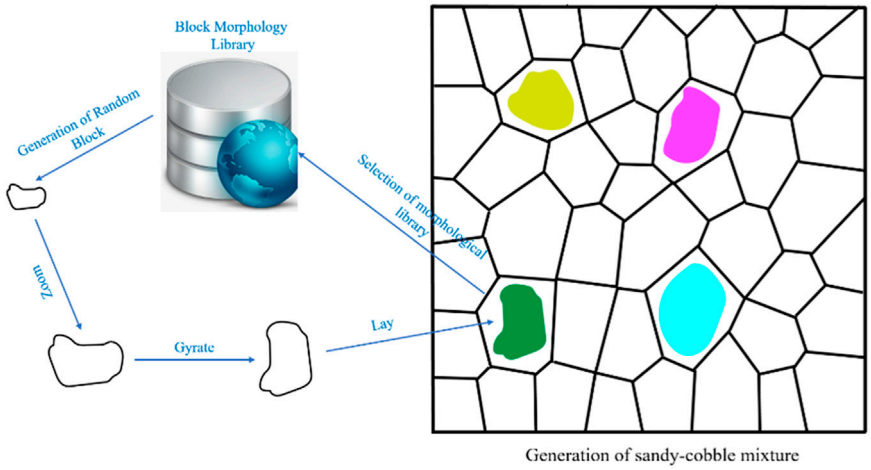

FIGURE 6
Stochastic model generation process for sandy-cobble mixture.

materials and to use comprehensive mechanical parameters such as deformation modulus, cohesive force, and internal friction angle to investigate stability and ground settlement problems caused by tunnel excavation (Zhang et al., 2013; Huang et al., 2019). However, sand-cobble mixed strata are non-homogeneous materials with a large particle size distribution, and their internal microstructural features have an important influence on the overall mechanical properties. Ignoring the existence of large blocks of rock will lead to inaccurate predictions of the stability and deformation of tunnels in sandy cobble stratum during construction. Therefore, to accurately simulate sand-cobble mixture in actual engineering projects, it is necessary to construct a rock model with a similar particle size distribution and randomly shaped rocks. To characterize the true shape characteristics of the rock, this study first analyzes the shape features of actual rock from a quantitative perspective and then uses the discrete Fourier transform to reconstruct a block model and establish a cobble database. The Fourier descriptors have been proven to be able to well describe the real shape of large blocks of rock and generate blocks with specific shapes (Mollon and Zhao, 2012).

To begin, it is necessary to study the shape characteristics of actual rock blocks. In previous studies, Barrett (1980) proposed three shape descriptors (as shown in Figure 2) that can be used to fully describe the shape characteristics of rock blocks, namely, the Form, Roundness and Surface texture. Referring to existing methods (Hentschel and Page, 2003), the form described by flatness (OP) and sphericity (SP), while roundness is described by angularity (AP), concavity (AC), and shape factor (SF). The roughness of the rock is

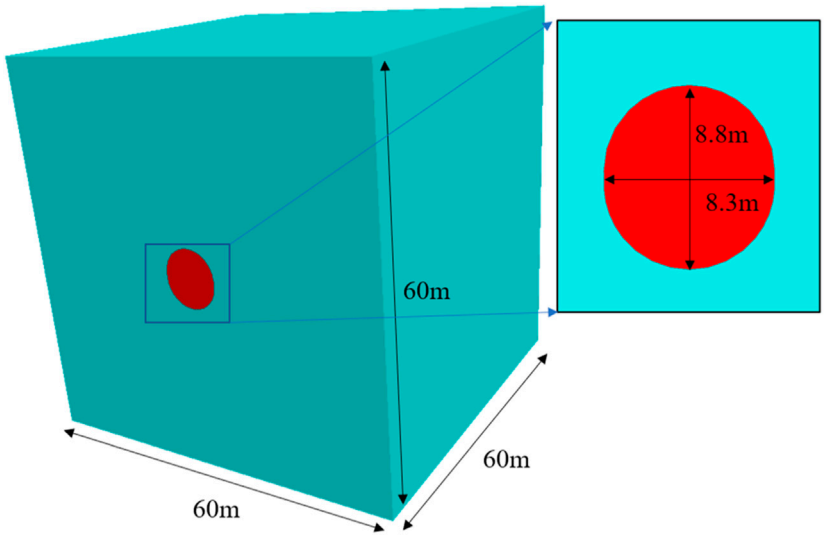

FIGURE 8
Numerical model.

described by the roughness (RO) index. The representation of the above indicators is shown in Figure 3, and can be expressed as:

$$OP = \frac{L_{\min}}{L_{\max}} \tag{1}$$

$$SP = \frac{R_{in}}{R_{out}} \tag{2}$$

$$AP = \frac{C_e}{C_p} \tag{3}$$

$$AC = \frac{S_a}{S_p} \tag{4}$$

$$SF = \frac{2\sqrt{\pi S_a}}{C_a} \tag{5}$$

$$RO = \frac{C_p}{C_a} \tag{6}$$

Where, $L_{\max}$ is the maximum values of the rock, $L_{\min}$ is the minimum values, R_{in} represents the maximum radius of the inscribed circle of the block, R_{out} and represents the minimum radius of the circumscribed circle of the block. C_e denotes the perimeter of the ellipse with the same area as the rock block, while C_P and S_p respectively represent the perimeter and area of the minimum circumscribed convex polygon of the rock block. S_a denote the area of the rock and C_a denote the perimeter of the rock.

Once the metrics that describe specific shapes of the blocks have been obtained, the block model can be reconstructed using Fourier transform. As shown in Figures 4A, B, the contour of the block can be transformed into a discrete signal. Firstly, the contour of the block $O(x_0, y_0)$ shown in Figure 4A is divided into m segments based on the center point θ at equal angles θ_1, θ_2, θ_3., θ_4. θ_m. The intersection between the angle side and the boundary of the rock contour represents a sampling point Q_i. The distance from Q_i to the center point $O(x_0, y_0)$ is r_i, and the position of each discrete point on the boundary of the block can be represented by the angle θ_i and the length r_i, which from the point to the center point.

$$r_i = f(\theta_i) \tag{7}$$

In the Cartesian coordinate system:

$$\begin{cases} x_i = x_0 + r_i \cos(\theta_i) \\ y_i = y_0 + r_i \sin(\theta_i) \end{cases} \tag{8}$$

After converting the obtained rock block outline into a discrete signal, the rock block model is reconstructed using the discrete Fourier inverse transform. The distance r_i from Q_i to the center point $O(x_0, y_0)$ can be regarded as a discrete time-domain signal and is expressed in terms of Fourier series:

$$r_i = r_0 + \sum_{n=1}^{m/2} [A_n \cos(n\theta) + B_n \sin(n\theta)] \tag{9}$$

$$r_0 = \frac{1}{m} \sum_{i=1}^{m} r_i \tag{10}$$

Where, r_0 is the average radius of the block. Chosen 128 scattered points to form the outline of the block. Das N. (2007) found that the high-order harmonic frequencies have less impact when the order is greater than m/2. Therefore, in this study, the total number of harmonics selected is m/2. By polarizing Formula (9) and normalizing it (dividing both sides by r_0), we obtain:

$$\frac{r_i}{r_0} = 1 + \sum_{n=1}^{m/2} \left[\frac{\sqrt{A_n^2 + B_n^2}}{r_0} \sin(n\theta_i + \varphi_n) \right] \tag{11}$$

Where, D_n is the Fourier descriptor, the formula of D_n is:

$$D_n = \frac{\sqrt{A_n^2 + B_n^2}}{r_0} \ (1 \le n \le 64, n \in N^*) \tag{12}$$

The coefficients A_n and B_n represent the Fourier coefficients. The Python implementation process for

TABLE 1 Mechanical parameters of the sandy cobble strata.

Parameters	*E* (MPa)	*v*	*c* (MPa)	*φ* (°)	Tensile strength (MPa)	Density
Value	37.78	0.32	23	26	0	1850

TABLE 2 Physical and mechanical parameters of pre-reinforced materials.

Materials	Thickness (mm)	Diameter (mm)	Length(m)	Ring spacing(m)	*E* (MPa)	*v*
Advance small pipes	5	42	6	0.4	210	0.3
Pipe-roof	8	100	12	0.4	210	0.3

TABLE 3 Physical parameters of lining.

Parameters	Thickness(m)	*E* (GPa)	*v*	Density
Value	0.3	23	0.2	2,200

reconstructing the rock based on the discrete Fourier inverse transform is illustrated in Figure 5. Using the above block stone surface shape library, a random model of sandy cobble strata can be generated, and the process for generating the random model is shown in Figure 6.

3.2 Numerical simulation

3.2.1 Simulation method

According to the engineering background, the tunnel passes through the sand-cobble stratum, and based on the characteristics of mechanized construction, the stability analysis of surrounding rock under different pre-reinforcement methods is carried out. According to the design requirements, the mechanical construction adopts the core soil method, focusing on the stability of the soil in front of the face. In the numerical simulation, excavation is carried out in steps of 1 m (as shown in

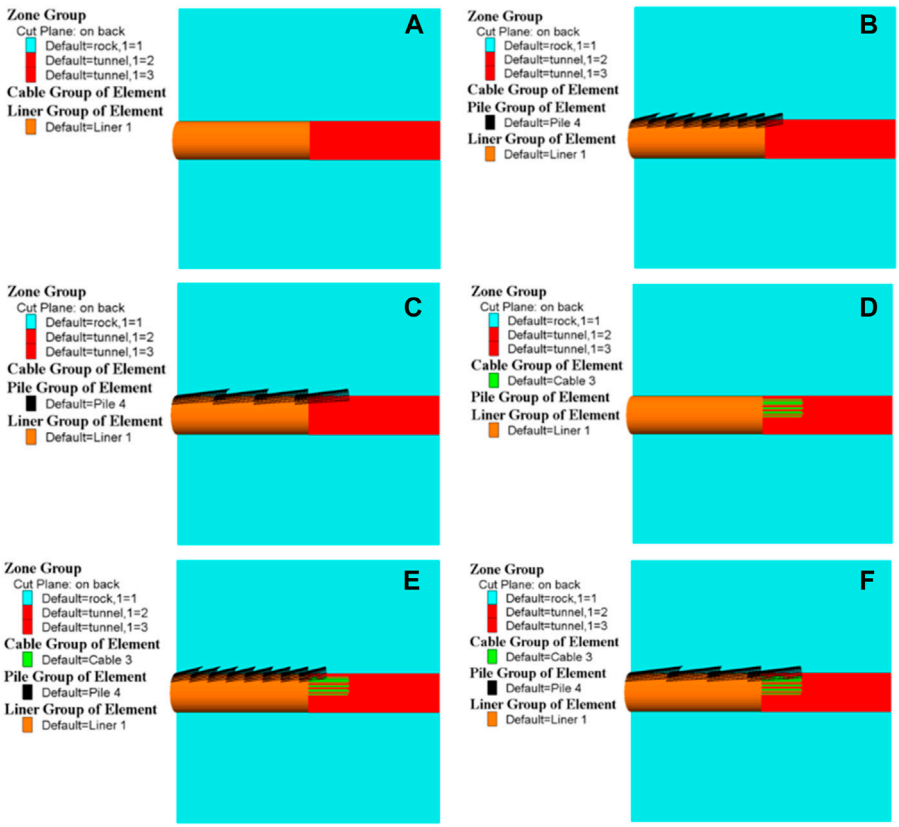

FIGURE 9
Numerical model of pre-reinforcement for different working conditions of **(A)** conditions 1, **(B)** conditions 2, **(C)** conditions 3, **(D)** conditions 4, **(E)** conditions 5 and **(F)** conditions 6.

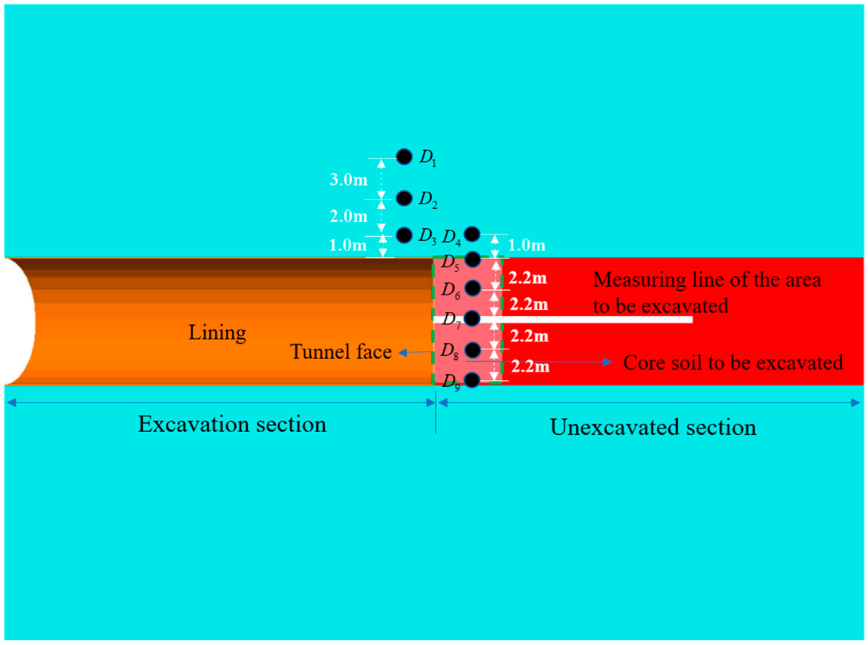

FIGURE 10
Arrangement of monitoring points.

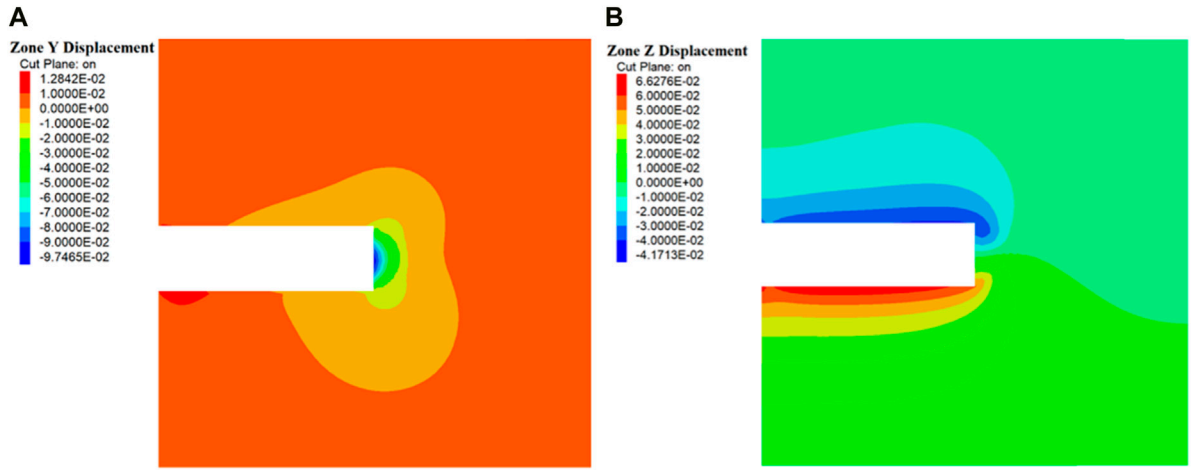

FIGURE 11
(A) Horizontal displacement and **(B)** vertical displacement clouds without reinforcement.

Figure 7). The construction steps are as follows: the tunnel is first advanced supported, and the core soil is reserved by excavating the upper step, then concrete is sprayed in a timely manner, followed by the installation of steel supports and timely locking of foot anchor rods, and then the system anchor rods and steel mesh are laid. Afterwards, concrete is sprayed to the design thickness. Then, the core soil is excavated with a lag of 3–5 m, and the lower step excavation is carried out, followed by immediate support after excavation completion. After the lower cross-section support is completed, the bottom plate support is carried out, followed by the tight-fitting of the bottom plate concrete and steel-reinforced concrete lining.

3.2.2 Modelling

A numerical model of the tunnel face in sand-cobble strata with various reinforcement measures was established using the finite difference software FLAC3D. The influence of different pre-reinforcement measures on Earth pressure and instability area was investigated. According to the geological survey report of the dependent project, we designed the 3D numerical model of the

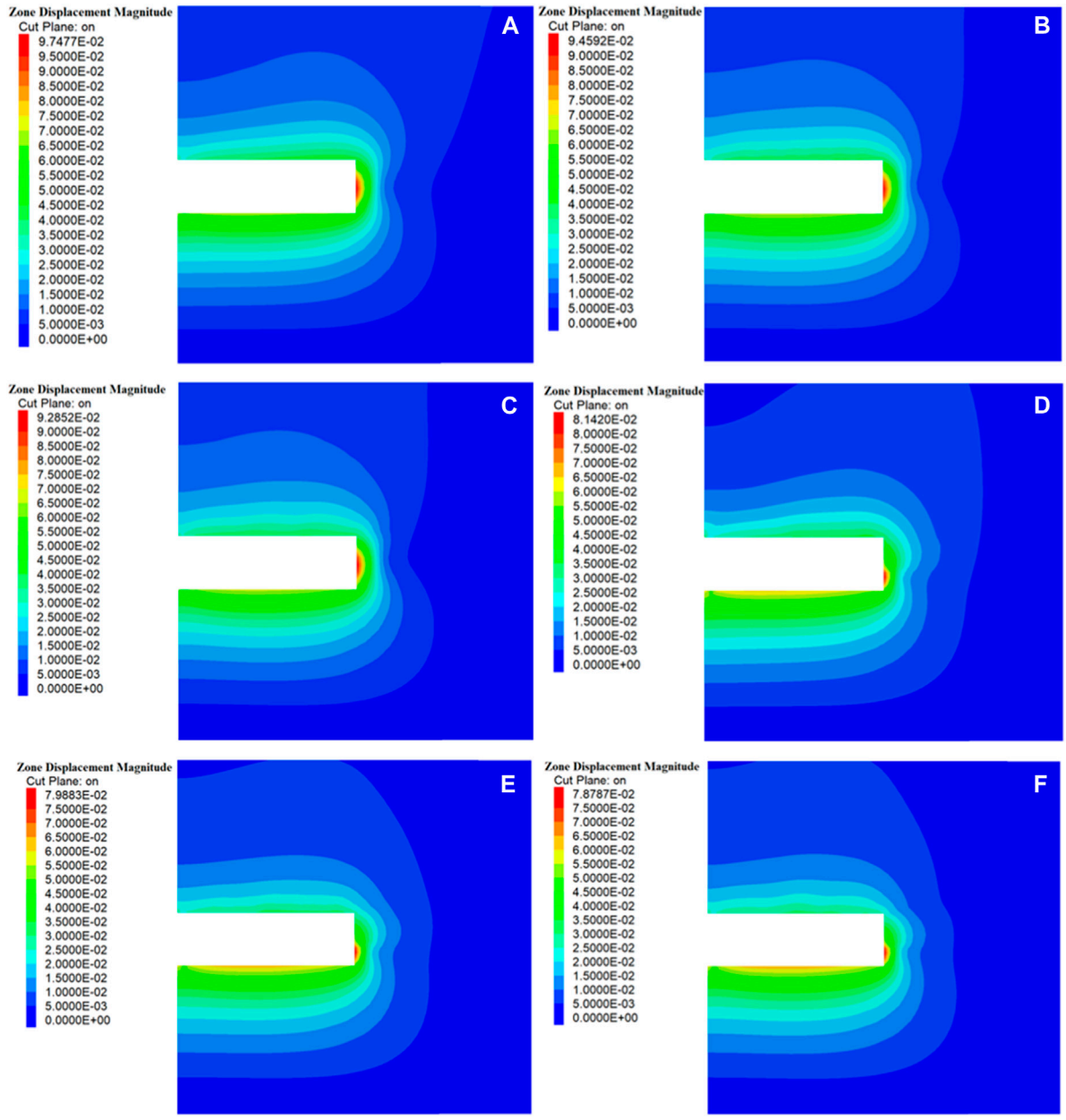

FIGURE 12
Overall displacement cloud of surrounding rock under various working conditions of **(A)** conditions 1, **(B)** conditions 2, **(C)** conditions 3, **(D)** conditions 4, **(E)** conditions 5 and **(F)** conditions 6.

tunnel in sand-cobble mixed strata shown in Figure 8. The model simplifies the surrounding soil of the tunnel into a binary soil consisting of sand and cobble, and based on the method of establishing a cobble database in Section 3.1, establishes a sand-cobble strata model with a stone content of 10%. The model size is $60m \times 60m \times 60m$, adopted with a tunnel depth selected according to the actual situation, and the tunnel excavation section span is 8.3 m with a height of 8.8 m. Ignoring the effect of boundary adjustment, a 3D non-uniform mesh with a grid size of 0.5–2.0 m, all of which are hexahedral grids, was used for the numerical simulation. Note that, the boundary conditions were set as follows: the top surface was a free boundary, while normal constraints were applied to the bottom and side surfaces. The soil and rocks in the model were modeled as solid elements, and the mechanical properties and deformation behavior of the soil matrix were described using the classical Mohr-Coulomb elastoplastic constitutive model. Since the tensile and compressive strengths of the rocks are relatively high, they usually do not undergo failure under the loading of tunnel excavation, so they can be treated as elastic materials. The tunnel lining was simulated using Liner shell elements, which closely followed the tunnel face. The advance small guide tube and pipe shed were simulated using Pile elements, which can simulate bending and shear friction characteristics. Glass fiber anchor rods were modeled using cable anchor rod

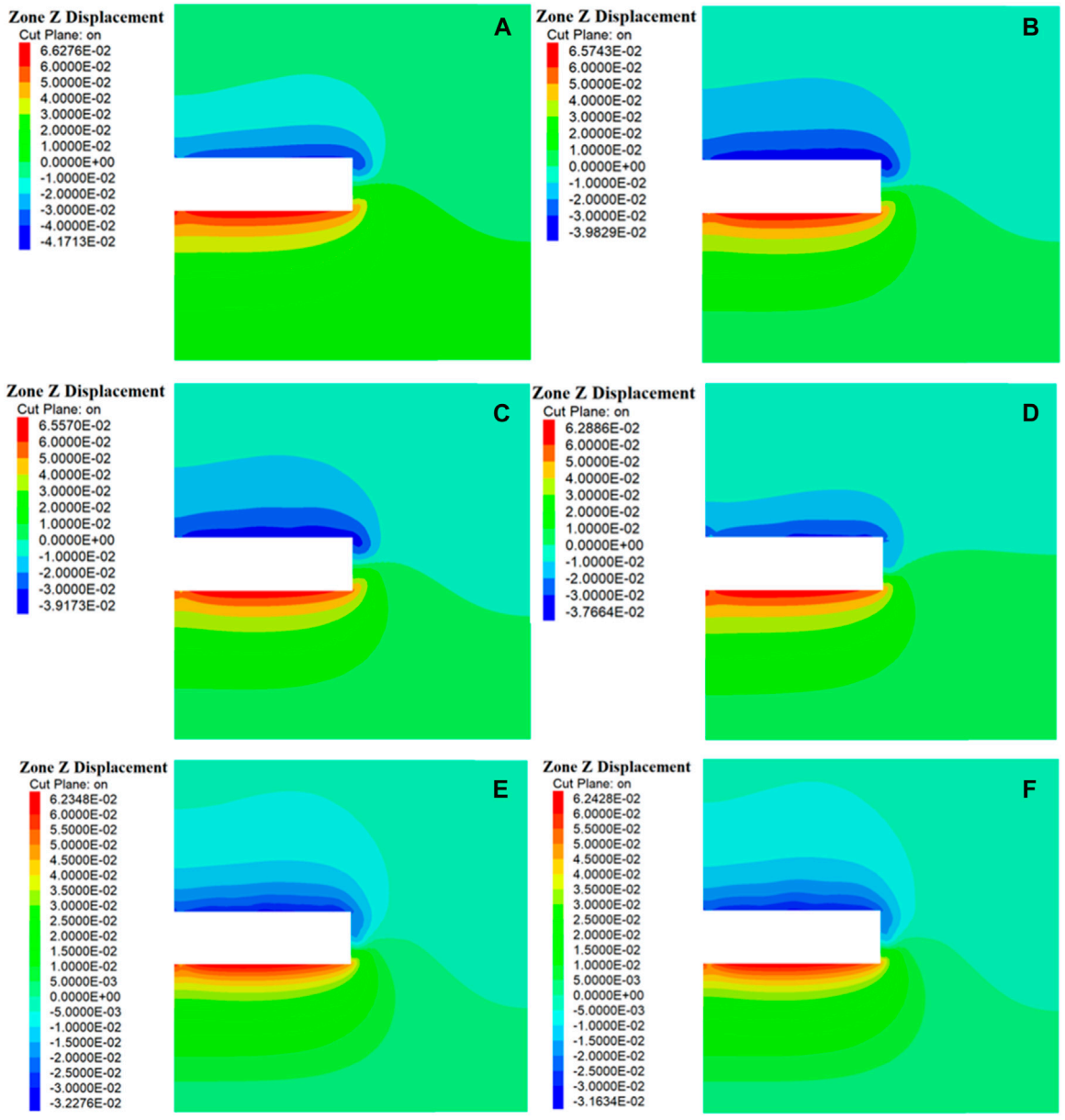

FIGURE 13
Vertical displacement cloud of surrounding rock under various working conditions of **(A)** conditions 1, **(B)** conditions 2, **(C)** conditions 3, **(D)** conditions 4, **(E)** conditions 5 and **(F)** conditions 6.

elements, which can only simulate shear friction characteristics with the soil.

3.2.3 Material parameters

In order to reflect the physical and mechanical parameters of the surrounding rock of the excavation area of the tunnel, the parameters of the superficial soil were determined based on the geological survey report and the specifications (Transportation Department of the People's Republic of China, 2010), and the material parameters used are shown in Table 1. The parameters of the pre-reinforcement measures were based on similar engineering experiences, and the main supporting parameters are shown in Table 2 and Table 3.

3.3 Simulation working conditions

To further investigate the impact of different pre-reinforcement measures on the excavation stability of sand and gravel formations in tunnels, numerical simulations were performed on a tunnel model with a 10% stone content, under six pre-reinforcement conditions: non-reinforced, pre-reinforcement with advance small pipes, pre-reinforcement with pipe-roof, pre-reinforcement with GFRP bolt, pre-reinforcement with advance small pipes and GFRP bolt, and pre-reinforcement with pipe-roof and GFRP blot. The numerical models of the six pre-reinforcement conditions are shown in Figure 9.

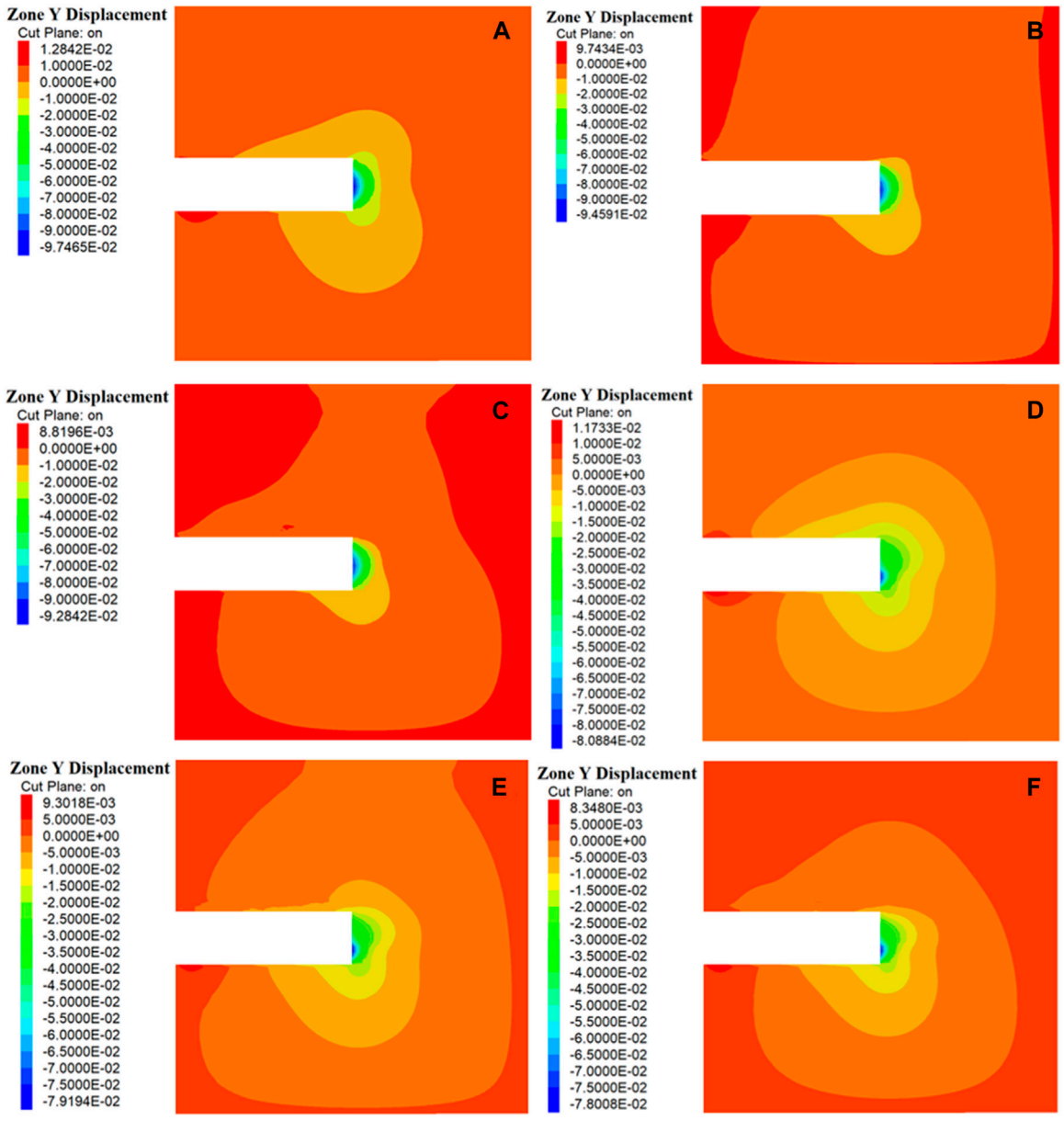

FIGURE 14
Horizontal displacement cloud of surrounding rock under various working conditions of **(A)** conditions 1, **(B)** conditions 2, **(C)** conditions 3, **(D)** conditions 4, **(E)** conditions 5 and **(F)** conditions 6.

Condition 1: Excavation with no reinforcement of the surrounding geological formation.

Condition 2: Excavation supported by advance small pipes. The pipe is 6 m in length and has a 2 m overlapping section.

Condition 3: Excavation supported by pipe-roof. Each pipe segment is 12 m in length and has a 3 m overlapping section.

Condition 4: Excavation supported by glass fiber reinforced plastic (GFRP) rock bolts. Each bolt is 15 m in length and has a 3 m overlapping section.

Condition 5: Excavation supported by a combination of advance small pipes and GFRP bolts. The green parts represent GFRP bolts, each of which is 15 m in length with a 3 m overlapping section. The black parts represent the s advance small pipes, which is 6 m in length with a 2 m overlapping section.

Condition 6: Excavation supported by a combination of pipe-roof and GFRP bolts. The green parts represent GFRP bolts, each of which is 15 m in length with a 3 m overlapping section. The black parts represent the pipe-roof, with each segment being 12 m in length and having a 3 m overlapping section.

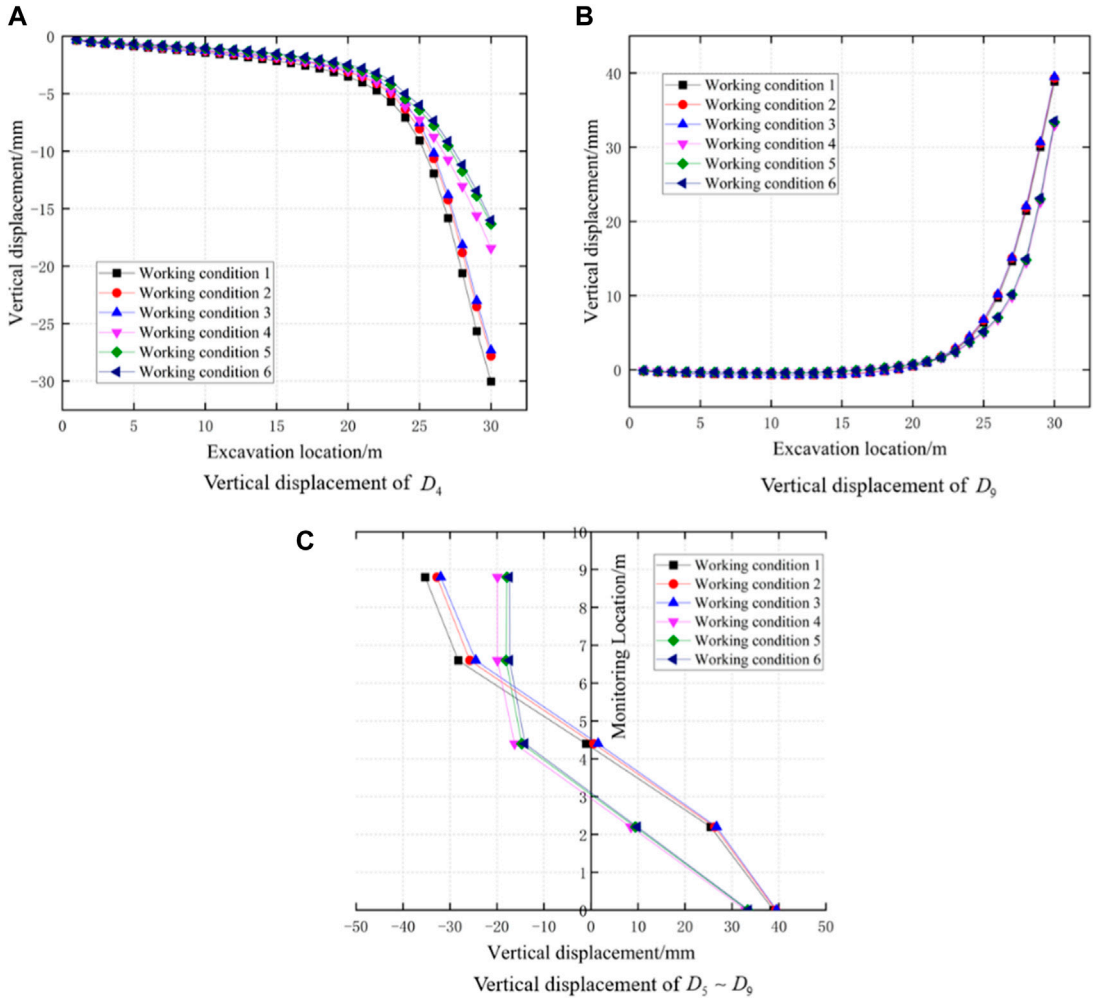

FIGURE 15
Change of vertical displacement of **(A)** D_4, **(B)** D_9 and **(C)** D_5~D_9.

3.4 Layout of monitoring points

In previous studies, many scholars analyzed the evolution law of ground deformation during the instability process of sand-cobble strata in tunnel face, and found that the rock in front and behind the tunnel face would undergo deformation. In relatively loose sand-cobble strata, the deformation of the rock in front and behind the tunnel face is more significant (Di et al., 2022). Considering the deformation law of the ground in the instability and failure process of the tunnel, the monitoring points in the numerical experiments were arranged as shown in Figure 10. Three monitoring points were vertically set above the arch crown behind the tunnel face, and five monitoring points were uniformly set vertically at the location of the core soil in front of the tunnel face to be excavated. The distance between each monitoring point was 2.2 m, and one monitoring point was set 1 m above the core soil to be excavated and below the crown. A 20 m measuring line was also set in the excavation area. By analyzing the displacement and stress changes of the monitoring points under different pre-reinforcement projects, the stability of tunnel excavation under different conditions was studied.

4 Numerical modelling results and discussions

4.1 Validation for numerical tests

Figure 11 shows the horizontal and vertical displacement contour maps of tunnel in the sandy cobble mixed strata with 10% stone content under Working condition 1. It can be observed that the maximum horizontal displacement occurs at the tunnel face, while the vertical displacement mainly occurs at the tunnel crown and the tunnel invert, where the tunnel crown undergoes settlement and the tunnel invert experiences uplift. The variation in horizontal and vertical displacement of the tunnel surrounding rock and the soil in front of the tunnel face during tunnel excavation is consistent with existing numerical test results (Wang et al., 2020). Therefore, it can be concluded that the numerical model proposed in this study can accurately reflect the deformation characteristics of the tunnel in sandy cobble stratum during excavation.

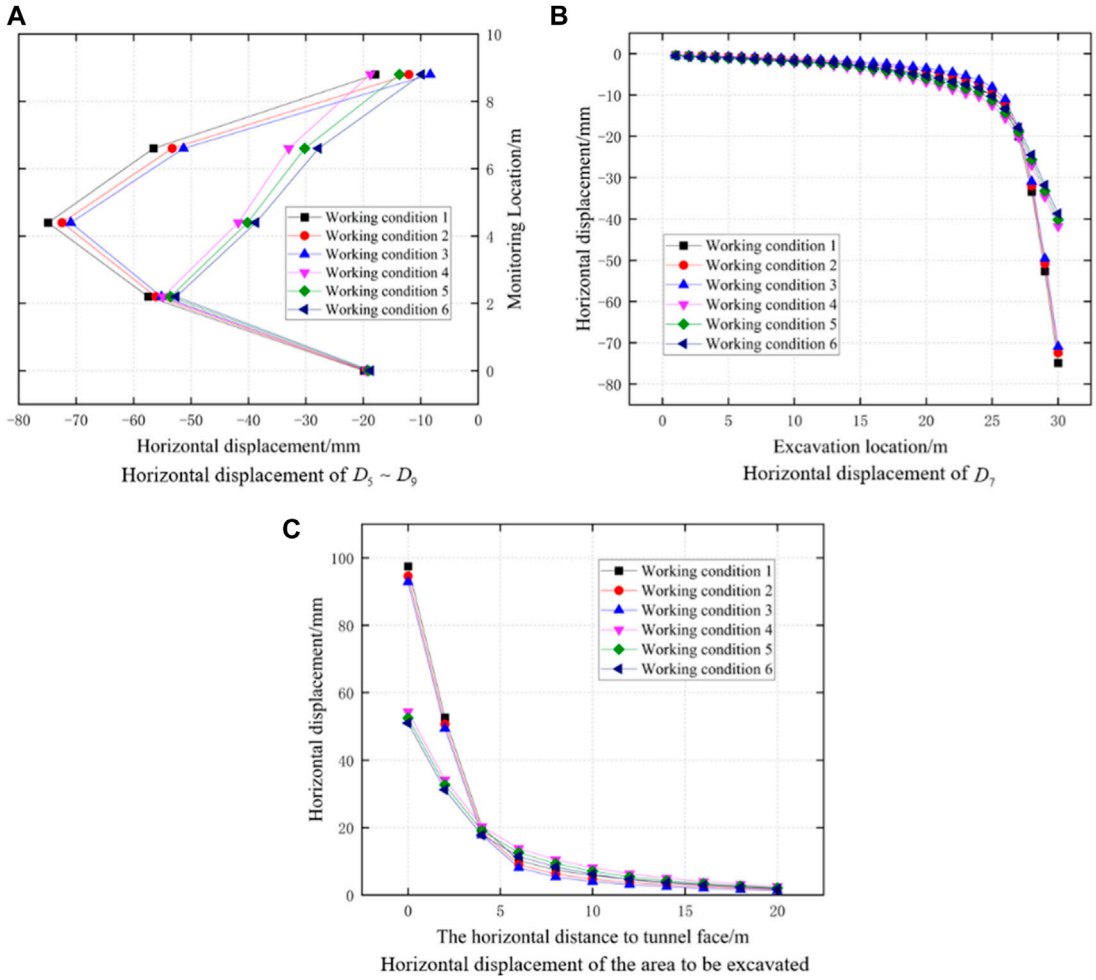

FIGURE 16
Change of horizontal displacement of **(A)** D_5~D_9, **(B)** D_7 and **(C)** the area to be excavated.

4.2 Displacement analysis

4.2.1 Surrounding rocks deformation under different working conditions

Displacement is the most commonly used, intuitive, and convenient monitoring indicator during underground construction. The effectiveness of tunnel pre-reinforcement measures in controlling the displacement deformation of surrounding rocks can be reflected by monitoring the horizontal displacement of the tunnel face, surface displacement, and settlement displacement of the front and rear arch crowns of the tunnel face. In order to analyze the deformation characteristics of surrounding rocks under different pre-reinforcement schemes and study their impact on the stability of a tunnel in sandy cobble mixed strata, numerical models were established for different pre-reinforcement methods. The overall displacement contour map, vertical displacement contour map, and horizontal displacement contour map of the tunnel excavation under different pre-reinforcement scheme conditions were calculated and presented in Figures 12–14, respectively.

According to Figure 12, it can be seen that under various working conditions, the deformation of the tunnel surrounding rock mainly occurs at the tunnel surrounding rock and the tunnel face, and the red area is mainly concentrated at the soil in front of the tunnel face. Therefore, the displacement at the soil in front of the tunnel face is the largest. In working conditions 1–3, the red area is mainly concentrated at the center of the tunnel face, and the maximum displacement during the excavation process is located at the center of the tunnel face. Compared with working conditions 1–3, when simulating with working conditions 4–6, the red area is reduced and mainly concentrated below the tunnel face. The displacement of the soil in front of the tunnel face is reduced, and the maximum displacement occurs at the lower part of the tunnel face. From Figure 13, it can be seen that the vertical displacement of the surrounding rock mainly occurs at the top and bottom of the tunnel, the top sinking and the bottom uplifting, and the displacement of the bottom uplifting is greater than the sinking of the top. When there is no reinforcement in the strata, the vertical displacement of the tunnel surrounding

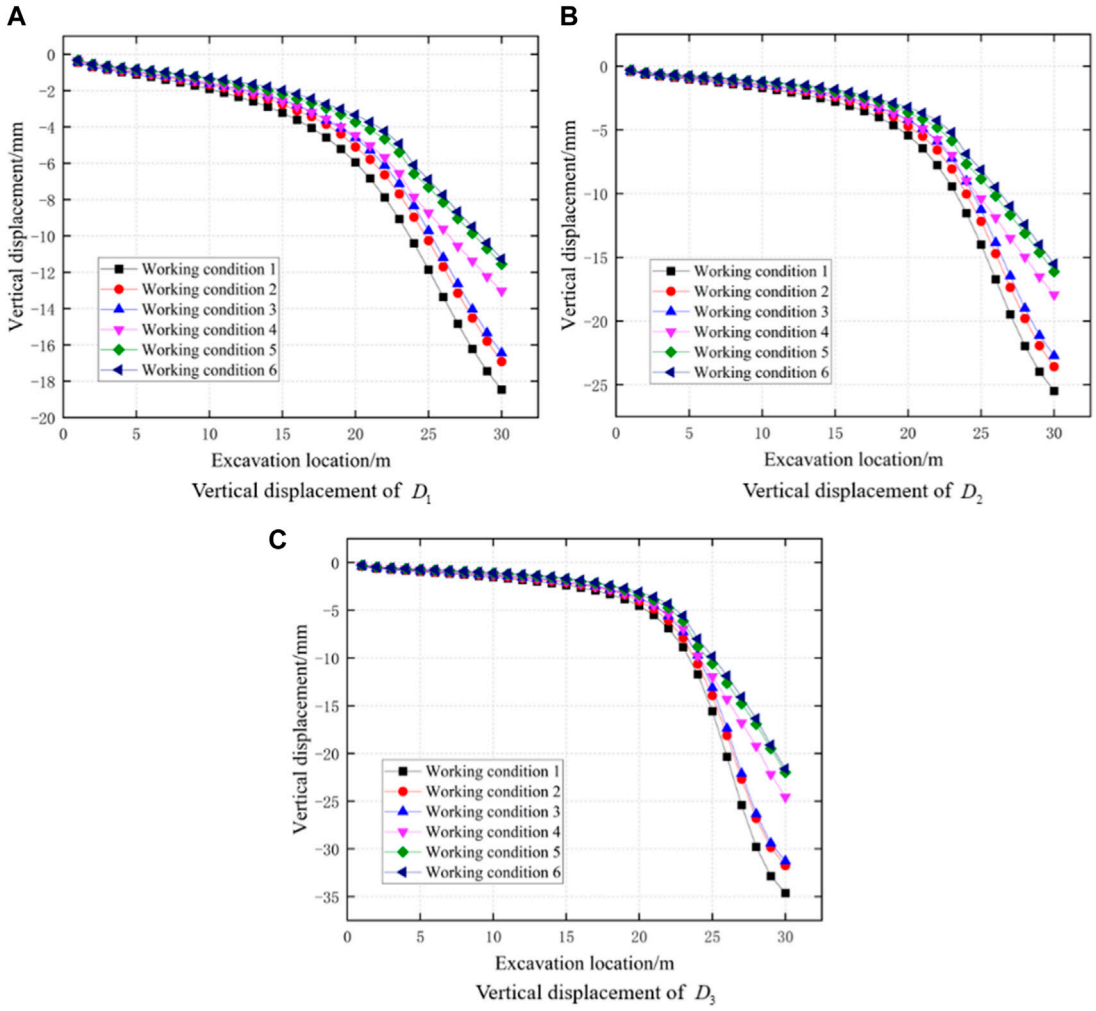

FIGURE 17
Change of vertical displacement of **(A)** D_1, **(B)** D_2 and **(C)** D_3.

rock is relatively large compared to other reinforced measures. When simulating with working conditions 2 and 3, the vertical displacement of the tunnel surrounding rock is reduced. When simulating with working conditions 4–6, the range of maximum vertical displacement of the tunnel surrounding rock is significantly reduced compared to working conditions 1–3. From Figure 14, it can be seen that the horizontal displacement is the largest at the tunnel face, and the displacement of the tunnel surrounding rock is relatively small. Under working conditions 1–3, the horizontal displacement mainly occurs at the center position of the heading face, while under working conditions 4–6, the horizontal displacement mainly occurs below the tunnel face, and the deformation area is significantly reduced compared to working conditions 1–3. It can be found that using advance small pipes and pipe-roof for pre-support can reduce the deformation of the tunnel surrounding rock and the tunnel face. Using GFRP bolts, advance small pipes and GFRP bolts, pipe-roof and GFRP blots for support can achieve better results.

4.2.2 Deformation characteristics of the rock in front of the tunnel face

The vertical and horizontal displacement changes of the soil mass in front of the tunnel face are shown in Figure 15A–C and Figure 16A–C, respectively. From Figures 15A, B, it can be observed that under Condition 1, the maximum settlement of the tunnel arch is 30.04 mm, and the maximum uplift of the invert is 38.85 mm. Under Conditions 2 and 3, the maximum settlement of the tunnel arch decreases to 27.82 and 27.32 mm, respectively, while the maximum uplift of the invert remains almost unchanged compared to Condition 1. When the pre-strengthening methods of Conditions 4, 5, and 6 are used, the settlement of the arch decreases to 18.44, 16.33, and 15.99 mm, respectively. Compared with Conditions 1–3, the maximum uplift displacement of the invert decreases to 32.94, 33.37, and 33.56 mm, respectively. As clearly shown in Figure 15C, the vertical displacement of the core soil in front of the tunnel face is reduced when pre-reinforcement methods of Conditions 4–6 are employed.

From Figure 16A, the expansion deformation of the tunnel face under different conditions can be clearly observed. When the strata

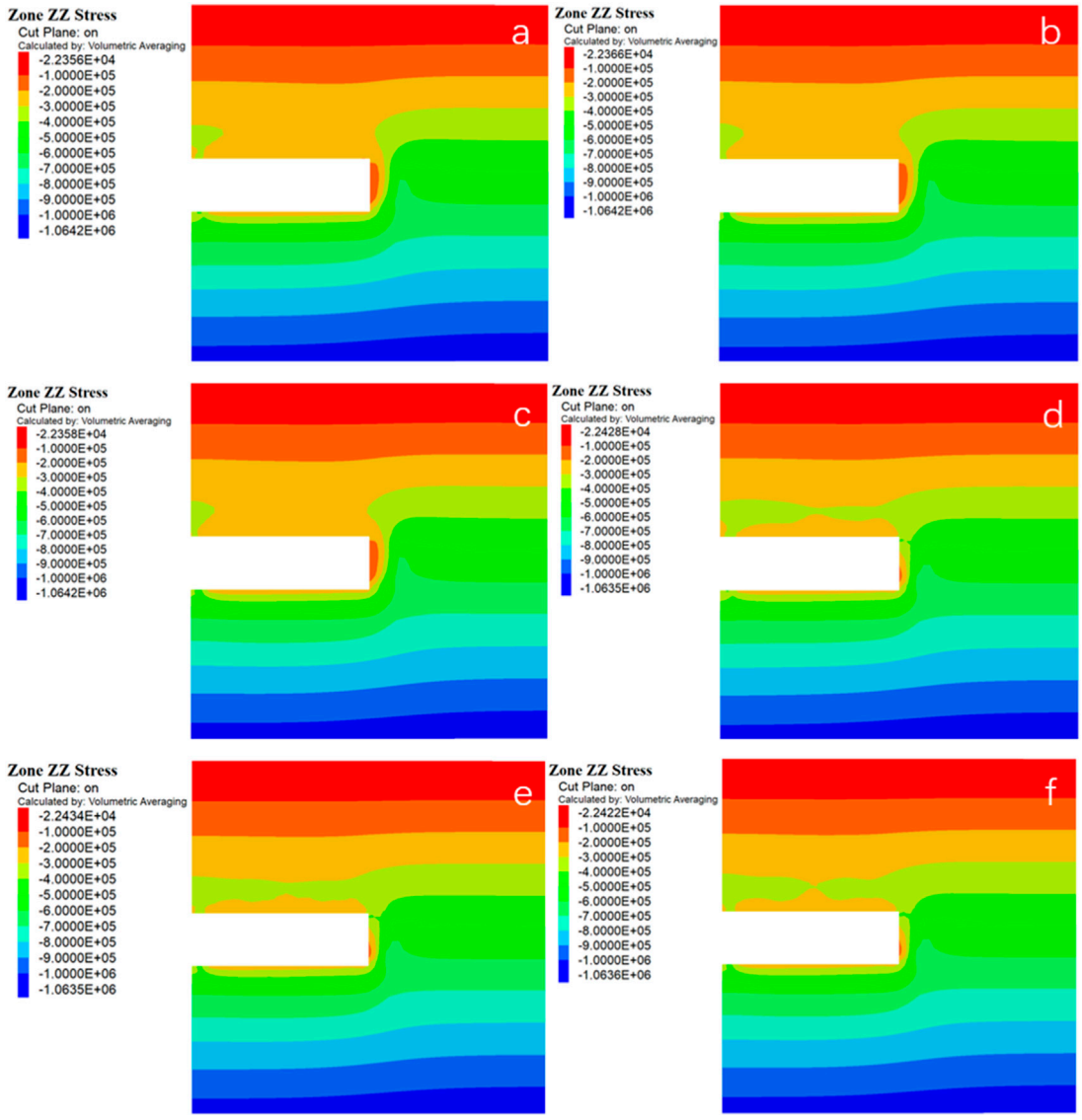

FIGURE 18
Vertical stress cloud of surrounding rock under various working conditions of **(A)** conditions 1, **(B)** conditions 2, **(C)** conditions 3, **(D)** conditions 4, **(E)** conditions 5 and **(F)** conditions 6.

are not reinforced, the expansion displacement of the tunnel face is significant. Under Conditions 2 and 3, there is little improvement in the expansion deformation of the tunnel face compared to Condition 1. The maximum extrusion displacement of the tunnel face under Conditions 1–3 occurs at the center position of the tunnel face. Under Conditions 4–6, the expansion displacement of the tunnel face decreases significantly, and the extrusion deformation of the three conditions is basically the same. At the same time, the location of the maximum deformation of the tunnel face shifts downward. From Figures 16B, C, it can be observed that the horizontal displacement at the midpoint of the core soil in front of the tunnel face is significantly reduced when using glass fiber anchor rods. The horizontal displacement at the center point of the core soil in front of the tunnel face decreases as the distance from the tunnel face increases, with the displacement being greatest at the tunnel face. The experimental results indicate that GFRP blots can effectively control the extrusion deformation of the tunnel face. This is mainly because GFRP blots can improve the shear strength of the core soil to be excavated, which keeps most of the strata near the tunnel face in an elastic stress state, thereby limiting the extrusion expansion deformation of the tunnel face. In addition, GFRP blots have strong bonding properties (Li et al., 2023), which can be used to bond with the soil and apply a restraining force on the soil in front of the tunnel face through the anchoring effect of the anchor rods, thereby suppressing the extrusion deformation of the tunnel face.

4.2.3 Deformation characteristics of the rock behind the tunnel face

The vertical displacement of the soil behind the tunnel face is shown in Figure 17. When the stratum is not reinforced, the maximum settlement occurs in the soil behind the tunnel face. The maximum settlements of the monitoring points D_1, D_2, and

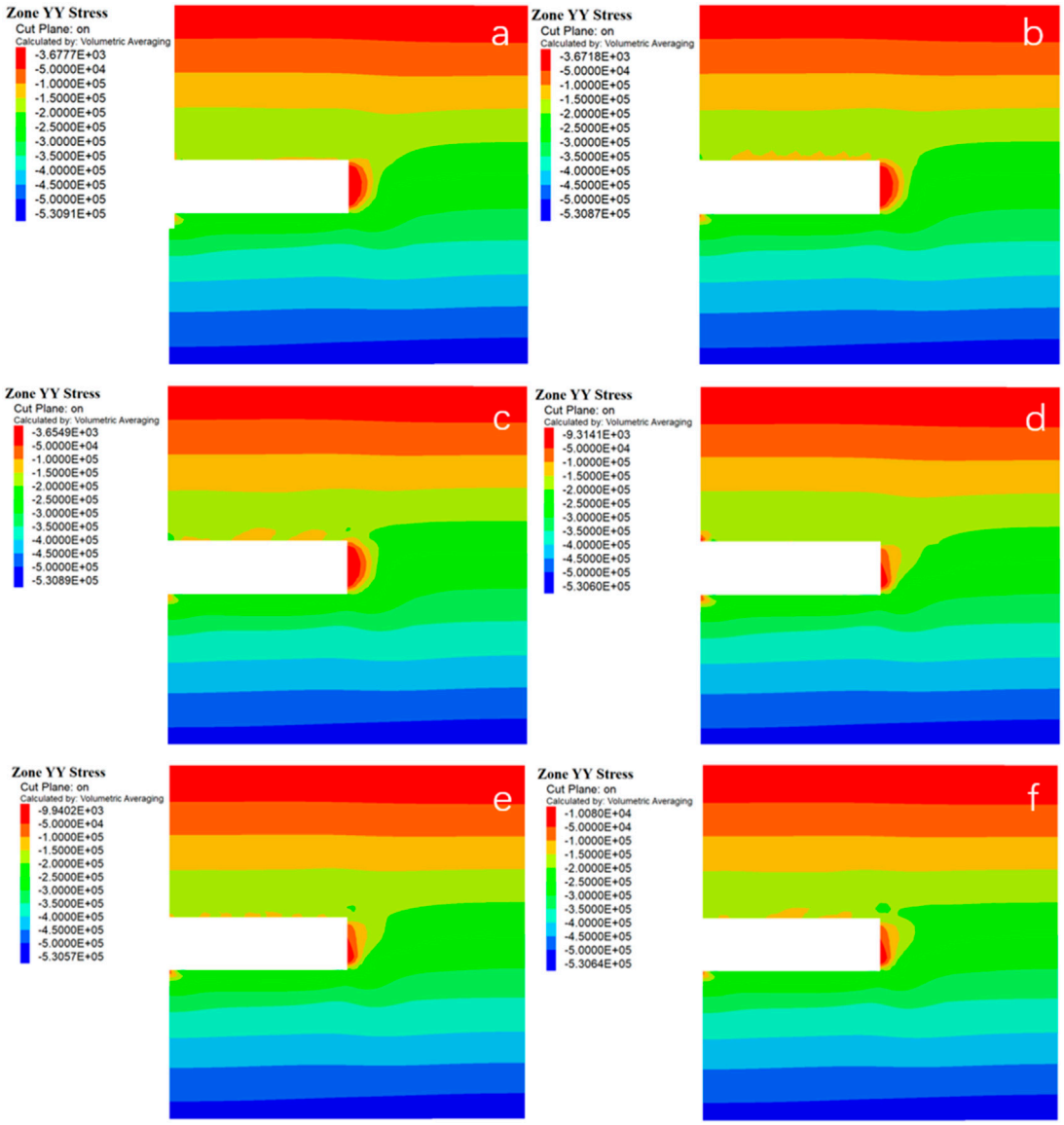

FIGURE 19
Horizontal stress cloud of surrounding rock under various working conditionsof **(A)** conditions 1, **(B)** conditions 2, **(C)** conditions 3, **(D)** conditions 4, **(E)** conditions 5 and **(F)** conditions 6.

D_3 are 18.46mm, 25.48, and 34.64 mm, respectively, and the maximum settlement of the surrounding rock behind the tunnel face decreases with the distance from the crown. As observed from Figure 17, under the conditions of reinforcement in scenarios 2 and 3, the maximum settlement of the surrounding rock behind the tunnel face at each monitoring point decreases, while under the conditions of scenarios 4–6, the maximum settlement of the surrounding rock behind the tunnel face decreases significantly. This is due to the effect of the small guide pipe and the canopy, which bear and transfer the load, promote and form the supporting arch and improve the mechanical parameters of the reinforced rock. Moreover, a cofferdam foundation is usually added in the entrance section of the reinforcement, which extends into a relatively intact and hard rock mass in the tunnel surrounding, forming a stable support structure that can reduce the settlement of the tunnel crown. The GFRP blots also reduce the convergent deformation of the tunnel surrounding rock behind the tunnel face by suppressing the extrusion deformation of the soil in front of the tunnel face.

Based on the analysis of deformation of tunnel surrounding rock and face under different working conditions as mentioned above, it was found that the reinforcement of advance small pipes and pipe-roof can reduce the settlement of the tunnel vault; GFRP blots are superior to advance small pipes and pipe-roof in controlling face deformation; the comprehensive reinforcement method using GFRP blots and advance small pipes or pipe-roof can better ensure the stability of the tunnel during excavation.

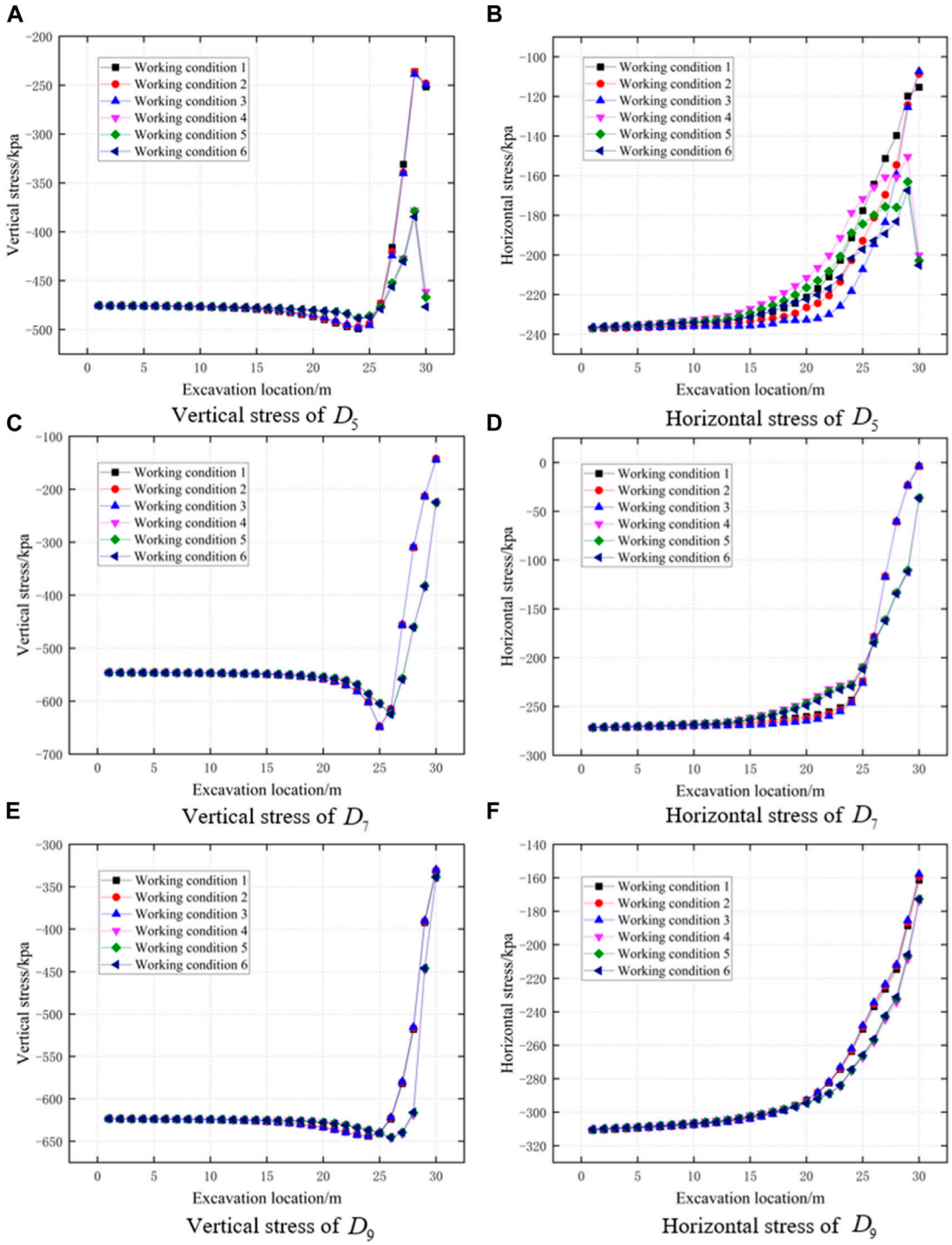

FIGURE 20
Change of vertical stress of **(A)** D_5, **(C)** D_7, **(E)** D_9 and horizontal stress of **(B)** D_5, **(D)** D_7, **(F)** D_9.

4.3 Stress analysis

4.3.1 Surrounding rocks stress under different working conditions

The vertical stress cloud map and horizontal stress cloud map of the tunnel surrounding rock during excavation under different working conditions were obtained through FLAC3D, as shown in Figures 18, 19. Overall, the horizontal stress of the surrounding rock is smaller than the vertical stress, and the horizontal stress and vertical stress of the surrounding rock are distributed relatively evenly. The overlying soil layer of the tunnel surrounding rock decreases vertically with the distance from the tunnel roof. The overlying soil layer close to the tunnel roof has obvious disturbance during the excavation process, while this phenomenon is not so

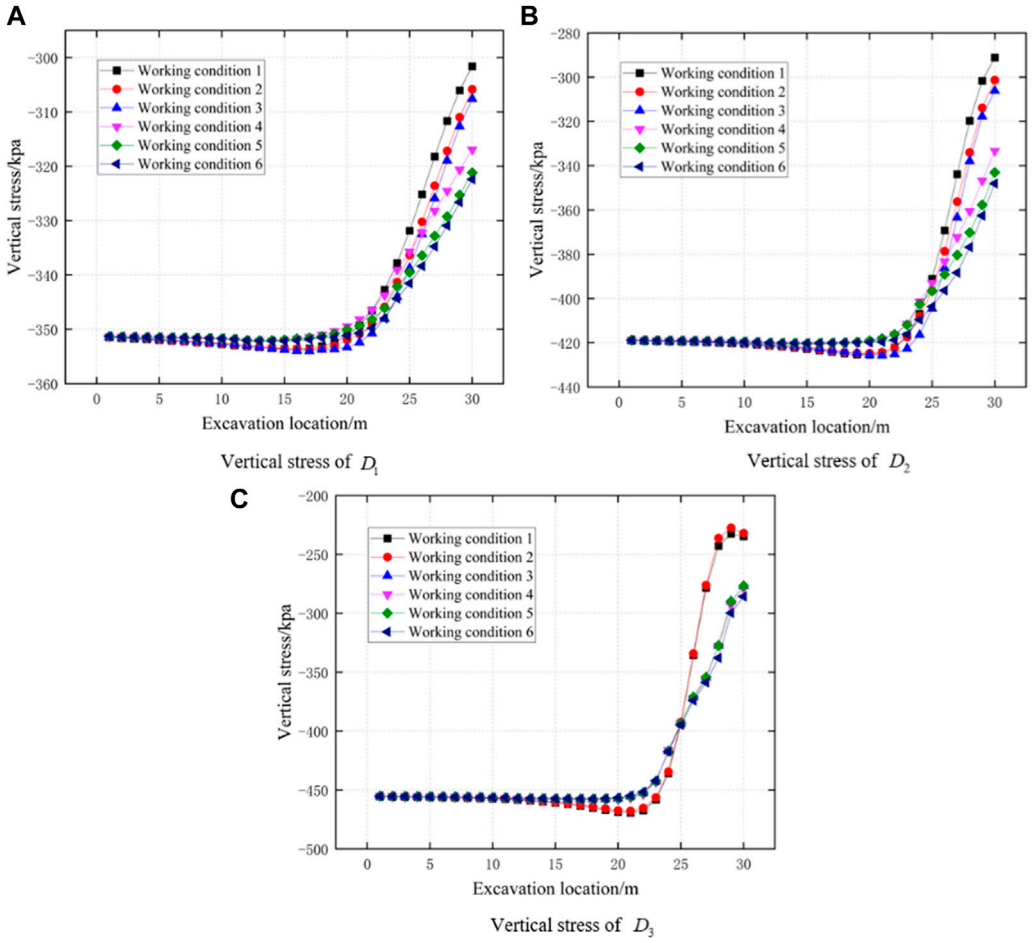

FIGURE 21
Change of vertical stress of **(A)** D_1, **(B)** D_2 and **(C)** D_3.

evident for the soil layer far from the roof. Observing the stress at the tunnel face, it can be seen that the stress of the soil in front of the tunnel face is relatively small. The mechanical properties of the surrounding rock at the tunnel face under working conditions 4–6 have been improved due to the effective reinforcement of the GFRP blots in controlling the deformation caused by the excavation of the tunnel face (Chen et al., 2008).

4.3.2 Stress characteristics of the rock in front of the tunnel face

The changes in vertical and horizontal stress at monitoring points D_5, D_7, and D_9 in the core soil ahead of the tunnel face are shown in Figures 20A, B. It can be observed that, as the depth of the soil increases, the vertical and horizontal stresses in the soil ahead of the tunnel face gradually increase in the range above the tunnel excavation contour. Under the working conditions 2 and 3, there is little difference in the stress changes of the surrounding rocks ahead of the tunnel face compared to the situation without reinforcement. When using working condition 4–6 for pre-reinforcement, the horizontal and vertical stresses at monitoring point D_5 increase significantly, the increment in horizontal and vertical stresses at monitoring point D_7 is relatively small, and the stress at monitoring point D_9 remains basically unchanged. Therefore, it can be concluded that, with the use of glass fiber anchor reinforcement, the stresses in the soil above the core soil ahead of the heading face are relatively large compared to those without reinforcement, while the stresses in the lower part of the core soil remain unchanged compared to those without reinforcement. This is due to the fact that the glass fiber anchor enhances the shear strength of the core rock mass ahead of the excavation, thereby increasing the stress in the soil and improving the stability of the heading face.

4.3.3 Stress characteristics of the rock behind the tunnel face

The stress changes of the surrounding rock behind the palm surface are shown in Figure 21. When the geological strata are not reinforced, the vertical stress of the soil behind the palm surface gradually decreases with increasing depth. When using pre-support methods such as advance small guide pipes or pipe sheds, the vertical stress at monitoring points D_1 and D_2 at the arch of the soil behind the palm surface increases, and there is basically no change in vertical stress at D_3. When using GFRP blots, a combination of GFRP blots and pipe-roof or a combination of GFRP blots and advance small pipes for pre-support, the vertical stress at each

monitoring point behind the tunnel face increases to varying degrees. It can be found that the mechanical properties of the surrounding rock behind the tunnel face can be improved by using pipe-roof, advance small pipes or GFRP blots. Among them, using GFRP blots can not only reduce the support pressure of the tunnel face but also reduce the degree of stress release in the surrounding rock, thereby further reducing the scope of damage, which is consistent with previous research results (Zhang et al., 2022). In the absence of considering economic benefits, using a comprehensive support of advance pipe-roof and GFRP blots or advance small pipes and GFRP blots can better ensure the stability of the tunnel surrounding rock during excavation.

5 Conclusion

Based on the Da Zhuang tunnel project in Qinghai Province, this paper uses the FLAC3D finite difference software to simulate the tunnel in the sand-cobble mixed strata and analyze the deformation and stress of the tunnel face and surrounding rock under different pre-reinforcement conditions. The following conclusions are drawn:

(1) Without pre-reinforcement, the tunnel in the sandy cobble stratum is prone to rock instability and effective pre-reinforcement measures must be taken based on the site geological conditions. Meanwhile, in addition to the pre-reinforcement around the tunnel, the tunnel face should also be reinforced to ensure construction safety.
(2) All pre-reinforcement measures can control the settlement and failure of surrounding rocks to some extent. However, using only the pipe-roof or advanced small pipes alone is basically ineffective in controlling extrusion deformation and failure at the tunnel face.
(3) Reinforcing the core soil in front of the excavation face with GFRP blots can significantly improve the mechanical performance of the surrounding rock, control the arch failure of the surrounding rock, and reduce the horizontal displacement and surface settlement of the tunnel face and the sinking displacement of the front and rear arches.
(4) Comprehensive reinforcement with pipe-roof and GFRP blots, or advanced small pipes and GFRP blots, can better control the settlement and deformation of the front and rear soil at the tunnel face, reduce the extrusion displacement of the tunnel face, and the pre-reinforcement effect is better than using only glass fiber anchor rods for support.

Data availability statement

The raw data supporting the conclusion of this article will be made available by the authors, without undue reservation.

Author contributions

XL: methodology, writing—original draft. YZ: software, formal analysis, methodology, writing—review and editing. HX: investigation, resources. LZ: investigation, resources. XG: investigation, resources. All authors contributed to the article and approved the submitted version.

Funding

This research is financially supported by the Key R&D and Transformation Plan of Qinghai Province (Grant No. 2021-SF-167).

Conflict of interest

Authors XL, HX, LZ, and XG were employed by the company Qinghai Xihu Expressway Management Co., Ltd.

The remaining author declares that the research was conducted in the absence of any commercial or financial relationships that could be construed as a potential conflict of interest.

Publisher's note

References

Aksoy, C. O., and Onargan, T. U. R. G. A. Y. (2010). The role of umbrella arch and face bolt as deformation preventing support system in preventing building damages. *Tunn. Undergr. space Technol.* 25 (5), 553–559. doi:10.1016/j.tust.2010.03.004

Barrett, P. J. (1980). The shape of rock particles, a critical review. *Sedimentology* 27 (3), 291–303. doi:10.1111/j.1365-3091.1980.tb01179.x

Bin, L., Taiyue, Q., Wang, Z., and Longwei, Y. (2012). Back analysis of grouted rock bolt pullout strength parameters from field tests. *Tunn. Undergr. Space Technol.* 28, 345–349. doi:10.1016/j.tust.2011.11.004

Cao, R., Peng, L., and Zhao, Y. (2021). Control of strata deformation in subway interval tunnels crossing a high-speed rail shield tunnel at a short distance. *Arabian J. Sci. Eng.* 46, 5013–5022. doi:10.1007/s13369-020-05225-8

Chen, T., Mei, Z., and Li, C. (2008). Application research of full section pre reinforcement technology with glass fiber anchor in tunnel. *Mod. Tunn. Technol.* 45, 226–231.

Cui, J., Xu, W. H., Fang, Y., Tao, L. M., and He, C. (2020). Performance of slurry shield tunnelling in mixed strata based on field measurement and numerical simulation. *Adv. Mater. Sci. Eng.*, 2020, 1–14. doi:10.1155/2020/6785260

Das, N. (2007). *Modelling three-dimensional shape of sand grains using discrete element method*. Tampa, Florida: University of South Florida.

Di, Q., Li, P., Zhang, M., and Cui, X. (2023). Experimental investigation of face instability for tunnels in sandy cobble strata. *Undergr. Space* 10, 199–216. doi:10.1016/j.undsp.2022.10.004

Di, Q., Li, P., Zhang, M., and Cui, X. (2022). Influence of relative density on deformation and failure characteristics induced by tunnel face instability in sandy cobble strata. *Eng. Fail. Anal.* 141, 106641. doi:10.1016/j.engfailanal.2022.106641

Du, X., Zhang, P., Jin, L., and Lu, D. (2019). A multi-scale analysis method for the simulation of tunnel excavation in sandy cobble stratum. *Tunn. Undergr. Space Technol.* 83, 220–230. doi:10.1016/j.tust.2018.09.019

Funatsu, T., Hoshino, T., Sawae, H., and Shimizu, N. (2008). Numerical analysis to better understand the mechanism of the effects of ground supports and reinforcements on the stability of tunnels using the distinct element method. *Tunn. Undergr. Space Technol.* 23 (5), 561–573. doi:10.1016/j.tust.2007.10.003

Han, R. G. (1987). *NATM for underground engineering*. Beijing, China: Science Press.

Hentschel, M. L., and Page, N. W. (2003). Selection of descriptors for particle shape characterization. *Part. Part. Syst. Charact. Meas. Descr. Part. Prop. Behav. Powders Other Disperse Syst.* 20 (1), 25–38. doi:10.1002/ppsc.200390002

Hisatake, M., and Ohno, S. (2008). Effects of pipe roof supports and the excavation method on the displacements above a tunnel face. *Tunn. Undergr. Space Technol.* 23 (2), 120–127. doi:10.1016/j.tust.2007.02.002

Huang, J., Zhang, Y., Ouyang, X., and Xu, G. (2019). Lagged settlement in sandy cobble strata and Earth pressure on shield tunnel. *Math. Biosci. Eng.* 16 (6), 6209–6230. doi:10.3934/mbe.2019309

Jin, D., Yuan, D., Li, X., and Zheng, H. (2018). Analysis of the settlement of an existing tunnel induced by shield tunneling underneath. *Tunn. Undergr. Space Technol.* 81, 209–220. doi:10.1016/j.tust.2018.06.035

Juneja, A., Hegde, A., Lee, F. H., and Yeo, C. H. (2010). Centrifuge modelling of tunnel face reinforcement using forepoling. *Tunn. Undergr. Space Technol.* 25 (4), 377–381. doi:10.1016/j.tust.2010.01.013

Kang, Y., Hou, C., Li, K., Liu, B., and Sang, H. (2021). Evolution of temperature field and frozen wall in sandy cobble stratum using LN2 freezing method. *Appl. Therm. Eng.* 185, 116334. doi:10.1016/j.applthermaleng.2020.116334

Li, B., Hong, Y., Gao, B., Qi, T. Y., Wang, Z. Z., and Zhou, J. M. (2015). Numerical parametric study on stability and deformation of tunnel face reinforced with face bolts. *Tunn. Undergr. Space Technol.* 47, 73–80. doi:10.1016/j.tust.2014.11.008

Li, H., Fu, J., Chen, B., Zhang, X., Zhang, Z., and Lang, L. (2023). Mechanical properties of GFRP bolts and its application in tunnel face reinforcement. *Materials* 16 (6), 2193. doi:10.3390/ma16062193

Li, R., Zhang, D., Fang, Q., Liu, D., Luo, J., and Fang, H. (2020). Mechanical responses of closely spaced large span triple tunnels. *Tunn. Undergr. Space Technol.* 105, 103574. doi:10.1016/j.tust.2020.103574

Liang, R., Xia, T., Huang, M., and Lin, C. (2017). Simplified analytical method for evaluating the effects of adjacent excavation on shield tunnel considering the shearing effect. *Comput. Geotechnics* 81, 167–187. doi:10.1016/j.compgeo.2016.08.017

Lin, Q., Lu, D., Lei, C., Tian, Y., Gong, Q., and Du, X. (2021). Model test study on the stability of cobble strata during shield under-crossing. *Tunn. Undergr. Space Technol.* 110, 103807. doi:10.1016/j.tust.2020.103807

Lunardi, P. (2008). *Design and construction of tunnels: Analysis of controlled deformations in rock and soils (ADECO-RS*. Berlin, Germany: Springer Science and Business Media.

Martí, D., Carbonell, R., Flecha, I., Palomeras, I., Font-Capó, J., Vázquez-Suñé, E., et al. (2008). High-resolution seismic characterization in an urban area: Subway tunnel construction in Barcelona. Spain. *Geophysics* 73 (2), B41–B50. doi:10.1190/1.2832626

Mei, Y., Zhang, X., Nong, X., and Fu, L. (2021). Experimental study of the comprehensive technology of grouting and suspension under an operating railway in the cobble stratum. *Transp. Geotech.* 30, 100612. doi:10.1016/j.trgeo.2021.100612

Mitarashi, Y., Matsuo, T., Tezuka, H., Okamoto, T., Nishimura, S., and Matsui, T. (2003). Evaluation of effect of long face reinforcement method (FIT method) in tunneling. *Dob. Gakkai Ronbunshu* 2003 (743), 213–222. doi:10.2208/jscej.2003.743_213

Mollon, G., and Zhao, J. (2012). Fourier-Voronoi-based generation of realistic samples for discrete modelling of granular materials. *Granul. Matter* 14 (05), 621–638. doi:10.1007/s10035-012-0356-x

Ocak, I. (2008). Control of surface settlements with umbrella arch method in second stage excavations of Istanbul Metro. *Tunn. Undergr. Space Technol.* 23 (6), 674–681. doi:10.1016/j.tust.2007.12.005

Peila, D. (1994). A theoretical study of reinforcement influence on the stability of a tunnel face. *Geotechnical Geol. Eng.* 12, 145–168. doi:10.1007/bf00426984

Shin, J. H., Choi, Y. K., Kwon, O. Y., and Lee, S. D. (2008). Model testing for pipe-reinforced tunnel heading in a granular soil. *Tunn. Undergr. Space Technol.* 23 (3), 241–250. doi:10.1016/j.tust.2007.04.012

Tonon, F. (2010). Sequential excavation, NATM and ADECO: What they have in common and how they differ. *Tunn. Undergr. Space Technol.* 25 (3), 245–265. doi:10.1016/j.tust.2009.12.004

Wang, Y. S., Yang, C., Zhang, X. S., Zhang, H., and He, S. S. (2020). Stability evaluation method of tunnel face constructed by mining method in sandy pebble stratum. *Railw. Eng.* (12), 57–60.

Wang, Z., Wang, L. Z., Wang, J. C., and Li, L. L. (2016). Case study of rehabilitation of a damaged underwater tunnel in the construction phase. *J. Perform. Constr. Facil.* 30 (1), C4014003. doi:10.1061/(asce)cf.1943-5509.0000648

Wong, K. S., Ng, C. W. W., Chen, Y. M., and Bian, X. C. (2012). Centrifuge and numerical investigation of passive failure of tunnel face in sand. *Tunn. Undergr. Space Technol.* 28, 297–303. doi:10.1016/j.tust.2011.12.004

Yoo, C. (2002). Finite-element analysis of tunnel face reinforced by longitudinal pipes. *Comput. Geotechnics* 29 (1), 73–94. doi:10.1016/s0266-352x(01)00020-9

Yoo, C., and Shin, H. K. (2003). Deformation behaviour of tunnel face reinforced with longitudinal pipes—Laboratory and numerical investigation. *Tunn. Undergr. Space Technol.* 18 (4), 303–319. doi:10.1016/s0886-7798(02)00101-3

Zhang, C., Cai, Y., and Zhu, W. (2019). Numerical study and field monitoring of the ground deformation induced by large slurry shield tunnelling in sandy cobble ground. *Adv. Civ. Eng.*, 2019, 1–12. doi:10.1155/2019/4145721

Zhang, X., Wang, M., Lyu, C., Tong, J., Yu, L., and Liu, D. (2022). Experimental and numerical study on tunnel faces reinforced by horizontal bolts in sandy ground. *Tunn. Undergr. Space Technol.* 123, 104412. doi:10.1016/j.tust.2022.104412

Zhang, Z., Li, H., Liu, H., Li, G., and Shi, X. (2014). Load transferring mechanism of pipe umbrella support in shallow-buried tunnels. *Tunn. Undergr. Space Technol.* 43, 213–221. doi:10.1016/j.tust.2014.05.018

Zhang, Z. X., Zhang, H., and Yan, J. Y. (2013). A case study on the behavior of shield tunneling in sandy cobble ground. *Environ. Earth Sci.* 69, 1891–1900. doi:10.1007/s12665-012-2021-4

Zhao, R. L., Yao, H. Z., He, B., Guo, H. W., and Ye, F. (2019). 3D DEM analysis of stress-strain behavior of tunnel surrounding rock-support structure by benching method in sandy cobble stratum. *Tunn. Constr.* 39 (S1), 235–244.

frontiers | Frontiers in Earth Science

TYPE Original Research
PUBLISHED 13 July 2023
DOI 10.3389/feart.2023.1227753

OPEN ACCESS

EDITED BY
Liang Cui,
Lakehead University, Canada

REVIEWED BY
Shuangfeng Guo,
Nanjing Tech University, China
Kun Fang,
China University of Geosciences Wuhan, China

*CORRESPONDENCE
Guo-Jing Cui,
112314910@qq.com

RECEIVED 23 May 2023
ACCEPTED 26 June 2023
PUBLISHED 13 July 2023

CITATION
Cui G-J, Xie J-S, Sun Y-h, Tian X-x and Meng C (2023), Dynamic response of large-section inclined shallow-buried pipe tunnel under train loads.
Front. Earth Sci. 11:1227753.
doi: 10.3389/feart.2023.1227753

Dynamic response of large-section inclined shallow-buried pipe tunnel under train loads

Guo-Jing Cui[1,2]*, Jiang-Sheng Xie[3], Yin-hao Sun[3,4], Xiao-xu Tian[1,2] and Chen Meng[5]

[1]School of Civil Engineering, Xi'an University of Architecture and Technology, Xi'an, China, [2]Shaanxi Provincial Key Laboratory of Geotechnical and Underground Space Engineering, Xi'an, China, [3]China Railway 20th Bureau Group Corporation Limited, Xi'an, China, [4]China Railway 20th Bureau Group First Engineering Co., Ltd., Suzhou, China, [5]Hanjiang-to-Weihe River Valley Water Diversion Project Construction Co., Ltd., Hanjiang, China

To ensure the normal passage of an ascending road during the construction of a pipe-jacking tunnel, trains generally run at low speeds during the construction phase and adopt normal speeds later. Using Jingjiu Road, Xi'an, China, as an engineering case, this study evaluated and predicted the dynamic response of a tunnel structure and soil mass when trains run at low to normal speeds. When the train speed was controlled in the range of 30–60 km/h, the soil deformation change rate around the shallow-buried pipe-jacking tunnel was 0.41%. The maximum tensile stress growth rate of the pipe-jacking tunnel structure was 0.037%, the maximum compressive stress growth rate was 0.128%, and the maximum increase in the stress of the pipe-jacking structure was 1.82%. Thus, the soil and structure of the pipe-jacking tunnel were in a safe-stress state. The results show that the influence of train speed on soil and structural stress is small and can be ignored.

KEYWORDS

train load, large section, oblique shallow buried, pipe jacking tunnel, dynamic response

1 Introduction

With rapid and large-scale construction of pipe-jacking tunnels in cities where important buildings or traffic lines exist, the engineering route will inevitably be orthogonal and oblique. (Degrande et al., 2006; Zhou et al., 2022; Liu et al., 2023). Ensuring the safe operation of established traffic lines is crucial in urban traffic. Owing to the long construction cycle times of the pipe-jacking tunnel projects, disturbance due to construction activities can be significant, and the repeated vibration load of trains can adversely impact the structure of the pipe-jacking tunnels. Trains usually travel at a low speed when passing through the construction section and regain their normal speed once they exit the construction section. Presently, urban, shallow, buried tunnel construction is still in its early stages in China. To ensure the stability of the upper environment, it is important to study the trains running over shallow, buried tube tunnels and the structural deformations after construction.

Many experts and researchers have studied the soil and structural deformation properties of pipe-jacking tunnels subjected to the influences of train speeds and dynamic loads (Li et al., 2019; Liu et al., 2020). Wenhua et al. (2007) used

instruments such as a strong seismoscope and dynamic earth pressure box to perform field tests on the engineering section of the Lianyan Expressway. They analyzed the dynamic response characteristics of pavements and subgrades at different depths for different vehicle types and speed conditions. Based on a three-hole parallel tunnel project where an underpass of a railway trunk line was built, Lun and Yu (2008) studied the dynamic responses of trains running through parallel tunnels at different speeds using ANSYS finite element numerical simulations and determined the changes in the vault pressure as a function of the buried depth and the longitudinal tunnel. To calculate the dynamic responses of the strata of the Guangzhou–Shenzhen–Hong Kong high-speed railway tunnel subject to high-speed trains and analyze the influence of groundwater, Bao et al. (2011) established a three-dimensional numerical model using the FLAC3D software. Yufang (2013) considered a tunnel running through the Beijing–Shanghai high-speed railways as a research object and simulated the dynamic response law of the lining structure of the tunnel at different construction stages subject to the action of train vibration loads. Their results indicated that the tunnel was in the most unfavorable construction position when trains passed through. Xiangqiu et al. (2005) conducted field tests and frequency-response analyses on the dynamic response of the Zhuting tunnel structure of the Beijing–Guangzhou line when the train speed was approximately 80 km/h. They established an analysis model and digital expression of the train vibration load and obtained the vertical displacement, acceleration, and internal force–time history curves of the tunnel lining structure. Dewu and Feng (1997) measured the influence of velocity on the vibration energy and structural vibration acceleration of the Jinjiayan and Zhalanyingzi tunnels when the train speed was approximately 50 km/h. Wang et al. (2022) performed numerical simulations to study the dynamic response characteristics of the bottom part of tunnel structures in water-rich soft strata subjected to heavy-duty train loads. With pore-water pressure and vertical dynamic stress as the evaluation indices, the response rules of the excess pore-water pressure and soil dynamic stress at bedrock were analyzed when subject to 25,000, 27,000, and 30,000 kg trains. Zhu et al. (2020) used the Newmark dynamic time-history analysis of three-dimensional finite element and seed equivalent linear methods to simulate the vibration softening of the subgrade. They performed numerical simulations to evaluate the passage of trains over the railway above a pipe-jacking group and obtained response curves for variables, including the instantaneous vertical displacement of the subgrade and additional dynamic pipe-jacking stress. Their analysis showed that when the pipeline depth was 12 m, the train speed was 100 km/h, and when the train speed was 200 km/h, the maximum vertical dynamic displacement of the two subgrades increased by 1.3 mm. The adjunctive stress/compressive dynamic stress of the pipe-jacking was approximately 0.14 MPa, and the influence of the pipe-jacking group on railway operation was within the allowable range. Yunfeng et al. (2022) showed that when the running speed of a train changes, the dynamic response of each part of the tunnel-reinforcement zone-formation system changes. The finite element method was used to analyze the influence of train speed on the acceleration, dynamic stress, and dynamic displacement of each part of a structure-formation system. Huinan (2022) established a finite element model of the overall track-tunnel-soil system and analyzed the vertical vibration variation of subway trains at 50, 80, and 120 km/h speeds, primarily from the perspectives of time and frequency domains.

Most research on railway tunnels has mainly focused on the influence of train vibration and train speed in deep-buried tunnels (Lipeng, 2013; Song et al., 2019b; Fan et al., 2020; Wang et al., 2022). There are relatively limited studies on the dynamic response of the soil and structure of shallow-buried rectangular pipe-jacking tunnels at oblique intersections. Most of these studies rely on numerical simulations. There are few data cases for field monitoring. Using the engineering case of the Xi'an Jingjiu Road, an underpass of the Longhai Railway line, for our study, we adopted the method of monitoring field test dynamic characteristics and running numerical simulations to predict the dynamic response law and safety of the soil and structures around the tunnel when trains passed at different speeds at oblique intersections during the postconstruction operation, thereby providing a technical reference to ensure the normal operation of the project.

2 Engineering background

The oblique shallow-buried pipe tunnel project of the Xi'an Jingjiu Road, an underpass of the Longhai Railway line, is located at the west side overpass of the Xi 'an East Railway Station under the railway. Reinforced concrete, an overpass tunnel, a box-interchange structure, a rectangular pipe, and an oblique railway line were used in the project. Additionally, a pipe tunnel with an orthogonal width of 50.5 m and oblique width of 56.45 m was divided into nine sections (1#–9#) from south to north. The fifth prefabricated pipe section was 50.5 m × 10.30 m in size and 1.5 m long. The engineering construction site is geologically complex and rich in groundwater. The bottom part of the structure was located in the saturated soft loess with poor geology (Figures 1, 2). This project had a large section, long top, and soft foundation, and it faced considerable construction challenges.

Based on the actual engineering geological data, the model was divided into six horizontal strata from top to bottom. These included mixed-fill soil, plain-fill soil, ①-loess, ②-loess, paleosol, and ③-loess. The physical and mechanical parameters of each soil layer are listed in Table 1.

3 Dynamic response of the pipe-jacking tunnel when trains run at low speeds

3.1 Layout of monitoring points

Following the safety regulations issued by the Railway Corporation and China's Railway Xi'an Bureau Group Co., Ltd. (Tieyun No. 146, 2006), trains pass through construction sections at low speeds to ensure the safety of ascending trains during the construction of a pipe-jacking tunnel. To ensure the normal operation of the upper traffic during pipe jacking construction, the construction project department has stipulated the train speed range to be 30–60 km/h. To study the dynamic response changes of

FIGURE 1
Schematic and photograph of the oblique interchange of the Xi'an Jingjiu Lu-Longhai railway project.

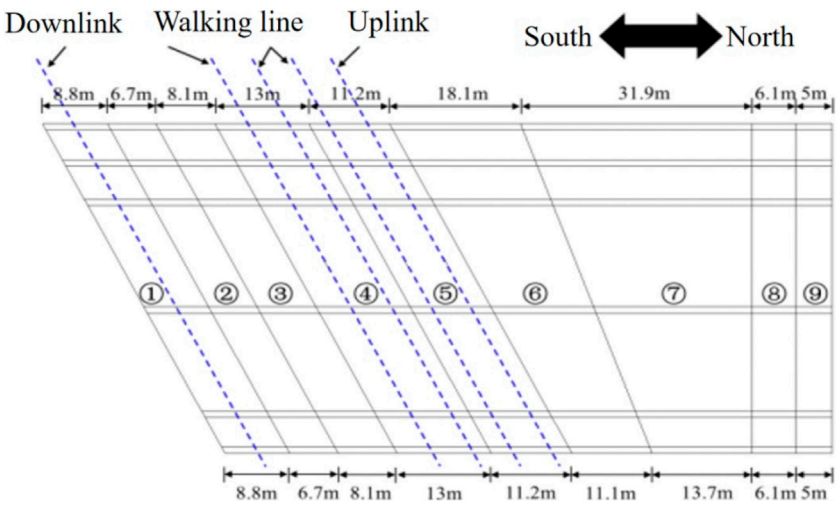

FIGURE 2
Plan of the 26.5° oblique interchange of the Xi'an Jingjiu Lu-Longhai Railway.

TABLE 1 Physical and mechanical parameters for each layer of the soil.

Name	Density/γ (KN/m^3)	Cohesion/ c (kPa)	Angle of friction/φ (°)	Modulus of elasticity/E (MPa)	Poisson's ratio/μ	Permeability coefficient/K (m^2/(Pa·s))
Miscellaneous fill	18.00	0.00	15.0	12.00	0.35	1e-11
Plain fill	17.00	7.00	15.0	14.64	0.35	1e-13
①-loess	17.00	22.00	19.5	15.32	0.33	1e-12
②-loess	17.00	27.00	20.0	15.32	0.33	1e-12
Ancient Soil	19.00	21.00	20.0	17.83	0.30	1e-13
③-loess	20.00	40.00	20.0	17.36	0.32	1e-13

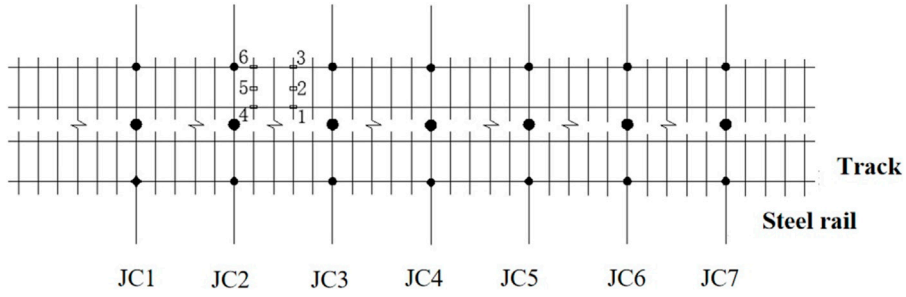

FIGURE 3
Schematic of the train-track monitoring point locations.

FIGURE 4
Field-measured data diagram of a passing train.

the soil mass around the pipe-jacking tunnel and structure when trains pass through, a train operation site-monitoring scheme was developed based on the actual engineering situation. Seven monitoring sections (JC1–JC7) were set along the train running line, and six measurement points were arranged on the lower side of the steel pillow to monitor the dynamic acceleration and strain of the steel pillow. Figure 3 shows the arrangement of the monitoring points. Point 1 was located in the middle of the rail pillow between the two transverse beams near the lower side of another track, point 2 in the middle of the rail pillow between the two transverse beams, point 3 in the middle of the rail pillow away from the lower side of another track, and point 4 on the side of the rail pillow near the lower side of the other track. Point 5 was located at the lower side of the middle position of the rail pillow on the side of the transverse beam. Point 6 was located at the lower side of the rail pillow on the side of the transverse beam away from the other track (see Figure 4 for onsite monitoring). A vertical acceleration sensor was arranged at each monitoring point. Relevant research showed that the dynamic load of the train is transferred along the structure of the track, sleeper, roadbed, foundation, and tunnel, and it gradually attenuates layer by layer. At the same time, considering the actual project, it is assumed that the bottom of the train sleeper directly contacts the soil mass and that the monitoring equipment components simultaneously contact the soil mass during the field dynamic monitoring. Therefore, it is assumed that the dynamic response variation law of the sleeper at each test point is approximately equivalent to the deformation law of the soil mass around the pipe jacking tunnel.

3.2 Analysis of field monitoring data

The peak vertical acceleration at each measurement point was monitored onsite when the train passed at a low speed of 45 km/h, and after the train had passed six times, the monitoring data were obtained. Figure 5 shows the vertical acceleration–time history curves for the six monitoring points when the train passed for the first time.

Figure 6 shows the peak vertical acceleration of the six monitoring points located on the steel pillow when a train passed through it on six occasions at 45 km/h. The observations are as follows: (1) The acceleration–time history curves of each monitoring point fluctuated during the six passes; the peak acceleration values at monitoring points 2 and 5 were relatively large; across all monitoring points, the minimum acceleration was 0.423 m/s^2; at 2.083 m/s^2, the maximum acceleration was 4.9 times larger than the minimum. (2) Among the monitoring points on the same steel pillow, the vertical acceleration response of point 1 was slightly less than that of point 3, and the response of point 4 was slightly less than that of point 6. The acceleration at points 1 and 4 on the inside of the track is less than that at points 3 and 6 on the outside. The variation law of each monitoring point is assumed to be the soil deformation law. Additionally, we considered that the maximum acceleration of soil deformation was 2.083 m/s^2 when the train passed at 45 km/h, indicating that the train influenced soil deformation.

4 Dynamic response of the pipe-jacking tunnel during operation

Based on the onsite monitoring of the shallow-buried pipe tunnel project of the Xi'an Jingjiu Road, we estimated the soil

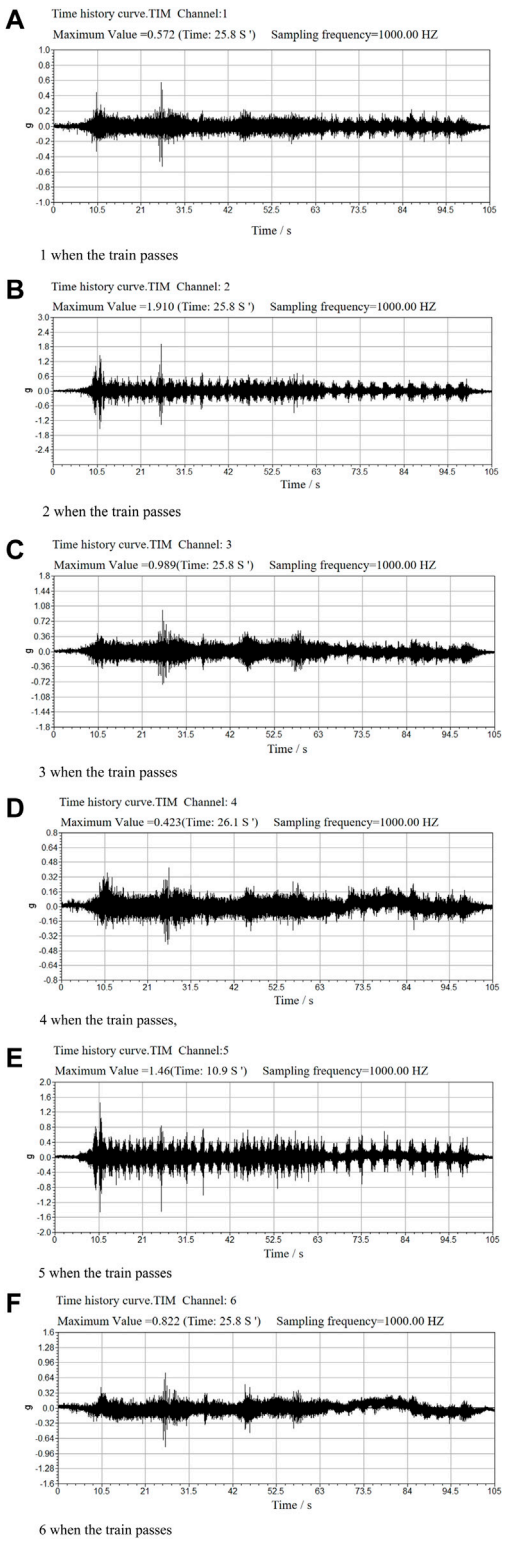

FIGURE 5
Acceleration–time history curves for all monitoring points. **(A)** 1 when the train passes, **(B)** 2 when the train passes, **(C)** 3 when the train passes, **(D)** 4 when the train passes, **(E)** 5 when the train passes, **(F)** 6 when the train passes.

deformation law for the case of trains passing at low speeds. The intersection angle between the train track and the jacking pipe axis was 26.5°. To further predict the deformation law of the inclined shallow buried pipe tunnel under the condition of a train running at high speed, a dynamic response analysis was performed using the FLAC3D numerical modeling software. Because the train vibration response was classified as a microvibration, the amplitude of the dynamic response was significantly small. Therefore, a linear elastic finite element model can be used to study the influence of train vibration on buildings and soil mass. For rock and soil mass, the Mohr-Coulomb criterion was selected, and the isotropic elastic model was employed for concrete in pipe-jacking tunnels.

The purpose of this study is to reveal the soil and structural deformation law of the roof tunnel at oblique intersections. Based on an extensive literature review of related studies, we selected several physical quantities, such as the overall surface deformation, vertical deformation, structural stress deformation, and acceleration, to analyze and evaluate the dynamic response. Surface deformation refers to micro- and macro-deformation phenomena such as displacement, settlement, uplift, tilt, deflection, and crack of rock and soil mass (TACGHP 014, Technical Specification of Ground Deformation Monitoring for Geohazard, 2018; Huo et al., 2019). Among them, the overall surface and vertical deformations mainly involve displacement and settlement, which are used to represent the settlement deformation of soil when the train speed changes. The greater the deformation, the more evident the influence of the speed change. Structural stress is the internal force generated in pipe jacking when the pipe jacking structure is deformed while resisting the effect of external causes. The size of structural stress reflects the influence degree of the jacking structure under dynamic load. The greater the structural stress, the more evident the influence of dynamic load. Based on relevant regulations (TB 10002.3. Code for Design of Reinforced Concrete and Prestressed Concrete Structures of Railway Bridges and Culverts, 2005; GB 50010, Code for Design of Concrete Structures, 2010; GB 50868, 2013; Song et al., 2019a), when the train speed was <120 km/h, the height and horizontal displacement of the track, steel pillow, and beam had to be controlled within 8 mm. The tensile and compressive principal stresses of concrete structures following repeated train loads should be consistent with $\sigma_{ct} \leq 0.7 f_{ct}$ and $\sigma_c \leq 0.55 f_c$, where σ_{ct} is the tensile stress of a concrete lining structure (MPa); f_{ct} is the ultimate tensile strength of concrete (MPa); σ_c is the compressive stress of the concrete lining structure (MPa); and f_c is the ultimate compressive strength of concrete (MPa). The acceleration limit of the building was 10.2 m/s^2. The structure can suffer damagedamages if its vibration acceleration exceeds this limit.

4.1 Numerical model

To develop the numerical model, a pair of trains were set to run simultaneously at the same speed in opposite directions from

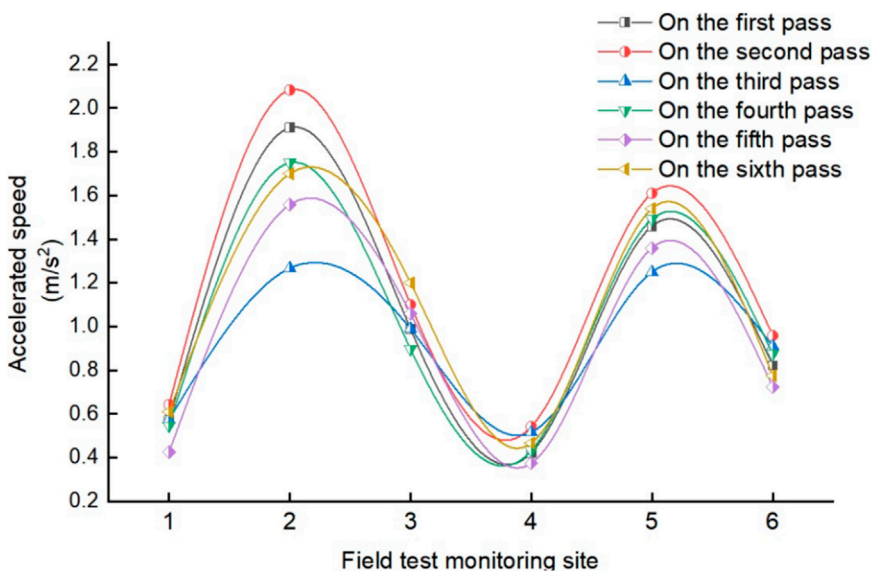

FIGURE 6
Variations in the peak vertical acceleration of soil deformation at all monitoring points.

TABLE 2 Research conditions for train dynamic characteristics.

Influence factor	Working condition	Reserve injection
Train speed	30 km/h	In the opposite direction, the skew is 26.5°; pipe jacking depth is 0.5 m below the ground; and groundwater level rises to the structure base
	45 km/h	
	60 km/h	

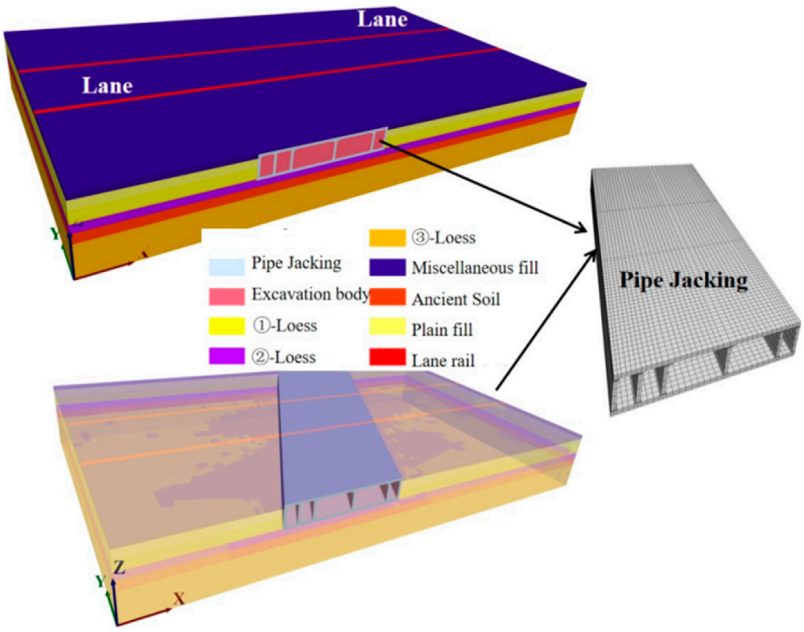

FIGURE 7
Standard model of the oblique shallow-buried pipe tunnel.

TABLE 3 Extreme values of the vibration load at different speeds.

Speed (km/h)	Extreme values of the vibration load/N	
	Maximum	Minimum
30	298,187.7	289,885.9
45	303,458.1	284,667.8
60	310,842.3	277,238.2

the boundary of the model. The trains had an axle weight of 140 kN and a running speed of 45 km/h, the pipe was buried at a depth of 0.5 m below the ground, and the underground water level was recovered at the base of the structure under standard operating conditions of the dynamic model. In addition, dynamic calculation models of different train speeds were established (The operating conditions are shown in Table 2). In the numerical simulation, only the soil weight and train traffic load were considered, and the latter was equal to the simulation load. The influence of the ground overload, equipment load, and groundwater change was not considered in the simulation;, hence the surrounding rock parameters, tunnel structure parameters, and supporting parameters were unchanged.

When FLAC3D was used to establish the soil mass and structural geometry model of the inclined shallow-buried and large-section pipe-jacking tunnel, based on Saint-Venant's principle (Kai, 2019), owing to the asymmetry between the train lane and the pipe-jacking position, a three-dimensional full-section modeling was required. After many calculations, the results of an inversion analysis were considered. The length, width, and height of the model were determined to be 250, 150, and 30 m, respectively.

The normal displacements around and at the bottom of the model were constrained, and the free-boundary conditions were applied as static boundary conditions at the top of the model. The dynamic boundary conditions were free around the model and static on the top-lane surface. Combined with the three working conditions listed in Table 2, the division of model units of the standard model was dominated by 8-node hexahedrons and supplemented by 4-node tetrahedrons. The model was divided into 93,013 nodes and 145,652 units. The specific geometric model is shown in Figure 7.

4.2 Train load simulations

For these simulations, the train speeds in the study area were provided by the Xi 'an Railway Group Company; the uniform speeds were 30, 45, and 60 km/h. Referring to the relevant literature (BoLiang et al., 2006; Chang, 2017; Niu et al., 2020; Xiancong et al., 2022), this study adopted the track irregularity method by considering the train dynamic load to maintain vibrations at the top of the model for 5 s and expressing the train vibration load with a fitting function (Eq. 1) containing medium, low, and high-frequency excitation forces. Eq. 2 represents the modified wheelset force of the train on the line.

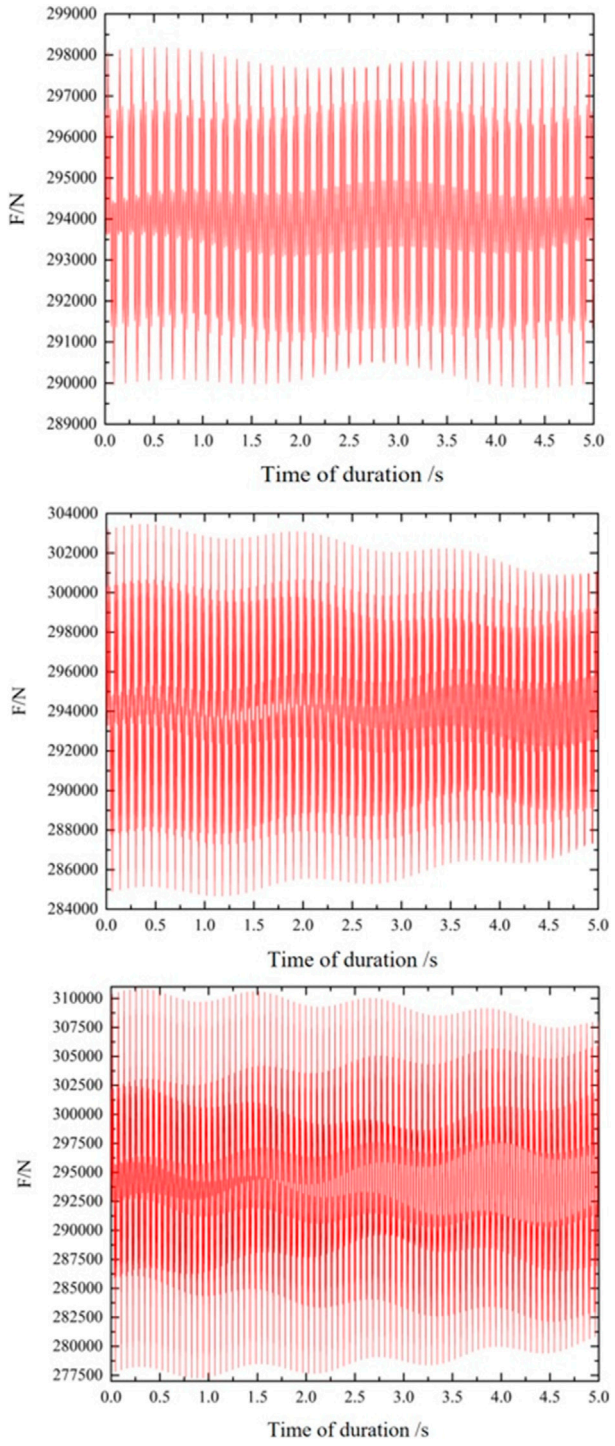

FIGURE 8
Vertical vibration load curves of trains as a function of the time interval at different speeds.

$$F(t) = P_0 + P_1 \sin \omega_1 t + P_2 \sin \omega_2 t + P_3 \sin \omega_3 t + \ldots \quad (1)$$

$$F'(t) = k_1 k_2 F(t) = P_0 + k_1 k_2 (P_1 \sin \omega_1 t + P_2 \sin \omega_2 t + P_3 \sin \omega_3 t) \quad (2)$$

In Eq. 2, P_0 is the static load of train wheels; P_1, P_2 and P_3 are vibration loads, which represent the forces generated by the train in

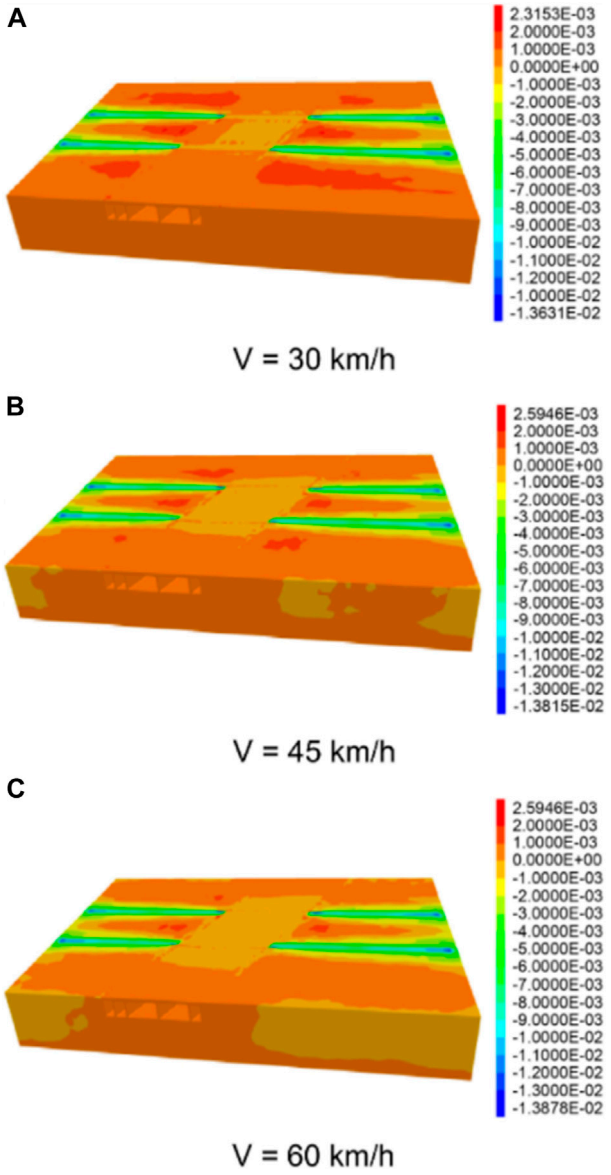

FIGURE 9
Model cloud map of the overall vertical deformation at different train speeds. **(A)** when V = 30 km/h; **(B)** when V = 45 km/h; **(C)** when V = 60 km/h.

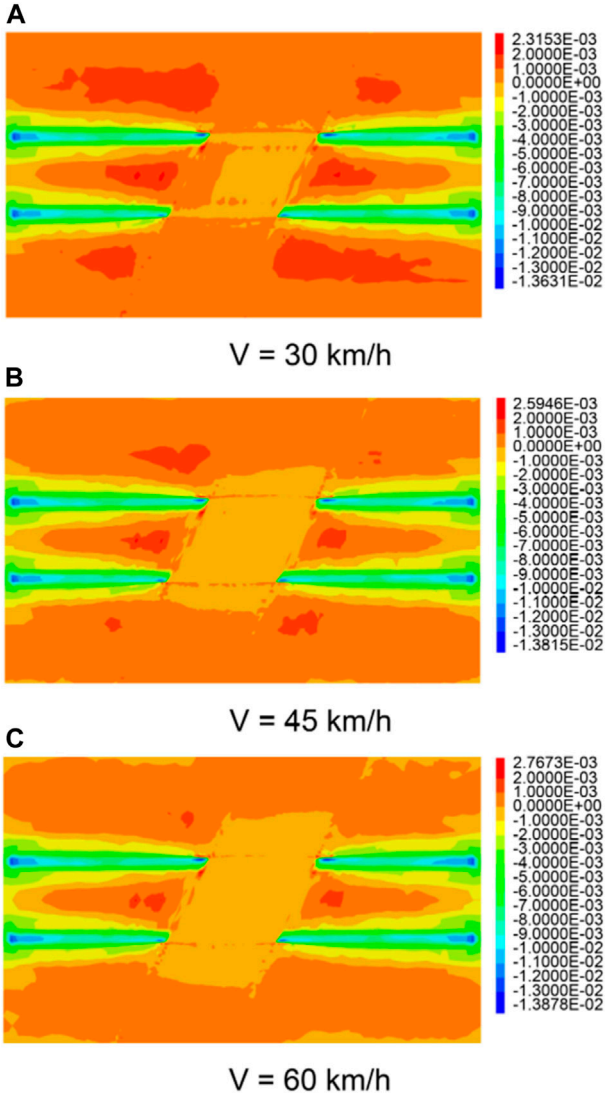

FIGURE 10
Model cloud map of the vertical surface deformation at different train speeds. **(A)** when V = 30 km/h; **(B)** when V = 45 km/h; **(C)** when V = 60 km/h.

the low, medium, and high-frequency ranges, respectively; k_1 is the superposition coefficient ranging from 1.2 to 1.7; and k_2 is the dispersion coefficient ranging from 0.6 to 0.9. We considered the sprung mass of the train to be M, its running speed V, and vibration circle frequency ω_i. This study considered that each train had two bogies and four axles. The maximum axle weight of each train was 14,000 kg, and the resulting stress was evenly distributed on the ground covered by the train. By referring to previous studies (Lei, 2019), the static load of train wheels was the maximum weight of a single bogie (28,000 kg); the gravitational acceleration g was 10.0 m/s^2; the unsprung mass was 2,100 kg; and coefficients k_1 and k_2 were 1.5 and 0.7, respectively. The train excitation load function $F(t)$ with respect to time t at the three set speeds was calculated as follows:

At V = 30 km/h,

$$F(t) = 1.05[280000 + 129.30\sin(2.62t) + 1724.05\sin(52.31t) + 2155.06\sin(261.56t) \quad (3)$$

At V = 45 km/h,

$$F(t) = 1.05[280000 + 129.17\sin(3.93t) + 3882.22\sin(78.50t) + 4852.77\sin(392.50t) \quad (4)$$

At V = 60 km/h,

$$F(t) = 1.05[280000 + 517.84\sin(5.23t) + 6904.48\sin(104.69t) + 8630.6\sin(523.44t) \quad (5)$$

TABLE 4 Peak values of the vertical displacement of soil at different train speeds.

Speed (km/h)	Overall peak vertical displacement/mm		Peak vertical displacement of surface/mm	
	Max	Min (E-04)	Max	Min (E-04)
30	−12	−0.667	−11.9	−0.676
45	−12	−0.669	−11.9	−0.672
60	−12	−0.674	−11.9	−0.677

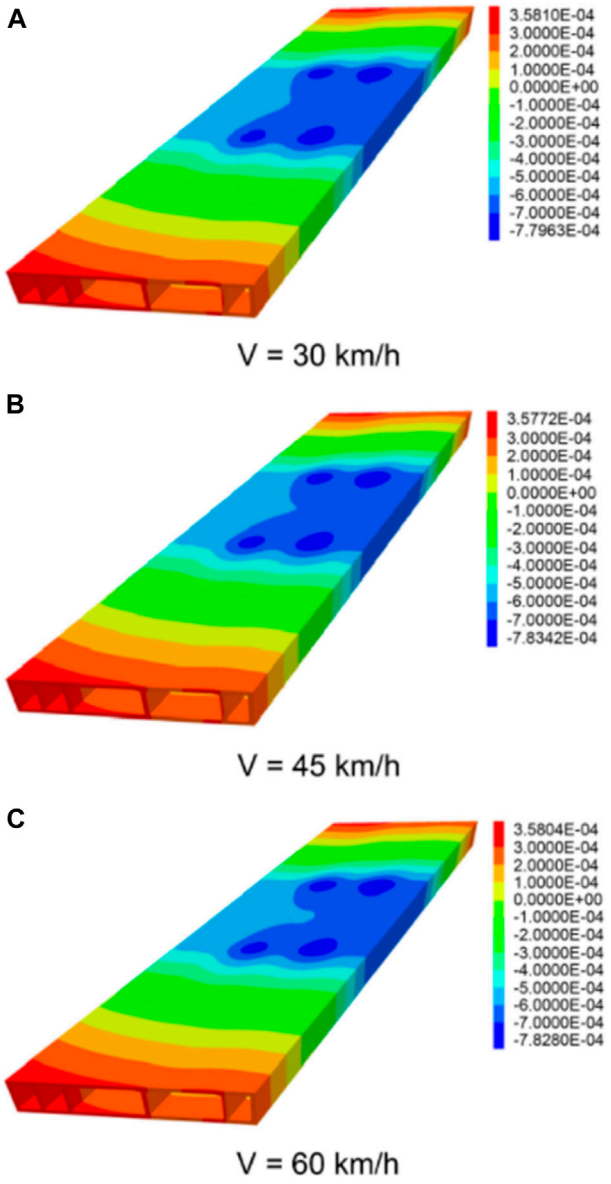

FIGURE 11
Nephogram showing the overall vertical deformation of the pipe-jacking tunnel structure at different train speeds. **(A)** when V = 30 km/h; **(B)** when V = 45 km/h; **(C)** when V = 60 km/h.

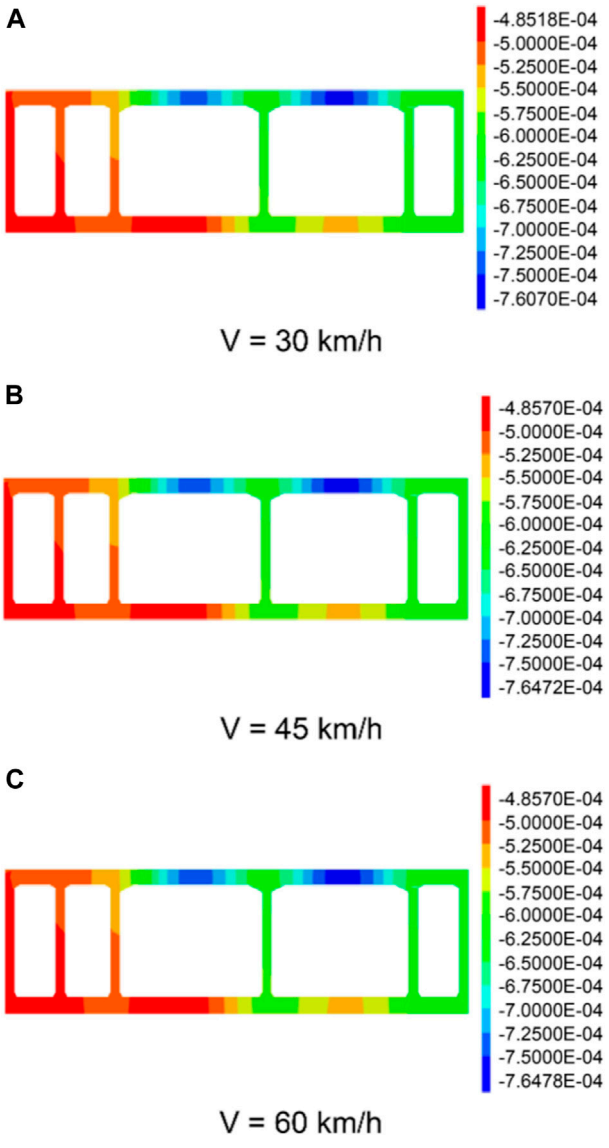

FIGURE 12
Cloud map showing the vertical deformation of the pipe-jacking section y = 54.25 m at different train speeds. **(A)** when V = 30 km/h; **(B)** when V = 45 km/h; **(C)** when V = 60 km/h.

Based on the above equations, the extreme values of the vibration load at different speeds within 0–5 s were obtained (Table 3). Figure 8 shows the vertical vibration load $F(t)$ as a function of the time interval. The measured $F(t)$ of the trains at each speed was applied to the track to simulate the excitation of the tube jacking-tunnel structure when the trains passed through the station at a uniform speed.

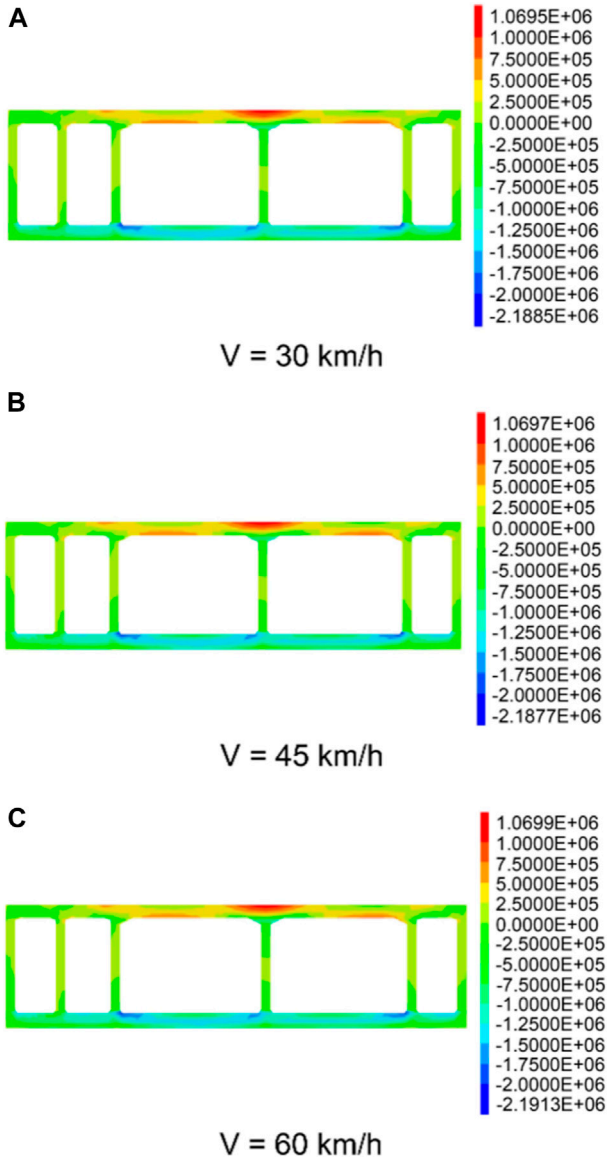

FIGURE 13
Stress (Pa) distribution cloud map of the pipe-jacking section y = 54.25 m at different train speeds. **(A)** when V = 30 km/h; **(B)** when V = 45 km/h; **(C)** when V = 60 km/h.

4.3 Analysis of the soil displacement response

Figures 9, 10 show the nephograms of the overall and surface vertical displacement of the pipe-jacking tunnel at different speeds. The vertical (downward) deformations of the surface of the model are 13.63, 13.81, and 13.87 mm at different train speeds (V = 30, 45, and 60 km/h, respectively) when the groundwater level rises to the structural basement. The surface deformation of the model gradually increases with train speed, reaching a maximum of 1.81%. Table 4 lists the overall peak vertical displacement of soil and the peak vertical displacement of the ground at different train speeds. The overall peak value of the vertical displacement when the train was running ranged from −12.00 to 0.674 mm, and that of the ground ranged from −11.90 to 0.67 mm. At higher train speeds, the maximum values of the overall and surface vertical displacements were unchanged, while the corresponding minimum values increased by 1.04% and 0.74%, respectively. Thus, train speed had minimal effect on soil deformation.

4.4 Stress response analysis of a pipe-jacking structure

Figures 11, 12 show the overall vertical deformation of the pipe-jacking tunnel structure at different train speeds and the vertical deformation cloud map of section y = 54.25 m. The figures show that as the train speed increased, the vertical deformation of the top-pipe structure fluctuated: -0.77, −0.78, and −0.78 mm, and the vertical deformation increased from −0.76 to −0.76 mm at a growth rate of 0.4%–0.54%.

Figure 13 shows the cloud map of stress distribution of the pipe-jacking section y = 54.25 m at different train speeds. The pipe-jacking stresses at the three train speeds manifest as tension and pressure principal stress, and they are concentrated primarily in the lower left and lower right corners of the left motor lane and the lower right corner of the right motor lane. The maximum tensile and compressive stresses were 1.06 and 2.18, 1.06 and −2.18, and 1.06 and −2.19 MPa at V = 30, 45, and 60 km/h, respectively. The maximum tensile and compressive stresses grew at a rate of 0.037% and 0.128%, respectively. Thus, train speed had minimal effect on the pipe-jacking stress and structure deformation.

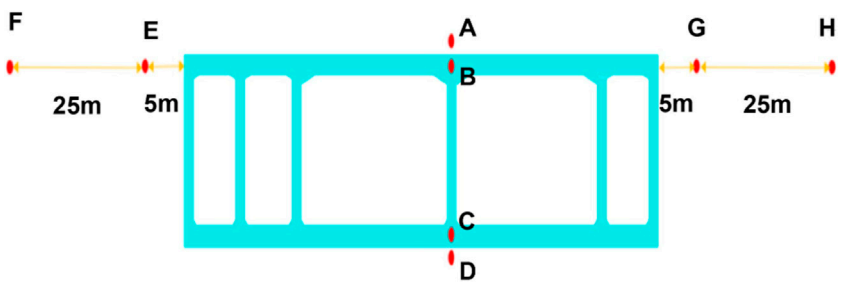

FIGURE 14
Schematic of monitoring sites.

TABLE 5 Peak values of soil deformation above pipe jacking at different train speeds.

Speed (km/h)	Vertical deformation/mm				
	F	E	A	G	H
	Soil layer to the left		Top layer of the pipe	Soil layer to the right	
30	−0.749	−0.845	−0.485	−0.790	−0.742
45	−0.749	−0.846	−0.486	−0.791	−0.743
60	−0.752	−0.848	−0.487	−0.792	−0.744

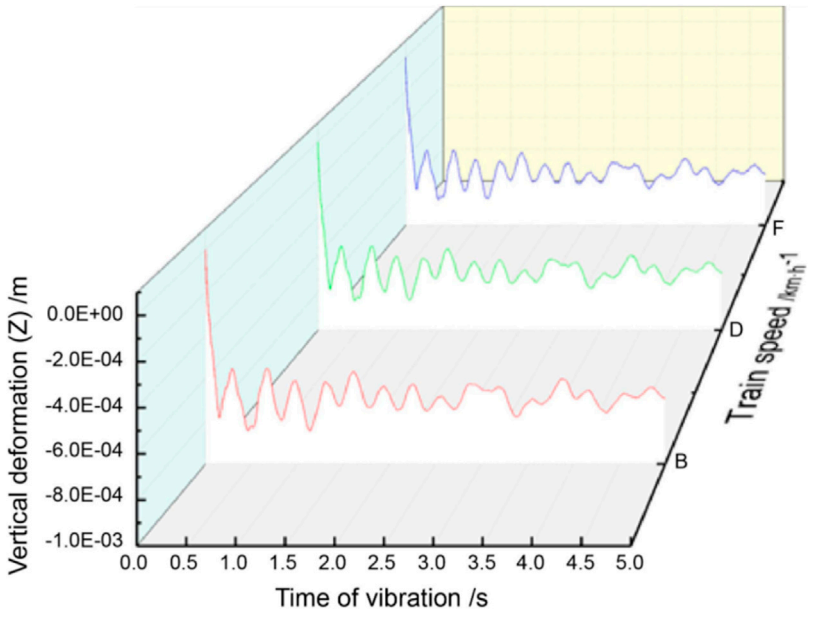

FIGURE 15
Vertical deformation law of soil in the top section of pipe jacking as a function of vibration time at different train speeds.

The deformation and stress of the pipe-jacking structure showed a minimal increase with train speed, indicating that the dynamic response of the pipe-jacking structure changes insignificantly in the range of 30–60 km/h.

5 Analysis of the influence law of train speed

To explore soil deformation under train speed variations, eight monitoring points (A–H) were set in the model to monitor the displacement and stress changes in soil mass and pipe jacking during train operations, as shown in Figure 14.

5.1 Analysis of the influence law of train speed on the dynamic response of soil displacement

The peak deformations of soil and structure points above the pipe-jacking structure were recorded after applying train loads at different speeds. The results are summarized in Table 5.

Figures 15, 16 show the vertical deformation of the soil and stress at monitoring point A, respectively, as a function of vibration time at different train speeds. Together with the study results presented in Table 5, we observe that the soil maintained a certain level of displacement settlement and stress, and the vertical deformation law is nearly identical at all three train speeds.

Figure 17 shows the variation law of each point at two monitoring sections: y = 54.75 and 95.25 m. The vertical displacement of soil at the axis of the top structure in the two monitoring sections is large. The vertical deformation gradually decreases on both sides and has a generally symmetrical distribution. Furthermore, from Table 5, the vertical deformation of the soil layer was the highest above the pipe-jacking axis at each point on the monitoring section, with a change rate of 0.41%. For example, at a train speed of 60 km/h, the peak vertical deformations were 7.92 and 7.44 mm at monitoring points G and H, respectively, and 8.48 and 7.52 mm at points E and F, respectively. Moreover, when the train speed was constant, the distance from the pipe-jacking structure increased. When the train moved horizontally, the vertical displacement of each monitoring point gradually

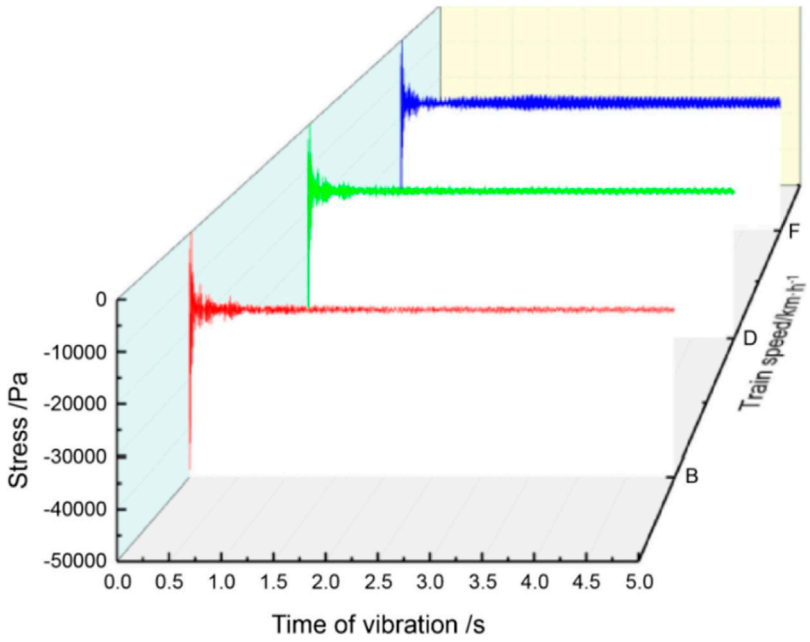

FIGURE 16
Stress at monitoring point A as a function of vibration time at different train speeds.

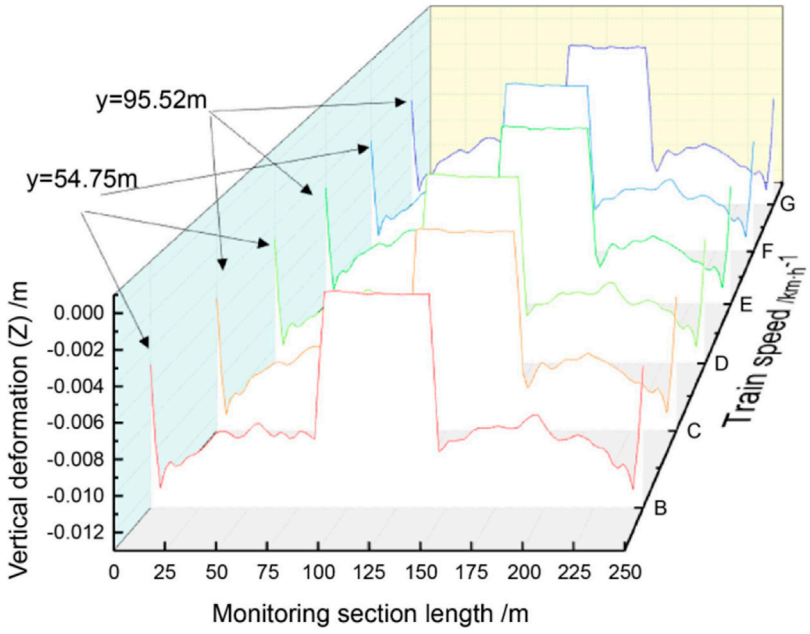

FIGURE 17
Vertical deformation curves at the top of the model.

decreased, indicating that the vibration wave generated by the slow-moving train attenuated during horizontal propagation. As the distance from the vibration source increased from 5 to 20 m, the peak values of the soil displacement and deformation decreased, and the maximum attenuation rate reached 93.9% within a distance of 20 m. Comprehensive analysis showed that soil deformation is marginally affected by train speeds in the range of 30–60 km/h.

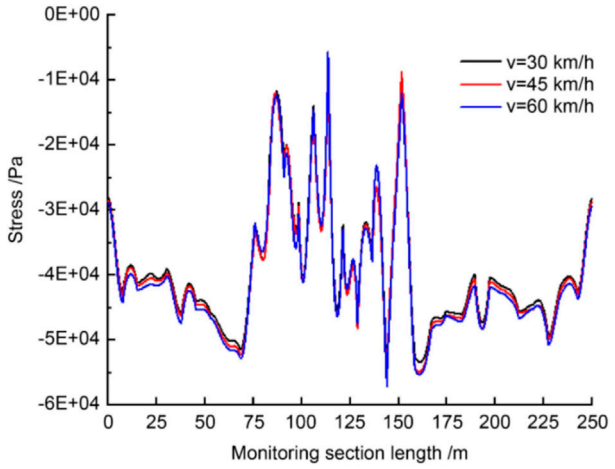

FIGURE 18
Stress variation law of model monitoring point B at different train speeds.

5.2 Analysis of the influence law of train speed on the dynamic response of pipe jacking

Figure 18 shows the stress on the middle line of the upper part of the pipe-jacking structure (monitoring point B) and its variations as a function of the distance of the pipe-jacking structure. The stress of the entire model increases in tandem at the three train speeds. Thus, the stress at monitoring point B is minimally affected by changes in train speed.

Figure 19 shows the stress at monitoring point B at different train speeds. The soil stress above the pipe-jacking structure fluctuates due to the vibrations induced by the moving train, the fluctuations being stronger at higher train speeds. The results of the analysis are as follows: (1) the changes in train speed have little effect on the stress–time history curve of the pipe-jacking structure, and (2) the peak stress increases with train speed; however, the increase is small.

5.3 Numerical simulations of train long-term action and verification analysis of allowable values

5.3.1 Comparative analysis of the soil displacement response

As discussed in Section 3.2, the variation law of each monitoring point is approximately equivalent to the soil deformation law around the pipe-jacking tunnel, and the maximum soil deformation acceleration is 2.08 m/s^2 when the speed of the train is 45 km/h.

Based on the numerical simulation results discussed in Section 5.1, the vertical deformation law of soil mass at the top of the pipe-jacking structure was obtained as a function of vibration time at different train speeds (Figure 16). We observed that the deformation of the soil mass varied with train speed. The acceleration curve of soil deformation at different train speeds was obtained using the quadratic derivation of the displacement change (Figure 20). The average value of vertical acceleration during 45 km/h operation was calculated to be 1.92 m/s^2, which is close to the measured value of 2.083 m/s^2 with a deviation of 8.49%. This confirms the effectiveness of numerical simulations and field-measured data analyses.

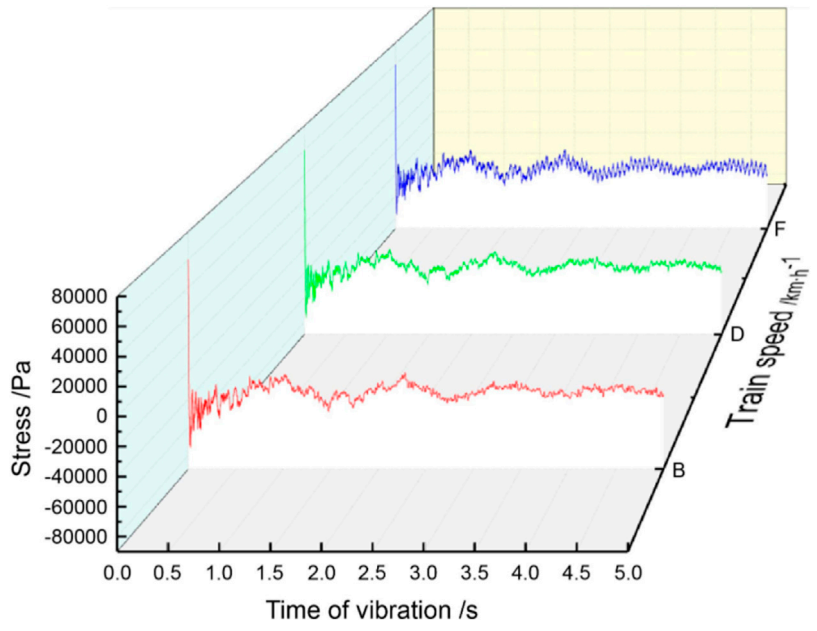

FIGURE 19
Stress at monitoring point B as a function of vibration time at different train speeds.

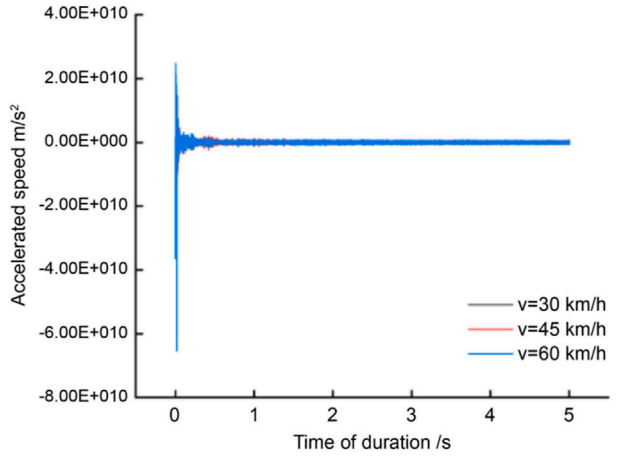

FIGURE 20
Temporal variations in the vertical acceleration of soil deformation at different speeds.

Furthermore, the peak acceleration of the building was <10.2 m/s^2, indicating that the soil deformation was within the allowable range (TB 10002.3. Code for Design of Reinforced Concrete and Prestressed Concrete Structures of Railway Bridges and Culverts, 2005).

5.3.2 Comparative analysis of the structural response of the pipe-jacking tunnel

The pipe-jacking tunnel in Jingjiu Road underrunning the Longhai Railway line has a concrete strength of C50 and an impermeability grade of P8. As discussed in Section 4, the limiting values of tensile and compressive stresses of the pipe-jacking tunnel structure at repeated train loads were 2.17 and 18.425 MPa, respectively. In the analysis of the influence of train speed on dynamic response, the maximum tensile and compressive stresses of the pipe-jacking structure were 1.0699 and 2.1913 MPa, respectively, at 60 km/h speed. For train speeds in the range of 30–60 km/h, the structural stress of the pipe-jacking tunnel was within the design requirements, and the structure was in a safe-stress state.

6 Conclusion and discussion

In this study, we monitored the dynamic characteristics of a shallow-buried pipe tunnel at the Longhai Railway line through the Ninth Road in Xi ʻan, China, and performed numerical simulations of the field tests. The dynamic response of the soil and structure around the pipe-jacking tunnel were studied with trains passing at an oblique intersection of 26.5° through the top of the tunnel at different speeds. The study results are as follows.

(1) At different train speeds (30, 45, and 60 km/h), vertical deformation was observed in the soil above the tunnel. Deformation was larger at higher speeds; however, the increase was only 1.04% (less than 10%), indicating that train speed had minimal effect on soil deformation.

(2) For train speeds in the range of 30–60 km/h, the maximum deformation rate of the soil layer above the pipe-jacking axis was 0.41%, and the vertical displacement of soil gradually decreased along the horizontal direction away from the pipe-jacking structure. The maximum attenuation rate was 93.9% within a 20-m distance. The peak acceleration was less than the standard limit value, and soil deformation was within the allowable range.

(3) As the train speed increased from 30 to 60 km/h, the maximum tensile and compressive stresses increased at rates of 0.037% and 0.128%, respectively. The tensile stress was less than the limiting stress of the pipe-jacking structure, and therefore, the structure was in a safe-stress state. Furthermore, speed variations had a negligible effect on the stress of the pipe-jacking structure.

Data availability statement

The data supporting the findings of this study are available from the corresponding author upon request.

Author contributions

Conceptualization, G-JC; data curation, G-JC; formal analysis, G-JC; writing—original draft, J-SX; funding acquisition, Y-HS; project administration, XT; writing—review and editing, CM; supervision, XT; validation, CM. All authors contributed to the article and approved the submitted version.

Funding

The present work is subsidized and supported by the Science and Technology Innovation Team of Shaanxi Innovation Capability Support Plan (No. 2020TD005), the Science and Technology Development Program of Shaanxi Provincial Department of Housing and urban-rural construction (No. 2019-K39), and the Shaanxi Province Hanjiang-to weihe river valley water diversion Joint Fund (2021JLM-52). The authors gratefully acknowledge the financial support.

Acknowledgments

We would like to acknowledge Editage (https://www.editage.com/) for English language editing. The authors gratefully acknowledge the financial support.

Conflict of interest

Authors J-SX, YS, and CM were employed by China Railway 20th Bureau Group Corporation Limited, China Railway 20th Bureau Group First Engineering Co., Ltd., Hanjiang-to-Weihe River Valley Water Diversion Project Construction Co., Ltd.

The remaining authors declare that the research was conducted in the absence of any commercial or financial relationships that could be construed as a potential conflict of interest.

Publisher's note

References

Bao, D. L., Guangdi, W., Bo, G., and Bo, Z. (2011). Analysis of ground displacement response caused by high-speed train vibration. *J. Railw. Constr.* 4, 98–100.

CED (2013). *Allowable vibration standard for construction engineering*. Beijing: China Planning Press.

Chang, Y. (2017). *Study on the influence law of freight train vibration on tunnel basement surrounding rock*. Beijing: Beijing Jiaotong University.

Degrande, G., Clouteau, D., Othman, R., Arnst, M., Chebli, H., Klein, R., et al. (2006). A numerical model for ground-borne vibrations from underground railway traffic based on a periodic finite element-boundary element formulation. *J. Sound. Vib.* 293, 645–666. doi:10.1016/j.jsv.2005.12.023

Dewu, L., and Feng, G. (1997). *Field test and analysis of train vibration in Jinjiayan tunnel*. Lanzhou: Lanzhou Railway University, 7–11.

Fan, S., Song, Z., Zhang, Y., and Liu, N. (2020). Case study of the effect of rainfall infiltration on a tunnel underlying the roadbed slope with weak inter-layer. *KSCE J. Civ. Eng.* 24, 1607–1619. doi:10.1007/s12205-020-1165-0

Geohazard (2018). *Technical specification of ground deformation monitoring for geohazard*. Beijing: China Building Industry Press.

Huinan, L. (2022). *Study on soil stability during shield excavation and operation of tunnel in rich water stratum*. Jiangxi: East China Jiaotong University.

Huo, R., Zhou, P., Song, Z., Wang, J., Li, S., and Zhang, Y. (2019). Study on the settlement of large-span metro station's baseplate caused by the tunnels newly built beneath it. *Adv. Mech. Eng.* 11 (2), 168781401882516–13. doi:10.1177/1687814018825161

Kai, L. (2019). *Study on dynamic response of tunnel structure at early age under dynamic load of overhead railway*. Sichuan: Southwest Jiaotong University.

Lei, Z. (2019). *Rapid rail subway train load under the action of long-term settlement of soft soil foundation research*. Tianjin: Tianjin University. doi:10.27356/d.cnki.gtjdu.2019.004752

Li, H., Yang, G., Song, Z., Niu, Z., and Hao, K. (2019). Research on calculation method of soil layer deformation caused by rectangular pipe jacking. *Chin. J. Undergr. Space Eng.* 15 (05), 1482–1489.

Liang, B., Luo, H., and Sun, C. X. (2006). Simulation study on vibration load of high-speed railway. *J. China Railw. Soc.* 28, 89–94.

Lipeng, K. (2013). *Study on dynamic response characteristics and influence zone of cross tunnel under high-speed train load*. Changsha: Central South University.

Liu, N., Li, N., Wang, S., Li, G., and Song, Z. (2023). A fully coupled thermo-hydro-mechanical model for fractured rock masses in cold regions. *J. Cold Regions Sci. Technol.* 205, 103707. doi:10.1016/j.coldregions.2022.103707

Liu, N., Li, N., Xu, C., Song, Z., and Yang, M. (2020). Mechanism of secondary lining cracking and its simulation for the dugongling tunnel. *J. Rock Mech. Rock Eng.* 53 (10), 4539–4558. doi:10.1007/s00603-020-02183-3

Lun, G., Yu, Z., and Wenge, Q. (2008). Three-dimensional numerical analysis of vibration of underpass tunnel caused by train dynamic load. *J. Tunn. Technol.* 4, 23–27.

Niu, Z., Cheng, Y., Zhang, Y., Song, Z., Yang, G., and Li, H. (2020). A new method for predicting ground settlement induced by pipe jacking construction. *Math. Probl. Eng.* 2020 (2), 1–11. doi:10.1155/2020/1681347

Railway Bridges and Culverts (2005). *Code for design of reinforced concrete and prestressed concrete structures of railway Bridges and Culverts*. Beijing: China: Railway Publishing House.

Song, Z., Cheng, Y., Yang, T., Huo, R., Wang, J., and Liu, X. (2019a). Experimental study on the effect of osmotic pressure on pore structure evolution of limestone. *Rock Soil Mech* 40, 4607. doi:10.16285/j.rsm.2018.1831

Song, Z., Tian, X., and Zhang, Y. (2019b). A new modified Peck formula for predicting the surface settlement based on stochastic medium theory. *Adv. Civ. Eng.* 2019, 1, 14. doi:10.1155/2019/7328190

The Constructor (2010). *Code for design of concrete structures*. Beijing: China Architecture and Building Press.

Tieyun (2006). *Tieyun No.146. Railway line repair rules*. Beijing: China railway publishing house.

Wang, D., Luo, J., Wang, G., Li, F., and Su, J. (2022a). Dynamic response of the tunnel bottom structure considering groundwater influence under heavy-haul train loading. *Structures* 46, 1469–1479. doi:10.1016/j.istruc.2022.11.020

Wang, J., Zhou, P., Song, Z., Li, S., and Zhang, Q. (2022b). A new calculation method for tunneling-caused stratum settlement. *KSCE J. Civ. Eng.* 26 (6), 2624–2640. doi:10.1007/s12205-022-1258-z

Wenhua, Z., Baoning, H., and Yi, X. (2007). Test and analysis of pavement subgrade vibration of low embankment expressway under traffic load. *J. Highw. Eng.* 125, 113–117.

Xiancong, M., Xiedong, Z., Lin, W., Haojie, Z., and Zhifeng, L. (2022). Dynamic response analysis of sleeper and lining of double tunnel under the action of train. *J. Tunn. Technol.* 59, 99–106. doi:10.13807/j.cnki.mtt.2022.03.012

Xiangqiu, W., Linde, Y., and Wenhua, G. (2005). Vibration test and load simulation of high-speed train in railway tunnel. *J. Vib. Shock.* 03 (99–102). doi:10.13465/j.cnki.jvs.2005.03.029

Yufang, C. (2013). *Study on the influence of tunnel underpass construction and train vibration on settlement of high railway foundationStudy on influence law of tunnel tunneling and train vibration on settlement of high railway foundation*. Chengdu, China: Southwest Jiaotong University.

Yunfeng, W., Yang, C., and Yurui, L. (2022). Influence of subway train speed on vibration characteristics of stratum with reinforcement. *J. Technol. Eng.* 22, 9770–9796.

Zhou, P., Wang, J., Song, Z., Cao, Z., and Pei, Z. (2022). Construction method optimization for transfer section between cross passage and main tunnel of metro station. *Front. Earth Sci.* 10, 770888. doi:10.3389/feart.2022.770888

Zhu, Q., Zhang, F., Shao, Y., He, Y., and Qin, Z. (2020). Dynamic deformation and stress of large-diameter pipe jacking group and subgrade under Moving train. *J. Yangtze River Sci. Res. Inst.* 37, 96. doi:10.11988/ckyyb.20190815

frontiers | Frontiers in Earth Science

TYPE Original Research
PUBLISHED 21 July 2023
DOI 10.3389/feart.2023.1223419

OPEN ACCESS

EDITED BY
Naifei Liu,
Xi'an University of Architecture and Technology, China

REVIEWED BY
Yi Xue,
Xi'an University of Technology, China
Zhe Qin,
Shandong University of Science and Technology, China

*CORRESPONDENCE
Xiao Ding,
dx0402@xatu.edu.cn

RECEIVED 16 May 2023
ACCEPTED 13 June 2023
PUBLISHED 21 July 2023

CITATION
Ding X, Deng X, Zhang X and Wang R (2023), Surrounding rock pressure calculation based on time functions and stress release rate determination of deep soft rock tunnel: taking Zhonghe Tunnel as an example.
Front. Earth Sci. 11:1223419.
doi: 10.3389/feart.2023.1223419

Surrounding rock pressure calculation based on time functions and stress release rate determination of deep soft rock tunnel: taking Zhonghe Tunnel as an example

Xiao Ding[1,2]*, Xianghui Deng[1,2], Xuan Zhang[1,2] and Rui Wang[1,2]

[1]School of Civil and Architecture Engineering, Xi'an Technological University, Xi'an, Shannxi, China, [2]Xi'an Key Laboratory of Civil Engineering Testing and Destruction Analysis on Military-Civil Dual Use Technology, Xi'an, Shannxi, China

On the basis of the Zhonghe Tunnel project of the An-Lan Expressway, the objective of this study was to determine the appropriate method of calculating the steel arch load and stress release rate during numerical simulation. First of all, based on the monitoring results of six similar tunnel sections where the surrounding rock exerts pressure on the steel arch, using time functions, the rock pressure time history curve could be fitted, two formulas for calculating stable rock pressure in deep tunnels were compared, and the calculation model suitable for the Zhonghe Tunnel project was constructed. Then, a simulation of the Zhonghe Tunnel was performed using Flac3D, and stress release was simulated using the Mana method. By comparing the surrounding rock characteristic curves and the initial support characteristic curves under different stress release rates, the impact pattern of the stress release rate on the support load was summarized, and an appropriate excavation stress release rate was determined based on the stable rock pressure value calculation. It was found that the Zhonghe Tunnel rock pressure calculation model could better depict the change in rock pressure over time based on the empirical formula and Weibull time function. A prediction of the steel arch load of the Zhonghe Tunnel could be made using this method, and the stress release rate of the numerically simulated rock excavation was determined to be 0.5. This study thus provides a basis for the future internal force analysis and support parameter design of support systems.

KEYWORDS

deep tunnel, soft rock, surrounding rock pressure, time function, stress release rate

1 Introduction

The tunnel engineering industry plays a vital role in transportation. Recent years have seen tunnel engineering develop vigorously in China's vast engineering construction projects, which are leading to deeper, longer, and larger tunnels. In the case of deep soft rocks, analyzing the stress characteristics of supporting structures and the pressure distribution in surrounding rock plays a critical role in the safe construction and operation of tunnels.

TABLE 1 Results of surrounding rock pressure calculation compared.

Tunnel name	Depth (m)	Strata lithology and grade	Measured stability value (kPa)	Calculated value by platts formula (kPa)	Calculated value by empirical formula (kPa)
Daliangmao Tunnel ZK81+044	56	IV	75	84.69	146.56
Daliangmao Tunnel YK81+695	84	IV	56	84.69	146.56
Daliangmao Tunnel ZK81+412	85	IV	59	84.69	146.56
Shiaoding Tunnel (Tu, 2019)	144	IV	97	73.15	126.72
Anding Tunnel (Wang, 2016)	170	IV	108	104.91	123.84
Heizhuangping Tunnel (Zhou, 2022)	175	IV	90.3	77.28	142.39
Taoshuya Tunnel (Zhu, 2008)	187	IV	150	98.20	156.47
Qinfeng Tunnel (Li, 2021)	200	IV	77.47	113.69	173.92
Zaosheng No. 3 Tunnel (Ye et al., 2019)	220	IV	110	153.75	161.5
Minxian tunnel (Wang et al., 2021)	235	V	248	131.79	250.27
Liancheng Mountain Tunnel (Chen et al., 2020)	253	V	311	187.95	344.12
Yangjiaping Tunnel (Li et al., 2017)	350	IV	120	93.89	192.96
Liancheng Mountain Tunnel (Han et al., 2021)	450	IV	105	99.78	203.69
Baoligang Tunnel (Chen, 2022)	696	IV	128	94.62	149.04

During the early construction of a deep soft rock tunnel, the steel arch is the main structure supporting its weight. In support design, the load acting on the support is an essential parameter. To reasonably design and construct a tunnel support system, the surrounding rock pressure must be determined first (Sakurai, 1978). A rapid development of rock mechanics theory and practice has been achieved through the continuous efforts of researchers (Liu et al., 2020; Liu et al., 2022; Xue et al., 2023a; Xue et al., 2023b; Liu et al., 2023). At present, the field test, indoor model test, numerical simulation, and limit theory are among the main research methods for determining surrounding rock pressure (Lei et al., 2014). The Platts theory, Caquot formula, Terzaghi theory and formulas recommended in China's codes for railway and highway tunnels design are commonly used for calculating tunnel rock pressure (JTG 3370. 1-2018, 2018; Shen and Chen, 2015; TB 10003-2016, 2016). Noteworthily, in the complex and diverse environment of rock pressure, many theories have different conditions and scopes for application (Tong, 2020).

Many scholars have studied rock pressure evolution characteristics by means of field measurement and numerical simulation. Sakurai (1978) pointed out that rock pressure generally increases over time, and the change in the pressure is caused by the time-dependent changes in materials' mechanical properties and also by the advance of the tunnel working face. Three typical stages of surrounding rock pressure evolution were identified by Zhou et al. (2021): rapidly growing, decelerating, and basically stable. The measured data of Tian et al. (2022) showed that surrounding rock pressure evolved with time, and the construction stage would cause the fluctuation of its time history curve, which finally tended to a stable value. Liang et al. (2020) explored the overall distribution characteristics of pressure on rock tunnels by statistically analyzing 71 monitoring sections of 39 tunnels in the past 20 years. The authors believed that the tunnel surrounding rock pressure had an obvious time effect, and its time history curve mainly presented a three-stage feature of "rapid growth—slow growth—gradual stabilizing," which generally stabilized about 40 days following tunnel excavation.

In order to determine the tunnel rock pressure, a number of factors need to be considered: the depth of burial, the span, the length of the tunnel, and the formation mechanics (Tong, 2021). For this reason, a project similar to the Zhonghe Tunnel was selected by this paper for research. The three-step construction method was employed to build the six tunnels surrounded by grade IV (V) rock. It was buried about 200 m deep with a span of 12–15 m and a height-to-span ratio of about 0.80 (Zhu, 2008; Wang, 2016; Ye et al., 2019; Chen et al., 2020; Han et al., 2021; Wang et al., 2021). This study analyzed the rock pressure distribution of the selected tunnels, calculated the stable pressure value using the normative empirical formula and Platts formula, introduced the logistic and Weibull time functions to fit the time history curve of the measured wall rock pressure, and compared and determined a more suitable fitting formula. Then, the load distribution pattern of the initial support under different excavation stress release rates was simulated by

TABLE 2 Surrounding rock pressure and time fitting parameters.

Tunnel location and name	Excavation span (m)	Excavation height (m)	High-to-span ratio	Depth (m)	Strata lithology and grade	Excavation method	Measured stability value (kPa)	Calculated value by empirical formula (kPa)	Calculated value by platts formula (kPa)	Regression function	Correlation index R^2
Yuxi City, Anding Tunnel (Wang, 2016)	12.20	8.67	0.71	170	Mudstone (IV)	Three-step method	108	123.84	104.91	$P = 123.84 \times [1 - \frac{1}{(1+(t/0.7011)^{0.4858})}]$	0.8723
										$P = 123.84 \times (1 - e^{-0.8858t^{0.2314}})$	0.8522
Hanzhong City, Liancheng Mountain Tunnel (Chen et al., 2020)	15.78	12.00	0.76	253	Schist (V)	Three-step method	311	344.12	187.95	$P = 344.12 \times [1 - \frac{1}{(1+(t/0.1144)^{0.3419})}]$	0.9111
										$P = 344.12 \times (1 - e^{-1.1998t^{0.1555}})$	0.9094
Dingxi City, Minxian tunnel (Wang et al., 2021)	12.38	10.15	0.82	235	Slate (V)	Three-step method	247.5	250.27	131.79	$P = 250.27 \times [1 - \frac{1}{(1+(t/11.0429)^{1.6848})}]$	0.9944
										$P = 250.27 \times (1 - e^{-0.049t^{1.0816}})$	0.9861
Qingyang City, Zaosheng No.3 Tunnel (Ye et al., 2019)	15.00	13.00	0.87	220	Loess (IV)	Three-bench seven-step excavation method	110	161.5	153.75	$P = 161.5 \times [1 - \frac{1}{(1+(t/11.2267)^{1.3801})}]$	0.9962
										$P = 161.5 \times (1 - e^{-0.0522t^{1.0568}})$	0.9962
Chongqing City, Taoshuya Tunnel (Zhu, 2008)	12.18	9.59	0.79	187	Silty mudstone (IV)	Three-step method	150	156.47	98.20	—	0.9218
										$P = 156.47 \times (1 - e^{2.6963t^{-0.2484}})$	0.9722
Hanzhong City, Liancheng Mountain Tunnel (Han et al., 2021)	19.60	12.00	0.61	450	Schist (IV)	Three-step reserved core earth method	175	203.69	99.78	—	0.5559
										$P = 203.69 \times (1 - e^{3.9469t^{-0.5306}})$	0.9670

10.3389/feart.2023.1223419

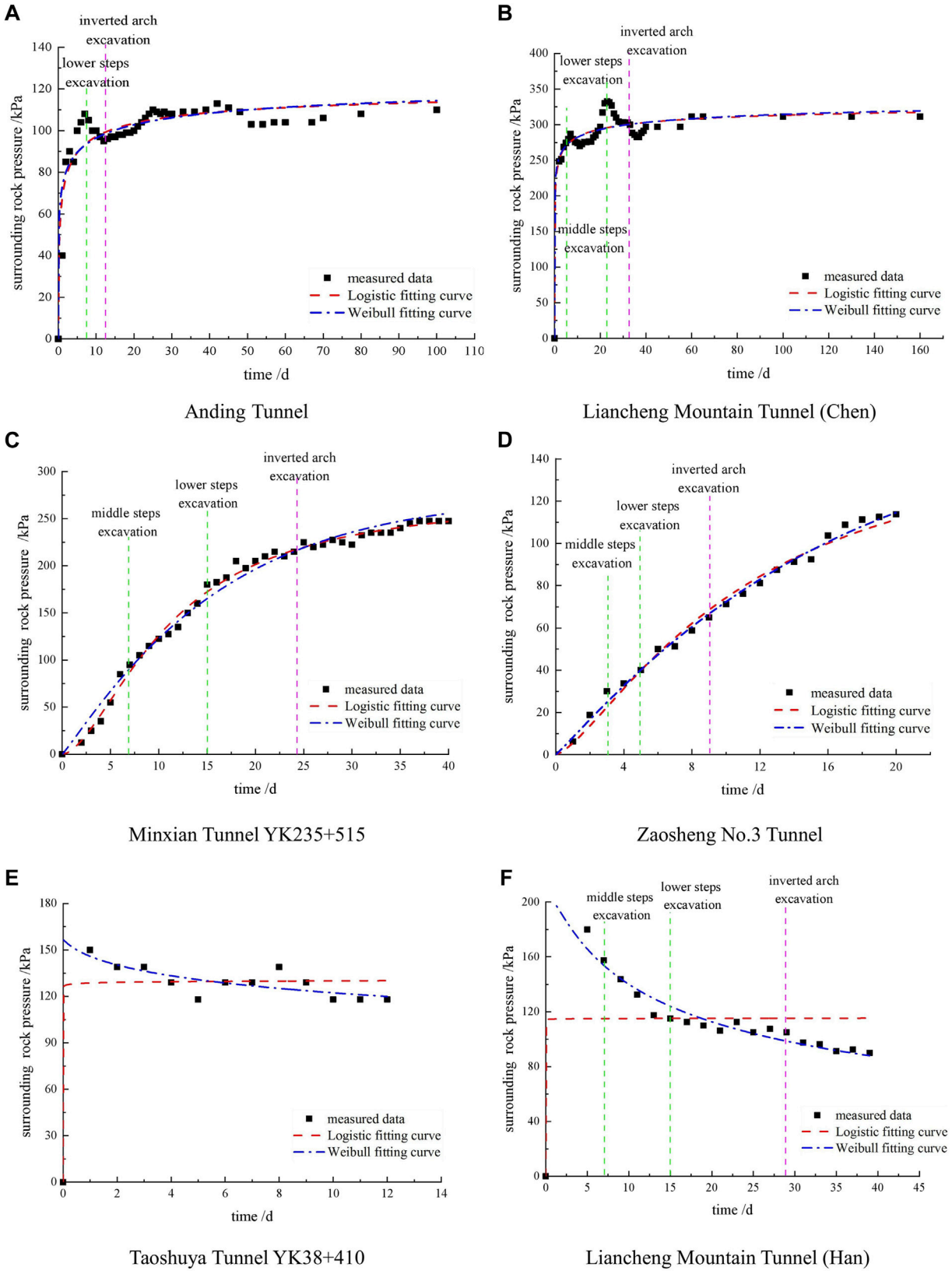

FIGURE 1
Time functions fitting curve of surrounding rock pressure.

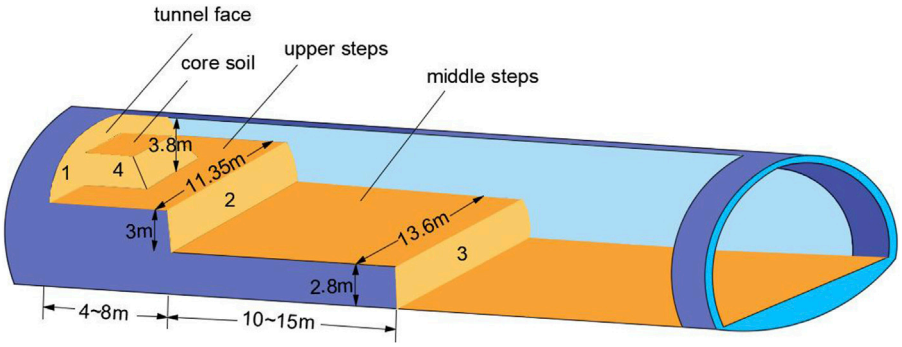

FIGURE 2
Schematic layout of the tunnel excavation with 3 steps.

Flac3D, and the stress release rate of the Zhonghe Tunnel was determined according to the theoretically calculated value, thus providing a basis for the subsequent internal force analysis and support parameter design of tunnel structures.

2 A time-based method of calculating surrounding rock pressure

2.1 A model for calculating the pressure around surrounding rocks

Time functions are a type of dimensionless function with time as the independent variable and the [0, 1] interval as the value range, controlling the curve shape and variation characteristics of the functions through relevant parameters (Dun et al., 2022). Once the research section has achieved stability, q can be used to represent the stability pressure value on tunnel rock, and $\varphi(t)$ is used to represent a time function; then, the rock pressure in tunnels at a given time t can be expressed by Eq. 1. It can be seen that q determines the convergence value of the pressure curve and has no direct effect on the curve's change trend.

$$q(t) = q \cdot \varphi(t) \tag{1}$$

The time function is often used to predict surface settlement. Common time functions include Knothe (Knothe, 1952), Sroka–Schober (Kwinta et al., 1996), normal distribution (Gonzalez-Nicieza et al., 2007), the Weibull model (Weibull, 1951), logistic model (Verhulst, 1838), and MMF model (Morgan et al., 1975). Among them, the logistic model can fully describe the occurrence, development, maturity, and stable growth process; Weibull models are widely used in many fields due to their ability to adapt to a variety of sample data types (Almalki and Nadarajah, 2014). Therefore, these two commonly used time functions were substituted into Eq. 1 to fit the measured data:

1. Logistic model:

$$\varphi(t) = \left[1 - \frac{1}{(1 + (t/x_0)^p)}\right] \tag{2}$$

where x_0 and p are influencing parameters related to geological mining conditions.

2. Weibull model:

$$\varphi(t) = \left(1 - e^{-at^h}\right) \tag{3}$$

where a and h are model parameters related to the properties of overlying rock and soil layers.

2.2 An analysis of surrounding rock pressure's stability value

The calculation formulas for the deep single-hole tunnel arch rock pressure are provided in the Highway Tunnel Design Code (JTG/, 2010; Gao et al., 2019) as follows:

1. Empirical formula:

$$q = \gamma h \tag{4}$$

where $h = 0.45 \times 2^{s-1}\omega$ is the equivalent height of the load; S, γ, and B represent the rock mass classifications, unit weight, and the excavation width maximum for tunnels, respectively; $\omega = 1 + i(B - 5)$ represents the factors affecting width. As B increases or decreases by 1 m, i is the increase–decrease rate of rock pressure in tunnel, and when B is less than 5 m, $i = 0.2$, while when B is greater than 5 m, $i = 0.1$.

2. Platts formula:

$$q = \gamma h_q \tag{5}$$

$$h_q = \frac{1}{2}\frac{B_m}{f_{kp}} \tag{6}$$

$$B_m = B_t + 2B_p \tag{7}$$

$$B_p = (H_t - H_0)\tan\left(45° - \frac{\varphi_c}{2}\right) \tag{8}$$

Specifically, $f_{kp} \approx (\frac{1}{12} \sim \frac{1}{15})R_b$ for hard rock; $f_{kp} \approx (\frac{1}{8} \sim \frac{1}{10})R_b$ for softer rock; $f_{kp} = \tan\varphi$ for loose soil or extremely broken rock; $f_{kp} = \frac{c}{R_b} + \tan\varphi$ for cohesive soil or loess.

TABLE 3 Parameters of the surrounding rock and the supporting structure.

Parameters	Surrounding rock	Steel frame	Feet-lock anchor pipe	Sprayed concrete	Cement mortar
Elastic modulus (GPa)	2.46	210	210	28	15
Poisson's ratio	0.31	0.25	0.3	0.17	0.13
Unit weight (kN/m^3)	21	78.5	76	24.5	19
Cohesion (MPa)	1.63	—	—	—	—
Internal friction angle (°)	43.2	—	—	—	—

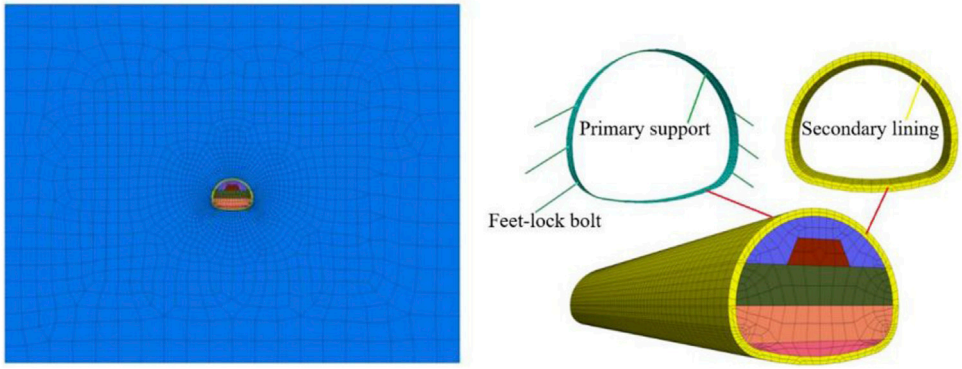

FIGURE 3
Numerical model of the Zhonghe tunnel.

TABLE 4 The contact surface parameters of the liner element.

Material	Normal stiffness (Pa/m)	Shear stiffness (Pa/m)	Tensile strength (MPa)	Cohesion (MPa)	Internal friction angle (°)
Contact surface	6.8×10^{10}	6.8×10^{10}	4×10^{6}	4×10^{6}	20

Among them, B_m, B_t, and B_p represent the span of the balance arch in the tunnel, spacing between tunnel excavation, and projected horizontal width of the fracture surface on each side, respectively; H_t and H_0 represent the tunnel excavation height and distance from the fracture surface to the wall foundation, respectively; φ_c and f_{kp} represent the computed friction angle and Platts firmness coefficient around the rock, respectively; R_b represents the rock mass' saturated strength in compression.

According to the Platts formula, rock pressure surrounding the tunnel is primarily determined by its span and height, its cohesion, and its internal friction angle. In empirical calculations, only the excavation span and rock grade are taken into account. There is no consideration of tunnel depth in the formulas above. The depth of tunnels and rock pressure are related in practical engineering.

Based on similar engineering profiles, measurements of surrounding rock pressure at the vault position were collected under conditions of grade IV (V) surrounding rock and step method construction. The constant value after section excavation and support was chosen as the stable rock pressure value. Using the above two formulas, the pressure value of surrounding rock can be determined and then compared to the measured stability value. As can be seen in Table 1, the rock pressure was statistically analyzed.

In Table 1, the measured rock pressure is compared with the theoretical calculation results. The result shows that the Platts' formula calculates rock pressure values that are smaller than the empirical formula calculations. In comparison with the surrounding rock's pressure stability value, the calculated value of the Platts formula is closer to the measured stability value with a smaller buried depth, and the calculated value of the empirical formula is more consistent with the measured stable value with greater buried depth.

2.3 Model assessment and selection

Six groups of surrounding rock pressure data from five tunnels were selected, and a summary of the tunnels' basic parameters can be found in Table 2. Firstly, the rock pressure value in comparison to

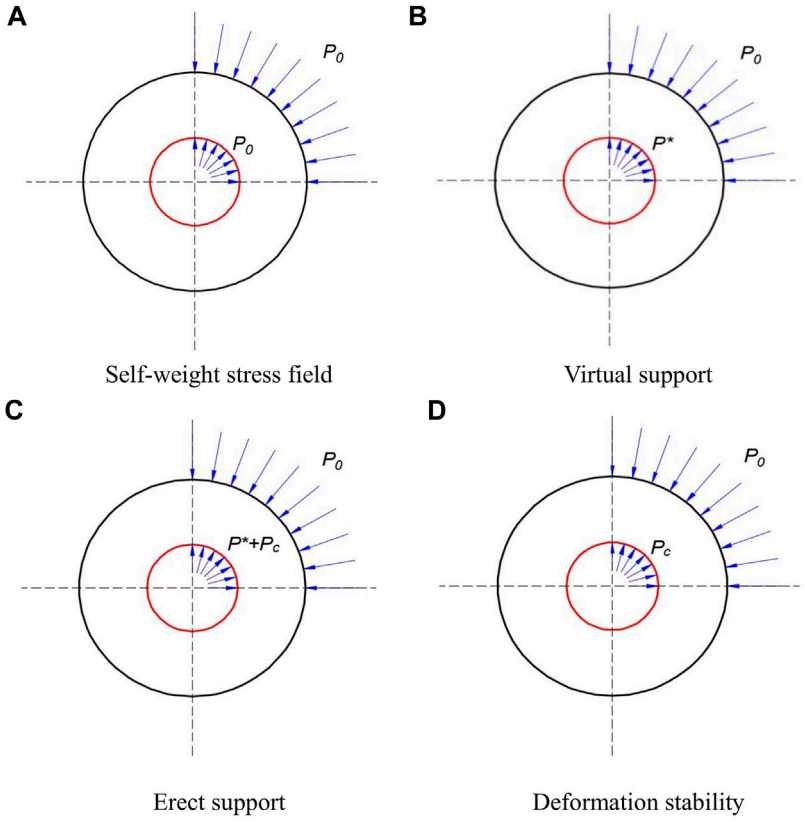

FIGURE 4
Simulation of the stress release process with the Mana method.

the measured value following stabilization was calculated, and an appropriate calculation formula for the convergence value of the pressure curve was selected. Then, time-dependent changes in rock pressure were fitted using two time functions. The fitting curves are shown in Figure 1.

Based on Table 1, the normative empirical formula produces a greater agreement between the measured and calculated rock pressure, so Eq. 4 was selected to calculate q in the model. As can be seen from Figure 1, pressure–time curves around surrounding rocks can be categorized into three types: the "steep increase—gentle" type (see Figures 1A, B), the "slow increase" type (see Figures 1C, D), and the "slow decrease" type (see Figures 1E, F). Both the logistic and Weibull models could well fit the first two types of surrounding rock pressure curves, while the third type (see Figures 1E, F) could only be fitted by the Weibull model; thus, the Weibull model has a wider scope of application. Consequently, Eq. 3 was selected for calculating $\varphi(t)$ in the model, namely, the model expression is Eq. 9. This model could predict the surrounding rock pressure of similar projects. For the Zhonghe Tunnel, displacement monitoring curves can indicate the type of rock pressure curve around a feature, and then the fitting parameters can be determined by selecting the tunnels with similar burial depth, span, and height–span ratio.

$$q(t) = \gamma h \cdot \left(1 - e^{-at^h}\right) \tag{9}$$

3 Determination of stress release rate

3.1 Project overview

The Zhonghe Tunnel is located near Yanba Town, Hanbin District, Ankang City, Shaanxi Province. It belongs to the fourth section of the An-Lan Expressway, passing through several mountains. The surrounding rocks are classified as grade IV and V. The tunnel burial depths are approximately 300 m, and end-wall entrances and exits are both present. The width of the excavation is 13.6 m, and the height of the excavation is 10.66 m. Excavations were conducted in three steps, with the upper step excavating at about 3.8 m high, the middle step at about 3 m, and the lower step at about 3.86 m. Specifically, the support for the lower step and the inverted arch were excavated at the same step, and the excavation schematic diagram is shown in Figure 2.

The mileage section between ZK20+620 and ZK20+820 of the grade IV rock surrounding the Zhonghe Tunnel on the left, with a burial depth of 170 m, was chosen as the object of research. Several mechanical properties were determined by uniaxial testing of the nearby rock (see Table 3). In this section, an I20a steel I-shape + concrete mortar spray layer with a thickness of 26 cm and 42 m feet-lock anchor pipe setting angle of 40° provide the initial lining of the surrounding rock.

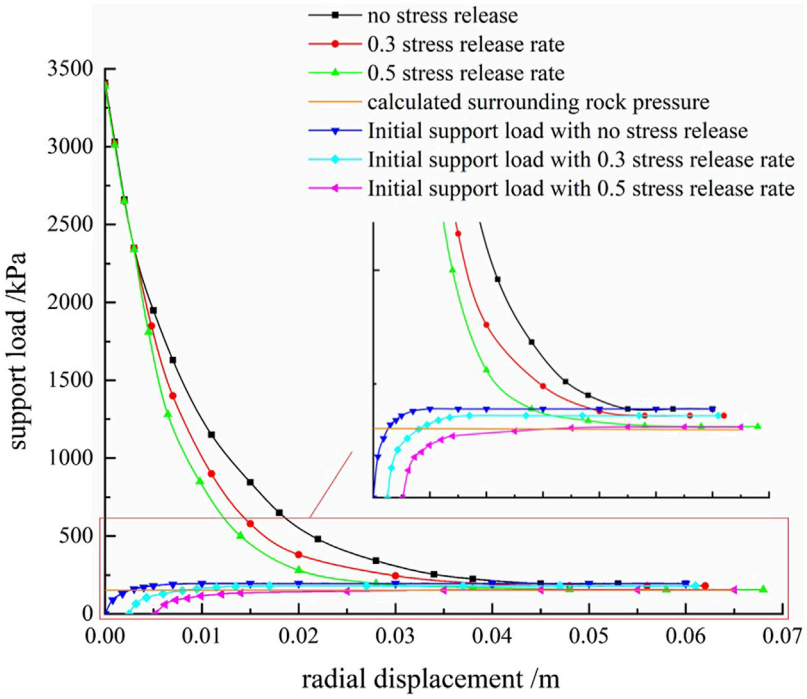

FIGURE 5
Characteristic curves of the surrounding rock and primary lining.

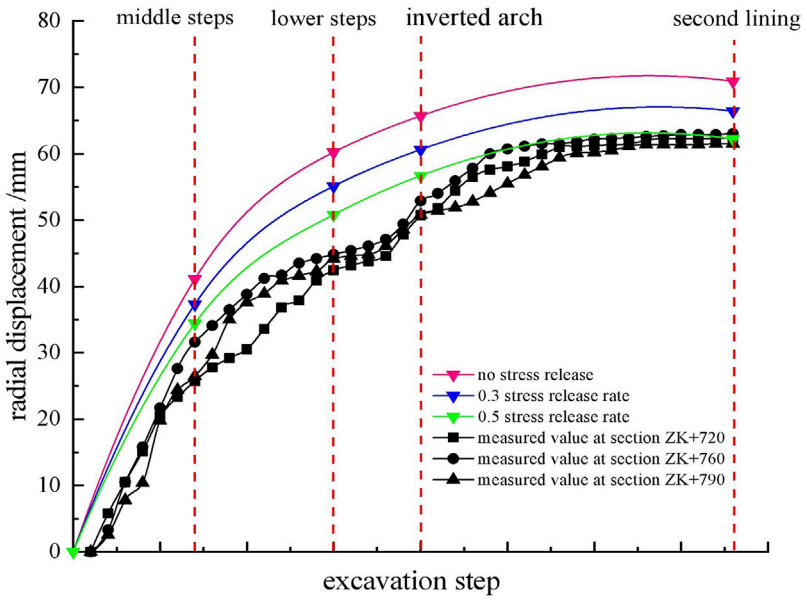

FIGURE 6
The comparison and verification of radial displacement of a steel arch roof.

3.2 Model establishment

The model was 120 m × 100 m × 60 m in size, as shown in Figure 3. It was constrained horizontally at the left and right edges and vertically at the bottom, and the vertical stress of 2.45×10^6 Pa was applied to the model's surface to simulate the self-weight of overlying rock and soil. Mohr–Coulomb was selected for the rock mass calculation model, the steel arch was simulated by using the beam element, the reinforcing mesh + shotcrete was simulated by the liner element, and the

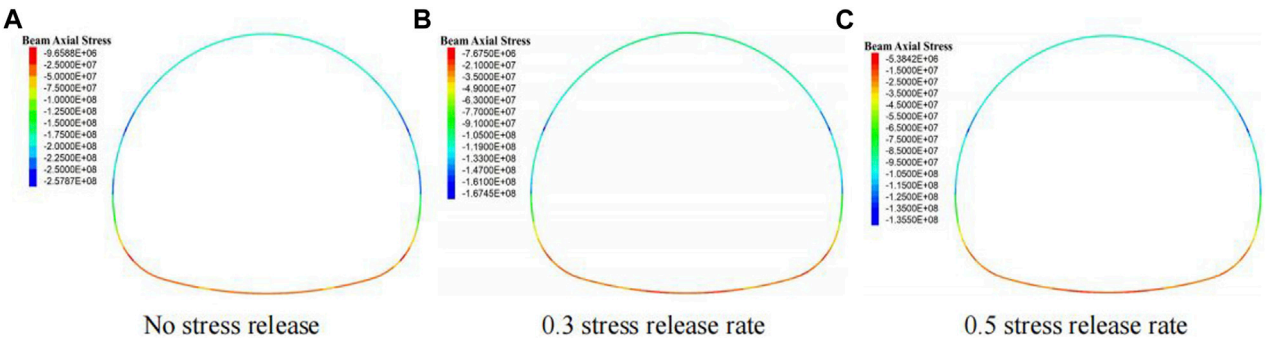

FIGURE 7
Axial stress distribution of steel arch under different stress release rates.

secondary lining was simulated by the solid element of the elastic constitutive model. Liner and rock contact surfaces would be generated automatically, which could simulate the shear slip, closed tension, and other interactions between the liner and rock. The normal spring was set between the liner element and the wall rock to simulate the separation and closure of the support. The pressure borne by the normal spring could be regarded as the force acting on the initial support by the wall rock. The numerical simulation parameters of the rock and the supporting structures can be found in Table 3, and the contact surface parameters of the liner element can be found in Table 4.

3.3 Data analysis and stress release rate determination

Using a reversed stress release method, the Mana method, this study simulated the stress release process (Abi et al., 2016), as shown in Figure 4, where P_0, P^*, and P_c represent the self-weight stress, virtual support effect, and stable support load of the primary reinforcement, respectively. Initially, the model's self-weight stress field was computed (see Figure 4A). Then, the tunnel was excavated, and the unbalanced force of the nodes around the tunnel was extracted to perform the stress release of the virtual support (see Figure 4B). Finally, the initial support was applied (see Figure 4C), the virtual support force was removed (see Figure 4D), and the preliminary support and wall rock interaction were calculated. With a stress release rate of 0.3, the virtual support force was set as 0.7 times the unbalanced force. All monitoring data were collected under one cycle footage. Figure 5 exhibits the characteristic curves of the wall rock and the primary reinforcement without considering the stress release and under different stress release rates. Figure 6 shows the comparison of the simulated and measured values of the vertical displacement of the steel arch roof without considering the stress release and under different stress release rates. Figure 7 shows the comparison of the axial stress of a steel arch under different stress release rates.

Figure 5 reveals that a steeper characteristic curve for surrounding rock occurs at greater stress release rates, indicating that the faster the rock stress release, the lower the final stress point. The support curves intersected with the wall rock characteristic curves at the same point, and the shapes of the initial support characteristic curves were the same under different stress release rates. The release rates increased as pressure on the initial support decreased. A load of 195 kPa was applied to the initial support without setting a stress release rate; a 0.3 stress release rate resulted in a 180 kPa support load, and a 0.5 stress release rate resulted in a 156 kPa support load, which is close to the rock pressure value of 152.24 kPa calculated by the empirical formula for highway tunnels, and this is the closest match between the vertical displacement of steel arch roofs and the measured value (see Figure 6). Therefore, the stress release rate of 0.5 should be selected for numerical simulation of the Zhonghe Tunnel.

Figure 7 illustrates the point: 1) By using the three-step method to excavate, the axial stress of the arch roof is larger, the lateral walls are smaller, and the invert is the smallest under different stress release rates. 2) There is a stress concentration at the joint point of the step arch feet caused by the step construction and anchor pipe application. 3) A comparison is made between the axial stress of the steel arch under the three stress release conditions. The arch axial stress of the arch roof is 178.44 MPa without stress release. At a 0.5 stress release rate, it decreases to 103.12 MPa, which is more economical and reasonable.

4 Conclusion

1. For deep soft rock tunnels, the monitoring data concerning surrounding rock pressure can be well fitted with time functions, of which the Weibull model is more applicable and can better simulate the time history curve of rock pressure with different trends around the rock.
2. A similar project's rock pressure was measured and statistically analyzed, and the proximity of rock pressure has been calculated using an empirical formula and Platt's formula as listed in the Highway Tunnel Design Code. The results show that the stable value calculated by the empirical formula matches the measured pressure more closely most of the time, thus verifying the suitability of using the normative empirical formula to estimate the rock pressure surrounding the Zhonghe Tunnel.
3. Simulating the stress release process of the surrounding rock excavation has been achieved using the Mana method. The

surrounding rock characteristic curves and support characteristic curves were drawn when the stress was released at different rates, and the effects of the stress release rate on the initial support load have been discussed. Finally, the stress release rate of the Zhonghe Tunnel has been determined according to the calculated pressure and verified by the vertical displacement of a steel arch roof, thereby shedding light on the reasonable load conditions for subsequent numerical simulations of supporting structures.

Data availability statement

The original contributions presented in the study are included in the article/Supplementary material, further inquiries can be directed to the corresponding author.

Author contributions

XoD: offered ideas and wrote the manuscript; XiD: revised the manuscript; XZ: analyzed the original data; RW: polished the article. All authors contributed to the article and approved the submitted version.

Funding

The research for this study was financially supported by the Science and Technology Planning Project of Shaanxi Province (2023-JC-YB-327), Shaanxi Provincial Department of Education service local special project (22JC040), and Qinchuangyuan Transportation Infrastructure Performance Perception and Intelligence Improvement "Scientists + Engineers" Team of Shaanxi Province.

Conflict of interest

The authors declare that the research was conducted in the absence of any commercial or financial relationships that could be construed as a potential conflict of interest.

Publisher's note

All claims expressed in this article are solely those of the authors and do not necessarily represent those of their affiliated organizations, or those of the publisher, the editors and the reviewers. Any product that may be evaluated in this article, or claim that may be made by its manufacturer, is not guaranteed or endorsed by the publisher.

References

Abi, E., Zheng, Y., Feng, X., and Xiang, Y. (2016). Study of the safety factor for tunnel stability considering the stress release effect. *Mod. Tunn. Tech.* 53 (2), 70–76. doi:10.13807/j.cnki.mtt.2016.02.010

Almalki, S. J., and Nadarajah, S. (2014). Modifications of the weibull distribution: A review. *Reliab. Eng. Syst. Saf.* 124, 32–55. doi:10.1016/j.ress.2013.11.010

Chen, J., Liu, W., Chen, L., Luo, Y., Wu, Y., and Shi, Z. (2020). *In-situ* experimental study on large-deformation control and reasonable support forms for a large-span highway tunnel in chlorite schist. *Chin. J. Highw. Transp.* 33 (12), 212–223. doi:10.19721/j.cnki.1001-7372.2020.12.017

Chen, Y. (2022). *Study on the constitutive model of carbonaceous slate and its application in tunnel engineering*. Sichuan: Xihua University. doi:10.27411/d.cnki.gscgc.2022.000428

Dun, Z., Wang, W., Zou, Y., Ren, L., Dun, Z., and Guo, W. (2022). Dynamic prediction of goaf surface subsidence and calculation of residual deformation based on time function combination model. *J. Chin. Coal. Soc.* 47 (S1), 13–28. doi:10.13225/j.cnki.jccs.2021.1583

Gao, H., He, P., Chen, Z., and Li, X. (2019). A novel calculation method of process load for extra-large section tunnels. *Symmetry* 11 (10), 1228. doi:10.3390/sym11101228

Gonzalez-Nicieza, C., Alvarez-Fernandez, M. I., Menendez-Diaz, A., and Alvarez-Vigil, A. E. (2007). The influence of time on subsidence in the central Asturian coalfield. *Bull. Eng. Geol. Environ.* 66 (3), 319–329. doi:10.1007/s10064-007-0085-2

Han, C., Zhang, T., Xu, C., and Xia, C. (2021). Research on the deformation characteristics of soft rock tunnel with large section and the deformation control with multilayer support. *Highw* 66 (01), 335–339.

JTG 3370. 1-2018 (2018). *Specifications for Design of highway tunnels JTG 3370 1-2018*. Beijing, China: People's Communications Press.

JTG/ (2010). *Guidelines for design of highway tunnel*. Beijing, China: China Communications Press. JTG/T D70-2010.

Knothe, S. (1952). Time influence on a formation of a subsidence surface. *Arch. Gómictwa i Hut. Kraków*, 1(1):1–3.

Kwinta, A., Hejmanowski, R., and Sorka, A. (1996). *A time function analysis used for the prediction subsidence. Proceeding of the Internation Symposium on Ming and Technology*. Xuzhou: Balkema, 419–424.

Lei, M., Peng, L., and Shi, C. (2014). Calculation of the surrounding rock pressure on a shallow buried tunnel using linear and nonlinear failure criteria. *Autom. Constr.* 37 (1), 191–195. doi:10.1016/j.autcon.2013.08.001

Li, L., Tan, Z., Guo, X., Wu, Y., and Luo, N. (2017). Large deformation of tunnels in steep dip strata of interbedding phyllite under high geostresses. *Chin. J. Rock. Eng.* 36 (07), 1611–1622. doi:10.13722/j.cnki.jrme.2016.1475

Li, S. (2021). *Study on cumulative damage law by blasting and stability of surrounding rock of large cross section tunnel*. Shijiazhuang: Tiedao University. doi:10.27334/d.cnki.gstdy.2021.000361

Liang, Q., Fang, J., and He, P. (2020). Analysis on tunnel surrounding rock pressure characteristics based on field measured statistics. *Chin. J. Undergr. Sp. Eng.* 16 (2), 555–566.

Liu, N., Li, N., Li, G., Song, Z., and Wang, S. (2022). Method for evaluating the equivalent thermal conductivity of a freezing rock mass containing systematic fractures. *Rock Mech. Rock Eng.* 55 (12), 7333–7355. doi:10.1007/s00603-022-03038-9

Liu, N., Li, N., Wang, S., Li, G., and Song, Z. (2023). A fully coupled thermo-hydro-mechanical model for fractured rock masses in cold regions. *Cold Reg. Sci. Technol.* 205, 103707. doi:10.1016/j.coldregions.2022.103707

Liu, N., Li, N., Xu, C., Li, G., and Yang, M. (2020). Mechanism of secondary lining cracking and its simulation for the dugongling tunnel. *Rock Mech. Rock Eng.* 53 (10), 4539–4558. doi:10.1007/s00603-020-02183-3

Morgan, P. H., Mercer, L. P., and Flodin, N. W. (1975). General model for nutritional responses of higher organisms. *Proc. Nat. Acad. Sci. USA.* 72 (11), 4327–4331. doi:10.1073/pnas.72.11.4327

Sakurai, S. (1978). Approximate time-dependent analysis of tunnel support structure considering progress of tunnel face. *Int. J. Num. Anal. Meth. Geomech.* 2, 159–175. doi:10.1002/nag.1610020205

Shen, R. M., and Chen, J. F. (2015). *Rock mass mechanics*. Shanghai: Tongji University Press.

TB 10003-2016 (2016). *Code for design of railway tunnel. TB 10003-2016*. Beijing, China: China Railway Publishing House.

Tian, X., Song, Z., Wang, H., Zhang, Y., and Wang, J. (2022). Evolution characteristics of the surrounding rock pressure and construction techniques: A case study from taoshuping tunnel. *Tunn. Undergr. Sp. Tech.* 125, 104522. doi:10.1016/j.tust.2022.104522

Tong, J. (2020). General formulas for calculating surrounding rock pressure of tunnels and underground spaces. *KSCE J. Civ. Eng.* 24 (4), 1348–1356. doi:10.1007/s12205-020-0943-z

Tong, J. (2021). Research on application of multi-factor surrounding rock pressure calculation theory in engineering. *KSCE J. Civ. Eng.* 25 (6), 2213–2224. doi:10.1007/s12205-021-0849-4

Tu, X. (2019). *Study on interaction mechanism and application of tunnel surrounding rock and supporting structure*. Nanchang: East China University of Technology.

Verhulst, P. F. (1838). Notice sur la loi que la population suit dans son accroissement. *Corresp. Mathématique Physique* 10, 113–121.

Wang, F., Guo, Z., Qiao, X., Fan, J., Li, W., Mi, M., et al. (2021). Large deformation mechanism of thin-layered carbonaceous slate and energy coupling support technology of npr anchor cable in minxian tunnel: A case study. *Tunn. Undergr. Sp. Tech.* 2021, 104151. doi:10.1016/j.tust.2021.104151

Wang, K. (2016). *Baoji-lanzhou high-speed railway Anding tunnel construction simulation and on-site monitoring and analysis* (USA: Lanzhou Jiaotong University). Master's Thesis.

Weibull, W. (1951). A statistical distribution function of wide applicability. *J. Appl. Mech.* 18 (3), 293–297. doi:10.1115/1.4010337

Xue, Y., Liu, J., Liang, X., Li, X., Wang, S., Ma, Z., et al. (2023b). Influence mechanism of brine-gas two-phase flow on sealing property of anisotropic caprock for hydrogen and carbon energy underground storage. *Int. J. hydrogen Energy* 48 (30), 11287–11302. doi:10.1016/j.ijhydene.2022.05.173

Xue, Y., Liu, S., Chai, J., Liu, J., Ranjith, P. G., Cai, C., et al. (2023a). Effect of water-cooling shock on fracture initiation and morphology of high-temperature granite: Application of hydraulic fracturing to enhanced geothermal systems. *Appl. Energy* 337, 120858. doi:10.1016/j.apenergy.2023.120858

Ye, W., Wu, Y., Chen, M., and Liu, J. (2019). Surrounding rock pressure distribution law and supporting structure stress characteristics of large cross-section paleosol tunnel: A case study of zaosheng No.3 tunnel on yinchuan-xi'an high-speed railway. *Tunn. Constr.* 39 (03), 355–361. doi:10.3973/j.issn.2096-4498.2019.03.003o

Zhou, F. (2022). *Study on over excavation control and stability of supporting structure of large section mud-sandstone tunnel*. Lanzhou: Jiaotong University. doi:10.27205/d.cnki.gltec.2022.001209

Zhou, Z., Chen, Z., He, C., and Kou, H. (2021). Investigation on the evolution characteristics and transfer mechanism of surrounding rock pressure for a hard-rock tunnel under high geo-stress: Case study on the erlang mountain tunnel, China. *Bull. Eng. Geol. Environ.* 80, 8339–8361. doi:10.1007/s10064-021-02439-4

Zhu, S. (2008). *Study on the stability of soft-weak surrounding rock and initial support in unsymmetrical loaded tunnels*. Chongqing, China: Chongqing university.

frontiers | Frontiers in Ecology and Evolution

TYPE Original Research
PUBLISHED 28 July 2023
DOI 10.3389/fevo.2023.1237250

OPEN ACCESS

EDITED BY
Naifei Liu,
Xi'an University of Architecture and Technology, China

REVIEWED BY
Xiao Wang,
Shandong University of Science and Technology, China
Hongbo Du,
Chongqing Jiaotong University, China

*CORRESPONDENCE
Yongqiang Zhou
yqzhou@whrsm.ac.cn

RECEIVED 09 June 2023
ACCEPTED 10 July 2023
PUBLISHED 28 July 2023

CITATION
Hu B, Xiao M, Fu X, Yang J, Xu C, Wu J and Zhou Y (2023) FDEM numerical study of the influence law of geostress on state and pressure of tunnel surrounding rock. *Front. Ecol. Evol.* 11:1237250. doi: 10.3389/fevo.2023.1237250

FDEM numerical study of the influence law of geostress on state and pressure of tunnel surrounding rock

Bo Hu[1,2], Mingqing Xiao[3,4], Xiaodong Fu[2,5], Jian Yang[3,4], Chen Xu[3,4], Jiaming Wu[3,4] and Yongqiang Zhou[2,5]*

[1]School of Civil Engineering, Chang'an University, Xi'an, China, [2]State Key Laboratory of Geomechanics and Geotechnical Engineering, Institute of Rock and Soil Mechanics, Chinese Academy of Sciences, Wuhan, China, [3]China Railway Siyuan Survey and Design Group Co., Ltd., Wuhan, China, [4]National & Local Joint Engineering Research Center Of Underwater Tunneling Technology, Wuhan, China, [5]School of Engineering Science, University of Chinese Academy of Sciences, Beijing, China

Surrounding rock pressure is a crucial parameter in tunnel engineering design, and its calculation is a classic challenge. The surrounding rock pressure is influenced by geostress, but existing calculation methods often do not take into account the effect of geostress. In this paper, finite discrete element method (FDEM) is used to study the design values of tunnel surrounding rock pressure under different geostress fields. Firstly, a set of calibration methods for input parameters of FDEM is summarized based on previous studies. Then, taking a high-speed railway tunnel in IV-level surrounding rock as an example, the excavation-induced failure process of the tunnel under the influence of gravity stress field and geostress field is simulated using the FDEM. By comparing the results with those of the finite element method simulation, the rationality of applying FDEM to the simulation of tunnel excavation is demonstrated. Next, a calculation method of surrounding rock pressure design value based on FDEM is proposed by introducing tunnel displacement criterion, and its validity is verified by comparing with the results of the theoretical formula. Finally, the surrounding rock pressure design values under different geostress are analyzed by using this calculation method. The results show that there are significant differences between the gravity stress field and the geostress field in the maximum principal stress distribution, failure zone form and crack distribution. The geostress directly influences the design value of surrounding rock pressure. As the geostress varies from 4MPa to 12MPa, the corresponding design value increases from 49KPa to 1,288KPa, illustrating a quadratic relationship between them. With the corresponding design support force, the displacement of the surrounding rock is controlled within a reasonable range, ensuring the stability of the tunnel is maintained.

KEYWORDS

FDEM, surrounding rock pressure, design value, state of surrounding rock, geostress

1 Introduction

The surrounding rock pressure is the foundation of tunnel design, construction and operation, and it is also the main factor affecting project costs (Ding et al., 2022; Keawsawasvong et al., 2022). The study of surrounding rock pressure has always been an important research subject in tunnel engineering and one of the most concerned problems in the engineering. However, due to the complexity of geological conditions, variations in construction methods, differing supporting parameters, and spatio-temporal effects, accurately determining the surrounding rock pressure is challenging (Wu et al., 2019; Liu et al., 2022; Zhang et al., 2022; Liu et al., 2023).

Various methods for calculating surrounding rock pressure are commonly used in practice. For example, (1) Q system and RMR system based on surrounding rock classification system comprehensively consider a variety of factors affecting surrounding rock pressure, and are mostly suitable for deep buried rock tunnels, but these methods have strong subjectivity in the value of calculation parameters (Lee et al., 2018). (2) Code for Design of Railway Tunnel (TB10003-2016) provides a formula for calculating surrounding rock pressure of deep-buried tunnels based on landslide statistics. However, this method does not consider the influence of burial depth. (3) The theoretical calculation methods of surrounding rock pressure based on circular tunnel, such as Caquot formula, Fenner formula (Cai, 2002) and Kastner formula (Cheng, 2012), etc., are mostly based on the research of deep buried circular tunnel, without considering the influence of surface load and boundary. In summary, most of the existing calculation methods of surrounding rock pressure have their limitations, and a universal method is needed.

Numerical simulation is a widely used research method in rock mechanics, which includes continuous and discontinuous methods. Many scholars have applied these two methods to study surrounding rock pressure and obtained fruitful results. For instance, the distribution law of surrounding rock pressure under different tunnel sections and different geological environments is studied by continuous method (Zhang et al., 2020; Ding et al., 2021; Qiu et al., 2022). The discontinuous method is used to investigate the influence of discontinuous conditions such as joints and faults on the surrounding rock pressure distribution, and some useful conclusions are obtained (Sun et al., 2018; Xue et al., 2019; Lee et al., 2021). However, the continuity requirement of the deformation equation limits the capability of the continuous method to deal with discontinuous materials such as rocks. Moreover, the discontinuous method has low calculation efficiency and high cost when analyzing actual projects (Liu et al., 2019; Liu et al., 2020). To overcome these limitations, scholar Munjiza proposed the finite discrete element method (FDEM), which combines the advantages of both methods and has shown promising results in simulating the crack initiation and propagation of rock-like brittle materials (Munjiza et al., 1995; Munjiza et al., 1999; Munjiza, 2004). The correctness and effectiveness of FDEM have been confirmed through laboratory and engineering scale simulations. FDEM has been widely applied in various fields including tunnel excavation (Lisjak et al., 2014; Lisjak et al., 2015a) and support (Lisjak et al., 2015b), surrounding rock reinforcement (Liu et al., 2019), slope stability analysis (Zhong et al., 2022), hydraulic fracturing (Yan and Zheng, 2017a; Yan and Zheng, 2017b), rock fracture acoustic emission (Lisjak et al., 2013; Zhao et al., 2015), complex rock block modeling (Yan et al., 2015), uniaxial compression (An et al., 2022), triaxial compression (Song et al., 2022), Brazilian splitting (Zhang et al., 2021), direct shear test (Min et al., 2020), rock thermal failure (Yan and Zheng, 2017c) and blasting failure (Trivino and Mohanty, 2015). However, the application of FDEM in studying surrounding rock pressure is still limited.

Geostress is the original force existing in the rock mass in nature, and also the fundamental force leading to the deformation and failure of underground engineering, which determines the basic mechanical properties of geotechnical mass (Zhang et al., 2018). It is necessary to analyze the stress state of surrounding rock and its influence on the stability of surrounding rock. At the same time, the study of the influence law of geostress on tunnel surrounding rock pressure can provide reference for improving the tunnel support method and analyzing the mechanism of surrounding rock pressure. FDEM has been utilized to investigate the internal force distribution and failure of the surrounding rock after tunnel excavation under different stress states (Han et al., 2021; Deng et al., 2022). However, there are few researchers who have used FDEM to conduct research on the influence of geostress on the surrounding rock pressure design value.

Therefore, based on the FDEM, this paper puts forward the idea of using the surrounding rock pressure design value as the design supporting force to solve the problem that the actual surrounding rock pressure is difficult to determine. Based on the correct calibration of the calculation parameters of FDEM, the excavation failure process of high-speed railway tunnel in IV-level surrounding rock is simulated under the gravity stress field and geostress field. And a method for calculating the surrounding rock pressure design value based on FDEM is proposed by introducing the tunnel displacement criterion, and its validity is verified. Finally, this method is used to analyze the surrounding rock pressure design value under different geostress. This study can provide theoretical basis for the design and construction of tunnel engineering.

2 The fundamentals of FDEM

FDEM discretizes the material into triangular elements of constant strain and incorporates 0-thickness quadrilateral joint elements as bonding agents along the common sides of adjacent triangles (Figure 1). Assuming that the triangular element is always in an elastic strain state without fracture, deformation stress is calculated via the generalized Hooke's law. Plastic deformation and fracture of the material are determined by the tensile and shear displacements of the joint element. Upon reaching the corresponding limit values, the joint element fails and generates a micro-crack, while the triangular elements on both sides of the joint element transition from a bonding to a contact state. The principle of FDEM is as follows (Munjiza, 2004).

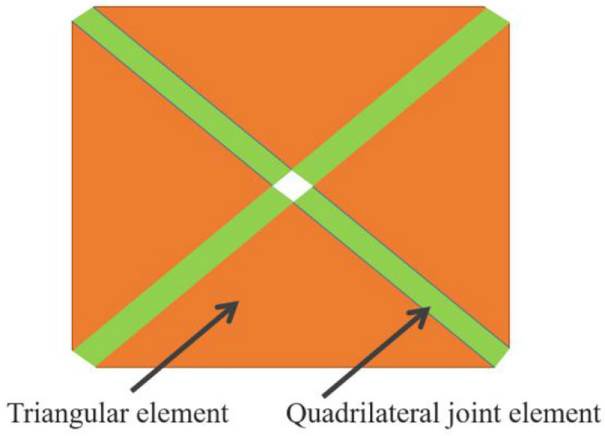

FIGURE 1
Meshing principle of FDEM.

2.1 Dynamical equation of FDEM

The dynamic equation of FDEM is solved by applying Newton's second law, and the equation for the nodes is solved using the Euler method:

$$M\ddot{x} + C\dot{x} = F(x) \tag{1}$$

where, M is the mass matrix of all element nodes in the system. $F(x)$ represents the unbalanced force vector of nodes. The damping matrix C is introduced in order to consume the kinetic energy of the system. According to Formula (1), coordinates and velocities of nodes of triangular elements in each time step are calculated by central difference method, and the formula is as follows:

$$v_i^{(t+\Delta t)} = v_i^t + \sum F_i^{(t)} \frac{\Delta t}{m_n} \tag{2}$$

$$x_i^{(t+\Delta t)} = x_i^{(t)} + v_i^{(t)} \Delta t \tag{3}$$

where, $F_i^{(t)}$ represents the total node force, Δt is the time step, and m_n is the mass of the node, which is one third of the mass of the element.

2.2 Contact stress of triangular element

Under external loading, contact between triangular elements will occur, resulting in the generation of contact forces. FDEM utilizes a contact force calculation method based on potential, which facilitates the treatment of point-to-point contact problems. The contact stress of the triangle is influenced by both the contact penalty value and the area and shape of the triangles in contact, as illustrated in Figure 2. The formula for calculating contact stress using this method is as follows:

$$f_c = P_n \oint_{\Gamma_{\beta_t \cap \beta_c}} n_\Gamma (\varphi_c - \varphi_t) d\Gamma \tag{4}$$

where P_n denotes the normal contact penalty value, $\Gamma_{\beta_t \cap \beta_c}$ represents the boundary of the overlapping region between active element β_c and passive element β_t, while φ_c and φ_t respectively represent the potential of the two elements. Additionally, n_Γ represents the outer normal vector of the overlapping region boundary.

2.3 Stress of triangular element

In FDEM, the strain and stress of the triangular elements are computed using the finite element method. As the triangular constant strain element is employed, stresses within the element remain uniform. Once the stress T of the deformed triangular element is calculated, the equivalent nodal force vector resulting from the element deformation on each side of the triangular element can be determined using the following formula:

$$f_n = \frac{1}{2} Tnl = \frac{1}{2} \begin{pmatrix} \sigma_{xx} & \sigma_{xy} \\ \sigma_{yx} & \sigma_{yy} \end{pmatrix} \begin{pmatrix} n_x \\ n_y \end{pmatrix} l \tag{5}$$

where n is the outer normal unit vector of the edge of the triangular element, l is the side length of the edge of the element, and 1/2 means to distribute the force equally between the two nodes of the edge.

2.4 Stress of joint element

The quadrilateral joint element is capable of withstanding compressive, tensile, and shear stresses. When the joint is subjected to stretching, compression, or sliding, normal and tangential stresses will arise in the joint element. The stress value is solely dependent on the relative tensile distance o, slip distance s,

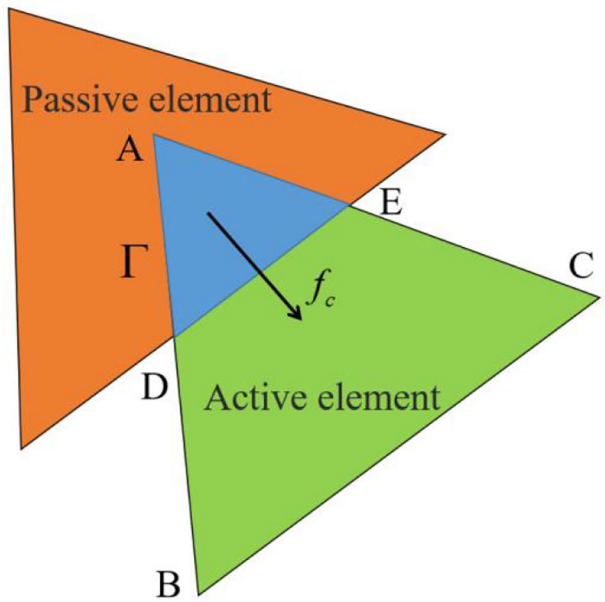

FIGURE 2
Contact between active element and passive element. Capital letters indicate different contact relationships.

joint penalty value P_f, tensile strength f_t, and shear strength f_s, as depicted in Figure 3. The specific calculation formula is as follows:

(1) In the unyielding state:

$$\sigma = \frac{o}{o_p} f_t,\ o < o_p \tag{6}$$

$$\tau = \frac{|s|}{s_p} f_s,\ |s| < s_p \tag{7}$$

where, σ is the normal stress; τ is shear stress; o_p and s_p are joint tensile and slip amounts at peak stress respectively, specifically, $o_p = hf_t/P_f$, $s_p = hf_s/P_f$, and h is the minimum size of the element.

(2) In the yield state:

$$\sigma = f(D) f_t,\ o > o_p \tag{8}$$

$$\tau = f(D) f_s,\ |s| > s_p \tag{9}$$

in the formula, D is the loss factor and $f(D)$ is the softening coefficient of the material. The relevant value and calculation method are relatively complex, and the specific content can be found in the relevant literature (Yan and Zheng, 2017a).

3 The numerical model

3.1 Engineering context

Wufeng Tunnel is a high-speed railway tunnel with a designed speed of 350km per hour. The length of the left line of the tunnel is 15471m, and the tunnel body mainly passes through Silurian shale and silty sandstone (Figure 4). And the surrounding rock of the left line of the tunnel is mainly IV-level. The lithology of the stratum in which the tunnel is situated is intricate and varied. The tectogenesis of the stratum is also evidently dynamic, while the engineering geological conditions are relatively complex. The construction process may encounter geological issues such as rockfalls and large deformation of soft rock. Furthermore, the mountainous terrain is characterized by substantial undulations, and the burial depth of the tunnel varies significantly, resulting in a complicated geostress environment for the tunnel. Therefore, it is essential to factor in the influence of geostress factors when devising the tunnel's design and construction plan.

3.2 FDEM calculation model of tunnel excavation

A high-speed railway tunnel model with a design speed of 350km/h and a buried depth of 200m in the IV-level surrounding rock is established, as shown in Figure 5. The model size is 135m×160m (width × height), in which the tunnel span is 14.7m and the tunnel section height is 12.23m. The distance between tunnel and model boundary is 5 times the span of tunnel, which is sufficient to eliminate the influence of boundary conditions on model excavation. To reduce the scale of the model and accelerate numerical calculation, the stress boundary was applied on the top surface of the model, making the equivalent buried depth of the tunnel equal to 200m. At the same time, the side of the model is set

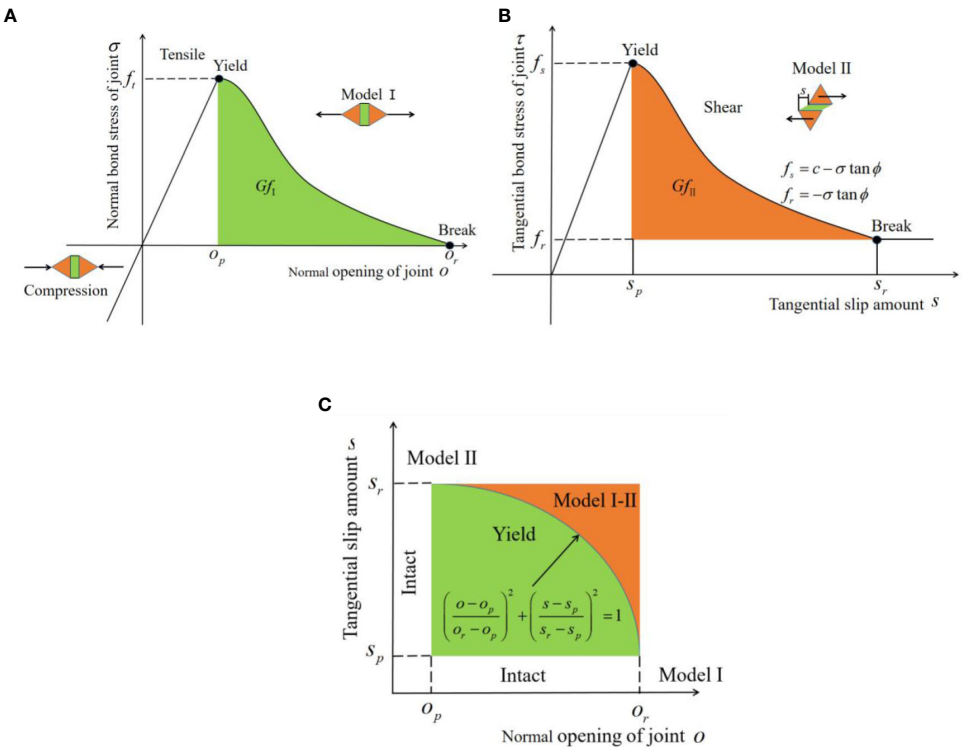

FIGURE 3
Failure mode of joint element. **(A)** Tensile failure. **(B)** Shear failure. **(C)** Tensile-shear mixed failure.

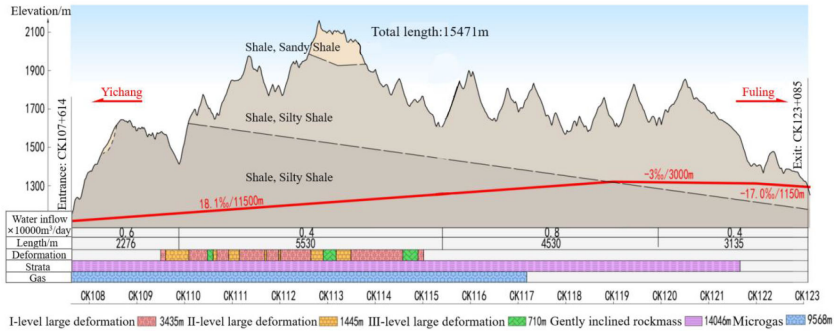

FIGURE 4
Geological profile.

as the normal displacement constraint boundary, and the bottom surface is set as the full constraint boundary. Tunnel excavation is simplified to the excavation of the whole section at one time. In order to improve the accuracy of the calculation results, mesh refinement was carried out around the excavation section of the tunnel. The mesh size h around the tunnel was set at 0.25m, and h gradually increased to 2.5m from the refinement area to the boundary. Surrounding rock and tunnel were divided by Delaunay triangle with 24,452 nodes and 49,494 elements.

3.3 Mechanical parameters

This study primarily focuses on the IV-level surrounding rock. According to the relevant engineering practice, the rock mass is assumed to be a continuous uniform medium. To ensure the research results are widely applicable, this paper refers to the value range of mechanical parameters of surrounding rock provided by Code for Design of Railway Tunnel (TB10003-2016), and utilizes the lower one-third of the value range. Specific mechanical parameters are shown in Table 1.

3.4 Parameter calibration

Before using FDEM to simulate tunnel excavation, it is necessary to calibrate the calculation parameters. Previous studies pointed out that parameter calibration can be conducted by comparing the results of numerical simulation with those of laboratory uniaxial compression and Brazilian splitting test (Tatone and Grasselli, 2015). When the failure mode, strength value, elastic modulus, Poisson's ratio and stress-strain curve obtained by simulation are consistent with those obtained by laboratory test or the deviation is within a certain range, It is deemed that this set of input parameters used in the simulation is reasonable. At the same time, this also implies that the final parameter calibration results are not unique, allowing the relevant parameters to have a range of adjustment, within which the simulation results and laboratory results can be well consistent.

The calculation parameters of FDEM can be divided into four categories: (1) calculation control parameters, such as calculation time step Δt; (2) triangle element parameters, including elastic modulus E, Poisson's ratio v, material density ρ; (3) Parameters of quadrilateral joint elements, including cohesive force c, internal friction angle φ,

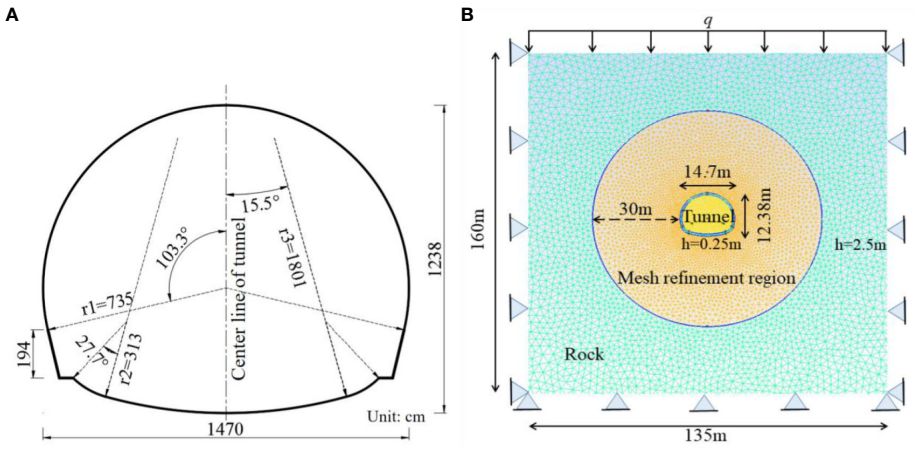

FIGURE 5
FDEM model. **(A)** Tunnel section. **(B)** Schematic diagram of the model.

TABLE 1 Values of mechanical parameters of surrounding rock.

	Level of surrounding rock	Volumetric weight (kN/m^3)	Elastic Modulus (GPa)	Poisson ratio	Internal friction angle (°)	Cohesive force (MPa)
Code	IV	20~23	1.3~6	0.3~0.35	27~39	0.2~0.7
Model	IV	21.00	2.87	0.317	31.00	0.367

tensile strength f_t, Mode I fracture energy G_{I} and Mode II fracture energy G_{II}; (4) Contact parameters of triangular element, including normal contact penalty P_n, tangential contact penalty P_t and fracture penalty P_f. Among these parameters, the macroscopic parameters (such as elastic modulus E, Poisson's ratio ν, density ρ, cohesive force c, internal friction angle φ, and tensile strength f_t) directly utilize values obtained from laboratory tests (Liu et al., 2019; Deng et al., 2022). The contact parameters define the contact stiffness between finite elements and control the limit distance of embeddedness and slip between elements. By setting a high penalty value, the tip deformation of joint elements and relative displacement between contact pairs can be effectively reduced, thereby improving the calculation accuracy. However, to ensure calculation stability, a small-time step should be selected, which will increase the computational workload dramatically. It has been founded that when P_n and P_t are set to 1 times the elastic modulus, and P_f is set to 100 times the elastic modulus, a good balance between calculation accuracy and cost can be achieved, and the simulation results can be ideally obtained (Yan et al., 2021; Wang et al., 2022). Based on the above parameters, the values of fracture energy G_{I} and G_{II} are adjusted constantly, and the simulation results are compared with the laboratory and theoretical results. Finally, the input parameters of the tunnel model are determined as shown in Table 2. The numerical model is calculated using MultiFracS, which is a FDEM software developed by Chengzeng Yan (Yan et al., 2021).

4 Failure process of tunnel after excavation

4.1 Failure process of tunnel after excavation under gravity stress field

4.1.1 Distribution of maximum principal stress

After the excavation of the tunnel, the maximum principal stress of surrounding rock is approximately symmetrical, and the maximum value appears at the vault, inflected arch and side wall. Figure 6A illustrates the distribution of the maximum principal stress of the model after geostress equilibrium. As a whole, the tunnel model is under pressure, and the maximum principal stress is approximately linear along the depth direction. After tunnel excavation, the surrounding rock is affected by excavation unloading effect, and the value of the maximum principal stress around the excavated section is greatly reduced, as shown in Figure 6B. The far end of the excavated section is less affected, and the maximum principal stress does not change. With the continuous action of the excavation disturbance, the stress disturbance area radiates annular from the excavation section. And the stress above and below the tunnel excavation section is symmetrical, as is the stress on the left and right sides, as shown in Figure 6C. At the 20,000th time step after tunnel excavation, the surrounding rock reaches the strength limit, and a crack germinates from the arch foot of the tunnel section. Meanwhile, the crack propagation in turn affects the distribution of the maximum principal stress, resulting in the stress concentration near the crack tip. The stress concentration phenomenon will induce the crack to continue to develop, so that the crack continues to expand to the deep of the rock mass (Figure 6D), and the location of the maximum principal stress concentration also moves to the deep of the rock mass simultaneously. Finally, the model is calculated to be convergent, cracks fully develop and expand, large deformation occurs on both sides of the spandrel, collapse happens at the vault, slight uplift occurs in the inflected arch, and tension areas are formed in the vault and inflected arch (Figure 6E). At this time, the maximum principal stress distribution tends to be stable, and the maximum principal stress is still symmetrically distributed about the center line of tunnel with the phenomenon of stress concentration.

4.1.2 Analysis of deformation process of surrounding rock after excavation

After excavation, the stress of rock mass in the tunnel is released, and the radial compressive stress provided by the rock

TABLE 2 Calculation parameters of the tunnel model.

Parameter	Value	Parameter	Value
Density (kg/m^3)	2,100	Mode I fracture energy (J/m^2)	325
Elastic modulus (GPa)	2.87	Mode II fracture energy (J/m^2)	1,250
Poisson's ratio	0.317	Fracture penalty (GPa)	287
Internal friction angle (°)	31	Normal contact penalty (GPa)	2.87
Cohesive force (MPa)	0.367	Tangential contact penalty (GPa/m)	2.87
Tensile strength (MPa)	0.4	Time step size (s)	2×10^{-6}

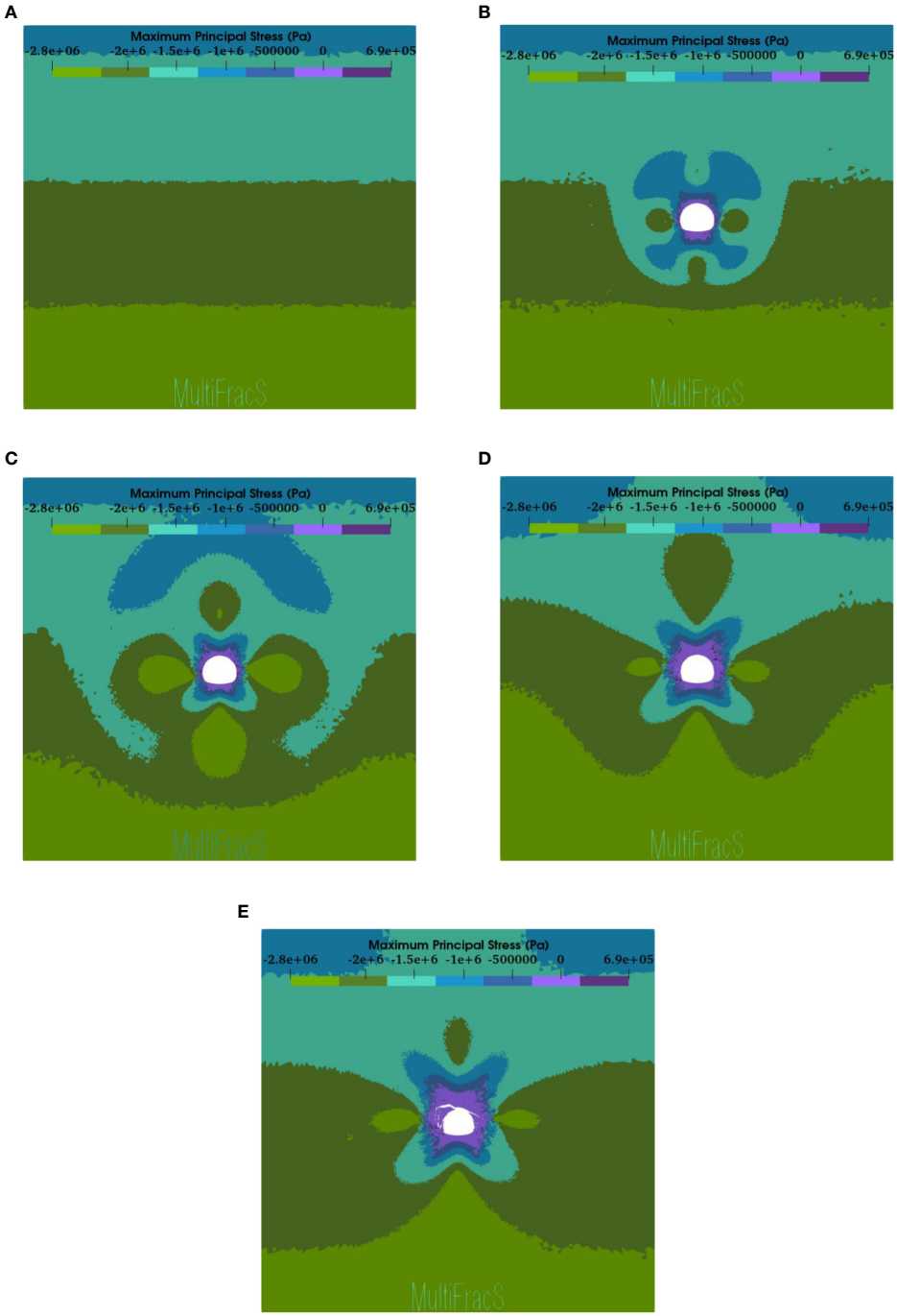

FIGURE 6
Nephogram of maximum principal stress of tunnel after excavation under gravity stress field. **(A)** Geostress equilibrium. **(B)** 10,000 time steps. **(C)** 20,000 time steps. **(D)** 110,000 time steps. **(E)** 300,000 time steps.

mass in the cavern disappears, resulting in the surrounding rock to transition from a state of two-direction compressive stress to unidirectional compressive stress. And the stress borne by the rock mass in the cavern is transferred to the surrounding rock, causing the increase of tangential stress in the surrounding rock. In essence, tunnel excavation is a process in which tangential pressure of surrounding rock increases and radial pressure decreases. The surrounding rock breaks when the tangential stress exceeds the compressive strength corresponding to the radial stress. During the failure process after excavation, cracks and spalling occur on both sides of the side wall first, the fracture zone develops along the radial direction, and cracks extend and develop on both sides of the cavern (Figure 7A). Subsequently, the cracks continued to grow at the spandrel and intersected at the vault, resulting in settlement deformation of the vault with significant collapse (Figure 7B). Eventually, the surrounding rock breaks and expands, and the rock mass moves toward the center of the cavern, causing the deformation of the tunnel section and the reduction of the area.

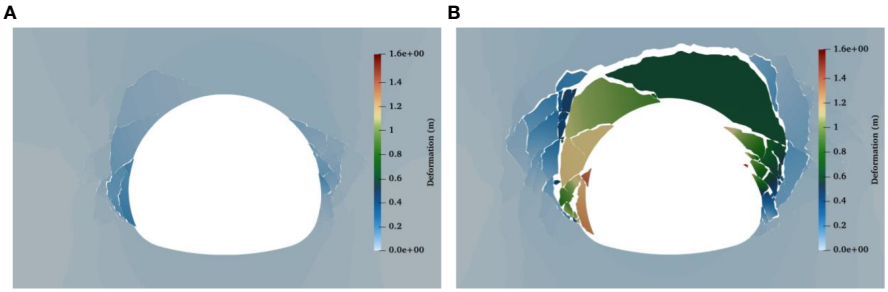

FIGURE 7
Deformation process of surrounding rock after excavation. **(A)** Radial convergent deformation of both side walls. **(B)** Large spandrel deformation and vault collapse.

4.1.3 Analysis of crack propagation process in surrounding rock

When the tunnel face was excavated, stress concentration occurred at the arch foot of the tunnel, and the crack was first generated at this position (Figure 8A). With the advance of tunnel excavation time, the stress concentration near both sides of the side wall intensifies, and the crack continues to expand to the deeper rock mass until the concentrated stress at the crack tip reaches the ultimate equilibrium state. As the whole surrounding rock is in a state of compression, the vertical geostress is much greater than the horizontal geostress, which makes the cracks mainly expand at the side wall, and the cracks are mainly tensile-shear mixed crack (Figure 9), showing a conjugate cross distribution (Figure 8B). After the shear crack has fully extended, the rock mass on both sides of the side wall gradually loosens and falls off, converging and deforming into the cavern. The broken rock blocks extrude each other, causing them to overturn into the cavern. This results in a decrease in stress in the fracture zone, forming a local tensile stress zone. Subsequently, cracks on both sides of the side wall gradually extended to the vault and intersected, causing the vault to collapse (Figure 8C). After tunnel excavation, the failure zone is mainly distributed in the spandrel, taking on an inverted V shape. Tensile cracks are the primary cracks in the shallow part of the surrounding rock, while shear cracks are the primary cracks in the deep. The conjugate shear angle gradually decreases and annihilates in the deep part.

4.1.4 Comparison of simulation results of FDEM and finite element method

The finite element model with the same mechanical parameters and geometric dimensions as the FDEM model is established to analyze the tunnel stability, in which the surrounding rock adopts the Mohr-Coulomb constitutive model. The plastic zone distribution after tunnel excavation was calculated, and the specific simulation results are presented in Figure 10. By comparing the plastic zone and fracture zone calculated by both methods, it can be observed that the failure location and degree are

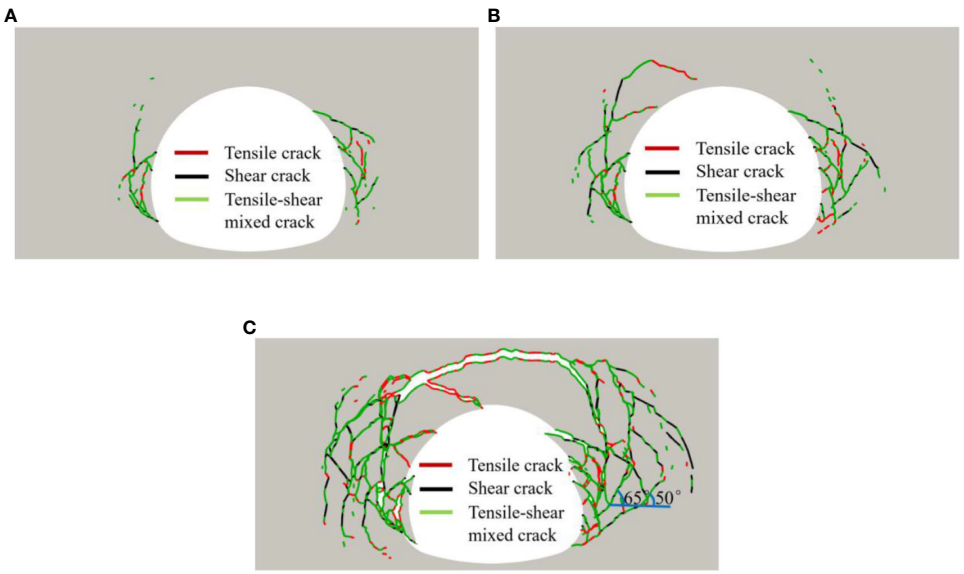

FIGURE 8
Crack propagation process of surrounding rock after excavation under gravity stress field. **(A)** 30,000 time steps. **(B)** 90,000 time steps. **(C)** 300,000 time steps.

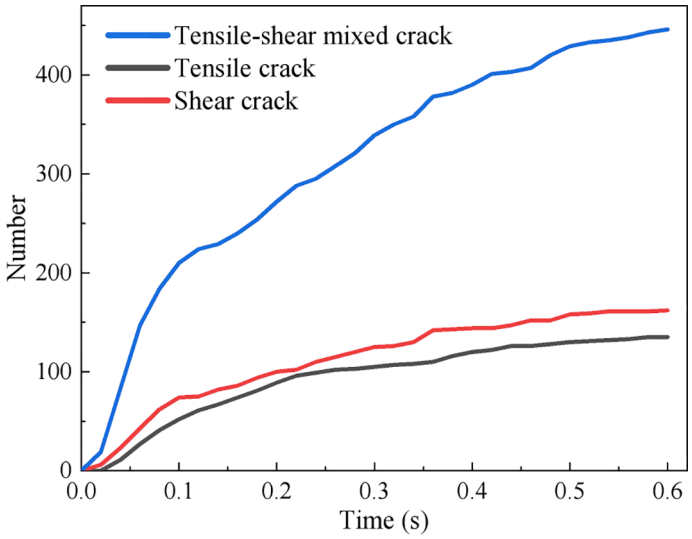

FIGURE 9
Variation of the number of cracks in surrounding rock after tunnel excavation under gravity stress field.

essentially identical, and the contours of the failure area are in good agreement. This verifies the validity and rationality of FDEM for tunnel stability analysis. Moreover, FDEM successfully simulates the gradual transformation process of the surrounding rock from continuous to discontinuous under the influence of excavation unloading effect. It also reproduces the process of crack germination, propagation, and collapse in the process of tunnel surrounding rock failure after excavation, which is more consistent with the failure mode of tunnel surrounding rock as a discontinuous medium. The simulation results are more realistic, intuitive, and consistent with actual tunnel excavation failure mode.

4.2 Failure process of tunnel after excavation under geostress field

4.2.1 Simulation scheme for geostress research

The model of a high-speed railway tunnel with a design speed of 350km/h in IV-level surrounding rock is utilized. The ratio of the uniaxial saturated compressive strength (R_c) of the rock to the maximum initial geostress (σ_{max}) in the vertical axis direction is used to reflect the initial geostress state, in accordance with the evaluation standard of the initial geostress state in the Code for Design of Railway Tunnel (TB10003-2016). Other calculation parameters are held constant, and the R_c/σ_{max} value is varied to 1.5, 3, 4.5, 6, 7.5, and 9, resulting in a total of six working conditions. This is used to simulate three stress states: general stress, high stress, and very high stress.

Based on the engineering geological conditions of the Wufeng Tunnel, Silurian shale has been chosen as the representative rock for the tunnel surrounding rock. The uniaxial saturated compressive strength of the shale has been determined to be 18MPa based on engineering data and serves as the benchmark for calculations. And then the simulated working conditions under various initial geostress are confirmed (Table 3). Since the deep buried tunnel is mainly affected by geostress, gravity is not considered in the model. The application method of initial geostress is shown in Figure 11.

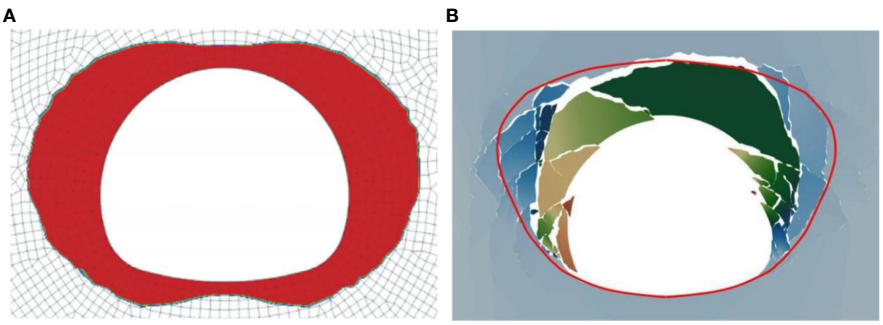

FIGURE 10
Comparison of simulation results of two methods. **(A)** Plastic zone calculated by finite element method. **(B)** Fracture zone calculated by FDEM.

TABLE 3 Simulation scheme of initial geostress (lateral pressure coefficient=1, σ_x / σ_y).

Geostress state	Very high stress		High stress		General stress	
R_c/σ_{max}	1.5	3	4.5	6	7.5	9
σ_x、 σ_y/MPa	12	8	6	4.8	4	2

4.2.2 Distribution of maximum principal stress

Three different conditions of geostress were chosen for analysis: general $R_c/\sigma_{max} = 9$, high $R_c/\sigma_{max} = 6$, and very high $R_c/\sigma_{max} = 3$. The simulation results are presented in Figure 12. When the geostress is low (Figure 12A), the tunnel's surrounding rock can maintain a stable state following excavation, and the tension area is limited to within 2 meters near the tunnel section. Meanwhile, the excavation's disturbance does not propagate deep into the surrounding rock, resulting in a small stress disturbance area. When $R_c/\sigma_{max} = 6$ (Figure 12B), the surrounding rock collapses, causing the tunnel's critical stable section to shift deeper. The distribution range of the tension zone increases to twice the tunnel diameter, and the stress disturbance zone caused by excavation forms an obvious evenly-distributed ring. When the geostress reaches a very high state ($R_c/\sigma_{max} = 3$, Figure 12C), the collapse range of the surrounding rock is further expanded, and the distribution range of the tension zone extends to three times the diameter of the tunnel. The stress disturbance caused by excavation also spreads to the boundary of the model. In conclusion, under a geostress field with a lateral pressure coefficient of 1, the stress value of the surrounding rock near the excavation section will sharply drop after excavation. The tension zone will appear near the excavation section, and the stress disturbance zone will be distributed annularly around the contour surface of the cavern. Then the surrounding rock stress gradually transition from tensile stress in shallow part to the original stress in deep part of tunnel face. Compared with the simulation results of gravity stress field, the maximum principal stress distribution in geostress field does not exhibit an obvious stress concentration phenomenon.

4.2.3 Analysis of deformation process of surrounding rock under geostress field

The working condition with high geostress ($R_c/\sigma_{max} = 6$) was selected for analysis, and the simulation results are presented in Figure 13. Following tunnel excavation, failure occurred around the tunnel face, and the overall failure form was circular. Initially, cracking and loosening occurred in the vault, side wall and inflected arch, and the fracture area gradually developed to the depth of surrounding rock (Figure 13A). The volume of rock block produced by shear crack cutting in deep surrounding rock increases gradually. Additionally, the deep crushed rock compresses the shallow rock, making the shallow rock turn over to the cavern (Figure 13B). The large overturning movement of rock blocks and the contact non-occlusion between the blocks make the surrounding rock produce the large deformation of crushing expansion in meter scale. Compared to the failure mode under the gravity stress field, the failure of the surrounding rock under the geostress field is influenced by both horizontal and vertical compressive stresses. There was significant uplift in the inflected arch and extensive collapse in the vault. Moreover, the failure zone of the surrounding rock exhibits no apparent directional preference. These observations suggest that the horizontal geostress plays a critical role in determining both the failure mode and the extent of surrounding rock.

4.2.4 Crack propagation process of surrounding rock after excavation under geostress field

High geostress ($R_c/\sigma_{max} = 6$) is selected for analysis. The simulation results demonstrate that the cracks produced due to tunnel excavation are primarily tensile-shear mixed crack, followed by shear cracks and a small proportion of tensile cracks. The overall distribution pattern of cracks appears to be annular and conjugate, with a higher density of cracks observed near the excavation section and a lower density in the deep surrounding rock. After the tunnel excavation, cracks appear in the shallow part of the surrounding rock due to the action of both vertical and horizontal geostress. These cracks are mainly tensile-shear mixed crack (Figure 14A). Subsequently, the cracks progressively extend to the depth of surrounding rock, with the maximum propagation depth being 30.4 m, approximately twice the tunnel's equivalent diameter. The cracks observed in the deeper surrounding rock are mainly shear cracks, exhibiting a distinct conjugate distribution pattern (Figure 14B). Eventually, the shear angle of the crack decreases gradually and becomes annihilated along the depth direction, which leads to the cessation of failure of the surrounding rock.

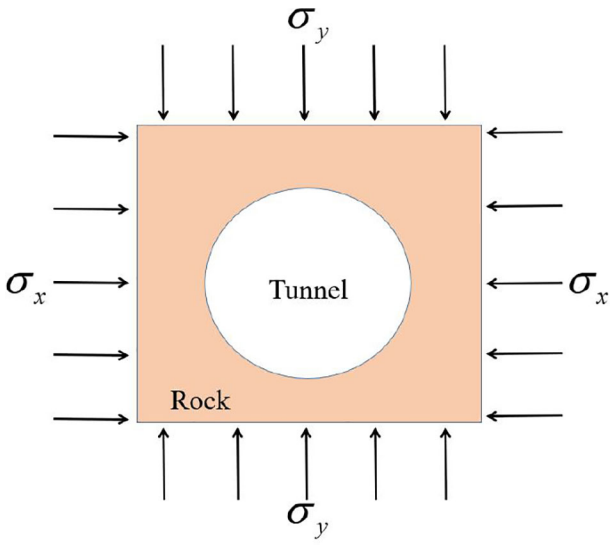

FIGURE 11
Schematic diagram of initial geostress field of tunnel.

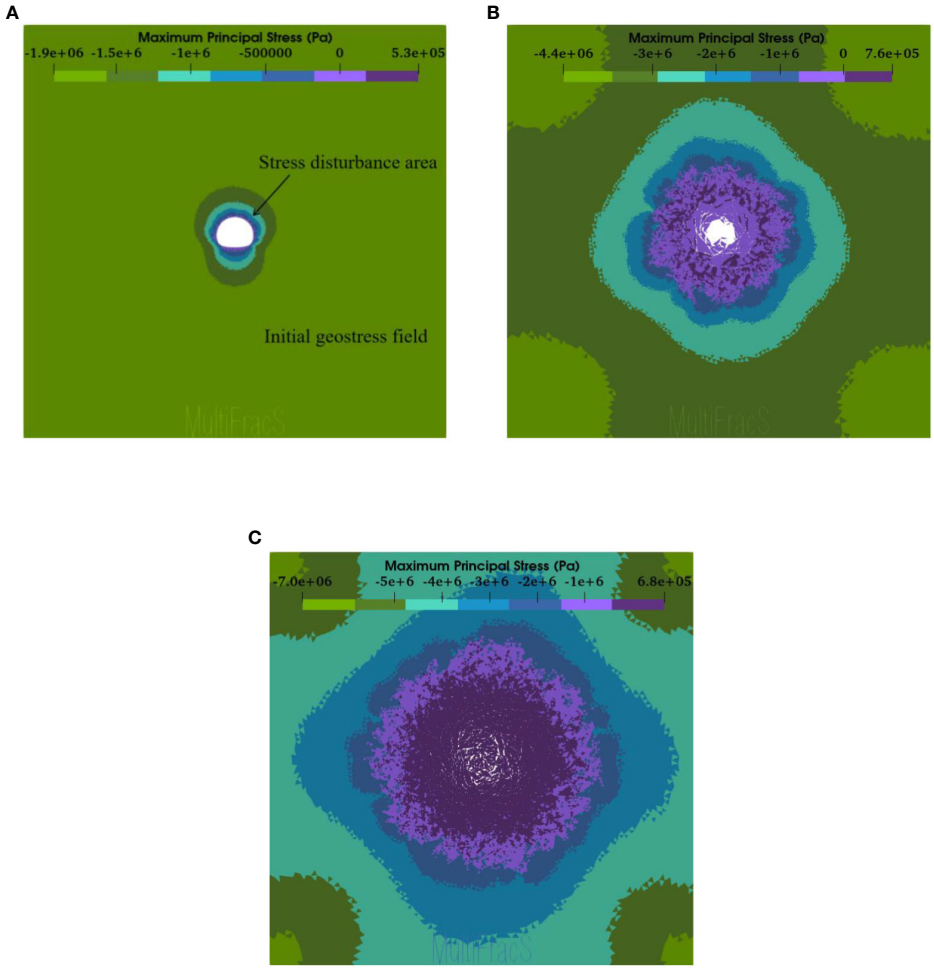

FIGURE 12
Maximum principal stress distribution of the tunnel after excavation under different geostress fields. **(A)** R_c / σ_{max} = 9. **(B)** R_c / σ_{max} = 6. **(C)** R_c / σ_{max} = 3.

4.2.5 Comparison of tunnel failure conditions after excavation under different geostress fields

Figure 15 illustrates the failure of the surrounding rock after excavation under six different geostress conditions. It is observed that only at a geostress of 2 MPa, the surrounding rock can maintain the stability. Under all other conditions, the tunnel experiences deformations at the meter-level after excavation, and large deformations occur under very high geostress conditions. This

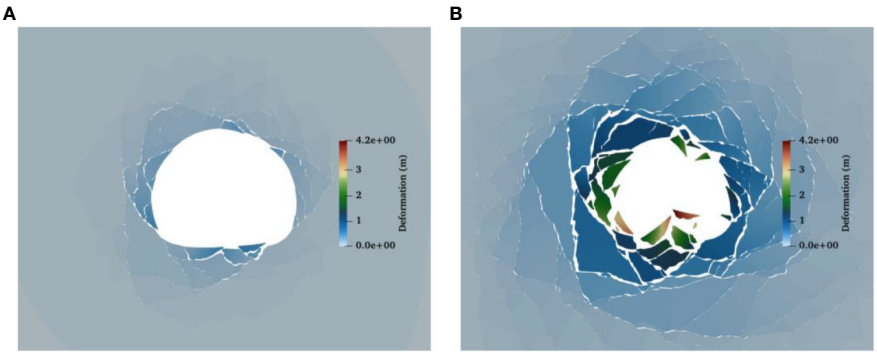

FIGURE 13
Displacement nephogram of surrounding rock under high geostress. **(A)** Surrounding rock begins to break. **(B)** Inflected arch uplift and vault collapse.

emphasizes the critical role of the stress state of the tunnel in maintaining the stability of the surrounding rock. When the geostress is 2 MPa (Figure 15A), the displacement of the surrounding rock after excavation is limited to the millimeter level, indicating robust tunnel stability. It is noteworthy that the maximum displacement of the surrounding rock is concentrated at the vault and inflected arch, whereas the maximum displacement of the tunnel after excavation under the gravity stress field is generated in both sides of the side wall. This is due to the presence of horizontal geostress that alter the stress state of the cavern. Therefore, when the tunnel is located in an engineering rock mass with a significant geostress field, special attention should be paid to the stress on the vault and inflected arch during the design and construction process. As the geostress increases to 4 MPa (Figure 15B), the surrounding rock begins to collapse in the shallow section, with the failure area distributed evenly around the cavern contour, and the maximum failure depth reaching 7.4 m. When the geostress gradually increases to 4.8MPa and 6MPa (high geostress), the failure zone begins to propagate to the depth of the surrounding rock. The deep broken rock began to extrude the shallow rock, forcing the shallow rock to overturn to the cavern. The maximum depth of the corresponding failure zone reaches 16m and 25m respectively (Figures 15C, D). Under very high geostress (Figures 15E, F), the failure zone of surrounding rock further radiates outward, and the maximum depth of the failure zone under 8MPa and 12MPa conditions reaches 31 meters and 42 meters respectively. Meanwhile, the surrounding rock at the excavated section is more broken, and loose and collapsed rock blocks jam the entire tunnel face.

In general, the IV-level surrounding rock can maintain a certain stability after excavation under general geostress conditions. However, as geostress increases, a failure zone appears around the excavation section and gradually develops deeper into the surrounding rock. At very high geostress conditions, the failure zone can extend more than three times of the tunnel diameter. At this point, the rock generated from collapse completely blocks the cavern, resulting in the overall collapse and destabilization of the tunnel.

5 Influence law of geostress on surrounding rock pressure design value

The determination of surrounding rock pressure is a fundamental problem in tunnel engineering. The calculation theory for this problem has gone through three stages: classical pressure theory, loose media pressure theory, and elastic-plastic pressure theory. Despite numerous achievements made by scholars in this field, the calculation method for surrounding rock pressure still has limitations due to the complexity and randomness of rock mass properties, geostress, boundary conditions, and construction methods. When using the traditional safety factor method for design, only the most unfavorable situation of surrounding rock pressure needs to be found (Xiao, 2020). Therefore, this paper proposes using the design value of surrounding rock pressure as the design support force to solve the problem that the actual surrounding rock pressure is difficult to determine. Additionally, this paper analyzes the impact of geostress on the design value of surrounding rock pressure.

5.1 Calculation method of surrounding rock pressure design value

5.1.1 Calculation principle

Based on the strength reduction method, the FDEM is utilized to determine the required minimum supporting force for maintaining the equilibrium of the failure zone of the surrounding rock at the tunnel vault. Then 1.4 times of the minimum supporting force is taken as the design value of surrounding rock pressure. Figure 16 shows the schematic diagram of the calculation principle of the design value of surrounding rock pressure. The specific steps are as follows:

(1) A numerical model of FDEM is established. Considering the weakening effect of groundwater, joint surface and other factors on the strength of surrounding rock, the strength of mechanical

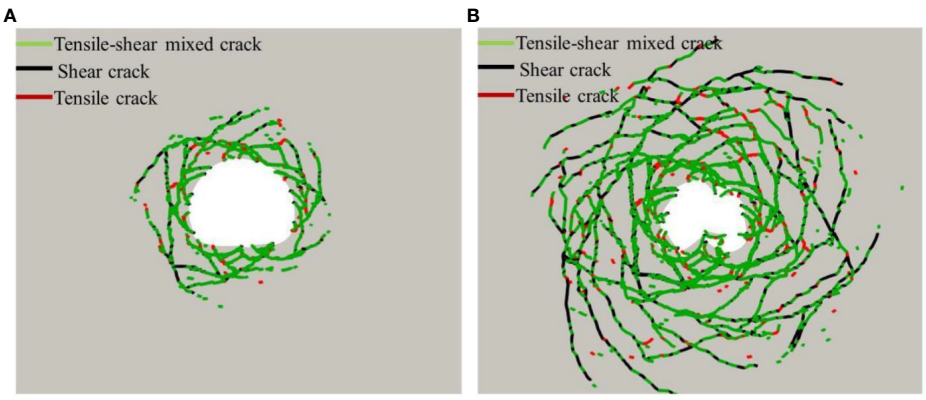

FIGURE 14
Crack distribution of surrounding rock under high geostress. **(A)** 12,000 time steps. **(B)** 36,000 time steps.

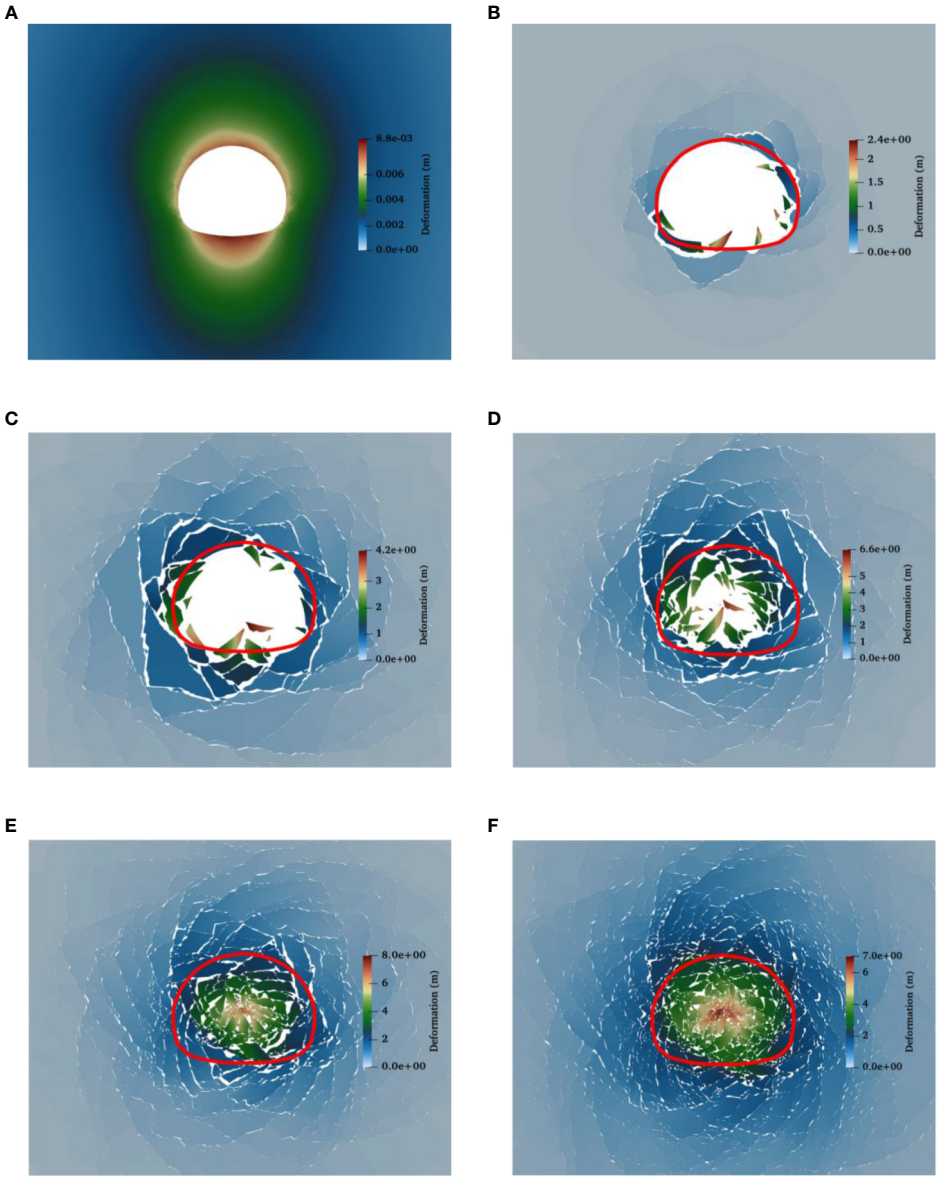

FIGURE 15
Failure of the tunnel after excavation under different geostress fields. **(A)** 2MPa. **(B)** 4MPa. **(C)** 4.8MPa. **(D)** 6MPa. **(E)** 8MPa. **(F)** 12MPa.

parameter of surrounding rock is reduced, and the reduction coefficient is generally 1.15 (Xiao, 2020). After the tunnel excavation, the model is calculated to converge, and the crack zone and failure zone of the surrounding rock are computed separately.

(2) The gravity of surrounding rock failure zone within the span of the cavern is calculated, and it is equivalent to the uniform load q_0 along the span direction.

(3) Following the tunnel model described in (1) an excavation simulation is again conducted. Normal supporting force of initial value q_0 is applied to the tunnel section, and the supporting force is gradually adjusted until there is no failure zone around the section. The supporting force is recorded at this point as the minimum supporting force $q_{\min}$. Then, the horizontal load is calculated by multiplying the vertical load $q_{\min}$ with the lateral pressure coefficient.

(4) The design value q of the surrounding rock pressure is determined by multiplying the minimum supporting force with the safety factor k. k is usually greater than 1.4 and can be adjusted based on factors such as the importance of the engineering project and the degree of deformation control required.

In the above steps, the failure zone is identified based on displacement. When the displacement of the surrounding rock near the excavation section reaches a specific value, it is considered locally unstable and the failure zone is formed. The displacement criterion refers to the allowable relative convergence value around the cavern (Table 4) in the Technical Code for Engineering of Ground Anchorages and Shotcrete Support (GB50086-2015). The relative convergence value around the cavern represents the ratio of the measured displacement between two measuring points and the distance

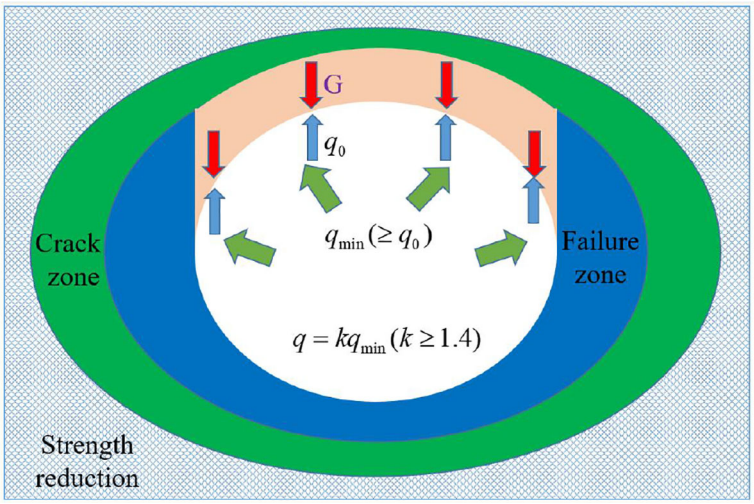

FIGURE 16
Schematic diagram of calculation principle of surrounding rock pressure design value.

between them, or the ratio of the measured displacement of the vault and the span of the tunnel.

5.1.2 Calculation of surrounding rock pressure design value

Taking a high-speed railway tunnel with a burial depth of 200m and a design speed of 350km/h in the IV-level surrounding rock as an example, the design value of surrounding rock pressure is calculated. After the tunnel excavation, the equivalent uniform load of gravity of the failure zone in the tunnel vault is calculated as 16kPa. Subsequently, excavation simulation is conducted again, followed by the application of supporting force, and the model is calculated until it converges. Finally, the supporting force is gradually adjusted until the surrounding rock no longer produces a failure zone after excavation.

The simulation results under different supporting forces are shown in Figure 17. When the supporting force is 16kPa (Figure 17A), the simulation results show that when the supporting force is small, the cracks will intersect at the tunnel vault, and the side walls on both sides will converge and deform towards the cavern. The surrounding rock around the cavern will collapse, and the excavation disturbance area will be large. With 25kPa supporting force applied (Figure 17B), the excavation disturbance area decreases significantly. Although cracks still appear at the vault and intersect at the right spandrel, no rock falls off from the rock mass. When the supporting force increases to 54kPa (Figure 17C), the excavation disturbance area is concentrated in a smaller region around the cavern. The cracks in the surrounding rock decreased obviously and mainly concentrated on both sides of the side wall. The cracks do not intersect at the vault, which remains stable, and no rock spalling occurs on both sides of the side wall. The relative convergence value of the tunnel is 0.99%, and the tunnel remains stable. Subsequently, the supporting force continues to increase, but the relative convergence value of the tunnel remains stable at about 1% (Figure 18), meeting the requirements of surrounding rock stability. Therefore, 54kPa is the minimum supporting force required for the high-speed railway tunnel.

5.1.3 Validity verification of calculation results

When the buried depth of the tunnel is no less than 10 ~ 15 times of the tunnel diameter, the formula for calculating the surrounding rock pressure is as follows for surrounding rock that conforms to the Mohr-Coulomb yielding criteria (Cai, 2002).

Vertical uniform load:

$$q = \alpha\gamma(R_{pd} - a) \tag{10}$$

Horizontal uniform load:

$$e = \beta\lambda q \tag{11}$$

TABLE 4 The allowable relative convergence value around the cavern.

Level of surrounding rock	The burial depth of the tunnel (m)		
	<50	50~300	300~500
III	0.10%~0.30%	0.20%~0.50%	0.40%~1.20%
IV	0.15%~0.50%	0.40%~1.20%	0.80%~2.00%
V	0.20%~0.80%	0.60%~1.60%	1.00%~3.00%

$$R_{pd} = R_0\left\{\frac{[p_0(1+\lambda)+2c\cot\varphi](1-\sin\varphi)}{2P_i+2c\cot\varphi}\right\}^{\frac{1-\sin\varphi}{2\sin\varphi}} \times\left\{1+\frac{p_0(1-\lambda)(1-\sin\varphi)\cos 2\theta}{[p_0(1+\lambda)+2c\cot\varphi]\sin\varphi}\right\} \quad (12)$$

where, γ is the volumetric weight of surrounding rock; λ is the lateral pressure coefficient of surrounding rock; α and β are the adjustment coefficients of surrounding rock pressure at the arch and side of the tunnel respectively; and R_{pd} is the radius of the tunnel plastic zone at 45° when the supporting force P_i =0. p_0, c, and φ represent the initial stress, cohesive force, and internal friction angle of the surrounding rock respectively. θ is the included angle with the horizontal axis of the tunnel; R_0 is the radius of tunnel. If the section is not circular, the radius of the outer circle of the tunnel section is taken. a is the distance from the center of the outer circle of the tunnel section to the tunnel excavation face in the direction of 45°.

When applying the aforementioned theoretical formula to resolve the surrounding rock pressure, the outer circle of tunnel section should be taken as the equivalent circular tunnel first. Subsequently, the theoretical solution for the plastic zone of the equivalent circular tunnel is computed, along with the determination of the depth of the plastic zone in the 45° direction. The gravitational force exerted by the surrounding rock within this depth range serves as the fundamental value of the surrounding rock pressure at the top of the tunnel. Ultimately, the approximate value of the surrounding rock pressure is obtained by multiplying the fundamental value by the adjustment coefficient.

The relevant parameters of the tunnel model in Section 5.1.2 are applied to equations (10) and (12), resulting in the calculation of a surrounding rock pressure of 62 kPa at the top of the tunnel. Although slightly higher than the minimum supporting force determined by the FDEM method in Section 5.1.2, the two values are close. The differences in the calculation results between the two methods are primarily attributed to the parameter related to the importance of the tunnel, which is the adjustment coefficient in the theoretical formula, as well as the allowable relative convergence value around the cavern in the FDEM-based calculation method. When the allowable relative convergence value is set to 0.75%, the calculation results from both methods can be equal (Figure 18). Therefore, it is important to select an appropriate allowable relative convergence value based on the significance of the tunnel. This finding further validates the accuracy of the FDEM-based calculation method for determining the design value of surrounding rock pressure. Moreover, it should be noted that the theoretical formula can solely provide the surrounding rock pressure for a circular tunnel in a homogeneous stratum, whereas the FDEM-based approach allows for the determination of the design value of surrounding rock pressure under complex section and surrounding rock conditions.

5.2 Analysis of the design value of surrounding rock pressure under varied geostress

5.2.1 Calculation of design value of surrounding rock pressure under varied geostress

The calculation method, based on FDEM as proposed in Section 5.1, was utilized for the calculations. Table 5 presents the calculation results for the design values of surrounding rock pressure of the high-speed railway tunnel with a design speed of 350km/h in the

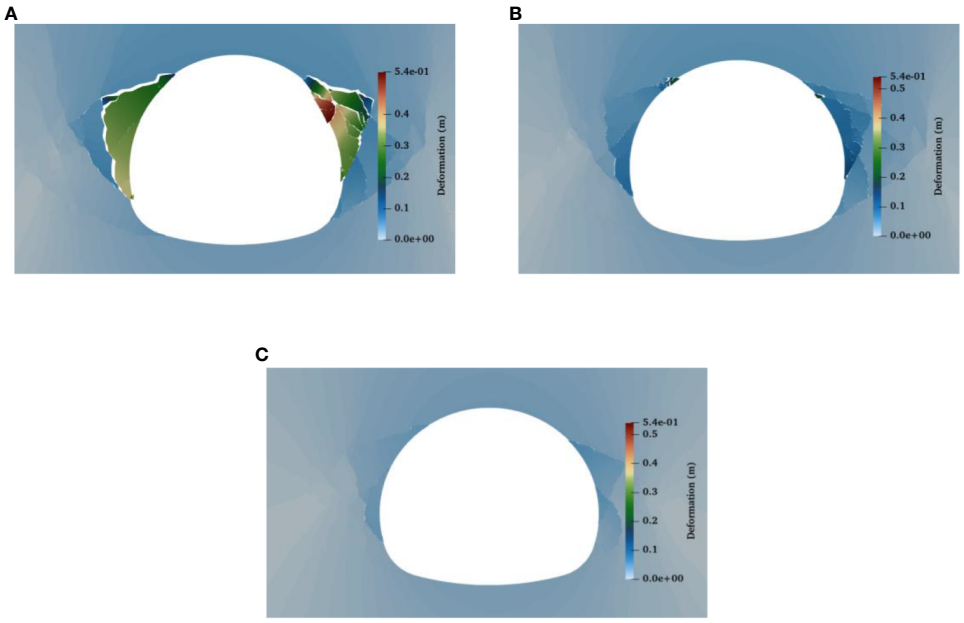

FIGURE 17
Deformation of cavern with different supporting forces. **(A)** 16kPa. **(B)** 25kPa. **(C)** 54kPa.

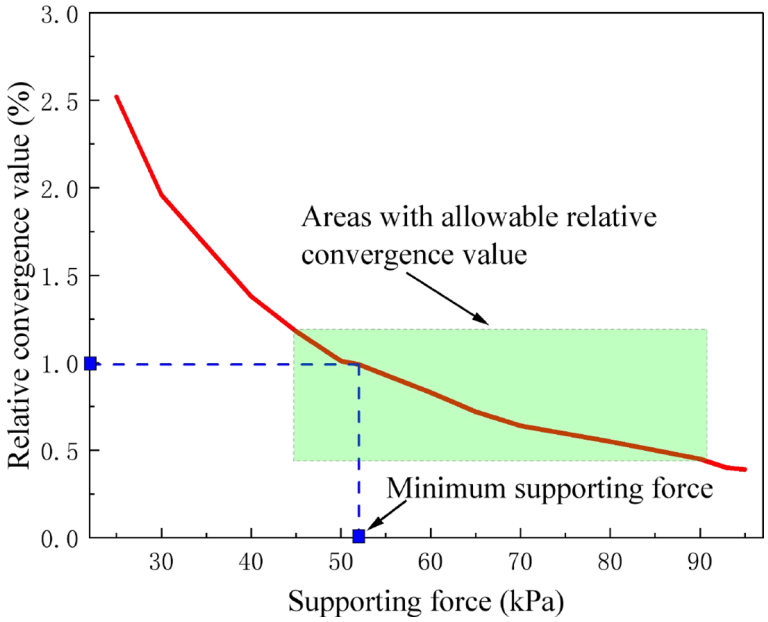

FIGURE 18
Variation curve of relative convergence value of tunnel under different supporting forces.

IV-level surrounding rock, considering various geostress. It should be noted that the safety factor "k" in the table is maintained at 1.4.

5.2.2 Analysis of calculation results of design values of surrounding rock pressure under varied geostress

Based on the calculation results of the design value of surrounding rock pressure, it is evident that engineering support measures need to be implemented in all five working conditions, except when the geostress is 2MPa, in order to meet the design requirements. As depicted in Figure 19, it can be observed that the equivalent uniform load, the minimum supporting force, and the design value of surrounding rock pressure exhibit a significant increase with the augmentation of geostress. Specifically, when the geostress varies from 2MPa to 12MPa, the corresponding equivalent uniform load ranges from 18KPa to 275KPa, the minimum supporting force escalates from 35KPa to 920KPa, and the design value of surrounding rock pressure rises from 49KPa to 1288KPa. The curve that represents the design value of the surrounding rock pressure in response to geostress approximately conforms to the quadratic function relation. By fitting the formula, the equation $q = 14.0637\sigma^2 - 68.5260\sigma + 85.8181$ is derived. Notably, all three indicators steadily increase in the general and high geostress stages but sharply increase in the very high geostress stage. Moreover, the curve that illustrates the design value of the surrounding rock pressure shows obvious nonlinearity. This is because under extreme geostress conditions, the tunnel's surrounding rock generally approaches the limit state. This results in a severe stress-release phenomenon after tunnel excavation, leading to a broad distribution of surrounding rock failure areas. To control the destabilization and collapse of the large-scale failure area, significant supporting force is necessary.

Additionally, it should be noted that there is an approximate linear relationship between the minimum supporting force and the

TABLE 5 Calculation results of design values of surrounding rock pressure under various geostress.

Geostress σ_x、σ_y (MPa)	Equivalent uniform load (kPa)	Minimum supporting force(kPa)	Design value of surrounding rock pressure (kPa)
2	0	0	0
4	18	35	49
4.8	37	65	91
6	56	110	154
8	113	320	448
12	275	920	1,288

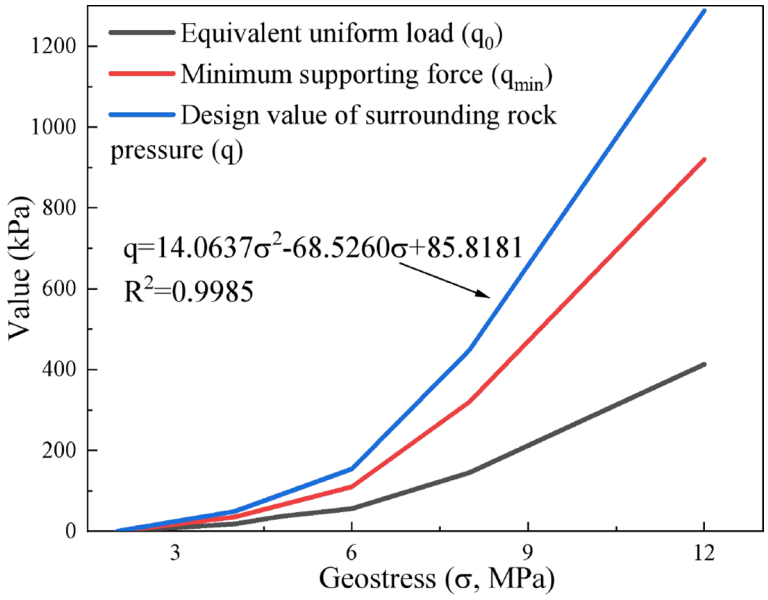

FIGURE 19
The variation curves of equivalent uniform load, minimum supporting force, and design values of surrounding rock pressure under different geostress.

equivalent uniform load (Figure 20), and the corresponding fitting formula is $q = 3.1473q_0 - 12.5888$. This supporting force can restrict the deformation of the surrounding rock of the tunnel after excavation to a small scale and ensure the integrity of the tunnel section. This calculation result also proves the correctness and reasonableness of computing the design value of the surrounding rock pressure based on the equivalent uniform load of the surrounding rock gravity in the failure zone within the cavern span.

In summary, geostress directly affects the design value of the surrounding rock pressure of tunnels, particularly under very high geostress. An obvious correlation exists between the minimum supporting force and the equivalent uniform load of the surrounding rock gravity in the failure zone within the cavern span, so the uniform load can be used as the reference value to calculate and verify the final design value of surrounding rock pressure.

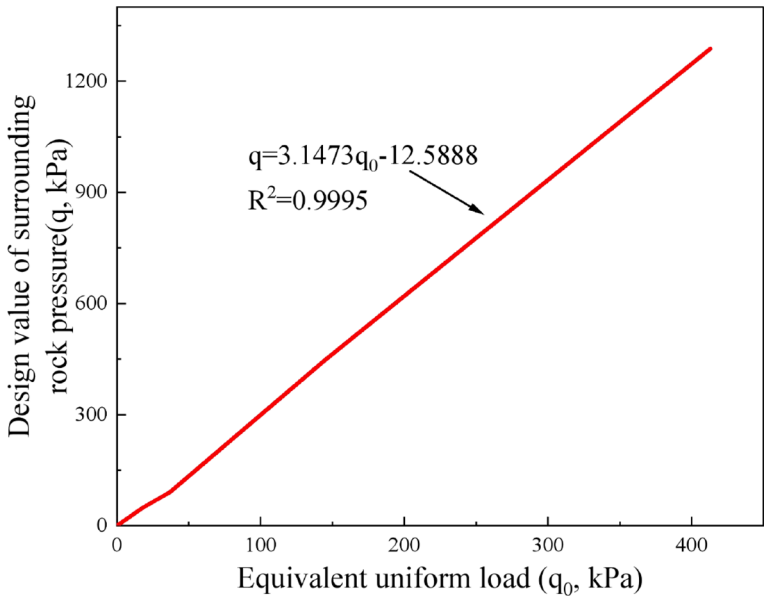

FIGURE 20
The variation curve of design value of surrounding rock pressure with respect to equivalent uniform load.

6 Conclusion

In this paper, FDEM is utilized to simulate the failure process of a tunnel after excavation under gravity stress field and geostress field. A method for determining the design value of surrounding rock pressure based on FDEM is proposed by introducing the tunnel displacement criterion. This method is then applied to investigate the influence of geostress on the surrounding rock pressure. The main conclusions of this study are as follows:

(1) For calibrating the calculation parameters of FDEM, the following approach is proposed: The macro parameters in FDEM can be acquired directly from laboratory tests. Contact penalty P_n and P_t are set as one times the elastic modulus, while fracture penalty P_f is set as 100 times the elastic modulus. Subsequently, the fracture energy G_{I} and G_{II} are adjusted iteratively until the reasonable calibration result is obtained. This method ensures the rationality of the calibration parameters while significantly expediting the calibration process.

(2) The failure zone and crack zone of the surrounding rock following tunnel excavation under the gravity stress field are mainly distributed in the spandrel and vault. In the geostress field, the failure zone and crack zone of the surrounding rock are distributed in a ring along the tunnel section. In both scenarios, the predominant type of cracks observed is tensile-shear mixed cracks, with shear cracks primarily concentrated at the far end of the section, while tensile cracks are mainly observed in the shallower portion of the section.

(3) A calculation method for determining the design value of surrounding rock pressure based on FDEM is proposed. This method incorporates a displacement criterion to identify the failure zone, followed by an assessment of the stability of the surrounding rock. The reasonableness of this FDEM-based calculation method is verified by comparing its results with those obtained from the theoretical formula for surrounding rock pressure.

(4) Geostress directly impacts the design value of surrounding rock pressure. These two variables follow a quadratic function relationship, namely $q = 14.0637\sigma^2 - 68.5260\sigma + 85.8181$. The design value of surrounding rock pressure and the equivalent uniform load of the surrounding rock gravity of the failure zone within the cavern span exhibit a linear relationship, specifically, $q = 3.1473q_0 - 12.5888$. The equivalent uniform load can serve as a reference value for calculating and verifying the results of the design value of surrounding rock pressure.

Data availability statement

The original contributions presented in the study are included in the article/supplementary material. Further inquiries can be directed to the corresponding author.

Author contributions

Conceptualization, BH and YZ. Methodology, MX, XF, and JY. Investigation, BH, CX and JW. Writing original draft, BH, JW and YZ. Writing – review and editing, MX and XF. Funding acquisition, MX, XF and YZ. Resources, XF, YZ and CX. Supervision, Y.Z. All authors contributed to the article and approved the submitted version.

Funding

This work was supported by the National Key Research and Development Program (No. 2021YFB2600404), the Knowledge Innovation Program of Wuhan (No. 2022010801020164), the Youth Innovation Promotion Association, CAS (No. 2021325), the Regional Innovation and Development Joint Fund of the National Natural Science Foundation of China (No. U21A20159) and the National Natural Science Foundation of China (No. 52179117).

Conflict of interest

Authors MX, JY, CX, and JW were employed by the company China Railway Siyuan Survey and Design Group Co., Ltd.

The remaining authors declare that the research was conducted in the absence of any commercial or financial relationships that could be construed as a potential conflict of interest.

Publisher's note

References

An, H., Wu, S., Liu, H., and Wang, X. (2022). Hybrid finite-discrete element modelling of various rock fracture modes during three conventional bending tests. *Sustainability* 14, 592. doi: 10.3390/su14020592

Cai, M. F. (2002). *Rock mechanics and engineering* (Science Press: Beijing, China), ISBN: ISBN:978-7-03-038440-9.

Cheng, Y. M. (2012). Modified Kastner formula for cylindrical cavity contraction in Mohr-Coulomb medium for circular tunnel in isotropic medium. *J. Mech.* 28, 163–169. doi: 10.1017/jmech.2012.17

Deng, P.-H., Liu, Q.-S., Huang, X., Pan, Y.-C., and Bo, Y. (2022).). Combined finite-discrete element numerical study on the buckling failure mechanism of horizontally layered soft rock mass. *Rock Soil Mech.* S2), 508–523+574. doi: 10.16285/j.rsm.2021.0701

Ding, W., Tan, S., Zhu, R., Jiang, H., and Zhang, Q. (2021). Study on the damage process and numerical simulation of tunnel excavation in water-rich soft rock. *Appl. Sci.* 11, 8906. doi: 10.3390/app11198906

Ding, Z., Zhao, L. S., Zhou, W. H., and Bezuijen, A. (2022). Intelligent prediction of multi-factor-oriented ground settlement during TBM tunneling in soft soil. *Front. Built Environ.* 8. doi: 10.3389/fbuil.2022.848158

GB50086-2015 (2015). *Technical code for engineering of ground anchorages and shotcrete support* (Beijing, China: China Planning Press).

Han, H., Fukuda, D., Liu, H., Fathi Salmi, E., Sellers, E., Liu, T., et al. (2021). Combined finite-discrete element modellings of rockbursts in tunnelling under high in-situ stresses. *Comput. Geotechnics* 137, 104261. doi: 10.1016/j.compgeo.2021.104261

Keawsawasvong, S., Seehavong, S., and Ngamkhanong, C. (2022). Application of artificial neural networks for predicting the stability of rectangular tunnels in Hoek-Brown rock masses. *Front. Built Environ.* 8. doi: 10.3389/fbuil.2022.837745

Lee, H., Choi, H., Choi, S.-W., Chang, S.-H., Kang, T.-H., and Lee, C. (2021). Numerical simulation of EPB shield tunnelling with TBM operational condition control using coupled DEM-FDM. *Appl. Sci.* 11, 2551. doi: 10.3390/app11062551

Lee, J., Rehman, H., Naji, A., Kim, J.-J., and Yoo, H.-K. (2018). An empirical approach for tunnel support design through Q and RMi systems in fractured rock mass. *Appl. Sci.* 8, 2659. doi: 10.3390/app8122659

Lisjak, A., Figi, D., and Grasselli, G. (2014). Fracture development around deep underground excavations: Insights from FDEM modelling. *J. Rock Mech. Geotechnical Eng.* 6 (6), 493–505. doi: 10.1016/j.jrmge.2014.09.003

Lisjak, A., Garitte, B., Grasselli, G., Müller, H. R., and Vietor, T. (2015a). The excavation of a circular tunnel in a bedded argillaceous rock (Opalinus Clay): Short-term rock mass response and FDEM numerical analysis. *Tunnelling Underground Space Technol.* 45, 227–248. doi: 10.1016/j.tust.2014.09.014

Lisjak, A., Liu, Q., Zhao, Q., Mahabadi, O. K., and Grasselli, G. (2013). Numerical simulation of acoustic emission in brittle rocks by two-dimensional finite-discrete element analysis. *Geophys. J. Int.* 195 (1), 423–443. doi: 10.1093/gji/ggt221

Lisjak, A., Tatone, B. S. A., Mahabadi, O. K., Grasselli, G., Marschall, P., Lanyon, G. W., et al. (2015b). Hybrid finite-discrete element simulation of the EDZ formation and mechanical sealing process around a microtunnel in opalinus clay. *Rock Mech. Rock Eng.* 49 (5), 1849–1873. doi: 10.1007/s00603-015-0847-2

Liu, Q.-S., Deng, P.-H., Bi, C., Li, W.-W., and Liu, J. (2019). FDEM numerical simulation of the fracture and extraction process of soft surrounding rock mass and its rockbolt-shotcrete-grouting reinforcement methods in the deep tunnel. *Rock Soil Mech.* 10), 4065–4083. doi: 10.16285/j.rsm.2018.1032

Liu, N. F., Li, N., Li, G. F., Song, Z. P., and Wang, S. J. (2022). Method for evaluating the equivalent thermal conductivity of a freezing rock mass containing systematic fractures. *Rock Mech. Rock Eng.* 55, 7333–7355. doi: 10.1007/s00603-022-03038-9

Liu, N. F., Li, N., Wang, S. J., Li, G. F., and Song., Z. P. (2023). A fully coupled thermo-hydro-mechanical model for fractured rock masses in cold regions. *Cold Regions Sci. Technol.* 205, 103707. doi: 10.1016/j.coldregions.2022.103707

Liu, N., Li, N., Xu, C., Li, G., Song, Z., and Yang, M. (2020). Mechanism of secondary lining cracking and its simulation for the dugongling tunnel. *Rock Mech. Rock Eng.* 53, 4539–4558. doi: 10.1007/s00603-020-02183-3

Min, G., Fukuda, D., Oh, S., Kim, G., Ko, Y., Liu, H., et al. (2020). Three-dimensional combined finite-discrete element modeling of shear fracture process in direct shearing of rough concrete–rock joints. *Appl. Sci.* 10, 8033. doi: 10.3390/app10228033

Munjiza, A. (2004). *The combined finite-discrete element method* (London: John Wiley&Sons, Ltd), ISBN: . (Cloth: alk.paper).

Munjiza, A., Latham, J. P., and Andrews, K. R. F. (1999). Challenges of a coupled combined finite-discrete element approach to explosive induced rock fragmentation. *Fragblast* 3 (3), 237–250. doi: 10.1080/13855149909408048

Munjiza, A., Owen, D. R. J., and Bicanic, N. (1995). A combined finite-discrete element method in transient dynamics of fracturing solids. *Eng. Computations* 12 (2), 145–174. doi: 10.1108/02644409510799532

Qiu, H., Qiu, R., Luo, G., Ayasrah, M., and Wang, Z. (2022). Study on the mechanical behavior of fluid-solid coupling in shallow buried tunnels under different biased terrain. *Symmetry* 14, 1339. doi: 10.3390/sym14071339

Song, Y., Fan, Y., An, H., Liu, H., and Wu, S. (2022). Investigation of the dynamic pure-mode-II fracture initiation and propagation of rock during four-point bending test using hybrid finite–discrete element method. *Sustainability* 14, 10200. doi: 10.3390/su141610200

Sun, X., Li, G., Zhao, C., Liu, Y., and Miao, C. (2018). Investigation of deep mine shaft stability in alternating hard and soft rock strata using three-dimensional numerical modeling. *Processes* 7, 2. doi: 10.3390/pr7010002

Tatone, B. S. A., and Grasselli, G. (2015). A calibration procedure for two-dimensional laboratory-scale hybrid finite–discrete element simulations. *Int. J. Rock Mech. Min. Sci.* 75, 56–72. doi: 10.1016/j.ijrmms.2015.01.011

TB10003-2016 (2016). *Code for design of railway tunnel* (Beijing, China: China Railway Publishing House).

Trivino, L. F., and Mohanty, B. (2015). Assessment of crack initiation and propagation in rock from explosion-induced stress waves and gas expansion by cross-hole seismometry and FEM–DEM method. *Int. J. Rock Mech. Min. Sci.* 77, 287–299. doi: 10.1016/j.ijrmms.2015.03.036

Wang, T., Yan, C., Zheng, H., Zheng, Y., and Wang, G. (2022). Microfracture behavior and energy evolution of heterogeneous mudstone subjected to moisture diffusion. *Comput. Geotechnics* 150, 104918. doi: 10.1016/j.compgeo.2022.104918

Wu, P., Yang, F., Zheng, J., and Wei, Y. (2019). Evaluating the highway tunnel construction in western sichuan plateau considering vocational health and environment. *Int. J. Environ. Res. Public Health* 16, 4671. doi: 10.3390/ijerph16234671

Xiao, M. Q. (2020). *Total safety factor method of tunnel support structure design* (China Communications Press Co., Ltd), ISBN: 9787114165580.

Xue, G., Fang, X., and Wei, T. (2019). A case study on large deformation failure mechanism and control techniques for soft rock roadways in tectonic stress areas. *Sustainability* 11, 3510. doi: 10.3390/su11133510

Yan, C., Tong, Y., Luo, Z., Ke, W., and Wang, G. (2021). A two-dimensional grouting model considering hydromechanical coupling and fracturing for fractured rock mass. *Eng. Anal. Boundary Elements* 133, 385–397. doi: 10.1016/j.enganabound.2021.09.013

Yan, C., and Zheng, H. (2017a). FDEM-flow3D: A 3D hydro-mechanical coupled model considering the pore seepage of rock matrix for simulating three-dimensional hydraulic fracturing. *Comput. Geotechnics* 81, 212–228. doi: 10.1016/j.compgeo.2016.08.014

Yan, C., and Zheng, H. (2017b). Three-dimensional hydromechanical model of hydraulic fracturing with arbitrarily discrete fracture networks using finite-discrete element method. *Int. J. Geomech.* 17 (6), 04016133. doi: 10.1061/(asce)gm.1943-5622.0000819

Yan, C., and Zheng, H. (2017c). A coupled thermo-mechanical model based on the combined finite-discrete element method for simulating thermal cracking of rock. *Int. J. Rock Mech. Min. Sci.* 91, 170–178. doi: 10.1016/j.ijrmms.2016.11.023

Yan, C.-Z., Zheng, H., Sun, G.-H., and Ge, X.-R. (2015). Polygon characterization of coarse aggregate and two-dimensional combined finite discrete element method analysis. *Rock Soil Mech.* S2), 95–103. doi: 10.16285/j.rsm.2015.S2.012

Zhang, H., Chen, L., Chen, S., Sun, J., and Yang, J. (2018). The spatiotemporal distribution law of microseismic events and rockburst characteristics of the deeply buried tunnel group. *Energies* 11, 3257. doi: 10.3390/en11123257

Zhang, Q., Guo, X., Yu, T., Shen, Y., and Liu, X. (2022). Effect of constructing a new tunnel on the adjacent existed tunnel in weak rock mass: A case study. *Buildings* 12, 1845. doi: 10.3390/buildings12111845

Zhang, T., Nie, L., Zhang, M., Dai, S., Xu, Y., Du, C., et al. (2020). The unsymmetrical coefficient of unsymmetrical-loaded tunnel based on field monitoring and numerical simulation. *Symmetry* 12, 1793. doi: 10.3390/sym12111793

Zhang, S., Qiu, S., Kou, P., Li, S., Li, P., and Yan, S. (2021). Investigation of damage evolution in heterogeneous rock based on the grain-based finite-discrete element model. *Materials* 14, 3969. doi: 10.3390/ma14143969

Zhao, Q., Tisato, N., Grasselli, G., Mahabadi, O. K., Lisjak, A., and Liu, Q. (2015). Influence of in-situ stress variations on acoustic emissions: a numerical study. *Geophys. J. Int.* 203 (2), 1246–1252. doi: 10.1093/gji/ggv370

Zhong, J., Mao, Z., Ni, W., Zhang, J., Liu, G., Zhang, J., et al. (2022). Analysis of formation mechanism of slightly inclined bedding mudstone landslide in coal mining subsidence area based on finite–discrete element method. *Mathematics* 10, 3995. doi: 10.3390/math10213995

frontiers | Frontiers in Ecology and Evolution

TYPE Original Research
PUBLISHED 03 August 2023
DOI 10.3389/fevo.2023.1253328

OPEN ACCESS

EDITED BY
Naifei Liu,
Xi'an University of Architecture and Technology, China

REVIEWED BY
Yajiao Li,
Xi'an University of Science and Technology, China
Xiaolong Zhang,
Chinese Academy of Sciences (CAS), China

*CORRESPONDENCE
Jiqiang Lyu
lvjiqiang0721@chd.edu.cn

RECEIVED 05 July 2023
ACCEPTED 18 July 2023
PUBLISHED 03 August 2023

CITATION
Lyu J, Huang Y, Nie Q, Lu C, Zhang Y, Fu X, Guo P and Luo P (2023) Spatiotemporal variations and risk characteristics of potential non-point source pollution driven by LUCC in the Loess Plateau Region, China.
Front. Ecol. Evol. 11:1253328.
doi: 10.3389/fevo.2023.1253328

Spatiotemporal variations and risk characteristics of potential non-point source pollution driven by LUCC in the Loess Plateau Region, China

Jiqiang Lyu[1,2,3,4]*, Yuanjia Huang[1,2,3,4], Qiyang Nie[1], Chen Lu[1,2,3,4], Yueyan Zhang[1,2,3,4], Xianghang Fu[1,2,3,4], Peng Guo[5,6] and Pingping Luo[1,2,3,4]

[1]School of Water and Environment, Chang'an University, Xi'an, China, [2]Key Laboratory of Subsurface Hydrology and Ecological Effects in Arid Region, Chang'an University, Ministry of Education, Xi'an, China, [3]Xi'an Monitoring, Modelling and Early Warning of Watershed Spatial Hydrology International Science and Technology Cooperation Base, Chang'an University, Xi'an, China, [4]Key Laboratory of Eco-hydrology and Water Security in Arid and Semi-arid Regions of the Ministry of Water Resources, Chang'an University, Xi'an, China, [5]Institude of Soil and Water Conservation, Northwest Agriculture and Forestry University, Yangling, Shaanxi, China, [6]Institute of Soil and Water Conservation, Chinese Academy of Sciences and Ministry of Water Resources, Yangling, Shaanxi, China

With increasing human activities, regional substrate conditions have undergone significant changes. These changes have resulted in temporal and spatial variations of non-point source pollution sources, which has a significant impact on the quality of the regional soil, surface water, and groundwater environments. This study focused on the human-disturbed Loess Plateau region and used an enhanced potential non-point-source pollution index (PNPI) model to explore the dynamic changes of regional potential non-point-source pollution (PNP) and the associated risk due to land use and land cover change (LUCC) over the past 31 years. The Loess Plateau region is mainly composed of cultivated land, grassland and forest, which together account for 93.5% of the watershed area. From 1990 to 2020, extensive soil and water conservation measures were implemented throughout the Loess Plateau region, resulting in a significant reduction in the non-point source pollution risk. Using the quantile classification method, the study area's PNP risk values were categorized into five distinct levels. The results revealed a polarization phenomenon of PNP risk in the region, with an increase in non-point source pollution risk in the human-influenced areas and a rapid expansion of the very high-risk area. However, the non-point source pollution risk in the upstream water source area of the watershed reduced over the study period. In recent years, the rapid urbanization of the Loess Plateau region has been the primary reason for the rapid expansion of the very high PNP risk area throughout the watershed. This study highlights the significant impact of LUCC on the dynamic changes in PNP risk within the Loess Plateau region, providing crucial insights into future conservation and urban planning policies aimed at enhancing the ecological health and environmental quality of the region.

KEYWORDS

LUCC, non-point pollution, Loess Plateau Region, PNPI model, Potential non-point-source pollution risk

1 Introduction

The Loess Plateau region in China is a unique ecological environment, known for its dramatic landscapes, including the Yellow River and the high mountains of the Tibetan Plateau. However, the poor soil and water resources in the region make it vulnerable to non-point source pollution, which is a major issue (Wang, 2006; Ting, 2010; Sun et al., 2012; Shen et al., 2015; Guo et al., 2022). In recent years, the Chinese government has taken active steps to protect the regional environment because the rapid urbanization of the region has had a significant impact on the quality of both surface water and groundwater within the watershed (Ritter et al., 2002; Zhang et al., 2014; Shen et al., 2015; Yang et al., 2017). As a result, water resource scarcity and pollution have emerged as serious challenges to sustainable development and the well-being of local populations (Shen et al., 2013; Lyu et al., 2019; Tao et al., 2020). While government policies and land managers have effectively controlled many water pollution problems, non-point source pollution still has an impact on environmental quality. Non-point source pollution is complex, widespread, and latent, making governance and control more difficult (Yang et al., 2013; Park et al., 2019).

Non-point source pollution, resulting from the uncontrolled runoff of various contaminants from agricultural land, urban areas, and other sources, is a significant threat to the environment (Cecchi et al., 1982; Puccinelli et al., 2013; Yang et al., 2013). Its destructive impacts include reductions in water quality, accelerated soil erosion, and increased air pollution levels (Lyu et al., 2018). This is a major cause of concern for environmental scientists and policymakers worldwide because it poses a formidable challenge to achieving the sustainable development goals (Xu et al., 2022). Non-point source pollution has been linked to the degradation of natural habitats and biodiversity loss, and has negative impacts on human health (Vörösmarty et al., 2010; Puccinelli et al., 2013; Ouyang et al., 2016; Ge et al., 2022). To address this issue, it is imperative to adopt a comprehensive and integrated approach that considers the unique characteristics of each pollution source and their interactions with the environment. Effective management strategies, such as land-use planning, implementation of best management practices, and the promotion of sustainable agricultural practices, are essential to mitigate the negative impacts of non-point source pollution (Novotny and Chesters, 1981; Mohammadi, 2001; Loague and Corwin, 2005; Gémesi et al., 2011; Yang et al., 2013). To mitigate non-point source pollution and soil erosion in the Loess Plateau, the Chinese government has implemented various projects and initiatives since 1995. These include sustainable agricultural practices since 2001, afforestation since 1999, and sediment control structures since 1995. These measures have been implemented to improve the ecological health and overall environmental quality of the region (Munafò et al., 2005; Zhang, 2008; Wang et al., 2010; Hao and Lu, 2021). These efforts have significantly decreased soil erosion and non-point source pollution, leading to improved water quality, better agricultural productivity, and increased biodiversity. However, quantifying non-point source pollution remains a challenge, because it is highly variable and difficult to predict.

Quantifying non-point source pollution is critical for effective watershed management. There has been significant progress in recent years in measuring and modeling non-point source pollution using methods such as remote sensing, watershed modeling, and field sampling (Munafò et al., 2005; Cotman et al., 2008; Lee et al., 2009; Zhang and Huang, 2011; Geng et al., 2015; Liu et al., 2019; Alnahit et al., 2020; Luo et al., 2022). There are still many challenges in accurately measuring the sources and impacts of non-point source pollution because they are highly variable and difficult to predict (Ouyang et al., 2010). The current methods used to quantify non-point source pollution in watersheds are mostly based on modeling, with the most widely used models being the Soil and Water Assessment Tool, Areal Nonpoint Source Watershed Environment Response Simulation (Borah and Bera, 2004; Cecchi et al., 2005; Sharma and Tiwari, 2019; de Mello et al., 2020; Hou et al., 2022). However, these models have high data volume and accuracy requirements, making them less applicable in areas with a lack of monitoring data (Borah and Bera, 2004; Cecchi et al., 2005). The potential non-point-source pollution index (PNPI) is a geographical information system (GIS)-based watershed non-point source pollution risk assessment tool (Cecchi et al., 2007; Shen et al., 2014), which describes the PNP risk of a region by generalizing the production, degradation, and transportation processes of pollutants, and has received increasing attention from researchers due to its low data requirements (Loague and Corwin, 1996; Gossweiler et al., 2021; Liu et al., 2021; Qian et al., 2021; Xu et al., 2021; Li et al., 2022). Researchers have used the PNPI model to assess the PNP risk in various regions, including the middle of Italy's Viterbo Province (Cecchi et al., 1982) and typical watersheds in China (Munafò et al., 2005; Fan and Fang, 2020; Li H. L. et al., 2021; Ouyang et al., 2010). However, studies using the PNPI and its incorporation in improved models have mostly focused on evaluating the current situation regarding PNP in small watersheds, with much less research on the evolutionary characteristics of PNP risk in watersheds under the influence of historical land use change (Ierodiaconou et al., 2005; Clément et al., 2017; Li et al., 2020; Li et al., 2022).

The Loess Plateau region is known for having one of the highest population densities in the world, and has unfortunately experienced non-point source pollution due to human activities in the region. This has led to pollution of the water environment throughout the area (Wang, 2006; Ting, 2010; Ai et al., 2015; Shen et al., 2015; Li L. et al., 2021; Shi et al., 2022). The far-reaching effects of this pollution have had a substantial impact on both the environment and health of local inhabitants. With the continuous urbanization, water pollution levels have been rising throughout the region (Shen et al., 2015; Yang et al., 2017; Lyu et al., 2019). This study investigated the temporal and spatial variations of PNP and the risk it presents in the Loess Plateau region, considering the impact of historical LUCC from 1990 to 2020. The results will enable a better understanding of non-point source pollution in the region and enable effective strategies for pollution management and control to formulated. The findings of the study will be critical for

implementing effective policies and regulations to mitigate the negative impacts of non-point source pollution. Ultimately, it is hoped that this research will contribute to a more sustainable and equitable future for the inhabitants of the Loess Plateau region, where the natural environment and human populations can thrive in harmony.

2 Materials and methods

2.1 Overview of the study area

The Loess Plateau, also referred to as the Huangtu Plateau, is a region situated in the upper and middle reaches of the Yellow River in China, ranging in latitude from 34°N to 42°N and in longitude from 105°E to 117°E. With an area covering approximately 640,000 km^2, it constitutes 12.5% of the total area of China (Fu 2010; Wang et al., 2010; Lyu et al., 2019; Zhang et al., 2020). The vast area of the Loess Plateau in northern and northwestern China encompasses several provinces, including Inner Mongolia, Shanxi, Ningxia, Shaanxi, and Gansu. This area is home to approximately 40 million inhabitants and is characterized by unique geological features, which have significant ecological and environmental implications.

Characterized by its yellow-brown loess soil, steep mountains, and deep valleys, the Loess Plateau has an average elevation of 1000-1500 m. Its temperate continental climate is defined by strong winds, significant temperature differences between day and night, and abundant precipitation. This region is highly significant ecologically and serves as a critical source of water for the Yellow River, hence it has been referred to as the "water tower of the Yellow River." The Loess Plateau is also renowned for its agricultural significance, with its loess soil proving highly suitable for cultivating crops such as wheat (Ierodiaconou et al., 2005; Li et al., 2020; Li et al., 2022). Figure 1 shows the geographic location of the Loess Plateau in the northwestern region of China. This region remains a critical area for ecological preservation and agricultural development within China.

2.2 Research methods

2.2.1 An enhanced PNPI model based on the coefficient of variation decision-making

The PNPI is a widely recognized tool that has been used to quantitatively assess the potential risk of non-point source pollution across various land use types within the Loess Plateau region (Ritter et al., 2002; Shen et al., 2013; Tao et al., 2020). It simplifies the processes of pollutant generation, degradation, and transport into a land cover index (LCI), distance index (DI), and runoff index (ROI), with a spatial distribution. The spatial PNP risk of the watershed can be expressed as a function of these three indexes. The enhanced PNPI model structure is shown in Figure 2.

The PNPI integrates the function expressions of the LCI, DI, and ROI into fixed weights, which are then divided by an expert scoring method (Munafò et al., 2005). This approach lacks objectivity and applicability, making it necessary to adopt an objective weighting method based on the principle of information entropy and the coefficient of variation decision-making to improve the model. Figure 2 shows the new weighting method for the improved PNPI model. Using the enhanced PNPI model, this study simulated the temporal and spatial dynamics of PNP risk in the study area over the past 31 years, considering the influence of land use changes. By combining the results of this model with an analysis of the temporal and spatial changes in land use, this study

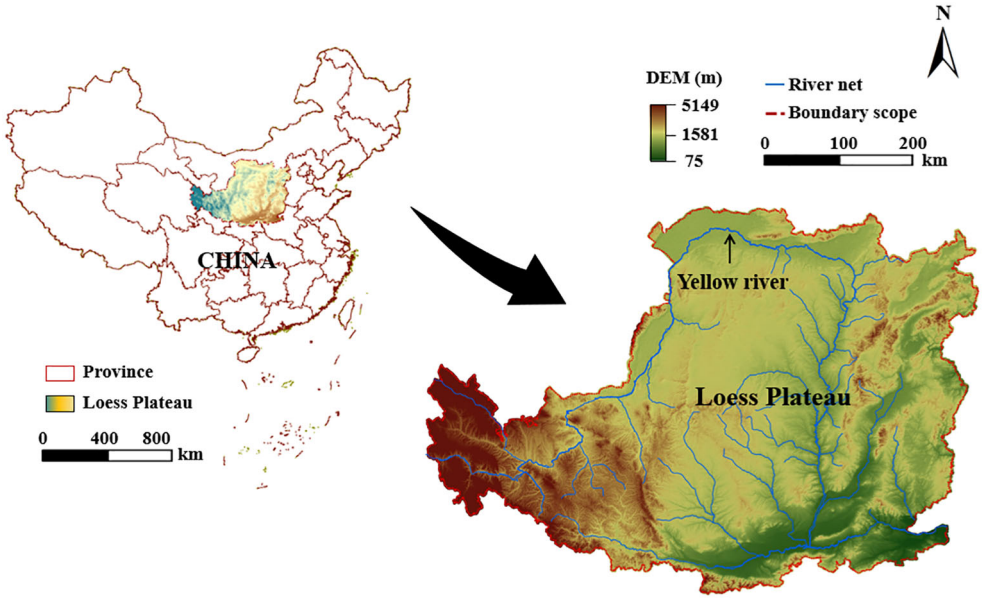

FIGURE 1
Location of the Loess Plateau.

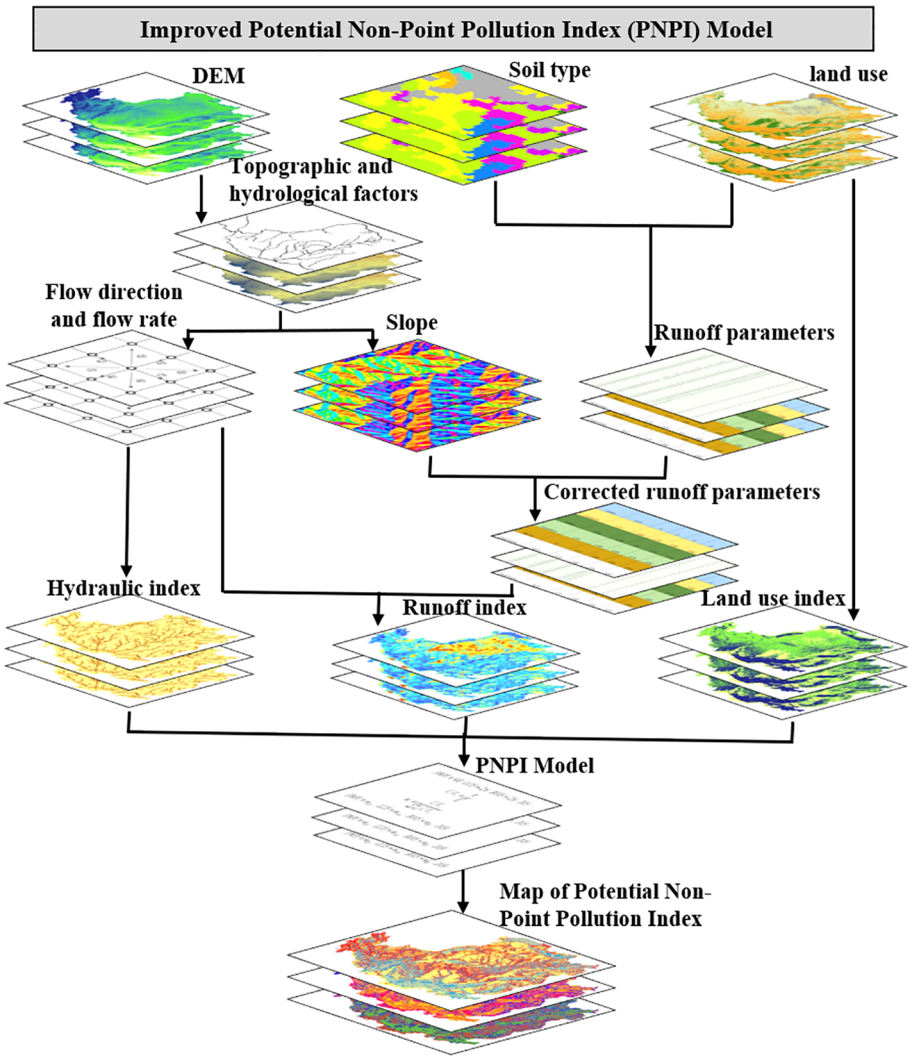

FIGURE 2
Improved PNPI Model Structure.

explored the primary evolutionary characteristics of PNP risk in the Loess Plateau region and identified its dominant factors. To achieve this goal, this study developed an objective and applicable weighting method to enhance the rationality and accuracy of the PNPI model. This enhanced model was then used to investigate the potential risk of non-point source pollution in the study area. The results of this analysis revealed the distribution characteristics and dominant factors controlling the PNP risk in the Loess Plateau region.

2.2.2 Data used

The data used in the PNPI model was primarily composed of spatial and attribute data. The former encompassed digital elevation model (DEM) data, soil types, and land use and land cover change (LUCC) data (Lyu et al., 2019; Yang and Huang, 2021; Shi et al., 2022). The latter included soil permeability and land use attributes. Table 1 presents the data sources required for model calculation.

The soils in the Loess Plateau region are diverse and can be classified into several types based on their physical, chemical, and biological properties (Fu 2010; Zhang et al., 2020; Li L. et al., 2021; Shi et al., 2022). The Harmonized World Soil Database (HWSD) provides a comprehensive dataset of the distribution of soil types in the region. According to the HWSD, the dominant soil types in the Loess Plateau include Cambisols, Calcisols, and Luvisols, which together account for more than 80% of the total area. Cambisols are mainly distributed in the northwestern and northeastern parts of the plateau, while Calcisols are distributed in the central and southeastern areas. Luvisols are mainly found in the western and southern parts of the plateau. In addition to these dominant soil types, there are also other soil types present in the region, such as Fluvisols, Gleysols, and Vertisols. Fluvisols are distributed along the rivers and streams in the plateau, while Gleysols are found in low-lying areas with poor drainage. Vertisols are mainly distributed in the southern and southeastern parts of the plateau. The HWSD database provides valuable information on the distribution and characteristics of soil types in the Loess Plateau.

The soil permeability classification was based on the HWSD database. The saturated infiltration rate of each soil was determined using the SPAW 6.02 software developed by the US Department of

TABLE 1 The satellite data used in the PNPI model.

Data Type	Name	Data Format	Data Overview	Data Name	Data Source
Spatial Data Base	Digital Elevation Map	Grid	30m×30m Resolution	ASTERGDEMV3	Chinese Academy of Sciences Computer Network Information Center Geospatial Data Cloud Platform (www.gscloud.cn)
	Soil Type Map	Grid	1km×1km Resolution	HWSD	Cold and Arid Regions Science Data Center (www.ncdc.ac.cn)
	Land Use Map	Grid	30m×30m Resolution	Annual China Land Cover Dataset (CLCD)	Institute of Remote Sensing Information Processing (http://irsip.whu.edu.cn/)
Attribute Data Base	Soil Permeability Data	csv	Permeability Level in the Study Area	——	Calculated by Experiential Formula or SPAW Based on Soil Parameters in HWSD
	Land Use Attribute Data	csv	Experiential Parameters of Various Land Use Types in the Study Area	——	Compared with European CORINE Land Use Classification and Existing Experiential Coefficients of PNPI Model

Agriculture. This value was then compared with the hydrological group (HYDGRP) standard of the US National Natural Protection Agency (NRCS) to categorize the soil permeability into one of four groups: A, B, C, or D. The soil hydrological groups in the study area were predominantly B and C. Land use attribute data comprises index values for each land use and the runoff parameters associated with different hydrological groups. These data were acquired from the existing expert rating and parameter system of PNPI. In some cases, field measurements and experimental research were used to supplement the data. Because of the diverse sources of spatial data, varying coordinate systems were used. Consequently, these systems should be projected or transformed to a consistent projection coordinate system to facilitate subsequent calculations. The soil types in the Loess Plateau are shown in Figure 3.

2.2.3 The LCI

The LCI denotes the potential pollution load produced by various land use types to the receiving water body. Higher LCI values indicate a greater potential for pollution, and therefore, pose a higher pollution risk. To determine the LCI in this study, the LCI value obtained through expert scoring in the PNPI model was adopted, as detailed in previous studies (Munafò et al., 2005). Experts assigned potential pollutant production scores to different land use types based on their professional knowledge, using a scoring system ranging from 0 to 10. The involvement of more experts in the scoring process, along with a wider research field and lower scoring standard deviation, yielded more reliable results. The LCI values and scoring standard deviations associated with the

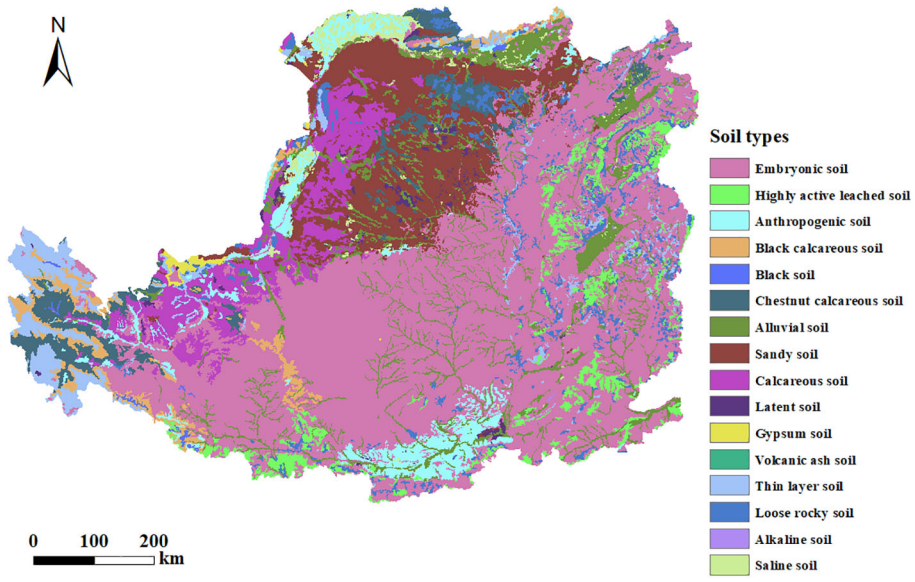

FIGURE 3
Soil type map of the Loess Plateau.

TABLE 2 The LCI values.

Land Use Type	Land Cover Index (0-10)	Standard Deviation
Water	0.14	0.38
Cropland	7.73	2.16
Forest	0.44	0.88
Grassland	1.94	2.27
Barren	0	0
Impervious	8.22	2.22

research area were screened and are presented in Table 2, as per Cecchi and Munafo (Munafò et al., 2005; Cecchi et al., 2007).

2.2.4 The DI and ROI

The DI was used to generalize the degradation processes occurring along the migration path of the pollution source in the confluence (Cecchi et al., 2007). A higher DI value indicates a shorter confluence distance, closer proximity to the river network, smaller degradation effect, and greater pollution risk. The DI was calculated by equation (1):

$$DI = Exp(-(D \cdot k)) \tag{1}$$

where DI is the value of the distance index, D is the confluence distance in units of cells, and k is a constant. Referring to Cecchi et al. (Shen et al., 2013; Tao et al., 2020), the value of k was determined as 0.090533.

The ROI is used to generalize the process of pollutant transport and the influence of terrain, soil, and land use on infiltration filtration. A high ROI value indicates lower infiltration filtration intensity, greater pollutant inflow into the receiving water body, and a higher pollution risk. The ROI was calculated by equation (2):

$$ROI = (\sum_{i=1}^{n} CROP_i)/n \tag{2}$$

$$CROP = ROP + C \tag{3}$$

where ROI is the value of the runoff index, and $CROP_i$ is the runoff parameter of the i-th unit on the runoff path after slope correction, which ranges from 0 to 1. When the calculated result of (3) is greater than 1, the value is taken as 1. The value of n corresponds to the number of units on the runoff path, while ROP is the runoff parameter. This study used the runoff coefficient table (Table 3) and slope correction coefficient C provided by Cecchi and Wu (Shen et al., 2013; Tao et al., 2020) for different land use and hydrological groups in the study area.

TABLE 3 Runoff coefficients for different land use types [11].

Land Use Type	A	B	C	D
Water	0	0	0	0
Cropland	0.66	0.78	0.85	0.89
Forest	0.36	0.6	0.73	0.79
Grassland	0.49	0.69	0.79	0.84
Barren	0.77	0.86	0.91	0.94
Impervious	0.75	0.85	0.9	0.92

2.2.5 Improvement of the PNPI model

The PNPI was used to comprehensively assess the intensity of the pollution load to rivers and other surface water bodies from the various land use types in the study area. It is a comprehensive function that integrates the LCI, DI, and ROI. However, the original PNPI uses the expert scoring method (Munafò et al., 2005; Cecchi et al., 2007), and the weight is fixed, which results in insufficient objectivity and practicability.

The original PNPI formula is expressed as follows,

$$PNPI = 4.8 \cdot LCIS + 2.6 \cdot ROIS + 2.6 \cdot DIS \tag{4}$$

where PNPI is the potential non-point source pollution index, *LCIS* is the standardized land use index value, *ROIS* is the standardized ROI, and *DIS* is the standardized DI.

To overcome the limitations of the original PNPI model, this study used the coefficient of variation decision-making method to assign weights to variables according to the relative changes of each index, which was not affected by subjective factors and was a more rigorous approach (Cecchi et al., 2007). The weight assigned to each index was optimized by employing the coefficient of variation decision-making method. The following calculations were undertaken:

1. The coefficient of variation of each index was calculated,

$$C.V._{\cdot i} = \frac{\sigma_i}{\overline{X_i}} \tag{5}$$

where $C.V._{\cdot i}$ is the coefficient of variation of the ith index set, $\overline{X}_i$ is the mean of the ith index set, and σ_i is the standard deviation of the ith index set.

2. The weights of each index were calculated and the PNPI was obtained,

$$w_i = \frac{C.V._{\cdot i}}{\sum_{i=1}^{m} C.V._{\cdot i}} \tag{6}$$

$$PNPI = w_{lci} \cdot LCIS + w_{roi} \cdot ROIS + w_{di} \cdot DIS \tag{7}$$

where w_i is the weight of the ith index set, and w_{lci}, w_{roi} and w_{di} are the weight coefficients of the LCI, ROI, and DI, respectively. The use of the coefficient of variation decision-making method improved the objectivity and practicability of the PNPI model.

3 Results

3.1 Land use/cover change and spatio-temporal transformation

The Loess Plateau region has undergone significant changes in LUCC in the past 31 years. A statistical analysis of LUCC in the region from 1990 to 2020 was conducted, and regional maps of land

use types were obtained for each year. The distribution of land uses for the representative years is shown in Figure 4. Grassland and cropland were the dominant land use types, accounting for approximately 79.8% of the total area. The area of water bodies remained relatively stable from 1990 to 2020. However, the area of cropland and barren land displayed a decreasing trend, with cropland displaying the most significant reduction. In contrast, forest, grassland, and impervious surfaces displayed an increasing trend, with the speed of impervious surface expansion being the most substantial.

The different land uses in the Loess Plateau region between 1990 and 2020 are presented in Figures 4, 5. They include cropland, forest, grassland, water bodies, barren land, and impervious surfaces. These different land uses provide an insight into how the region has been used over the past three decades. The figures show that the Loess Plateau region has experienced significant changes in land use over the past three decades, with some land uses experiencing declines and others experiencing increases. These changes are likely to have significant impacts on the environment, the local ecosystems, and the livelihoods of people living in the region.

Figures 4, 5 show a decline in cropland over the past 30 years. In 1990, the total area of cropland was 19,539.927 km², which reduced to 17,324.595 km² in 2020, accounting for approximately 3.8% of the region. In contrast, the area of forest and grassland increased slightly over the study period, with forest cover increasing from 7,477.452 km² in 1990 to 9,074.907 km² in 2020 and grassland cover increasing from 28,370.457 km² in 1990 to 29,236.518 km² in 2020. The area of water bodies, barren land, and impervious surfaces remained relatively stable over the three decades, with only minor fluctuations. The area of barren land also increased slightly from 3,176.451 km² in 1990 to 1,687.104 km² in 2020. The area of impervious surfaces increased from 630.918 km² in 1990 to 1,818.351 km² in 2020, accounting for approximately 2.0% of the region.

The changes in land use in the Loess Plateau region of China were likely driven by a combination of factors, including urbanization, economic development, and environmental degradation. The reduction in the area of cropland, forest, and grassland may have negative consequences for the region's ecosystem services, while the increase in the area of barren land and impervious surfaces may exacerbate environmental problems, such as soil erosion, water scarcity, and non-point source pollution.

The large-scale expansion of impervious surfaces in the downstream and middle-upper stream of the basin resulted in the conversion of grassland, barren land, and cropland to impervious surfaces from 1995 to 2020. In contrast, the establishment of ecological protection and returning farmland to forest projects in the upper stream caused the conversion of shrubland, barren land, and cropland to forest, resulting in an increase of nearly 1597.5 km² of forest in the region. To better understand the intrinsic conversion relationship of each land use type, a spatial data analysis was performed on the land use spatial data in 1990, 2000, 2010, and 2020, resulting in a land use transfer matrix (Table 4) and a land use conversion map (Figure 6) for the study area during four time periods. Combined with the results of Table 4 and Figure 6, the conversion of cropland to forest and grassland resulted in a slight increase in the area of these two types of land uses from 1990 to 2000. In the subsequent period of 2000 to 2010, the conversion of a large amount of barren land and cropland to impervious surfaces caused the rapid expansion of impervious surfaces. The small decrease in the area of grassland was mainly due to the conversion to cropland, and the small increase of forest was mainly due to the reduction of cropland and grassland from 2015 –2020. Finally, the expansion of impervious surfaces from 2015 to 2020 was mainly due to the conversion from cropland.

A comprehensive analysis of the LUCC patterns and spatiotemporal transformations of the Loess Plateau region over the past two decades was conducted. The results highlight the significant impact of urbanization and ecological protection

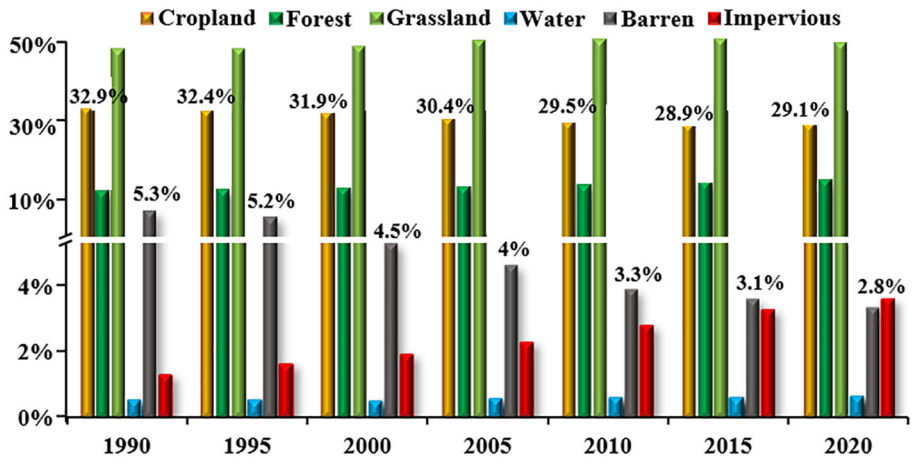

FIGURE 4
Proportional area of different land uses on the Loess Plateau from 1990 to 2020.

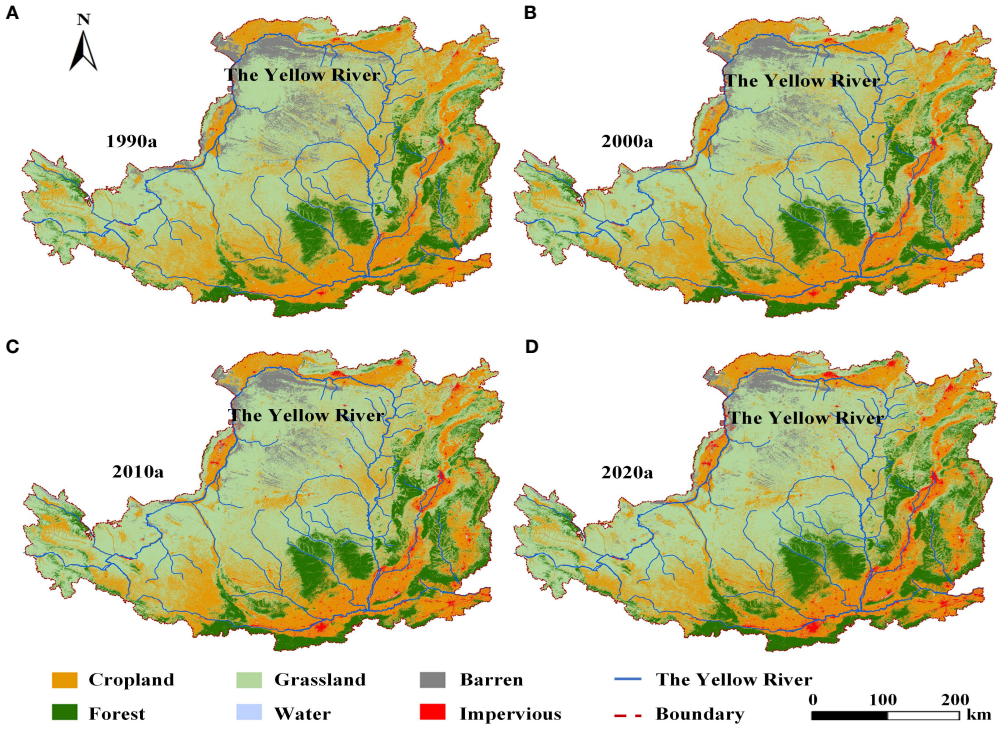

FIGURE 5
Land uses in the representative years. [**(A)** year 1990, **(B)** year 2000, **(C)** year 2010 **(D)** year 2020].

policies on LUCC in the region, providing valuable information for decision-makers to manage and utilize the region's natural resources sustainably.

3.2 Variations in PNP risk

Using the quantile classification method, the PNPI in the Loess Plateau was categorized into five risk levels: very low, low, moderate, high, and very high. Taking 1990 as the reference year, the changes in PNP risk levels in the Loess Plateau from 1990 to 2020 were assessed (Figure 7). The results showed a significant change in the distribution of PNP risk levels, with an increase in high and very high-risk areas downstream of urban areas along the Yellow River. The temporal changes of the proportional area of PNP risk in the Loess Plateau (Table 5) indicated that the very low-risk area remained stable from 1990 to 2020. However, the area of moderate-risk and very high-risk areas decreased, with very high-risk areas decreasing by almost 5.6% in 2020 compared to 1990. In contrast, the region designated as low-risk and moderate-risk expanded progressively over time. Specifically, the low-risk area increased by 6.45% between 1990 and 2005, followed by additional growth of 2% between 1990 and 2020. However, between 2005 and 2020, the low-risk area reduced by nearly 4.2%.

To accurately depict the inherent transformation in the area of each risk level, a comprehensive spatial analysis of the PNPI data from 1990 to 2020 was conducted. The aim was to provide a detailed assessment of the PNP risk distribution over time. The results of the analysis are presented in Figure 8, which shows a PNP risk distribution map, and Figure 9, which shows the proportional area of PNP risk grading. The area under each risk level changed slightly from 1990 to 2020. There was a modest transformation from moderate risk areas to low-risk areas, resulting in a slight increase in the latter category. Similarly, there was a partial shift from very high-risk to high-risk areas, which led to a slight increase in high-risk areas. These changes were consistent over the entire study period and were supported by the statistical analyses.

From 1990 to 2000, the area of each risk level experienced relatively minimal changes, except for a considerable increase in the very low-risk area. The observed increase in the very low-risk area was primarily due to the transformation from moderate-risk, high-risk, and very high-risk areas to very low-risk areas. Between 2000 and 2005, the area of each risk level underwent significant changes, with a considerable decrease in very high-risk areas. The observed decrease in the very high-risk area was primarily transformed to moderate and high-risk areas. Additionally, there was a partial increase in the low-risk area, which was attributable to the transformation from moderate-risk areas to low-risk areas. From 2005 to 2010, there was a slight decrease in the number of low-risk areas and an increase in the proportion of very high-risk areas. mainly due to the shift from high-risk areas and low-risk areas to very high-risk areas. Between 2010 and 2015, the area of each level of risk underwent significant changes, while the proportion of very high risk areas decreased, shifting towards high risk areas and low

risk areas. Finally, from 2015 to 2020, there was a further change in each level of risk, with an increase in the high-risk area mainly due to the transformation from moderate-risk, very low-risk, low-risk, and high-risk areas to very high-risk areas. These findings provide valuable insights into the dynamic nature of risk level transformations and highlight the importance of the ongoing monitoring and assessment of such areas.

High-risk and very high-risk areas were concentrated in the middle and lower reaches of the Yellow River for much of the study period. From 1990 to 2020, the PNP risk in the Loess Plateau region changed in a polarized manner. Moderate-risk areas in heavily affected urban areas, such as Guanzhong Plain urban agglomeration area (GPUAA) (Figure 7), transformed into high-risk areas, while very high-risk areas expanded radially along the downstream riverbank, increasing by 40%. The increase in very high-risk areas was the result of transformation from a large area of high-risk areas. Additionally, the PNP risk decreased upstream toward the water source area.

3.3 Dynamic characteristics of PNP risk and risk transformation

The dynamic characteristics of PNP risk in the Loess Plateau region were analyzed by considering the LUCC and PNP risks. To accurately capture the spatiotemporal transformation relationships of different risk level areas, a rigorous analysis of the spatial PNPI data transformation process was conducted for three distinct periods:1990–2000, 2000–2010, and 2010–2020. The results obtained from this analysis were expressed as a PNPI risk transfer matrix (Table 6) and PNPI risk transformation diagram (Figure 9), which offered valuable insights into the dynamics of risk transfer and transformation across time and space.

It was observed that the downstream basin areas of towns and farmland were consistently identified as high-risk and very high-risk areas. Specifically, during the period of 1990–2020, the downstream basin was primarily dominated by irrigated farmland, and the urbanization level was relatively low. The very high PNP risk areas were mainly concentrated in downstream towns and along the riverbanks. Since 2005, the towns in the Loess Plateau have undergone rapid expansion, leading to a corresponding rapid expansion of very high PNP risk areas surrounding these towns. The expansion of towns is considered the main contributing factor for the increase in very high-risk areas.

Additionally, since 1999, ecological protection projects such as returning farmland to forest and afforestation have been implemented in the Loess Plateau (Fu, 2010; Zhang et al., 2020). This has led to the transformation of shrubland, agroforestry land, and arable land into forest, resulting in a year-on-year increase in the forest area. This has ultimately led to a decrease in PNP risk in the upstream basin. The spatial transformation of PNP risk from 1990 to 2020 is shown in Figure 9.

TABLE 4 Land Use Transfer Matrix in the Loess Plateau region (Unit: km^2).

Time (Year)	Land Use Type	Cropland	Forest	Grassland	Water	Barren	Impervious
1990-2000	Cropland	160106.57	1352.33	29178.37	276.79	57.92	2852.88
	Forest	1105.01	71631.77	2155.49	2.24	0.03	4.93
	Grassland	25660.39	5683.04	250586.02	227.42	4389.71	321.70
	Water	480.66	4.21	176.35	1518.73	58.19	149.85
	Barren	414.63	0.04	8980.87	101.82	21405.05	98.59
	Impervious	310.79	1.16	71.97	48.32	3.14	4932.29
2000-2010	Cropland	152440.92	2196.35	29211.39	523.69	24.17	3681.49
	Forest	684.16	75775.18	2202.74	3.75	0.10	11.99
	Grassland	20164.30	5544.28	261378.57	282.95	2902.08	878.82
	Water	317.80	10.46	100.95	1621.41	28.38	96.53
	Barren	184.28	0.04	9506.69	144.63	15921.18	156.53
	Impervious	430.26	2.45	80.14	153.01	6.02	7689.06
2015-2020	Cropland	144366.01	1890.55	23891.49	463.79	56.01	3552.87
	Forest	1699.68	80029.68	1758.34	8.80	0.59	31.46
	Grassland	25193.61	8607.57	263936.48	235.08	3543.51	963.94
	Water	315.25	7.22	123.57	2005.30	140.23	137.86
	Barren	283.71	0.11	6067.80	72.41	12336.93	120.38
	Impervious	545.37	4.94	93.45	143.10	7.59	11720.73

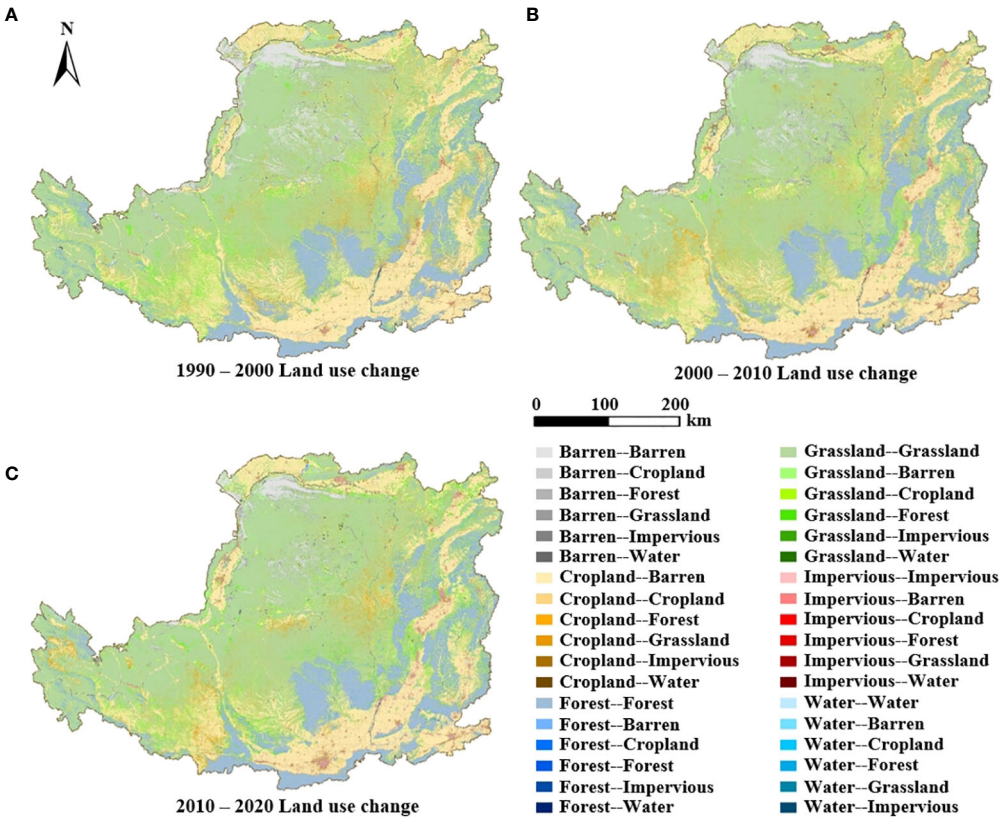

FIGURE 6
Land use conversion in the Loess Plateau from 1990 to 2020. [**(A)** 1990-2020 Land use change. **(B)** 2000-2010 Land use change. **(C)** 2010-2020 Land use change].

4 Discussion

1. The Loess Plateau region is characterized by a dominant land use pattern of grassland, cropland and forest, which are primarily concentrated in the middle and lower reaches of the watershed, accounting for approximately 93.5% of the total watershed area. From 1990 to 2020, there was a significant increase in the area of impervious surfaces in the middle and lower reaches of the watershed, which replaced a substantial portion of the original grassland and cropland. In the upper reaches of the watershed there was a transformation of barren land, grassland, and cultivated land into forest, resulting in an annual increase in forest area of approximately 1600 km^2 over the 31-year period.
2. Over the 31-year period spanning from 1990 to 2020, the Loess Plateau region experienced significant spatiotemporal changes in the risk of non-point source pollution, which exhibited a clear bipolarization trend. Specifically, the risk of PNP in the middle and lower reaches of the watershed and the cultivated land along the river channel, which are highly influenced by human activities, exhibited a notable increase of 40%. This increase was accompanied by a significant expansion of the high-risk area. In contrast, the risk of PNP in the upper reaches of the watershed exhibited a decreasing trend over the same period. These findings indicate the need for targeted management strategies aimed at mitigating the risk of PNP in the middle and lower reaches of the watershed, especially in cultivated areas that are highly influenced by human activities.
3. The spatiotemporal changes of PNP risk showed a high degree of consistency with land use patterns, with the high-risk and very high-risk areas mainly concentrated in the urban land in the middle and lower reaches and the cultivated land along the river channel. Low-risk and very low-risk areas were mainly concentrated in forest areas in the upper reaches. The expansion of urban areas in the watershed was the primary reason for the growth of very high-risk PNP areas, while the growth of forest areas was the primary reason for the expansion of low-risk and very low-risk PNP areas.
4. From 1990 to 2020, the combination of urbanization development and ecological protection measures had a significant impact on land use changes in the Loess Plateau region. Consequently, the PNP risk faced by the downstream water environment increased year-on-year, while the PNP risk in the upper reaches of the watershed decreased annually.

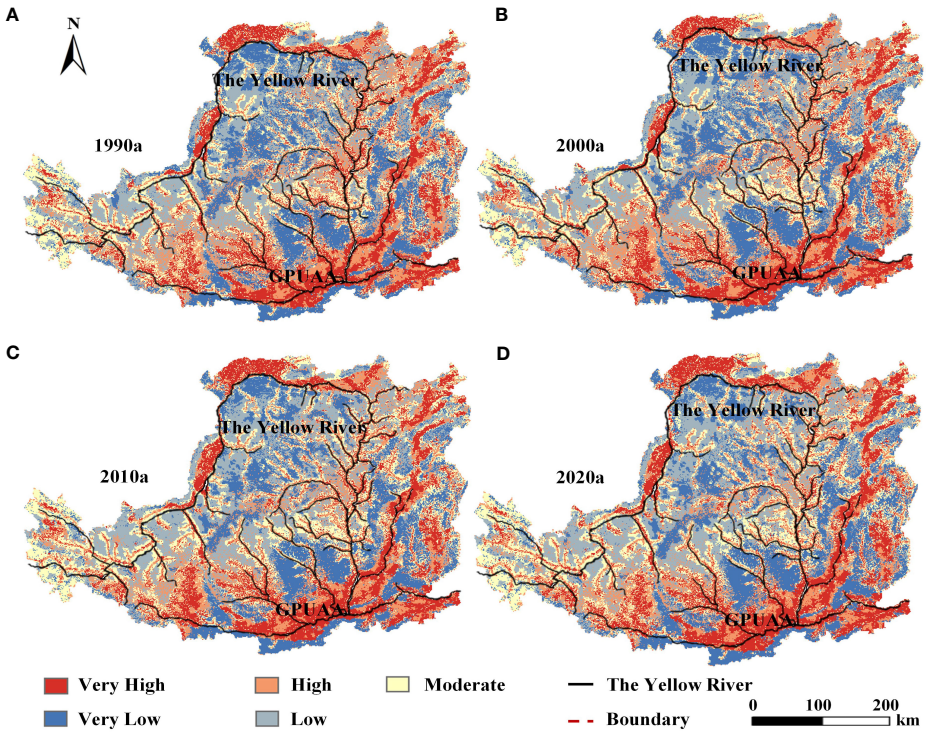

FIGURE 7
Distribution of the PNP risk on the Loess Plateau over time. [**(A)** year 1990, **(B)** year 2000, **(C)** year 2010, **(D)** year 2020].

5. In the future, the urban land in the lower reaches and the cultivated land along the river channel should be prioritized as the key management areas for watershed comprehensive management. To mitigate pollution risks, low impact development measures such as vegetation filtration belts and artificial wetlands should be implemented. The implementation of these measures can significantly reduce the NPSP risk and improve the ecological health and environmental quality of the region.
6. As a decision support system, the PNPI model has several advantages, including its simplicity, ease of use, minimal data requirements, and production of results that are easy to understand. The model can quickly provide the spatial distribution of PNP and evaluate the environmental impact of different land use plans in areas with limited or no data. However, due to climate conditions, land use intensity, and land use management patterns in different regions, some empirical parameters and weights in the PNPI model may not be universally applicable. They will require adjustments based on the specific characteristics of each region to ensure their universality and applicability. Overall, the PNPI model can effectively evaluate the PNP risk and spatial distribution in the Loess Plateau region, and it has the potential for application in other regions with similar characteristics.
7. The present study has shed light on the underlying causes and patterns of non-point source pollution in the Loess Plateau, thereby enabling the development of more effective and sustainable management strategies.

TABLE 5 Proportional Areas of Different Non-Point Source Pollution (PNP) Risk Levels from 1990 to 2020 (Unit: %).

Risk levels Year	Very low	Low	Moderate	High	Very high
1990	19.25	19.85	21.85	19.36	19.69
1995	19.46	20.18	21.73	20.24	18.39
2000	19.70	19.93	21.75	19.05	19.58
2005	18.90	21.13	21.57	20.25	18.15
2010	18.89	20.78	21.64	19.27	19.42
2015	19.41	20.68	21.37	19.78	18.76
2020	19.38	20.25	21.44	20.34	18.59

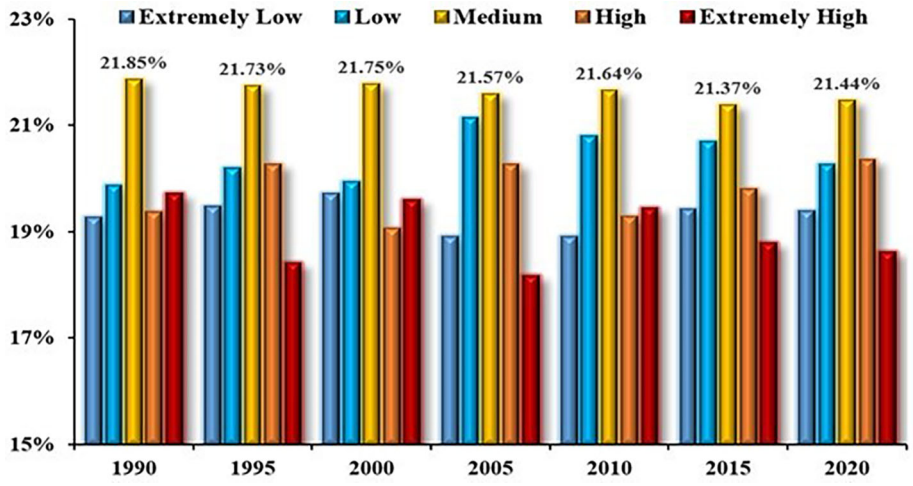

FIGURE 8
Proportional areas of the different PNP risk levels on the Loess Plateau from 1990 to 2020.

Despite the contributions of this study, some limitations should be acknowledged. For instance, the study area was not analyzed from multiple perspectives. Therefore, future research should be conducted on the Loess Plateau from different angles, such as sustainable agricultural practices, afforestation, and sediment control structures. This will allow for a more comprehensive investigation of measures to control non-point source pollution from various perspectives.

5 Conclusion

This study examined the spatiotemporal changes of PNP risk in the Loess Plateau region over the past 31 years using an improved PNPI model. The Loess Plateau, which is heavily influenced by human activities, was selected as a case study to explore the impact of different historical environmental conditions on PNP risk.

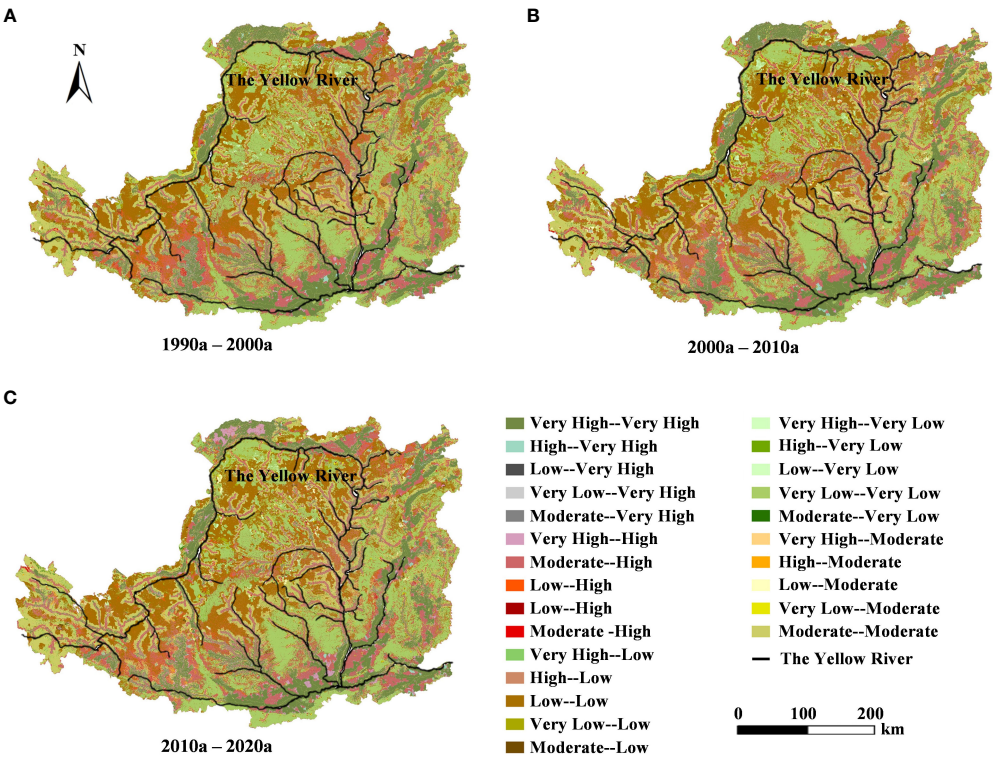

FIGURE 9
Conversion of PNP risk levels on the Loess Plateau from 1990 to 2020. [**(A)** 1990-2000 PNP risk levels change, **(B)** 2000-2010 PNP risk levels change, **(C)** 2010-2020 PNP risk levels change].

TABLE 6 Transfer matrix of PNP risk levels from 1990 to 2020 (Unit: km^2).

Time (Year)	PNP risk level	Very low	Low	Moderate	High	Very high
1990-2000	Very low	102490.52	6445.89	3124.89	2385.85	425.39
	Low	8628.16	98600.73	2271.79	9316.97	208.94
	moderate	3461.60	4598.63	108679.25	4855.25	8929.32
	high	2584.91	9541.40	5327.20	88690.41	7106.05
	Very high	303.18	249.52	10594.48	6376.35	99150.12
2000-2010	Very low	100619.77	11108.10	3485.13	1942.69	312.46
	Low	5790.33	99789.44	6822.61	6671.86	362.17
	moderate	2913.11	2585.72	105026.25	11276.49	8186.36
	high	2639.97	10828.58	4911.29	86472.84	6761.46
	Very high	470.53	313.45	9019.46	6786.07	99230.24
2010-2020	Very low	100746.13	6385.03	2537.96	2298.25	468.03
	Low	7007.72	103222.02	5211.45	8684.48	499.64
	moderate	4636.92	3128.20	107368.52	6004.60	8129.16
	high	2362.57	8502.91	5140.27	89963.94	7202.93
	Very high	455.79	244.78	7781.26	12772.07	93598.39

To accurately reflect the actual situation in the watershed, the PNPI model, which was originally developed by Italian researchers to measure PNP, was improved in three aspects: the land use categories were expanded, comparisons of land use categories were made, and the soil types were divided into different permeability levels. This enhanced model could comprehensively evaluate non-point source pollution characteristics in a watershed influenced by human activities. The spatial distribution maps of the LCI, ROI, and DI, as well as the PNPI and qualitative analysis results, were consistent with the actual situation in the Loess Plateau region (Wang et al., 2010; Liang et al., 2015; Li H. L. et al., 2021; Liu et al., 2021; Qian et al., 2021; Li et al., 2022; Shi et al., 2022). Therefore, the model was found to be applicable to the study area.

Our study provides valuable insights into the spatial and temporal distribution of PNP risk. The results of this study could serve as a basis for the development of effective policies and strategies aimed at mitigating the risk of PNP. It is recommended that future studies should further investigate the underlying causes of the observed changes and assess their potential implications on the environment and public health.

Data availability statement

The original contributions presented in the study are included in the article/supplementary material. Further inquiries can be directed to the corresponding author.

Author contributions

QN: Methodology, Software, Writing – original draft. XF: Conceptualization, Data curation, Writing – original draft. CL: Data curation, Methodology, Writing – original draft. YZ: Conceptualization, Data curation, Writing –original draft. PG: Data curation, Formal Analysis, Writing – original draft. YH: Data curation, Methodology, Writing – original draft. PL: Conceptualization, Writing – review and editing. JL: Conceptualization, Supervision, Writing – original draft, Writing – review and editing.

Funding

This research was funded by the Shaanxi Postdoctoral Science Foundation 2018 (2018BSHEDZZ21), the National Natural Foundation of China (51679185), and the General Financial Grant from the China Post-doctoral Science Foundation (2017M623088). Yinshanbeilu Grassland Eco-hydrology National Observation and Research Station, China Institute of Water Resources and Hydropower Research, Beijing 100038, China, Grant NO. YSS2022004. And the APC was funded by the Fundamental Research Funds for the Central Universities, CHD (300102292903).

Acknowledgments

We express our sincere gratitude to the esteemed Key Laboratory of Subsurface Hydrology and Ecological Effects in the Arid Region, Ministry of Education, for their invaluable support and contributions to our research endeavor.

Conflict of interest

The authors declare that the research was conducted in the absence of any commercial or financial relationships that could be construed as a potential conflict of interest.

Publisher's note

References

Ai, L., Shi, Z. H., Yin, W., and Huang, X. (2015). Spatial and seasonal patterns in stream water contamination across mountainous watersheds: linkage with landscape characteristics. *J. Hydrol.* 523, 398–408. doi: 10.1016/j.jhydrol.2015.01.082

Alnahit, A. O., Mishra, A. K., and Khan, A. A. (2020). Quantifying climate, streamflow, and watershed control on water quality across Southeastern US watersheds. *Sci. Total Environ.* 739, 139945. doi: 10.1016/j.scitotenv.2020.139945

Borah, D. K., and Bera, M. (2004). Watershed-scale hydrologic and nonpoint-source pollution models: review of applications. *Trans. ASAE* 47 (3), 1553–1566. doi: 10.13031/2013.16110

Cecchi, G., Fabiani, C., Mancini, L., and Munafò, M. (2005). "Pollutant loading in the Tevere river basin," in *Tevere - Pilot River Basin Article 5 Report - Pursuant to the Water Framework Directive*. Eds. M. Ruisi, A. Prati and P. Traversa(Roma: Gangemi), 81–87.

Cecchi, G., Mancini, L., et al. (1982). *Assessment of Potential River Pollution From Non-Point Sources in the Viterbo Province[M]* (Academic Press).

Cecchi, G., Munafò, M., Baiocco, F., Andreani, P., and Mancini, L. (2007). Estimating river pollution from diffuse sources in the Viterbo province using the potential non-point pollution index. *Annali dell'Istituto superiore di sanità* 43 (3), 295–301.

Clément, F., Ruiz, J., Rodríguez, M. A., Blais, D., and Campeau, S. (2017). Landscape diversity and forest edge density regulate stream water quality in agricultural catchments. *Ecol. Indic.* 72, 627–639. doi: 10.1016/j.ecolind.2016.09.001

Cotman, M., Drolc, A., and Koncan, J. Z. (2008). Assessment of pollution loads from point and diffuse sources in small river basin: case study Ljubljanica river. *Environ. Forensics* 9 (2-3), p.246–p.251. doi: 10.1080/15275920802122965

de Mello, K., Taniwaki, R. H., de Paula, F. R., Valente, R. A., Randhir, T. O., Macedo, D. R., et al. (2020). Multiscale land use impacts on water quality: assessment, planning, and future perspectives in Brazil. *J. Environ. Manage.* 270, 110879. doi: 10.1016/j.jenvman.2020.110879

Fan, Y. P., and Fang, C. L. (2020). A comprehensive insight into water pollution and driving forces in Western China—case study of Qinghai. *J. Clean. Prod.* 274, 123950. doi: 10.1016/j.jclepro.2020.123950

Fu, B. (2010). Soil erosion and its control in the loess plateau of China. *Soil Use Manage.* 5 (2), 76–82. doi: 10.1111/j.1475-2743.1989.tb00765.x

Ge, X. J., Huang, B., Yuan, Z. J., Wang, D. D., Wang, Q. Q., Chen, J. C., et al. (2022). Temporal and spatial variation characteristics and source analysis of agricultural non-point source pollution load in Guangdong during the past 20 years. *Huan Jing Ke Xue.* 43 (6), 3118–3127.

Gémesi, Z., Downing, J. A., Cruse, R. M., and Anderson, P. F. (2011). Effects of watershed configuration and composition on downstream lake water quality. *J. Environ. Qual.* 40 (2), 517–527. doi: 10.2134/jeq2010.0133

Geng, R., Li, M., Wang, X., and Pang, S. (2015). Effect of land use/landscape changes on diffuse pollution load from watershed based on swat model. *Trans. Chin. Soc. Agric. Eng.* 31 (16), 241–250.

Gossweiler, B., Wesström, I., Messing, I., Villazón, M., and Joel, A. (2021). Impact of land use change on non-point source pollution in a semi-arid catchment under rapid urbanisation in Bolivia. *Water* 13 (4), 410. doi: 10.3390/w13040410

Guo, P., Lyu, J. Q., Yuan, W. N., Zhou, X., Mo, S., Mu, D., et al. (2022). Detecting the quantitative hydrological response to changes in climate and human activities at temporal and spatial scales in a typical gully region of the loess plateau, China. *Water* 14, 257–280. doi: 10.3390/w14020257

Hao, Y., and Lu, J. (2021). Teleconnection between climate oscillations and riverine nutrient dynamics in southeast China based on wavelet analysis. *Environ. Sci. Pollut. Res.*, 28, 41807–41820. doi: 10.1007/s11356-021-13715-x

Hou, L., Zhou, Z., Wang, R., Li, J., Dong, F., and Liu, J. (2022). Research on the non-Point source pollution characteristics of important drinking water sources. *Water* 14, 211. doi: 10.3390/w14020211

Ierodiaconou, D., Laurenson, L., Leblanc, M., Stagnitti, F., Duff, G., Salzman, S., et al. (2005). The consequences of land use change on nutrient exports: a regional scale assessment in south-west Victoria, Australia. *J. Environ. Manage.* 74 (4), 305–316. doi: 10.1016/j.jenvman.2004.09.010

Lee, S. W., Hwang, S. J., Lee, S. B., Hwang, H. S., and Sung, H. C. (2009). Landscape ecological approach to the relationships of land use patterns in watersheds to water quality characteristics. *Landscape Urban Plann.* 92 (2), 80–89. doi: 10.1016/j.landurbplan.2009.02.008

Li, L., Gou, M., Wang, N., Ma, W., and La, L. (2021). Landscape configuration mediates hydrology and nonpoint source pollution under climate change and agricultural expansion. *Ecol. Indic.*, 129, 1470–1160. doi: 10.1016/j.ecolind.2021.107959

Li, C., Zhang, H., Hao, Y., and Zhang, M. (2020). Characterizing the heterogeneous correlations between the landscape patterns and seasonal variations of total nitrogen and total phosphorus in a peri-urban watershed. *Environ. Sci. Pollut. Res.* 27 (27), 34067–34077. doi: 10.1007/s11356-020-09441-5

Li, H. L., Zhang, J. J., Zhang, Y. F., Chang, G. L., Shi, D. D., Xu, W. J., et al. (2021). Analysis of spatial-temporal variation characteristics of potential non-point source pollution risks in the upper beiyun river basin using different weighting methods. *Huan Jing Ke Xue* 42 (6), 2796–2809. doi: 10.13227/j.hjkx.202010225

Li, H., Zhang, J., Zhang, S., Zhang, W., Zhang, S., Yu, P., et al. (2022). A framework to assess spatio-temporal variations of potential non-point source pollution risk for future land-use planning. *Ecol. Indic.* 137, 108751. doi: 10.1016/j.ecolind.2022.108751

Liang, W., Bai, D., Wang, F., Fu, B., Yan, J., Wang, S., et al. (2015). Quantifying the impacts of climate change and ecological restoration on streamflow changes based on a budyko hydrological model in China's loess plateau. *Water Resour. Res.* 51 (8), 6500–6519. doi: 10.1002/2014WR016589

Liu, Q., Yang, Z., Shi, H., and Wang, Z. (2019). Ecological risk assessment of geohazards in natural world heritage sites: an empirical analysis of Bogda, Tianshan. *Open Geosci.* 11, 327–340. doi: 10.1515/geo-2019-0026

Liu, Y., Yang, C., Yu, X., Wang, M., and Qi, W. (2021). Monitoring the landscape pattern and characteristics of non-point source pollution in a mountainous river basin. *Int. J. Environ. Res. Public Health* 18 (21), 11032. doi: 10.3390/ijerph182111032

Loague, K., and Corwin, D. L. (1996). "Uncertainty in regional-scale assessments of non-point source pollutants," in *Applications of GIS to the Modeling of Non-Point Source Pollutants in the Vadose Zone*. Eds. D. L. Corwin and K. Loague (Madison: Soil Science Society of America), 131–152.

Loague, K., and Corwin, D. L. (2005). "Point and nonpoint source pollution," in *Encyclopedia of Hydrological Sciences*. Ed. M. G. Anderson (Chichester, UK: John Wiley & Sons, Ltd), 1427–1439.

Luo, P., Zheng, Y., Wang, Y., Zhang, S., Yu, W., Zhu, X., et al. (2022). Comparative assessment of sponge city constructing in public awareness, Xi'an, China. *Sustainability* 14 (18), 11653. doi: 10.3390/su141811653

Lyu, J. Q., Liu, J., Shen, B., Sun, X. L., Hou, Z. Q., Mu, D. R., et al. (2018). Study on regulation and control of urban river dams based on distributed hydrological model GBHM. *Hydrol. Res.* 40 (9), 63–69.

Lyu, J., Mo, S., Luo, P., Zhou, M., Shen, B., and Nover, D. (2019). A quantitative assessment of hydrological responses to climate change and human activities at spatiotemporal within a typical catchment on the loess plateau, China. *Quaternary Int.* 527 (2019), 1–11. doi: 10.1016/j.quaint.2019.03.027

Mohammadi, H. (2001). Hydrological analysis of flood forecastin: Kasilaian watershed[D] (University of Mazandaran).

Munafò, M., Cecchi, G., Baiocco, F., and Mancini, L. (2005). River pollution from non-point sources: a new simplified method of assessment. *J. Environ. Manage.* 77 (2), 93–98. doi: 10.1016/j.jenvman.2005.02.016

Novotny, V., and Chesters, G. (1981). *Handbook of Nonpoint Source Pollution: Sources and Management* (New York, N.Y: Van Nostrand Reinold Co), ISBN: .

Ouyang, W., Jiao, W., Li, X. M., Giubilato, E., and Critto, A. (2016). Long-term agricultural non-point source pollution loading dynamics and correlation with outlet sediment geochemistry. *J. Hydrol.* 540, 379–385. doi: 10.1016/j.jhydrol.2016.06.043

Ouyang, W., Skidmore, A. K., Toxopeus, A. G., and Hao, F. (2010). Long-term vegetation landscape pattern with non-point source nutrient pollution in upper stream of Yellow River basin. *J. Hydrol.* 389 (3–4), 373–380. doi: 10.1016/j.jhydrol.2010.06.020

Park, M., Choi, Y. S., Shin, H. J., Song, I., Yoon, C. G., Choi, J. D., et al. (2019). A comparison study of runoff characteristics of non-point source pollution from three watersheds in South Korea. *Water* 11, 966. doi: 10.3390/w11050966

Puccinelli, C., Marcheggiani, S., Munafò, M., Andreani, P., and Mancini, L. (2013). Evaluation of Aquatic Ecosystem Health Using the Potential Non-Point Pollution Index (PNPI) Tool. *Diversity of Ecosystems, InTech, Crossref.* doi: 10.5772/36330

Qian, Y., Sun, L., Chen, D., Liao, J., Tang, L., and Sun, Q. (2021). The response of the migration of non-point source pollution to land use change in a typical small watershed in a semi-urbanized area. *Sci. Total Environ.* 785, 147387. doi: 10.1016/j.scitotenv.2021.147387

Ritter, L., Solomon, K., Sibley, P., Hall, K., Keen, P., Mattu, G., et al. (2002). Sources, pathways, and relative risks of contaminants in surface water and ground-water: a perspective prepared for the Walkerton inquiry. *J. Toxicol. Environ. Health Part A* 65 (1), 1–142. doi: 10.1080/152873902753338572

Sharma, A., and Tiwari, K. N. (2019). Predicting non-point source of pollution in maithon reservoir using a semi-distributed hydrological model. *Environ. Monit. Assess.* 191 (8), 522.1–522.13. doi: 10.1007/s10661-019-7674-y

Shen, Z., Chen, L., Ding, X., Hong, Q., and Liu, R. (2013). Long-term variation, (1960–2003) and causal factors of non-point-source nitrogen and phosphorus in the upper reach of the Yangtze River. *J. Hazard. Mater.* 252–253, 45–56. doi: 10.1016/j.jhazmat.2013.02.039

Shen, Z. Y., Hou, X. S., Li, W., and Aini, G. (2014). Relating landscape characteristics to non-point source pollution in a typical urbanized watershed in the municipality of Beijing. *Landscape Urban Plann.* 123, 96–107. doi: 10.1016/j.landurbplan.2013.12.007

Shen, Z., Zhong, Y., Huang, Q., and Chen, L. (2015). Identifying non-point source priority management areas in watersheds with multiple functional zones. *Water Res.* 68 (1), 563–571. doi: 10.1016/j.watres.2014.10.034

Shi, J., Jin, R., and Zhu, W. (2022). Quantification of effects of natural geographical factors and landscape patterns on non-point source pollution in watershed based on geodetector: Burhatong river basin, Northeast China as an example. *Chin. Geogr. Sci.* 32, 707–723. doi: 10.1007/s11769-022-1295-z

Sun, B., Zhang, L., Yang, L., Zhang, F., Norse, D., and Zhu, Z. (2012). Agricultural non-point source pollution in China: causes and mitigation measures. *Ambio* 41 (4), 370–379. doi: 10.1007/s13280-012-0249-6

Tao, Y., Liu, J., Guan, X., Chen, H., Ren, X., Wang, S., et al. (2020). Estimation of potential agricultural non-point source pollution for Baiyangdian Basin, China, under different environment protection policies. *PloS One* 15 (9), e0239006. doi: 10.1371/journal.pone.0239006

Ting, L. I. (2010). *Study on assessment of pollution load in small watershed based on PNPI[D]* (Tsinghua University).

Vörösmarty, C. J., McIntyre, P. B., Gessner, M. O., Dudgeon, D., Prusevich, A., Green, P., et al. (2010). Global threats to human water security and river biodiversity. *Nature* 467 (7315), 555–561. doi: 10.1038/nature09440

Wang, X. Y. (2006). Management of agricultural nonpoint source pollution in China: current status and challenges. *Water Sci. Technol.* 53 (2), 1–9. doi: 10.2166/wst.2006.033

Wang, Y., Shao, M., and Shao, H. (2010). A preliminary investigation of the dynamic characteristics of dried soil layers on the loess plateau of China. *J. Hydrol.* 381 (1–2), 9–17. doi: 10.1016/j.jhydrol.2009.09.042

Xu, W. J., Chang, G. L., Shi, D. D., Ye, Z. H., Zhang, Y. F., and Zhang, S. H. (2021). Spatial distribution of non-point source pollution risk in the upper Beiyun River Watershed. *Acta Scientiae Circumstantiae* 41 (1), 7–14. doi: 10.13671/j.hjkxxb.2020.0368

Xu, B., Niu, Y., Zhang, Y., Chen, Z., and Zhang, L. (2022). China's agricultural non-point source pollution and green growth: interaction and spatial spillover. *Environ. Sci. pollut. Res.* 29, 60278–60288. doi: 10.1007/s11356-022-20128-x

Yang, J., and Huang, X. (2021). The 30 m annual land cover dataset and its dynamics in China from 1990 to 2019. *Earth Syst. Sci. Data* 13 (8), 3907–3925. doi: 10.5194/essd-13-3907-2021

Yang, X., Liu, Q., Luo, X., and Zheng, Z. (2017). Spatial regression and prediction of water quality in a watershed with complex pollution sources. *Sci. Rep.* 7 (1), 8318. doi: 10.1038/s41598-017-08254-w

Yang, F., Xu, Z., Zhu, Y., He, C., Wu, G., Qiu, J. R., et al. (2013). Evaluation of agricultural nonpoint source pollution potential risk over China with a Transformed-Agricultural Nonpoint Pollution Potential Index method. *Environ. Technol.* 34 (21-24), 2951–2963. doi: 10.1080/09593330.2013.796008

Zhang, X. (2008). Responses of streamflow to changes in climate and land use/cover in the loess plateau, China. *Water Resour. Res* 44 (7). doi: 10.1029/2007WR006711

Zhang, Y., et al. (2014). Modeling potential non-point source pollution in a large-scale watershed using SWAT. *Environ. Sci. pollut. Res.* 21 (18), 10718–10733.

Zhang, T., Gao, Y., Xie, Z., and Zhang, B. (2020). How human activity has changed the regional habitat quality in an eco-economic zone: evidence from poyang lake eco-economic zone, China. *Int. J. Environ. Res. Public Health* 17 (17), 6253. doi: 10.3390/ijerph17176253

Zhang, H., and Huang, G. H. (2011). Assessment of non-point source pollution using a spatial multicriteria analysis approach. *Ecol. Model.* 222 (2), 313–321. doi: 10.1016/j.ecolmodel.2009.12.011

frontiers | Frontiers in Ecology and Evolution

TYPE Original Research
PUBLISHED 17 August 2023
DOI 10.3389/fevo.2023.1251765

OPEN ACCESS

EDITED BY
Naifei Liu,
Xi'an University of Architecture and Technology, China

REVIEWED BY
Jiqiang Lyu,
Chang'an University, China
Aizhong Luo,
Guizhou University of Engineering Science, China

*CORRESPONDENCE
Fengyin Liu
liufy211@163.com

RECEIVED 02 July 2023
ACCEPTED 18 July 2023
PUBLISHED 17 August 2023

CITATION
Zhong L, Wang B, Zhao X, Liu F, Miao M and Pu C (2023) Study on rainfall infiltration characteristic parameters of unsaturated soil.
Front. Ecol. Evol. 11:1251765.
doi: 10.3389/fevo.2023.1251765

Study on rainfall infiltration characteristic parameters of unsaturated soil

Lijia Zhong[1], Bo Wang[2], Xuguang Zhao[3], Fengyin Liu[1]*, Meng Miao[1] and Cheng Pu[4]

[1]Institute of Geotechnical Engineering, Xi'an University of Technology, Xi'an, Shaanxi, China, [2]JiKan Research Institute of Engineering Investigation and Design, Co., Ltd., Xi'an, Shaanxi, China, [3]Guangzhou Traffic Design & Research Institute Co., Ltd., Guangzhou, Guangdong, China, [4]PowerChina Northwest Engineering Co., Ltd., Xi'an, Shaanxi, China

The study of the rainfall infiltration mechanism of unsaturated soil has always been a hot issue in the field of geotechnical engineering. It is worth studying which parameters should be introduced to characterize the infiltration characteristics of unsaturated soil in the calculation and analysis of rainfall infiltration. In this paper, the Fredlund–Xing model was quoted in the SEEP/W module of the Geostudio software, and the transient numerical calculation of rainfall infiltration under the same rainfall duration T and different rainfall intensity I was carried out for a soil column. Three infiltration characteristic parameters were introduced: rainfall infiltration front depth WF, suction reduction depth MR_n, and section infiltration rate IR. The variation of these three parameters and rainfall intensity I during rainfall were sorted out and analyzed; it is indicated that WF increases with the extension of rainfall duration. MR_n decreases with the increase of suction reduction rate $n\%$, and when the rainfall duration is 24 h, the maximum depth of the soil column affected by rainfall is approximately 35% of the total depth. IR is mainly affected by the rainfall intensity I and the saturation permeability coefficient k_s. There is a limit value for the influence of I on WF, MR_n, and IR, and the limit rainfall intensity under the calculation conditions in this paper is $I = 2.5k_s$.

KEYWORDS

unsaturated soil, seepage, rainfall infiltration, numerical simulation experimentation, characteristic parameter

1 Introduction

Slope instability and landslide disasters occur frequently. Landslides are harmful, large scale, and difficult to predict. They not only seriously threaten the safety of people's lives, but also cause certain ecological damage. Many scholars (Anderson and Zhu, 1996; Rahardjo, 1996; Rahardjo et al., 2001; Tsaparas et al., 2002; Rahardjo et al., 2005; Rahardjo et al., 2007; Rahardjo et al., 2008) have summarized and analyzed the causes of many landslide accidents, and found that rainfall infiltration is the most important cause of landslides. For example, the landslide in Huaxian County, Shaanxi Province in 2006 was a

typical case of rainfall-induced loess slope instability. Therefore, it is of great significance to study the mechanism of the rainfall infiltration characteristics.

At present, many scholars have carried out a lot of related research. Romano et al. (1998), Corradini et al. (2000), and Cho and Lee (2002) studied the characteristics of rainfall infiltration from the perspectives of soil science, agricultural water, and soil engineering and hydrology. Based on the effective stress principle of unsaturated soil and the double stress strength theory, Zhou et al. (2014) established a nonlinear programming model, and verified the correctness of the proposed model through an example analysis, so that we have a further understanding of the law of soil slope instability under unsaturated unsteady seepage. Wang et al. (2015) found that there was no slope runoff phenomenon through numerical experiments, which was significantly different from the theory of orthogonal infiltration boundary. Moreover, the discrimination mechanism of soil moisture content, infiltration capacity, and slope boundary condition transformation of sandy slope surface calculated according to the orthogonal infiltration boundary theory was not consistent with the actual situation. Wu et al. (2017) conducted a physical model test on the anti-seepage effect of the slope of the unsaturated drainage structure, and found that the drainage-seepage control effect and ecological function of the binary structure were significantly better than that of a single structure. Zeng et al. (2020) found that the infiltration depth of the slope was the largest at the foot of the slope and the smallest at the middle of the slope, and the infiltration rate was the largest at the top of the slope and the smallest at the middle of the slope.

However, so far, no one has summarized the accurate infiltration law characteristics in the whole rainfall process, and the understanding of rainfall infiltration only stays on the qualitative level. Therefore, it is necessary to study the parameters or indicators that could quantitatively describe the characteristics of rainfall infiltration.

In this study, the Fredlund–Xing model is introduced into the software program, and the unsaturated seepage equation is used to calculate the water seepage in the soil. Three rainfall infiltration characteristic parameters are introduced into the data analysis of a rainfall infiltration numerical experiment: infiltration front depth *WF*, suction reduction depth MR_n, and section infiltration rate *IR*. These three parameters were used to describe the whole infiltration process, which not only is of great significance for the collation and comparative analysis of the large number of data in the numerical simulation of one-dimensional rainfall infiltration, but also can provide new important indicators for the analysis of rainfall infiltration mechanism in practical engineering.

2 Numerical test scheme and infiltration characteristic parameters

2.1 Calculation schemes

In this paper, by using the SEEP/W module in Geostudio2004 developed by the Geo-slope company (Yang, 1992), the finite element numerical calculation of one-dimensional transient saturated–unsaturated seepage for an isotropic homogeneous soil column with a height of 5 m and a width of 0.4 m is carried out, considering rainfall conditions. The influence of the rainfall intensity I and the infiltration characteristic parameters on the infiltration characteristics of unsaturated soil columns is studied.

The underground water level of the soil column model is located at its bottom and does not change during the whole rainfall process. Therefore, a total head boundary with constant 0 is set at the bottom of the soil column. The left and right sides of the soil column are impermeable, and the boundary condition of 0 flow is set at both sides. The surface runoff during rainfall and the evaporation of surface water after rain stop are not be considered in the model test. The seepage calculation and analysis of seven different rainfall intensities with a rainfall duration of 24 h are carried out for the soil column. The design values of rainfall intensity I and soil parameters under each working condition are shown in Table 1.

In Table 1, the rainfall intensity I is selected according to the multiple of saturated permeability coefficient k_s. For example, $0.5\times k_s$ indicates that the rainfall intensity I (surface rainwater flow) is equal to 50% of the saturated permeability coefficient of soil. In this way, the permeability coefficient of the soil is linked to the amount of rainfall flow applied. The rainfall time step indicates that the time from the beginning of rainfall is the starting point of timing. The rainfall duration of 24 h indicates that the rainfall stops at 24 h, and 24 h to 240 h indicate the time period after the rainfall stops.

In the finite element calculation, the mesh division of the soil column model, the water head boundary condition, and the flow boundary condition are shown in Figure 1A, and the pore water pressure u_w distribution is shown in Figure 1B.

The data calculated by the soil column of each working condition will be extracted and sorted out. The variation rules of volumetric water content, infiltration characteristic parameters, and rainfall intensity in the process of rainfall duration will be analyzed.

2.2 Definition of the rainfall infiltration characteristic parameters

The analysis of the law of the soil column in the rainfall duration introduces three parameters to describe the infiltration characteristics: infiltration front depth *WF*, suction reduction depth MR_n, and section infiltration rate *IR*. These three parameters are defined in detail as follows.

2.2.1 Infiltration front depth *WF*

The infiltration front depth *WF* is defined as the depth from the surface to the position of the soil where the volumetric water content θ begins to change due to rainwater infiltration, which can be determined by the graphical method shown in Figure 2. The depth of the intersection point of the section line of the initial volume water content and the section line of the water content at any time is *WF*. In other words, *WF* is the minimum depth at which the volumetric water content of the soil at a certain depth at any time is equal to the initial volumetric water content.

TABLE 1 The summary of parameters used during different series of numerical studies.

Working condition number	Rainfall intensity I		Saturated permeability coefficient k_s (m/s)	Underground water level WT (m)	Rainfall duration T (h)
	(Indicated by k_s)	(mm/h)			
1	$0.1\times k_s$	0.036	1.0×10^{-7}	5.0	24
2	$0.5\times k_s$	0.18			
3	$1.0\times k_s$	0.36			
4	$2.5\times k_s$	0.9			
5	$5.0\times k_s$	0.18			
6	$10.0\times k_s$	3.6			
7	$25.0\times k_s$	9.0			

The rainfall time step of each working condition is: 1 h, 3 h, 6 h, 12 h, 24 h, 48 h, 72 h, 96 h, 144 h, and 240 h.

WF is a depth index that is greatly affected by the rainfall conditions. In order to discuss this index in a more general case, the author introduces the dimensionless parameter of normalized infiltration front depth WF^{nor}, which can easily describe the infiltration characteristics of the soil column. It can be calculated as Eq. 1:

$$WF^{nor} = \frac{WF}{WT} \tag{1}$$

where WF is the infiltration front depth (m) and WT is groundwater level (m).

2.2.2 Suction reduction depth MR_n

While the finite element calculation of seepage is completed, the distribution of pore water pressure u_w with depth under different working conditions is extracted for further analysis. The suction reduction depth MR_n is defined as the depth at which the soil matric suction $(u_a - u_w)_r$ decreases to the initial matric suction $(u_a - u_w)_i$ during the rainfall process. n% is the matrix suction reduction rate.

In the numerical calculation, five kinds of matric suction reduction rates are set, i.e., n% is 10%, 20%, 30%, 40%, and 90%, respectively. The corresponding suction reduction depths are MR_{10}, MR_{20}, MR_{30}, MR_{40}, and MR_{90}. For example, MR_{10} means the corresponding soil position when the suction is reduced by 10%, that is, all the matric suction $(u_a - u_w)$ above this depth has been reduced by 10% compared with the initial matric suction.

MR_n is used to describe the distribution law of matric suction reduction of soil column section caused by the rainfall process. As shown in Figure 3, we can determine five suction reduction depths (i.e., MR_{10}, MR_{20}, MR_{30},

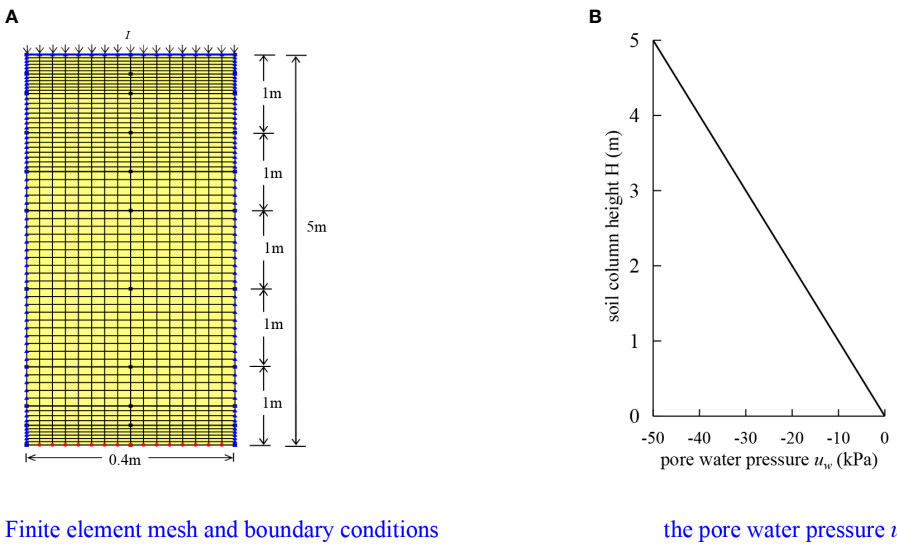

Finite element mesh and boundary conditions

the pore water pressure u_w

FIGURE 1
Finite element, boundary conditions, and initial pore water pressure conditions of the soil column. **(A)** Finite element mesh and boundary conditions, **(B)** The pore water pressure u_w.

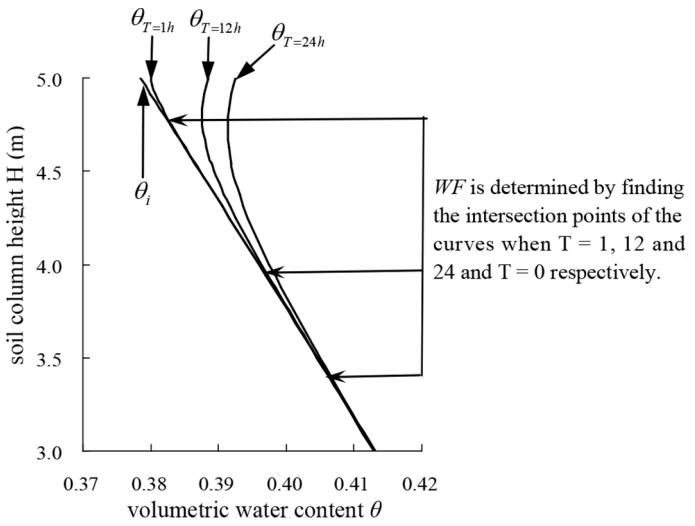

FIGURE 2
The schematic diagram of the determination method of the infiltration front depth *WF*.

MR_{40}, and MR_{90}) by the distribution of pore water pressure with depth. The influence of the whole rainfall process on the matric suction reduction of the soil column can be described according to this figure.

We then introduce a non-dimensional parameter of the normalized suction reduction depth MR_n^{nor} to characterize the suction reduction law of the soil column more conveniently. The calculation of MR_n^{nor} is as shown in Eq. 2:

$$MR_n nor = \frac{MR_n}{WT} \tag{2}$$

where MR_n is the suction reduction depth (m) and WT is groundwater level (m).

2.2.3 Section infiltration rate *IR*

In order to represent the flow velocity of rainwater in the soil column through the *Y* direction of a certain section, the parameter of section infiltration rate *IR* is introduced.

The soil column used in the seepage analysis of the model calculation in this paper is divided into seven sections along the horizontal direction, and the variation of the infiltration rate of each section with time is monitored. The height of each section is divided by the depth of the groundwater level, and are normalized to obtain the corresponding normalized height H^{nor}. The position of *IR* and its corresponding section normalized height H^{nor} are calculated for each section, as shown in Figure 4.

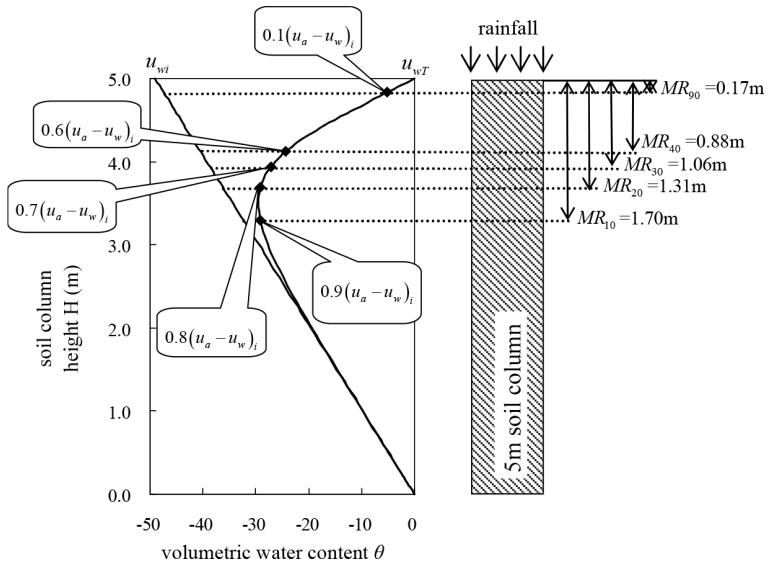

FIGURE 3
The schematic diagram of the determination method of the suction reduction depth MR_n.

The dimensionless parameter of the maximum infiltration rate IR_{max}^{nor} of the modeled section is introduced to describe the relative size of the infiltration rate of the soil column. The calculation formula is as shown in Eq. 3:

$$IR_{\max} nor = \frac{IR_{\max}}{I} \tag{3}$$

where IR_{max} is the section infiltration rate (m/s) and I is the rainfall intensity (mm/h).

After the seepage finite element calculation of the designed different working conditions, the influence of rainfall on the soil is analyzed by using the three defined rainfall infiltration characteristic parameters; the rainfall infiltration characteristics and mechanism of the soil column are described.

2.3 Hydraulic characteristic function used for the calculation

At present, the saturated permeability function and soil–water characteristic curve are mostly used to estimate the permeability function of unsaturated soil.

The SEEP/W module of the finite-element seepage analysis software Geostudio2004 developed by Geo-slope International Ltd (2004) used in this paper contains Fredlund–Xing formula [correction coefficient C(ψ) = 1] (Fredlund and Xing, 1994), as shown in Eq. 4. In this paper, this model (Fredlund et al., 1997) is used to describe the soil–water characteristic curve of unsaturated soil column.

$$\frac{\partial}{\partial y}\left(-k_{wy}\frac{\partial H_w}{\partial y}\right) + q = m_2^w \gamma_w \frac{\partial H_w}{\partial_t} \tag{4}$$

where k_{wy} is the permeability coefficient of water in the y direction (mm/h), q is the flow of rainwater applied on the surface (mm/h), H_w *is* the total water head (m), m_2^w is the slope corresponding to the suction at any point in the soil–water characteristic curve, γ_w is the bulk density of water (kN/m^3), and t is the time of rainfall (h).

The transient seepage analysis of unsaturated soil includes two hydraulic characteristic functions (i.e., soil–water characteristic curve and permeability function). The soil–water characteristic curve and permeability function used in this paper are the experimental curve data obtained by Professor Zhang Zhao (2009) according to the prediction method of Fredlund et al. (1994), as shown in Figure 5.

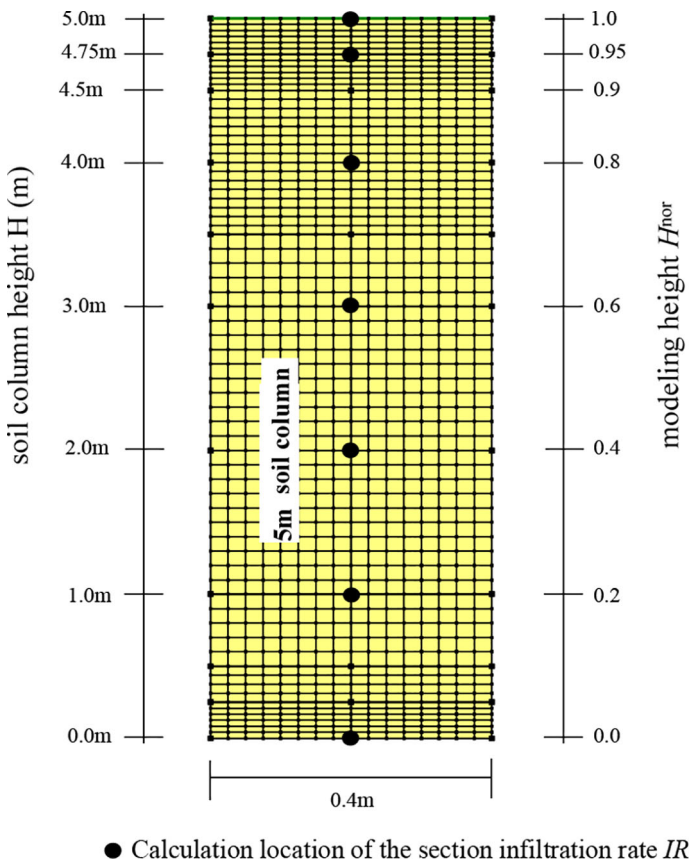

FIGURE 4
Sketch defining the normalized height H^{nor} and locations where sectional infiltration rates *IR* were computed.

3 Results and analysis

3.1 Results and analysis of *WF*

Firstly, the distribution curve of the volumetric water content θ of the soil column along its height at each time under different rainfall intensity I is sorted out, as shown in Figure 6.

As can be seen from Figure 6, during the continuous rainfall process, the volumetric water content θ gradually increases with time. However, when the rainfall stops (i.e., $T = 24$ h), the volumetric water content θ at the top of the soil column continues to decrease, while the θ at the bottom of the soil column continues to increase. Even 9 days after the rainfall stops (i.e., $T = 240$ h), the θ still does not return to the initial state. Analysis shows that with the passage of time, the water continues to penetrate downward gradually under the action of gravity and the matric suction. If the evaporation of water is not considered, the volumetric water content in the soil column will take a long time to return to the initial state.

It also can be seen from Figure 6 that under different rainfall intensities, the infiltration of rainwater in the soil column first increases the volumetric water content θ of the soil near the surface, and the θ section line gradually approaches the groundwater level line. Furthermore, in order to determine the value of *WF*, the distribution map of the volumetric water content θ along the depth of soil column is drawn, as shown in Figure 7.

From Figure 7, we can see that with the extension of rainfall duration, the *WF* is more and more large. With further analysis, from the beginning to the end of rainfall, the volume water content θ of the soil near the surface is most affected by the rainfall, and that of the soil at a greater depth is less affected. With the time extension, the rain continues to penetrate downward; thus, even if the rainfall stops for a long time, *WF* continues to increase.

3.2 Results and analysis of MR_n

Similarly, the curves of pore water pressure u_w at different heights of soil column under different rainfall intensity I and different rainfall time T are sorted out, as shown in Figure 8.

It can be seen from Figure 8 that the pore water pressure u_w increases with the extension of rainfall time gradually, and the matrix suction $(u_a - u_w)$ gradually decreases correspondingly. After the rain stops, the pore water pressure u_w at the top of the soil column begins to decrease in the direction of the initial hydrostatic pressure. However, after 10 days of rain stop (i.e., = 240 h), the pore water pressure is still not restored to the initial state, and the pore water pressure at the bottom of the soil column continues to increase slowly, that is, MR_n is still increasing. This analysis shows that the downward migration of rainwater in the soil column increases the u_w and reduces the $(u_a - u_w)$. The increase of MR_n indicates that the infiltration and suction reduction in the soil column continue after the rain stops. After the rain stops, the u_w gradually reduces to the initial hydrostatic pressure, which is the redistribution process of pore water pressure after the rain stops. This phenomenon is consistent with the *in situ* monitoring law of pore water pressure during rainfall by Rahardjo et al., (2007). The whole movement process is very slow, indicating that the pore water pressure in the soil column needs a long time to restore to the initial water pressure value.

Furthermore, according to the data of Figures 8D–G, the relationship curve of change of the normalized suction reduction depth MR_n^{nor} with the suction reduction rate n% under four higher rainfall intensities (i.e., $I = 2.5k_s$, $I = 5.0k_s$, $I = 10.0k_s$, and $I = 25.0k_s$, respectively) is sorted out, as shown in Figure 9.

Figure 9 shows that the MR_n^{nor} of the four rainfall intensities decreases with the increase of n%, which indicates that the shallower the depth in the soil column is, the more obvious the matrix suction reduction. In addition, the four curves show a good exponential function ($R^2 = 0.9767$). The four groups of data can be fitted to a curve, and the curve fitting formula is as Eq. 4. This also reflects that there is a limit of the effect of rainfall intensity I on the reduction of matric suction; that is, MR_n has a limit value. Beyond this limit value, the effect of I on the reduction of matric suction is not obvious.

$$MR_n^{nor} = a \ln(n) + b \tag{4}$$

where a and b are the curve fitting parameters, respectively, $a = -0.1361$, $b = 0.664$.

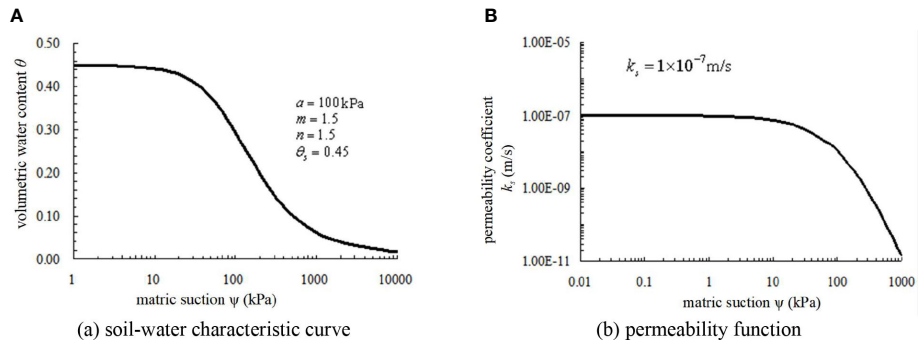

(a) soil-water characteristic curve (b) permeability function

FIGURE 5
The soil–water characteristic curve and permeability function used in the numerical test in this paper. **(A)** Soil–water characteristic curve, **(B)** Permeability function.

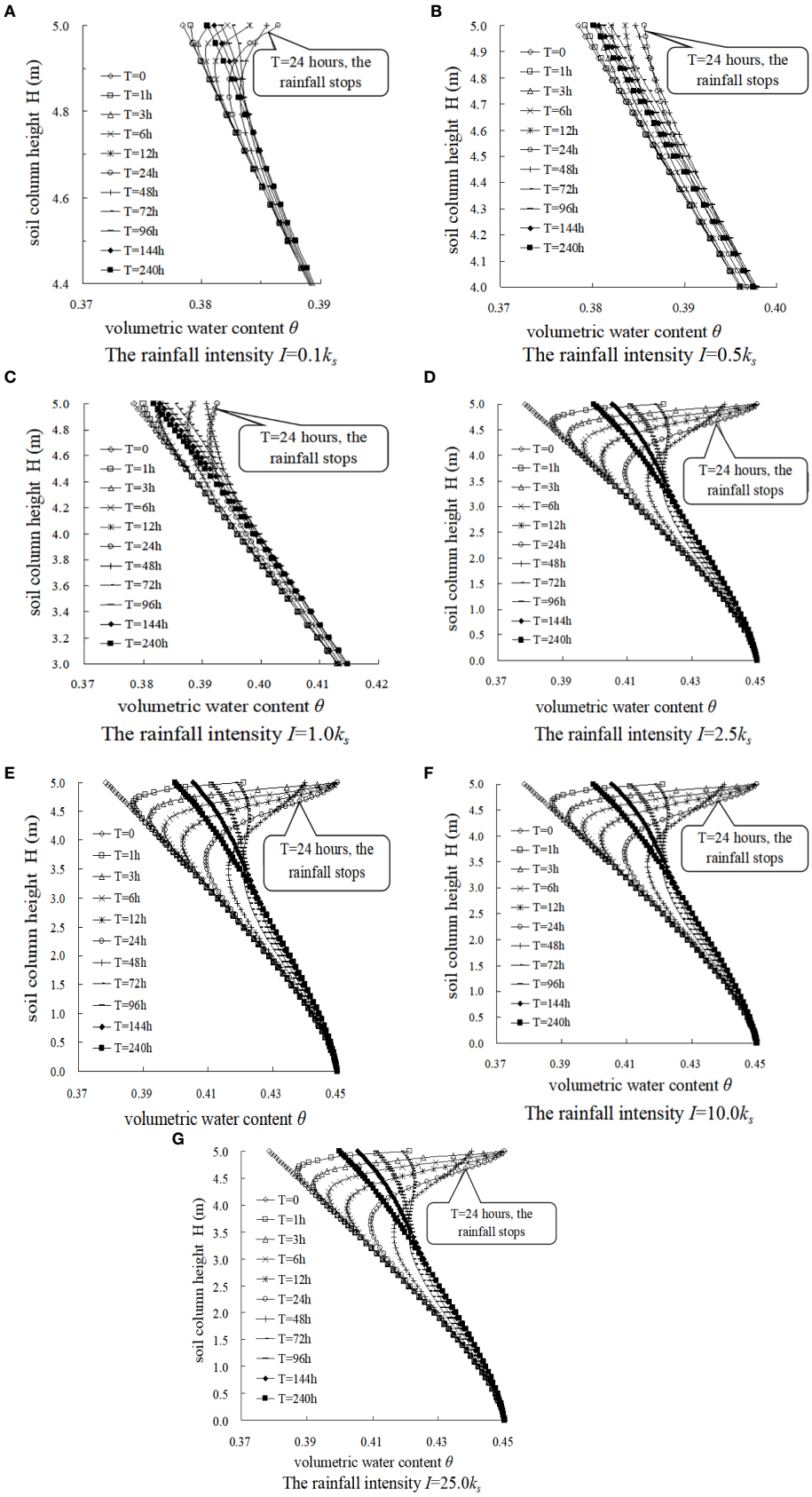

FIGURE 6
The relations between height of the soil column H and volumetric water content θ with time during and after several rainfall events under different rainfall intensities I.

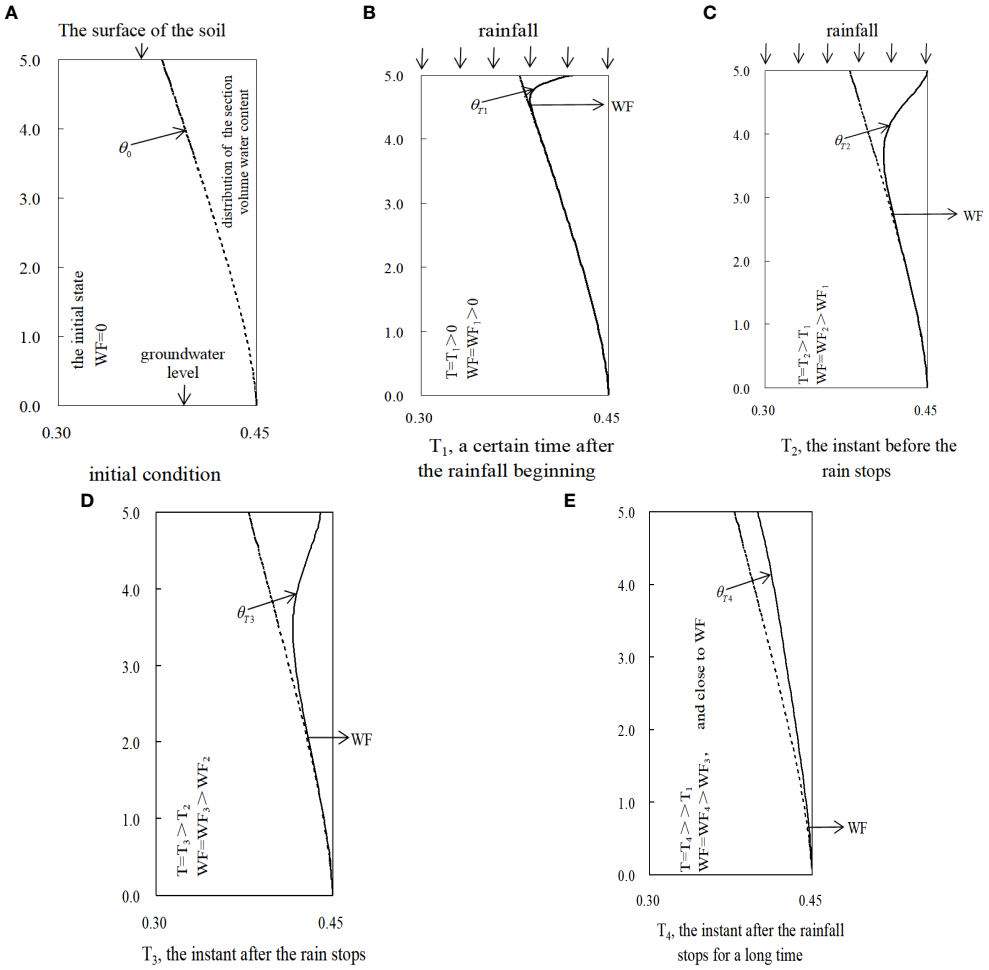

FIGURE 7
Generalized characterization of infiltration and the ingress of the wetting front into the soil column due to rainfall in terms of depth of wetting front *WF*.

Then, the distribution law of suction reduction at different depths of soil column during rainfall is sorted out, as shown in Figure 10.

According to Figure 10, the suction reduction caused by rainfall is unevenly distributed along the depth of the soil column. Under the condition of 24 h of rainfall duration, the maximum normalized suction reduction depth MN_n^{nor} is approximately 0.35; that is, the maximum depth of matrix suction affected by rainfall is approximately 35% of the total depth.

3.3 Results and analysis of *IR*

In order to analyze the variation of section infiltration rate *IR* during rainfall, we extracted the relationship curve of section infiltration rate *IR* with time corresponding to different normalized heights H^{nor} under condition $I = 1.0k_s$, as shown in Figure 11.

As can be seen from Figure 11, under each H^{nor}, the *IR* at the top of the soil column gradually increased with time during the rainfall process, but after the rain stops, it began to decrease again. The *IR* at the bottom of the soil column begins to increase again after a long period of rain stop. According to the analysis, the infiltrated rainwater moves slowly from the top of the soil column to the bottom, resulting in a lag in time. Therefore, as the rainfall continues, the *IR* of the surface gradually increases to the saturated permeability coefficient of the soil. After rain stops, the *IR* of the soil near the surface (the top of the soil column) decreases to zero, and at this time, the *IR* of the soil near the bottom of the soil column begins to increase. It can also be seen from Figure 11 that the maximum infiltration rate IR_{max} at the bottom of the soil column is significantly smaller than that of the top of the soil column. This is because the infiltration of rainwater into the bottom of the soil column becomes much slower due to the reduction of the hydraulic gradient. During the whole process of rainfall, the maximum infiltration rate IR_{max} near the surface (i.e., $H^{nor} = 1.0$) is the largest, and the IR_{max} decreases with the decrease of H^{nor}.

The curves in Figure 11 also show that the distribution of *IR* in the soil column along the depth direction is very uneven. Then, the relationship curves between the normalized height H^{nor} and the section infiltration rate *IR* under the conditions of $I \leq 1.0k_s$ and $I > 1.0k_s$ are drawn, as shown in Figure 12. In the figure, T_1 and T_2 are

10.3389/fevo.2023.1251765

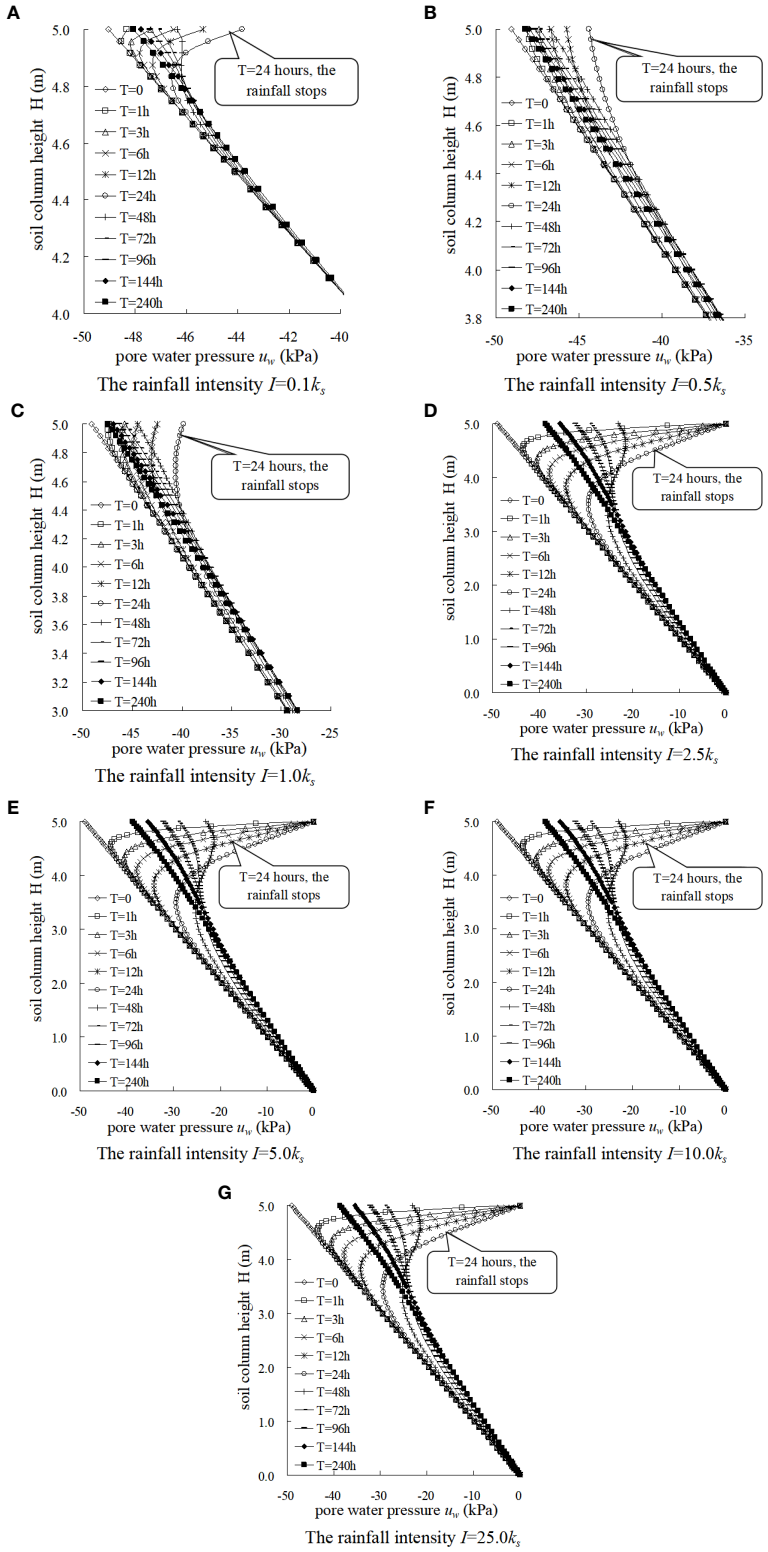

FIGURE 8
The relations between height of the soil column H and pore-water pressure u_w with time during and after several rainfall events under different rainfall intensities I.

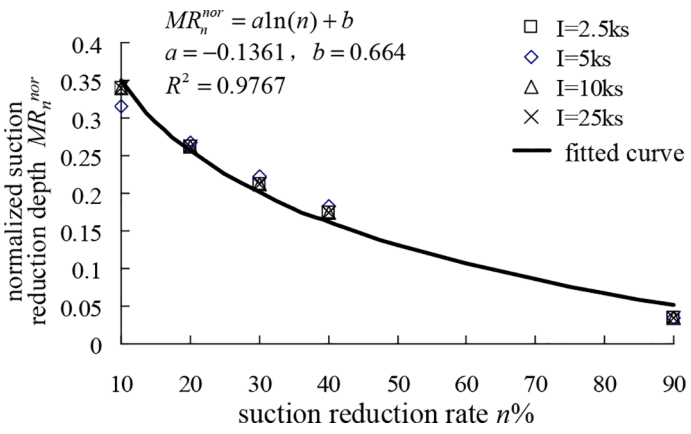

FIGURE 9
Normalized matric suction reduction depth MR_n^{nor} versus percent reduction in suction n% under four rainfall intensities I.

the different moments during the rain, and $T_1 < T_2$, T_3 is a certain moment after the rain stops.

3.4 Effect of I on the infiltration characteristic parameters

From the previous article, we can find that when the rainfall intensity I is different, the two parameters of the calculated normalized infiltration front depth WF^{nor} and the normalized suction reduction depth MR_n^{nor} are also different. We also sorted out the change of the WF^{nor} and the MR_n^{nor} of the soil column under different rainfall intensities I and different times T during the rainfall process, as shown in Figure 13.

Figure 13A shows the variation of WF^{nor} with the rainfall duration under different rainfall intensities. It can be seen from the figure that WF^{nor} generally increases exponentially with time, and with the increase of rainfall intensity I, the depth of infiltration front WF gradually approaches the depth of groundwater level WT (i.e., $WF = WT$). In addition, it can be seen that when the rainfall began, the movement of the infiltration front is very rapid, but it gradually slowed down over time, especially after the rain stops, where the movement of the infiltration front became slower. When the rainfall duration is 1 day under different rainfall intensities, the normalized infiltration front depth WF^{nor} under each working condition has a maximum value; that is, the influence depth of rainwater has a limit, and as the rainfall intensity increases, this limit value also increases. When $I \geq 2.5k_s$, the individual curves almost coincide; it can be considered that $I = 2.5k_s$ is an eigenvalue.

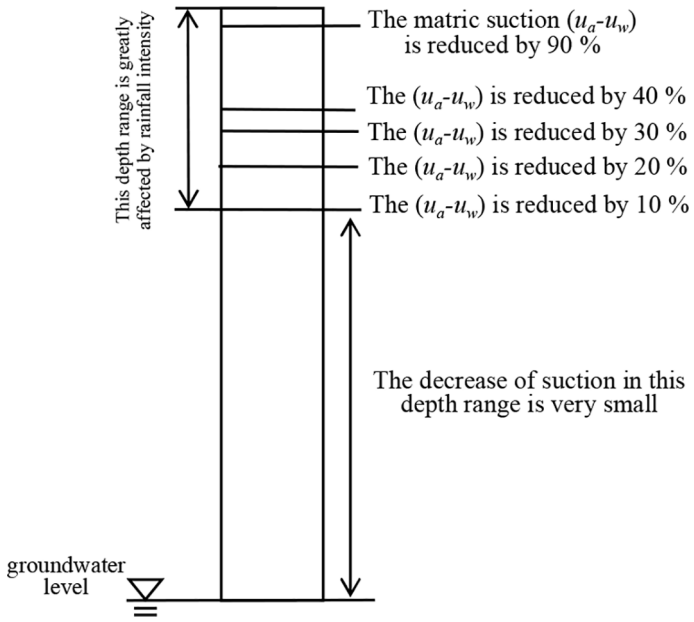

FIGURE 10
Generalized matric suction reduction profile in the soil column after a rainfall event.

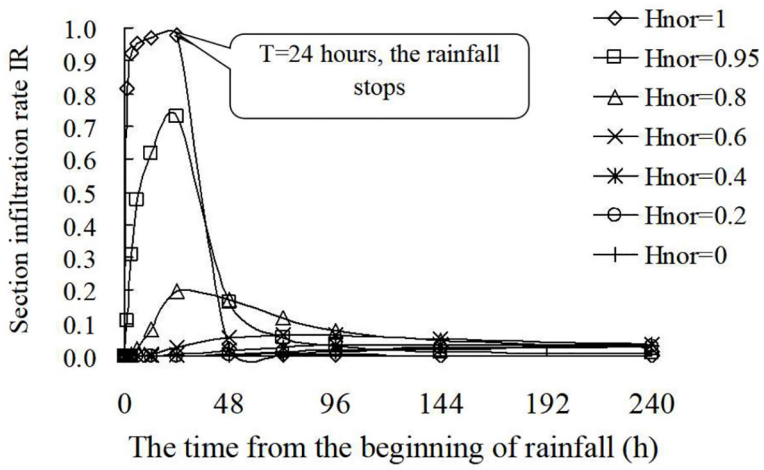

FIGURE 11
Section infiltration rate at different elapsed times under different normalized heights H^{nor} for the soil column.

Figure 13B shows the variation of the depth of normalized suction reduction MR_n^{nor} with rainfall intensity I under different suction reduction rates n%. It can be seen from the figure that the matric suction in the soil column is not completely lost after the rainfall: the area where the suction reduction in the soil column is more than 10% only accounts for approximately 35% of the height of the soil column. In other words, from the groundwater level up, the suction reduction of the soil column in the range of approximately 65% height is very small (i.e., the reduction is less than 10%). Therefore, only a small part of the soil column's shear strength is reduced.

It also can be seen from Figure 13 that the movement speed of the infiltration front increases with the increase of rainfall intensity I. Similarly, the amplitude of suction reduction and the section infiltration rate IR also increase with the increase of I. However, there is a limit to the influence of rainfall intensity on these parameters, that is, $I = 2.5k_s$.

All these phenomena indicate that there is indeed a "special" rainfall intensity when the soil column is affected by rainfall infiltration. In a certain range, increasing the rainfall intensity I will accelerate the infiltration of rainwater in the soil column, but there is a maximum limit ("special") rainfall intensity. At this time, the influence of I on the infiltration of the soil column reaches the maximum. When I exceeds this value, its effect on the infiltration of the soil column will be less obvious.

4 Conclusions

Based on the one-dimensional seepage theory of saturated–unsaturated soil, this paper studies the one-dimensional rainfall infiltration numerical test of a soil column model under different conditions. By introducing three infiltration characteristic parameters to sort out and analyze the calculation, the following conclusions are obtained:

1. The proposed three infiltration characteristic parameters of infiltration front depth WF, suction reduction depth MR^n, and section infiltration rate IR can qualitatively and

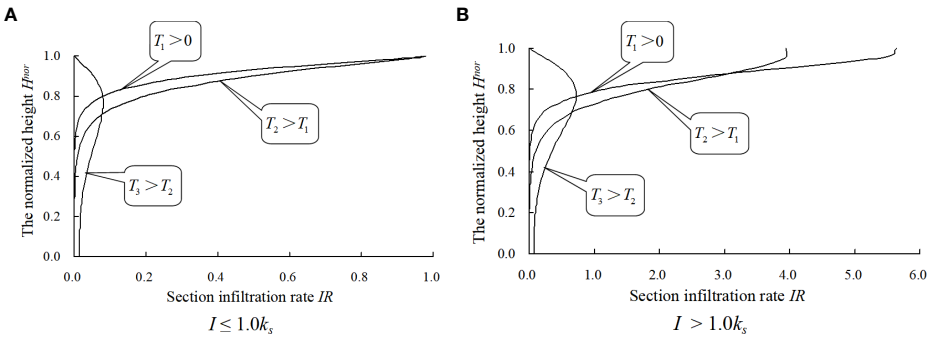

FIGURE 12
The relationship curve between the normalized height H^{nor} and section infiltration rate IR.

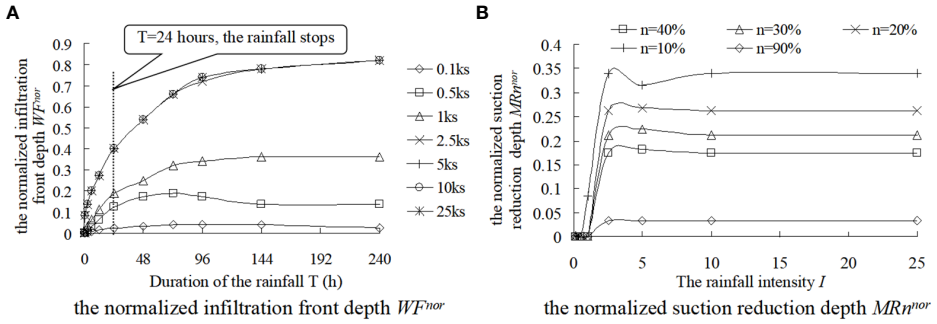

FIGURE 13
Influence of rainfall intensity *I* on the normalized infiltration front depth WF^{nor} and normalized matric suction reduction depth MR_n^{nor}.

quantitatively describe the infiltration characteristics of the soil column model under rainfall conditions.

2. During the rainfall, the volumetric water content θ near the surface first began to increase and gradually moves to the groundwater level, and the infiltration front depth *WF* increased with the extension of rainfall duration, and even continues to increase for a long time after the rain stops.
3. During the rainfall process, the suction reduction depth MR_n decreases with the increase of *n*%; that is, the shallower the depth, the more obvious the suction reduction of the soil matrix. When the rainfall duration is 24 h and the rainfall intensity is different, the normalized suction reduction depth MR_n^{nor} is approximately 35% of the total depth.
4. During the rainfall process, *IR* is mainly affected by rainfall intensity *I*, and the IR_{max} near the surface decreases with the increase of soil column depth. After the rain stops, *IR* is mainly affected by the saturated permeability coefficient k_s, and the *IR* increases first and then decreases with the increase of soil column depth, but the IR_{max} is less than the maximum value during the rainfall process.
5. The increase of rainfall intensity *I* can accelerate the infiltration of soil columns. The faster the *WF* changes, the greater the change range of MR_n and *IR*. However, there is a limit rainfall intensity value for the influence of rainfall intensity on the infiltration of soil columns. The limit rainfall intensity under the calculation conditions in this paper is $I = 2.5k_s$.

Data availability statement

The original contributions presented in the study are included in the article/supplementary material. Further inquiries can be directed to the corresponding author.

Author contributions

FL contributed to the conception of the study. BW executed numerical simulation experimentation. LZ and XZ contributed significantly to analysis and manuscript preparation. FL and CP performed the data analyses and wrote the manuscript. MM contributed to check the details of the article. All authors contributed to the article and approved the submitted version.

Funding

This study was funded by the National Natural Science Foundation of China (No. 12072260 and No. 51679198) and the State Key Laboratory of Eco-hydraulics in Northwest Arid Region of China (QNZX-2019-07).

Conflict of interest

Author BW is employed by the company JiKan Research Institute of Engineering Investigation and Design Co., Ltd. Author XZ is employed by the company Guangzhou Traffic Design & Research Institute Co., Ltd. Author CP is employed by the company PowerChina Northwest Engineering Co., Ltd.

The remaining authors declare that the research was conducted in the absence of any commercial or financial relationships that could be construed as a potential conflict of interest.

Publisher's note

References

Anderson, S. A., and Zhu, J. H. (1996). "Assessing the stability of a tropical residual soil slope," in *Proceedings of the 7th International Symposium on Landslides*, Trondheim, Norway. 1489–1495.

Cho, S. E., and Lee, S. R. (2002). Evaluation of surficial stability for homogeneous slopes considering rainfall characteristics. *J. Geotechnical Geoenvironmental Eng.* 128, 756–763. doi: 10.1061/(ASCE)1090-0241(2002)128:9(756)

Corradini, C., Melone, F., and Smith, R. E. (2000). Modelling local infiltration for a two-layered soil under complex rainfall patterns. *J. Hydrological* 237, 58–73. doi: 10.1016/S0022-1694(00)00298-5

Fredlund, D. G., and Rahardjo, H. (1997). *Unsaturated soil-soil mechanics*. Ed. C. Zhongyi (Beijing, China: China Construction Industry Press).

Fredlund, D. G., and Xing, A. Q. (1994). Equations for soil-water characteristic curve. *Can. Geotechnical J.* 31, 521–532. doi: 10.1139/t94-061

Fredlund, D. G., Xing, A., and Huang, S. Y. (1994). Predicting the permeability function for unsaturated soils use the soil-water characteristic curve. *Can. Geotechnical J.* 31, 533–546. doi: 10.1139/t94-062

Geo-slope International Ltd (2004). *Seep/W for infinite element seepage analysis* (Calgray, Alta: Geo-slope International Ltd.).

Rahardjo, H., Chang, M. F., and Lim, T. T. (1996). "Stability of residual soil slopes as affected by rainfalls," in *Proceedings of the 7th International Symposium on Landslides*, Trondheim, Norway. 1109–1114.

Rahardjo, H., Lee, T. T., Leong, E. C., and Rezaur, R. B. (2005). Response of a residual soil slope to rainfall. *Can. Geotechnical J.* 42, 340–351. doi: 10.1139/t04-101

Rahardjo, H., Leong, E. C., and Rezaur, R. B. (2008). Effect of antecedent rainfall on pore-water pressure distribution characteristics in residual soil slopes under tropical rainfall. *Hydrological Processes* 22, 506–523. doi: 10.1002/hyp.6880

Rahardjo, H., Li, X. W., Toll, D. G., and Leong, E. C. (2001). The effect of antecedent rainfall on slopr stability. *Geotechnial Geological Eng.* 19, 371–399. doi: 10.1023/A:1013129725263

Rahardjo, H., Ong, T. H., Rezaur, R. B., , E., and Leong, C. (2007). Factors controlling instability of homogeneous soil slope under rainfall. *J. Geotechnical Geoenvironmental Eng.* 133, 1532–1543. doi: 10.1061/(ASCE)1090-0241(2007)133:12(1532)

ROmano, N., Brunone, B., and Santini, A. (1998). Numerical analysis of one-dimensional unsaturated flow in layered soils. *Adv. Water Resource* 21, 315–324. doi: 10.1016/S0309-1708(96)00059-0

Tsaparas, I., Rahardjo, H., Toll, D. G., and Leong, E. C. (2002). Controlling parameters for rainfall-induced landslides. *Comput. Geotechnics* 29, 1–27. doi: 10.1016/S0266-352X(01)00019-2

Wang, C.-h., Wan, Z.-y., and Zhang, C.-l. (2015). Tests and numerical simulations of non-orthogonal rainfall infiltration on surfaces of unsaturated sand slopes. *Chin. J. Geotechnical Eng.* 37 (8), 1357–1364. doi: 10.11779/CJGE201508001

Wu, Q.-h., Zhang, J.-f., and Wu, j.-b. (2017). Physical model tests on slopes with control of infiltration by unsaturated drainage structures. *Chin. J. Geotechnical Eng.* 39 (1), 154–140. doi: 10.11779/CJGE201701014

Yang, D.-q. (1992). Nonlinear numerical model of two-dimensional generalized consolidation of unsaturated soils. *Chin. J. Geotechnical Eng.* 14 (9), 2–12.

Zeng, C.-l., Li, R.-j., Guan, X.-d., Zhang, S.-b., and Bai, W.-s. (2020). Experimental study on rainfall infiltration characteristics of loess slopes under different rainfall intensities. *Chin. J. Geotechnical Eng.* 42 (S1), 111–115. doi: 10.11779/CJGE2020S1022

Zhao, Z. (2009). *Experimental investigation of permeability function of unsaturated soil and its application* (Xi'an Shaanxi, China: Xi'an University of Technology).

Zhou, J.-F., Wang, J.-X., and Chen, W. (2014). Lower bound analysis of slope stability subjected to transient unsaturated seepage. *Chin. J. Geotechnical Eng.* 36 (12), 1357–1364. doi: 10.11779/CJGE201412019

frontiers | Frontiers in Environmental Science

TYPE Original Research
PUBLISHED 28 August 2023
DOI 10.3389/fenvs.2023.1242296

OPEN ACCESS

EDITED BY
Zhanping Song,
Xi'an University of Architecture and Technology, China

REVIEWED BY
Vinay Bhushan Chauhan,
Madan Mohan Malaviya University of Technology, India
Zhi Ding,
Zhejiang University City College, China

*CORRESPONDENCE
Wajahat Sammer Ansari,
wajahatsammeransari@yahoo.com

RECEIVED 19 June 2023
ACCEPTED 04 August 2023
PUBLISHED 28 August 2023

CITATION
Naseem A, Ansari WS, Kashif M, Sadiq S, Schotte K and De Backer H (2023), Evaluating the performance of the twin tunnel complex in soft soil subjected to horizontal ground shaking.
Front. Environ. Sci. 11:1242296.
doi: 10.3389/fenvs.2023.1242296

Evaluating the performance of the twin tunnel complex in soft soil subjected to horizontal ground shaking

Ahsan Naseem[1], Wajahat Sammer Ansari[2]*, Muhammad Kashif[3], Shamsher Sadiq[4], Ken Schotte[1] and Hans De Backer[1]

[1]Department of Civil Engineering, Ghent University, Ghent, Belgium, [2]School of Civil Engineering, Qilu Institute of Technology, Jinan, Shandong, China, [3]Department of Civil Engineering, University of Engineering and Technology (UET) Lahore, Lahore, Pakistan, [4]Department of Civil Engineering, Mirpur University of Science and Technology (MUST), Mirpur, Azad Kashmir, Pakistan

Tunnel construction in soft soil necessitates a thorough evaluation of soil behavior, embedment depth, ground heaves, and tunnel distortions, especially in earthquake-prone areas. This study presents a numerical parametric investigation of an unconventional tunnel complex formed by combining the closely located twin tunnels. The complex is subjected to varying horizontal ground vibrations, and the influence of lining thickness, embedment depth, and interface conditions on seismic-induced thrusts, shear forces, bending moments, tunnel distortions, and ground heaves is assessed. The applicability of analytical solutions from existing literature for singular tunnels is examined through detailed analyses of different embedment ratios. The study reveals that increased tunnel flexural rigidity leads to higher seismic-induced bending moments in the tunnel complex. Comparison of full-slip and no-slip interface conditions shows that the former exhibits reduced overall tunnel distortions. Furthermore, a comparison is made with a conventional-shaped rectangular tunnel complex. The results indicate that the twin tunnel complex behaves more rigidly under a constant embedment ratio and input motion amplitude. It also results in lower ground heaves and suffers lesser induced lining forces during seismic events, making it a superior performer in comparison. Overall, this research provides valuable insights into the behavior of twin tunnel complexes in soft soil under seismic conditions, showcasing their advantages over conventional shaped tunnels in terms of tunnel distortions, ground heaves, and overall structural response.

KEYWORDS

twin tunnel complex, soft soil, soil–structure interaction, seismic response, numerical analysis

1 Introduction

Tunnel construction is becoming the need of urban areas to cater to the higher traffic demands. Underground tunnels provide the benefit of uninterrupted traffic flow in areas where surface construction is not possible while keeping the surrounding area compact. Many cities are now planning and constructing underground tunnels. Apart from the singular tunnel, multiple tunnels including the twin tunnel and triplet tunnel complexes are also under consideration now. However, tunnels require extra attention when planned in an

TABLE 1 Soil properties used in the study.

No.	Soil type	Saturated unit weight (kN/m^3)	Shear strength (kPa)	Permeability (m/s)		Rayleigh coefficient	
				Horizontal	Vertical	α	β (×10^{-3})
1	Silty clay	18.4	29.9	5.5×10^{-7}	2.50×10^{-9}	9.660	0.776
2	Very soft silty clay	17.5	27.4	3.5×10^{-6}	1.70×10^{-8}	3.893	1.926
3	Very soft clay	16.9	19.8	5.13×10^{-8}	1.91×10^{-9}	1.771	4.238
4	Clay	18	26.3	3.40×10^{-6}	3.51×10^{-8}	1.744	4.301
5	Silty clay–silty sand	18.1	30	2.13×10^{-5}	2.67×10^{-6}	1.706	4.397

earthquake-prone area. It makes them more vulnerable to excessive settlements, thrusts, and severe damage in case of seismic activity. The condition becomes worse when the tunnels are lying in soft soil and when multiple tunnels lie close to each other. The literature explains that the major earthquakes of the past like the Kobe earthquake (Japan, 1995), the Loma Prieta earthquake (United States, 1989), and Chi-Chi earthquake (Taiwan, 1999) have caused severe damage to underground structures. The damage depends on the type of soil, groundwater condition, embedment depth of the tunnel, lining thickness of the tunnel, amplitude, duration of the earthquake, etc.

In the past, less attention was given to the effects of an earthquake on the tunnels, but the damages caused during major earthquakes have caused researchers to study this aspect as well. Many researchers are now working on the evaluation of the seismic response of tunnels analytically (Hoeg (1968), Wang (1993), Penzien (2000), Bobet (2003), Park et al. (2009), Bobet (2010), experimentally (Adalier et al., 2003; Lanzano, 2009; Lanzano et al., 2010; Bilotta et al., 2014; Ulgen, Saglam, and Ozkan, 2015), and numerically (Hashash et al., 2010; Sandoval and Bobet, 2017; Tsinidis, 2017; Sadiq et al., 2019; Naseem et al., 2020). Sharma and Judd (1991) studied the effect of the type of the soil medium and the embedment of the tunnel on seismic behavior. The study concluded that the tunnels in soft soil are more vulnerable than those in dense soil or rock. Similarly, shallower tunnels suffer more damage than deeper ones. Power et al. (1998) studied the effect of earthquake acceleration on the tunnels and found that the tunnels suffer very little damage for the peak ground acceleration (PGA) of 0.2 g while slight-to-heavy damage for PGA greater than 0.2 g. Penzien (2000), Wang (1993), and Anderson (2008) studied the seismic-induced thrusts and bending moments in tunnels and developed closed-form solutions for rectangular and circular tunnels. Chen et al. (2012) performed the numerical simulation of shake table tests and reported that the most affecting parameters in the case of mountain tunnels are embedment depth, lining thickness, distance from the epicenter, and amplitude of the seismic vibrations. Owen and Scholl (1981) studied the effect of PGA on rock tunnels and concluded that a PGA less than 0.4 g results in very slight damage. Cilingir and Madabhushi (2011c, b, a) performed centrifuge modeling to study the dynamic and post-earthquake behavior of rectangular and circular tunnels in sand and found out that after some vibrations, tunnels achieve dynamic equilibrium after which the earth pressures oscillate at a residual value around the tunnel lining. Yang et al. (2004) performed centrifuge tests to study the internal forces generated in the tunnel lining during the seismic activity. Chen and Shen (2014) recorded the seismic-induced bending moments, while Cao and Huang (2010) installed the strain gages in centrifuge tests to study the strains developed during the dynamic vibrations. Qiu et al. (2017) studied the dynamic behavior and interaction of twin tunnels in loess using centrifuge modeling to evaluate the optimum space and other tunnel parameters. Apart from experiments, numerical modeling has also been used to evaluate the dynamic behavior of tunnels. Tsinidis (2017) performed a detailed numerical parametric study on rectangular tunnels in soft soil to evaluate the forces developed in the tunnel lining, structure–ground interaction, and dynamic earth pressures. Chang, Travasarou, and Chacko (2008) evaluated the liquefaction-induced uplift of immersed tunnels using both centrifuge and numerical analyses. Azadi et al. (2010) numerically studied the uplift and the developed pore pressures of tunnels in liquefiable soils. Patil et al. (2018) performed the parametric numerical study of shallow circular tunnels in soft soils under horizontal ground shaking to evaluate tunnel forces, the effect of vibration's amplitude, etc. However, all the available literature consists of studies on rectangular and circular tunnels, either singular or in pair located in a close proximity. The seismic behavior of the combined multiple tunnels, leading to unconventional shapes, has not been studied.

This study evaluates the seismic performance of the twin tunnel complex which is an unconventional shape resulting from the combination of two closely located circular tunnels and one of the novel tunnel shapes that have been hypothetically proposed to carry multiple underground railway tracks. This research is divided into different parts. In the first part, the construction arrangement for different configurations of closely spaced multiple tunnels has been studied in terms of the produced ground settlements (Naseem et al., 2019). In the second part, three closely spaced circular tunnels combined into a novel triple tunnel complex have been parametrically estimated and compared to the equivalent rectangular tunnel complex (Naseem et al., 2020). This paper parametrically evaluates the behavior of a twin tunnel complex in soft soil, numerically using finite element (FE) software PLAXIS 2D. The study evaluates the effect of amplitude, embedment depth, and lining thickness on structural distortions, lateral pressures, and seismic-induced lining forces. A comparison is also made with the equivalent conventional-shaped rectangular tunnel complex to identify the better performer between the two.

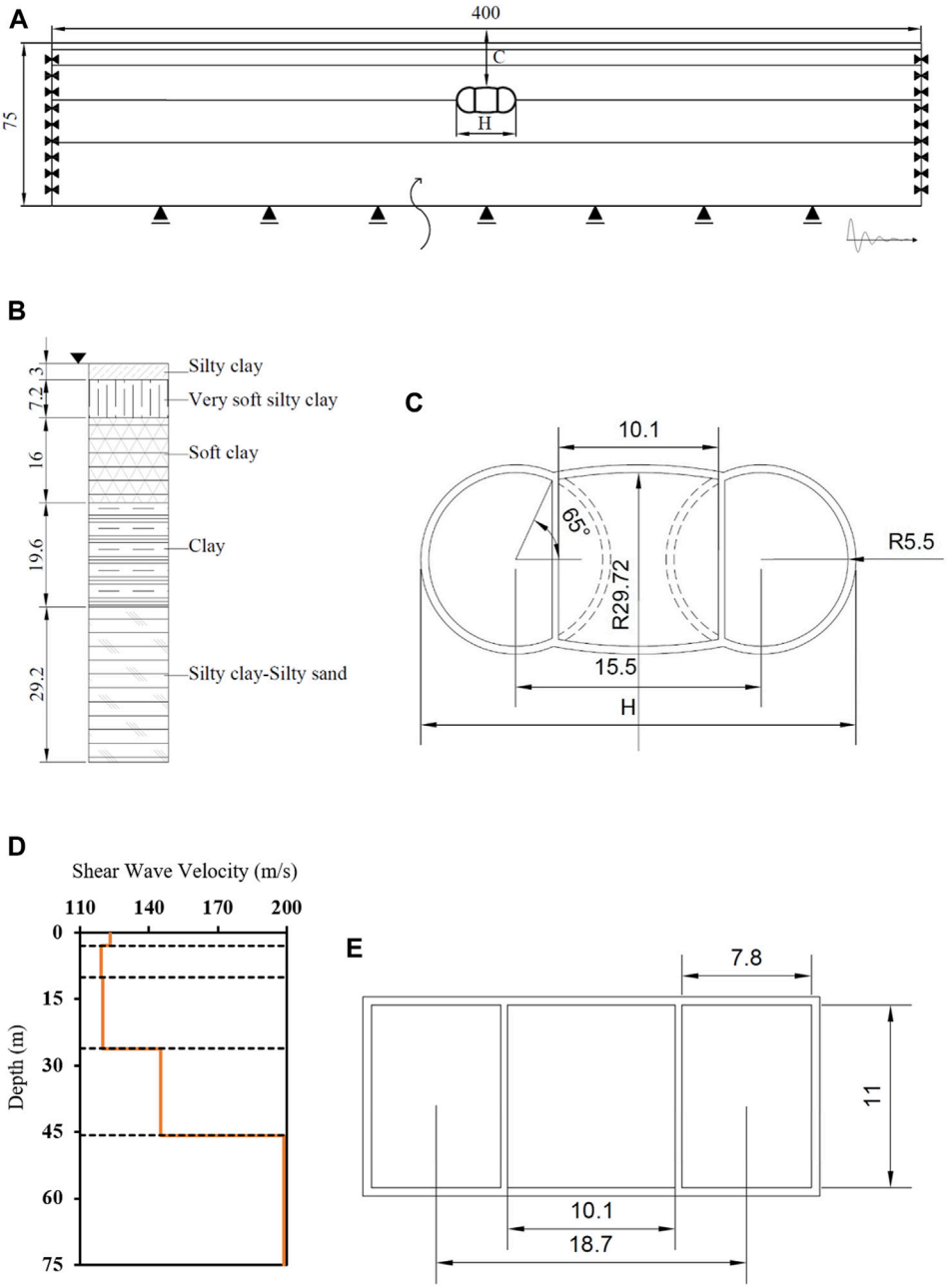

FIGURE 1
Soil–tunnel geometry **(A)**. Soil layers with the embedded triple tunnel complex **(B)**. Soil column with respect to the depth and type **(C)**. Enlarged twin tunnel complex section, also showing the truncated parts (units in "m") **(D)**. Shear wave velocity profile with respect to depth **(E)** Equivalent rectangular tunnel complex with dimensions (units in "m").

TABLE 2 Records of earthquake vibrations.

No.	Earthquake	Station	Year	Magnitude (Mw)	Epicenter distance (Km)	Peak ground acceleration PGA (g)	Peak ground velocity PGV (m/s)
1	Kocaeli, Turkey	Arcelik	1999	7.4	17	0.218	0.177
2	Coyote, United States	San Juan Bautista	1979	5.7	17.2	0.124	0.176
3	Kobe, Japan	0 KJMA	1995	6.9	0.6	0.821	0.813

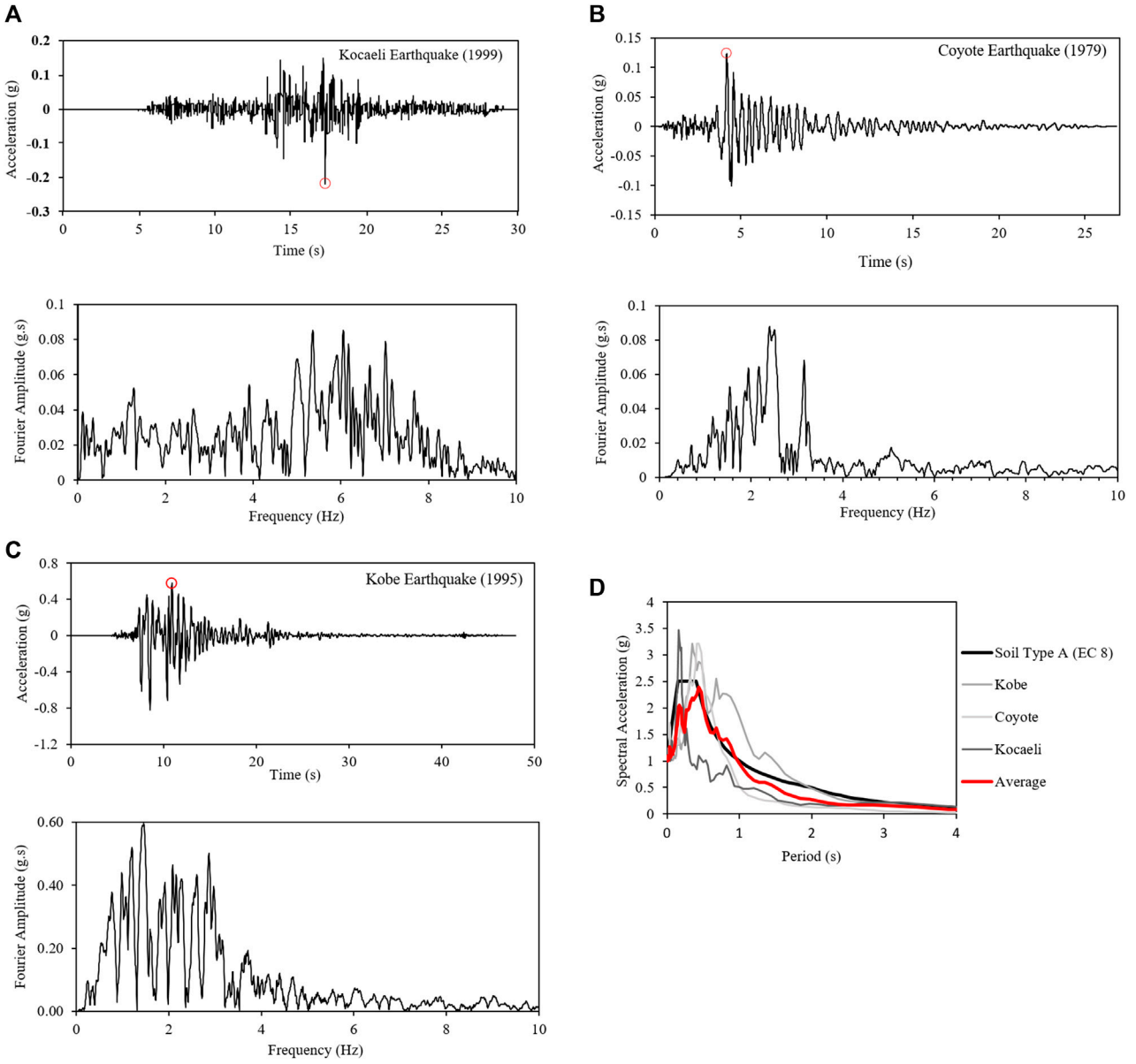

FIGURE 2
Acceleration–time history and the Fourier amplitude of **(A)** Kocaeli earthquake (1999), **(B)** Coyote earthquake (1979), and **(C)** Kobe earthquake (1995). **(D)** Comparison of the normalized spectral accelerations with the design spectrum of site class A (EC8).

2 Details of numerical modeling

2.1 Software and constitutive model

This study is carried out using the dynamic module of PLAXIS 2D which is a finite element (FE) software. It is capable of performing analyses on various types of soil types. The constitutive models available include hardening soil (HS), hardening soil with small strains (HS_{small}), concrete, and Mohr–Coulomb (MC) (Brinkgreve et al., 2010). This study is performed using the MC model. As it is an elastic-perfectly plastic model, to be able to use it for dynamic analyses, PLAXIS 2D makes use of the modified MC model. The input parameters, i.e., elastic modulus (E) and shear modulus (G), for the model are calculated for each soil layer based on its shear wave velocity (V_s). Apart from this, the variation in the moduli with respect to depth is also taken into account.

Seismic vibrations produce cyclic stresses, developing the hysteric loop with energy dissipation and damping. As the MC model is incapable of capturing this phenomenon, so to cater to this, frequency-dependent Rayleigh viscous damping parameters are incorporated in the model. The equations are given as

$$\alpha = 2\omega_1\omega_2\frac{\omega_1\xi_2 - \omega_2\xi_1}{\omega_1^2 - \omega_2^2}, \quad \beta = 2\frac{\omega_1\xi_1 - \omega_2\xi_2}{\omega_1^2 - \omega_2^2}, \tag{1}$$

While

$$\omega_1\,(rad/s) = 2\pi f_1, \quad \omega_2\,(rad/s) = 2\pi f_2, \tag{2}$$

$$f_1\,(Hz) = \frac{V_s}{4h}, \quad f_2\,(Hz) = \frac{3V_s}{4h}, \tag{3}$$

where α and β are the Rayleigh viscous damping coefficients, ω_1, and ω_2 are the angular frequencies, h is the thickness of the soil layer, V_s represents the shear wave velocity for the respective soil layer, f_1, and f_2 are the first and second target frequencies, and ξ_1 and ξ_2 are the respective damping ratios which are taken as 10% for soft soil.

2.2 Soil–tunnel model and boundary conditions

The layered soil system is used in this study. The top layer is silty clay which is followed by very soft silty clay and soft clay, underlain by clay and silty clay–silty sand layers. The soil system is categorized as soft soil type D according to Eurocode 8 (Code, 2005). The detailed geotechnical soil parameters are tabulated in Table 1, while the V_s profile with respect to the depth is given in Figure 1D. The ground conditions are considered fully saturated with the groundwater table (GWT) at the surface. The benefit of using a layered soil profile is to include the effect of variation of V_s along the depth as well as the different soil properties on the tunnel's C/H ratio. This is the same layered soil as previously used by Huo et al. (2005), Naseem et al. (2020), and Patil et al. (2018).

The 2D plane strain numerical model with 15-noded triangular elements is used, with the tunnel lining elements being considered the elastic plate elements. The elastic modulus of the liner (E_l) is taken as 37 GPa, while the unit weight as 25 KN/m^{3,} and the Poisson's ratio (υ_l) as 0.2. The detailed layered soil profile along with the tunnel geometry can be seen in Figures 1A–C. The tunnel width (H) and embedment depth (C) are kept as variables to study the effect of the embedment ratio (C/H) on the overall tunnel seismic behavior. The dimensions of the model are kept at 400 × 75 m. The boundaries of the model are so kept that they do not interfere with the wave propagation. The free-field boundaries are considered at the lateral ends to absorb the incident waves, while the bottom boundary is considered to be fully reflective. The mesh size is selected based on the Kuhlemeyer et al. (1973) equation so that the wave does not pass one element per single time step.

$$\Delta l = \frac{\lambda}{10}\ to\ \frac{\lambda}{8}, \tag{4}$$

And

$$\lambda = \frac{V_s}{f}, \tag{5}$$

where Δl is the length of the finite elements and λ is the wavelength, V_s is the least shear wave velocity, and f is the frequency. The time step also plays an important role in the overall accuracy of the results and hence is selected as

$$\delta t = \frac{t}{\Delta t}, \tag{6}$$

where δt is the time step, t is the total time duration of the seismic vibration, and Δt is the sub-step.

2.3 Input seismic motions

The major earthquakes in history are used to evaluate the seismic performance and design the structures in earthquake-prone regions. This study includes three earthquakes from the past. The Kocaeli (Turkey, 1999) earthquake, the Coyote (United States, 1979), and the Kobe (Japan, 1995) earthquake signals are applied to the tunnel–soil system to evaluate the seismic performance. The input motions (IMs) are scaled to the amplitude of 0.4 g for using them in this study. The details of the earthquake records are tabulated in Table 2, while the acceleration–time histories and Fourier amplitudes are given in Figures 2A–C. The normalized spectral acceleration curves plotted with the Eurocode 8 site class A can be seen in Figure 2D.

3 Validation model

This research studies an unconventional tunnel complex for which experimental data and specific analytical solutions are not available. To verify that the produced results by PLAXIS 2D are acceptable, a validation study is performed. A circular tunnel of 6 m diameter is considered in the same layered soil profile (Table 1) with no-slip conditions at the soil–structure interface (SSI) and the Kobe

TABLE 3 Tunnel lining thicknesses and induced thrusts and bending moments.

Lining thickness (m)	Flexibility ratio, F	Induced force (PLAXIS 2D)	
		Thrust (KN/m)	Moment (KN-m/m)
0.1	65.81	348.701	23.182
0.2	8.23	394.196	140.211
0.3	2.44	455.218	341.718
0.4	1.03	505.531	510.124
0.5	0.526	538.358	615.677
0.7	0.192	572.912	709.718
0.9	0.090	590.605	740.768
1.0	0.066	597.106	758.600

TABLE 4 Analytical solutions to calculate induced thrusts and moments.

Parameter	Wang (1993)	Penzien (2000)	Bobet (2010)
Thrust (T_{max})	$\pm \frac{1}{2} K_2 \frac{E_s \gamma_{max} r}{(1+\nu_s)}$	$-\frac{24 E_l I \Delta_{lining}}{D^3 (1-\nu_l^2)} \cos 2\left(\frac{\pi}{2}\right)$	—
Bending moment (M_{max})	$\pm \frac{1}{6} K_1 \frac{E_s \gamma_{max} r^2}{(1+\nu_s)}$	$-\frac{6 E_l I \Delta_{lining}}{D^2 (1-\nu_l^2)} \cos 2\left(\frac{\pi}{2}\right)$	$-\frac{12(1-\nu_s)G_s}{3(5-6\nu_s)+F'(1-\nu_s)} \gamma_{max} r^2 \sin 2\theta$
Flexibility ratio (F)	$F' = \frac{E_s (1-\nu_l^2) r^3}{6 E_l I (1-\nu_s^2)}$		

where E_s and E_l are elastic moduli of the soil medium and tunnel lining, respectively; ν_s and ν_l are the Poisson's ratio of the soil medium and tunnel lining, respectively; I is the moment of inertia; K_1 and K_2 are constants; F is the flexibility ratio; γ_{max} is the maximum shear strain at tunnel level; and r is the radius of the tunnel.

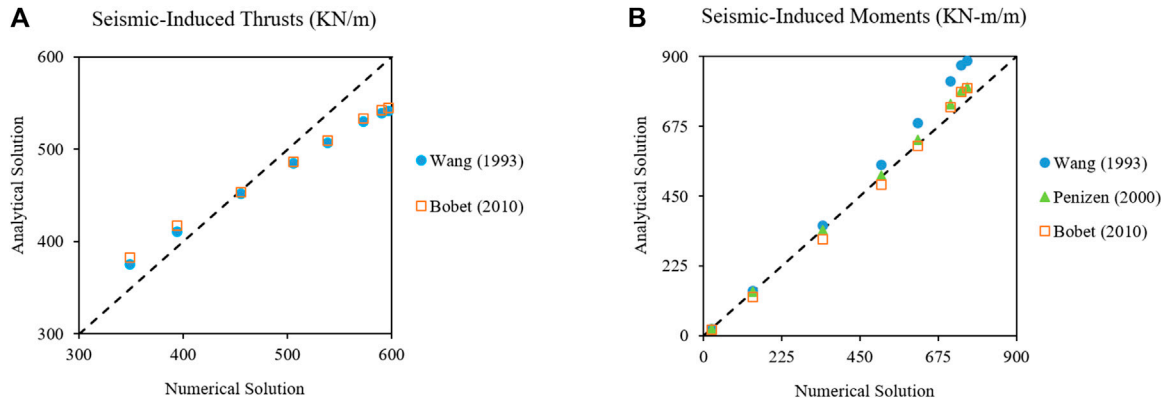

FIGURE 3
Comparison between numerical and analytical solutions: **(A)** thrust and **(B)** bending moment.

earthquake with 0.4 g amplitude is applied to the model. The lining thickness varies from 0.1 to 1 m to have a wide range of flexibility ratios (Table 3). The obtained shear strains from the 1D soil column analysis are converted to the pseudo-static displacements and applied to the soil–tunnel system to compute the lining forces. The calculated numerical values are then compared with the analytical solutions of Wang (1993), Penzien (2000), and Bobet (2010) tabulated in Table 4. The results can be seen in Figures 3A, B, which are in close agreement, hence depicting that the obtained numerical values are accurate. A similar type of a validation study was also conducted by Patil et al. (2018) and Naseem et al. (2020).

4 Parametric study

In this research, a detailed numerical parametric study is performed to evaluate seismic performance. The effect of variation in lining thickness, C/H ratio, and the amplitude of the seismic vibrations are studied to evaluate the produced ground deformations, tunnel distortions, seismic-induced thrusts, shear forces, and bending moments. An equivalent rectangular tunnel complex (Figure 1E) is also analyzed, and a detailed comparison is then made to evaluate the overall performance.

4.1 Flexibility ratio

The analytical solutions to calculate the flexibility ratio (F) that are available in the literature are for singular tunnels. To find their applicability to the combined circular twin tunnel complex, detailed dynamic analyses are performed by varying the tunnel lining thickness from 0.1 to 1.5 m to calculate the ratio of distortions in free-field (FF) and the tunnel complex. Three C/H ratios, i.e., 0.25, 0.5, and 0.75, are considered for this study. The F is obtained from the ratio of soil deformations (obtained using PLAXIS 2D) and structural deformations (obtained using the structural analyses program). The normalized tunnel distortions are also calculated using the closed-form solutions by Wang (1993), Penzien (2000), and Anderson (2008), and the results from the numerical and analytical methods are compared, which can be seen in Figures 4A–C. From the figures, it can be noticed that there is some minor difference between the numerically and analytically obtained values which is because the numerical analyses are performed taking into consideration the nonlinear behavior of soil, while the analytical solutions are developed considering the linear elastic behavior. The overall results are in good agreement with the analytical solutions; hence, they can be used to calculate the normalized structural distortions and F for the combined circular twin tunnel complex.

4.2 Variation in lining thickness

To study the variation in lining thickness, twin tunnel complexes with different lining thicknesses varying from 0.12 to 2 m are seismically analyzed. The range is so selected that it covers both flexible and rigid tunnels. All the other parameters, i.e., the C/H ratio, the amplitude of the IM, and the thickness of the inner structure, are kept constant. The thickness variation in the tunnel is represented in terms of F, and their

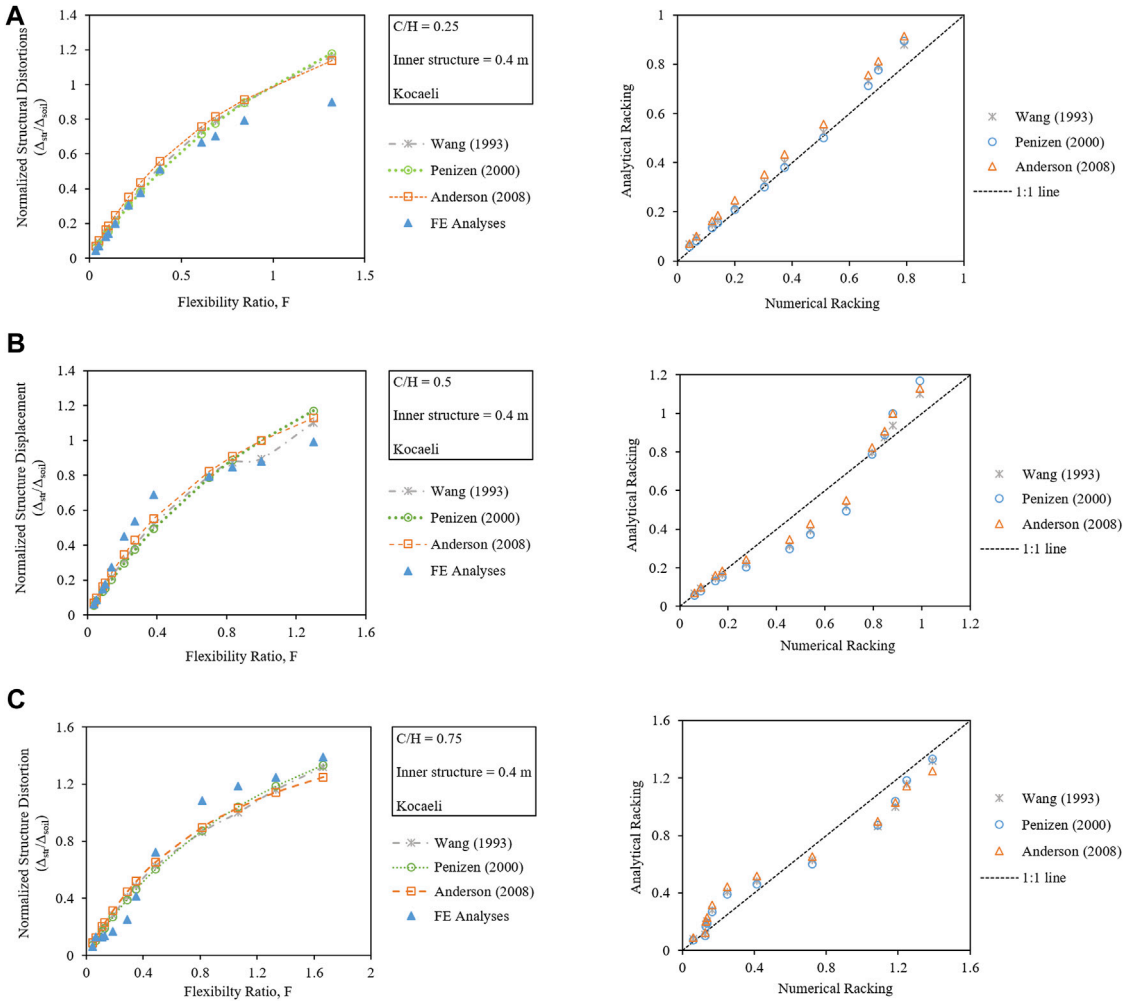

FIGURE 4
Validation of analytical R–F relationships for C/H ratios: **(A)** 0.25, **(B)** 0.5, and **(C)** 0.75.

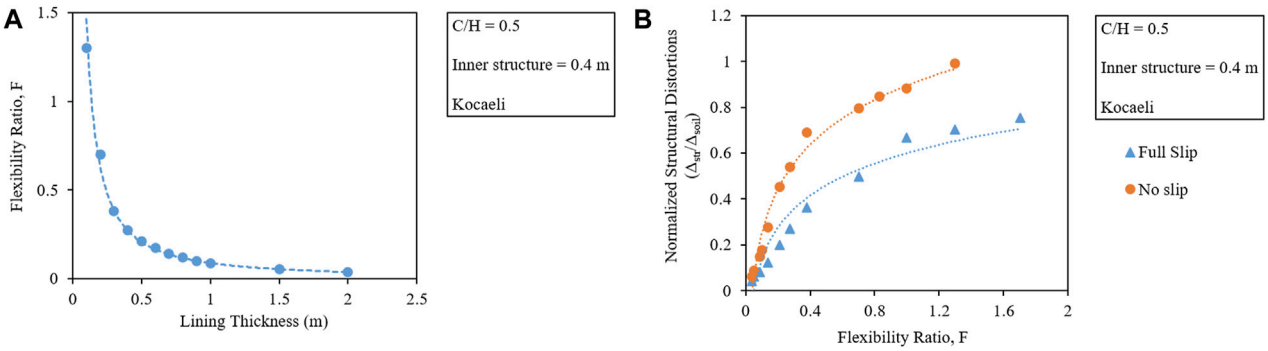

FIGURE 5
(A) Lining thickness representation in terms of flexibility ratios. **(B)** Comparison of tunnel distortions for full-slip and no-slip interface conditions.

relationship is represented in Figure 5A. From the figure, it can be observed that the tunnel section of approximately 0.15 m thickness is the critical section having F ≈ 1.

To study the tunnel distortions, both full-slip (μ = 1) and no-slip (μ = 0) cases are considered. From Figure 5B, it can be seen that the normalized tunnel distortions increase with the flexibility of the tunnel

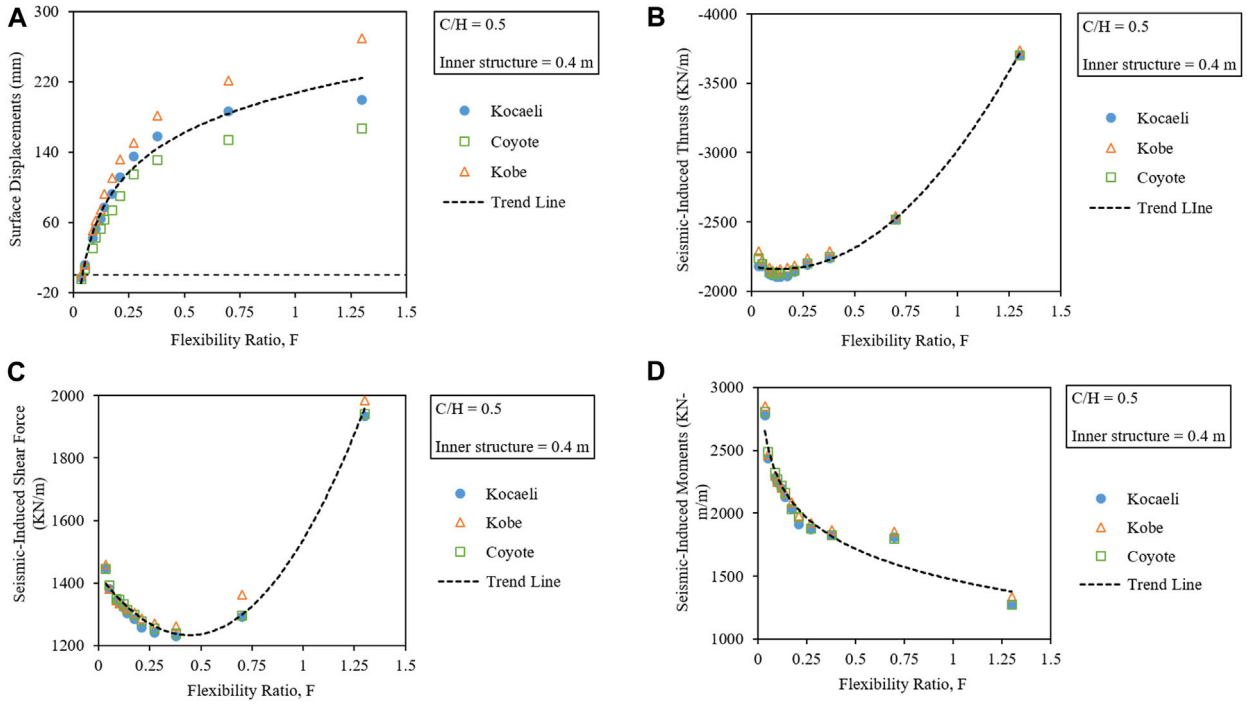

FIGURE 6
Variation in **(A)** surface displacements and seismic-induced **(B)** thrusts, **(C)** shear force, **(D)** and bending moments in a combined twin tunnel complex of varying F.

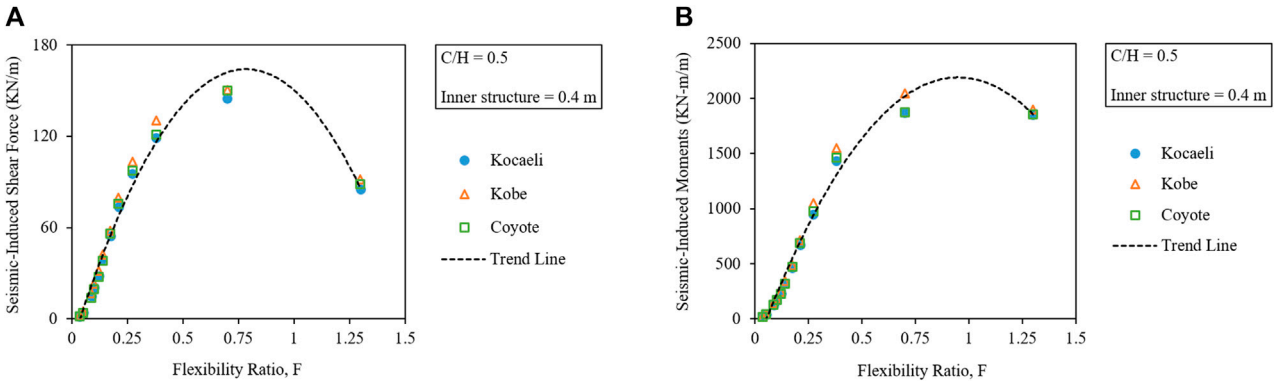

FIGURE 7
Variation in seismic-induced **(A)** shear forces and **(B)** bending moments in connecting members of a combined twin tunnel complex of varying F.

lining, while the same thickness of tunnel lining would undergo more distortions in case of no-slip condition as compared to when the slip is present in between the tunnel–soil interface. The reason is that the full slip allows for easier movements and rotation within the soil, hence reducing the distortions, which are in line with the results obtained by Tsinidis (2017) and Debiasi, Gajo, and Zonta (2013).

The produced ground deformations and seismic-induced forces (thrusts, shear forces, and bending moments) can be seen in Figures 6A–D, respectively. From the surface displacement curve, it can be noticed that the increased thickness of the tunnel lining makes the tunnel behave as rigid and results in lesser ground heave because the tunnel would resist the distortions produced by seismic vibrations, resulting in lesser seismic-induced thrusts (T) and more shear forces (Q) and bending moments (M). As the $F \geq 1$, the tunnel behaves almost like the soft soil medium; hence, the induced T and Q get excessively large and the M is reduced to the minimum as the capacity to resist is sufficiently reduced. These results are similar to those obtained by Azadi et al. (2010) and Abdel-Motaal, El-Nahhas, and Khiry (2014). Hence, to increase the tunnel resistance, reinforcement should be increased instead of providing thicker tunnel linings, as recommended by Hashash et al. (2001).

The induced forces in the internal connection members can be seen in Figures 7A, B. From the figures, it can be observed that the induced

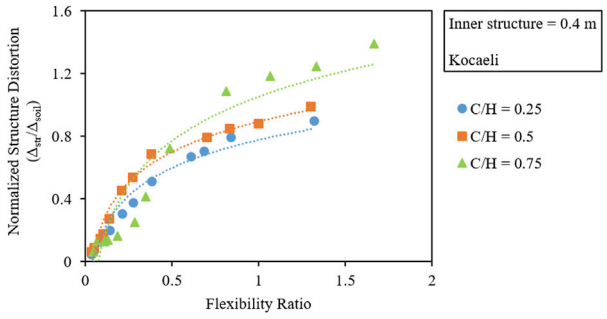

FIGURE 8
Effect of variation in the embedment depth on normalized tunnel deformations.

Q and M in the tunnel lining also have an impact on the forces generated in the internal connecting members. With a decrease in the F of the tunnel, the tunnel lining becomes stiff and more forces are taken up by it, resulting in lesser forces in the internal members, and hence the reduced dimensions of the members. On the contrary, if the tunnel structure is more flexible, the stability of the tunnel complex would be relying more on the internal connecting members as more forces will be generated in the internal connecting members, and hence will lead to the thicker dimensions of the internal members.

4.3 Variation in embedment depth ratio

To study the effect of variation in C/H, the lining thickness, the amplitude of the IM, and the thickness of the inner structure are kept

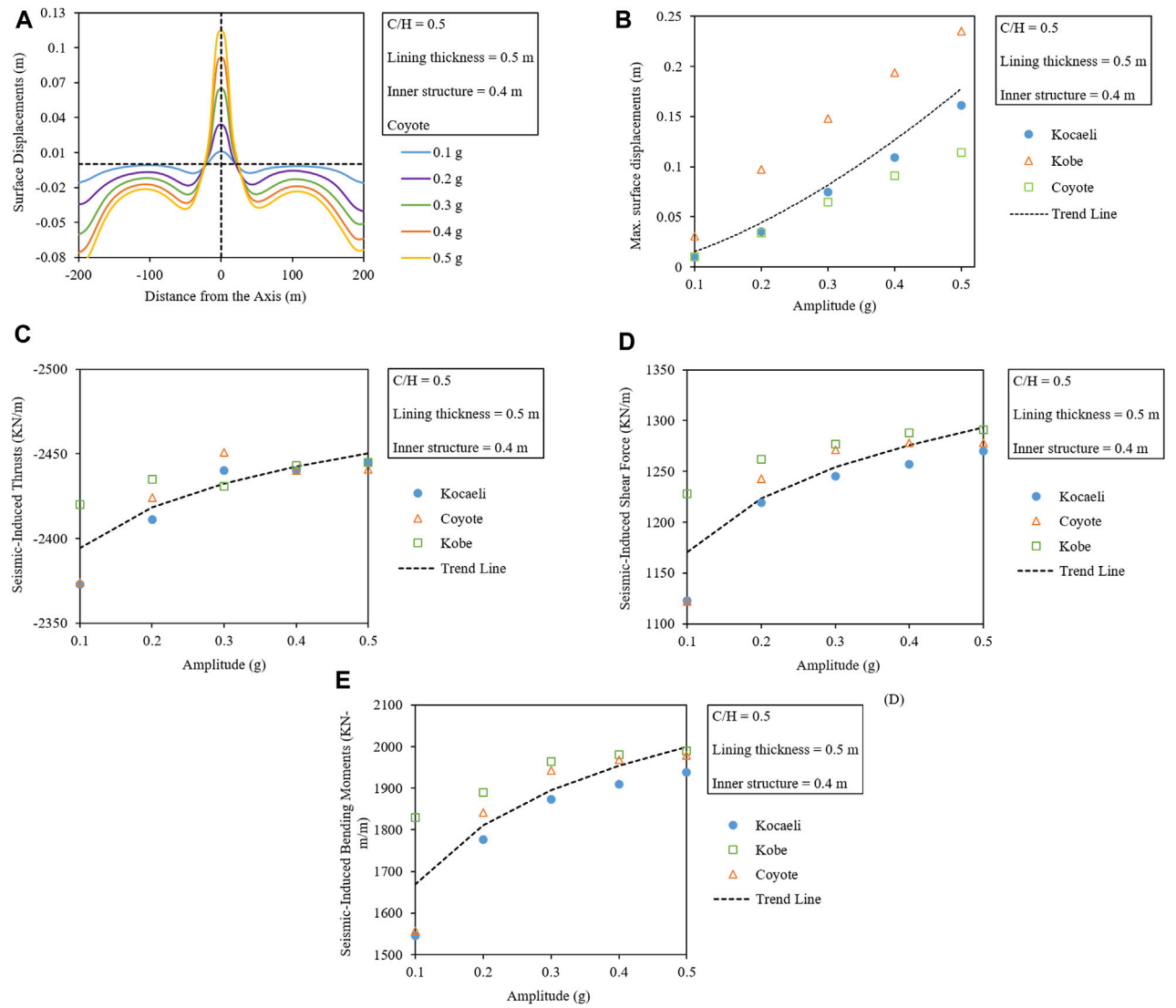

FIGURE 9
Comparison of **(A)** surface displacement troughs to the variation in amplitude **(B),** maximum ground displacements and seismic-induced maximum **(C)** thrusts, **(D)** shear forces, and **(E)** bending moments with respect to the amplitude of three IMs.

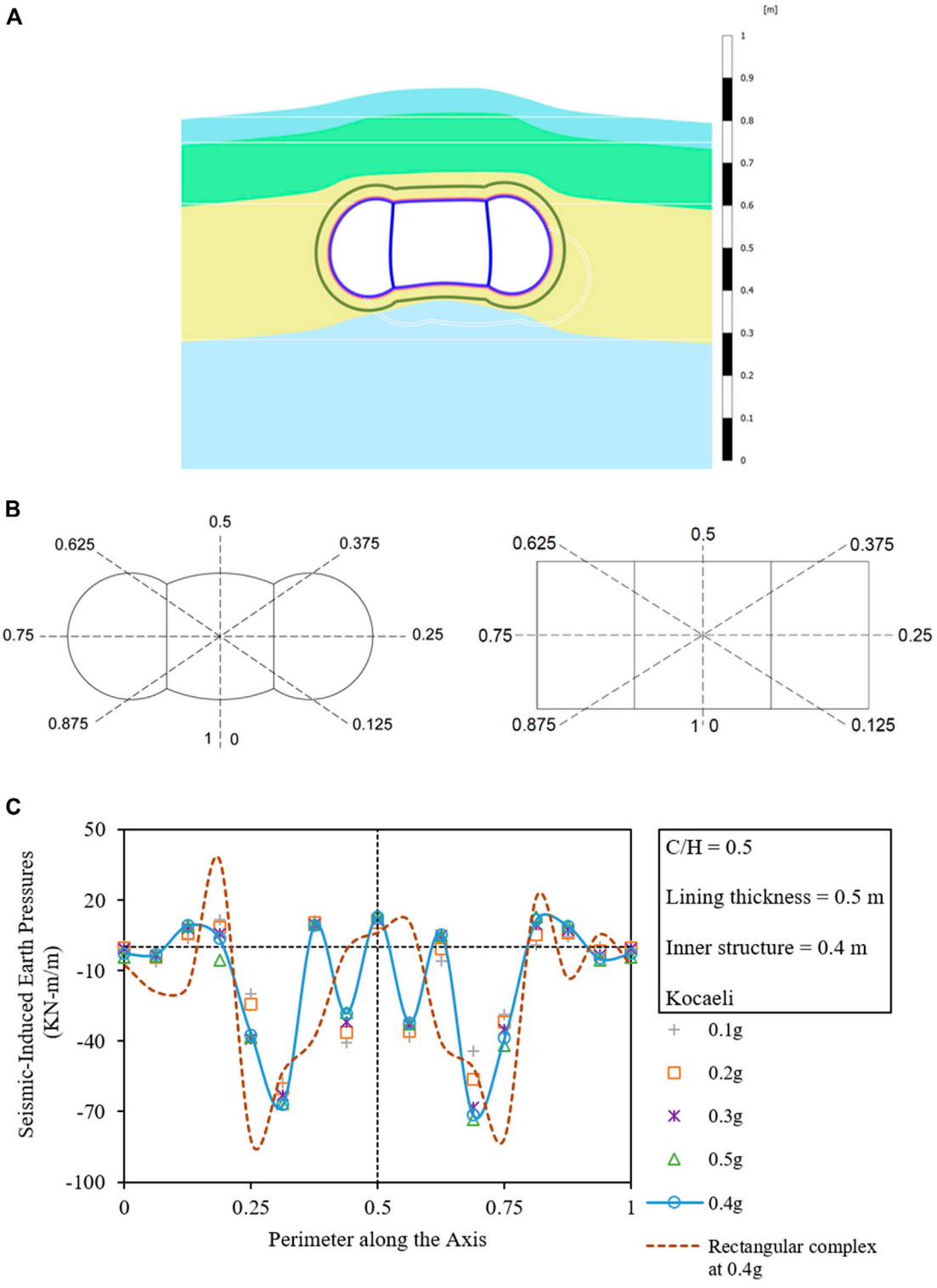

FIGURE 10
(A) Deformed complex under the seismic vibrations (50 x zoom). **(B)** Normalized tunnel perimeter for the circular twin and rectangular tunnel complex. **(C)** Variation in residual earth pressures with respect to the amplitude along with the circular twin tunnel perimeter and comparison with the rectangular tunnel complex.

constant. Three C/H ratios, i.e., 0.25, 0.5, and 0.75, are studied in this regard that produced ground deformations, and normalized tunnel distortions are plotted, which can be seen in Figure 8. The figure shows that although negligible but there are lesser structural distortions in case of the C/H ratio of 0.75 for F < 0.5. The reason is that for F ≤ 0.5, the lining thickness is more than the

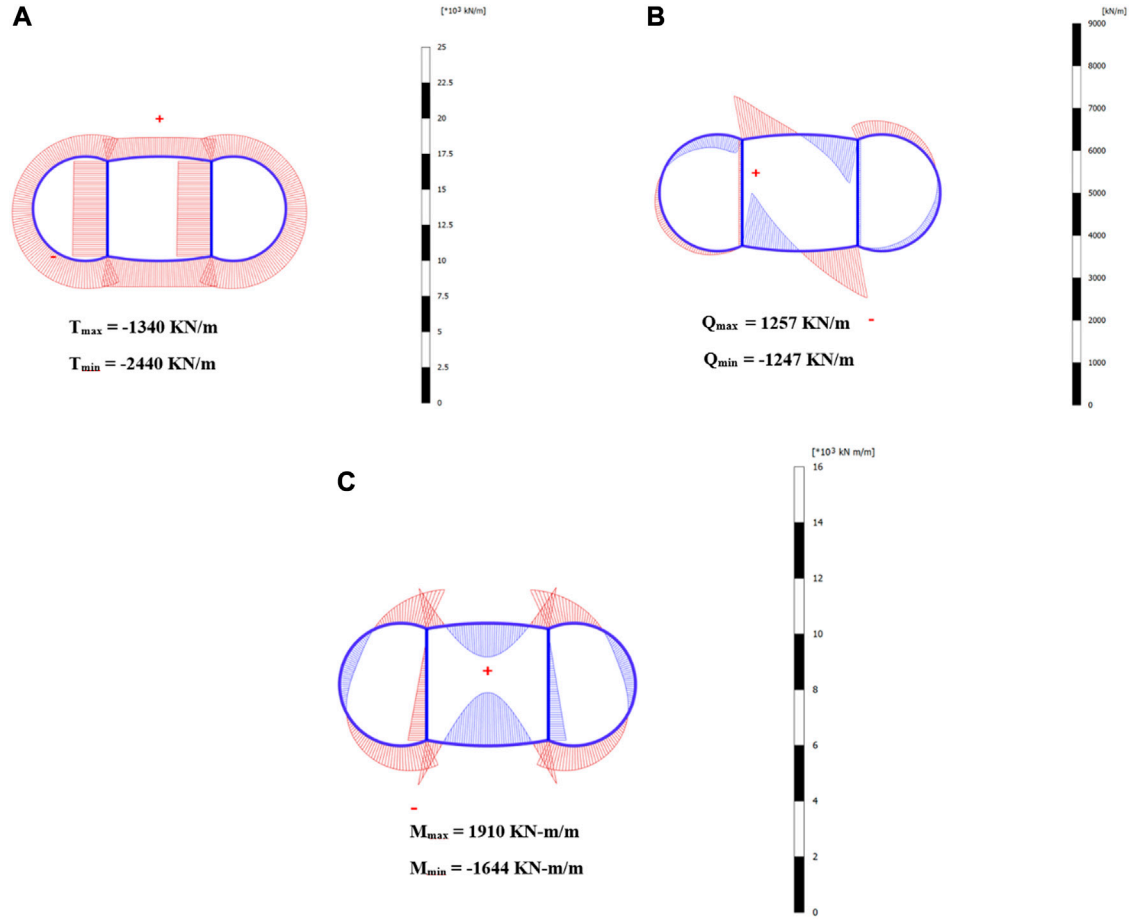

FIGURE 11
Seismic-induced **(A)** thrusts, **(B)** shear forces, and **(C)** bending moments in the circular twin tunnel complex.

inner connecting members; hence, embedment depth contributes to lesser distortions. As the lining thickness decreases than the inner members, the overburden pressure results in the buckling and collapse of inner structures, and thus results in more structural distortions. This explanation is corroborated by the drastically increasing seismic-induced M, Q, and T beyond the F of 0.5 plotted in Figures 5–7. From the obtained trendlines, it is evident that as the C/H ratio increases, the tunnel behaves more flexibly and undergoes increased tunnel distortions.

4.4 Variation in the amplitude of input motion

While keeping the lining thickness, C/H ratio, and thickness of the inner structure constant, the amplitude of input motion (IM) is varied from 0.1 g to 0.5 g. The variation in the settlement trough along the width, maximum produced ground displacements, and seismic-induced lining forces with respect to the amplitude for the three IMs is plotted in Figures 9A–E. From the figures, it can be seen that the increased amplitude of IM results in exponentially increased ground heaves, and also a logarithmic increase in the seismic-induced lining forces. The obtained results show a similar trend as those obtained by Azadi et al. (2010) and Patil et al. (2018).

4.5 Residual earth pressures

The residual earth pressures from the dynamic analyses are also calculated, which can be seen plotted along with the normalized tunnel perimeter (given in Figures 10B, C) and the deformed tunnel complex shape in Figure 10A. The figures show that the higher amplitude vibrations result in higher uplift pressures on the tunnel structure. This phenomenon causes the dynamic earth pressure to decrease at the invert (0) and on the crown (0.5) due to the heaving of soil and increase on the side walls (0.25 and 0.75) and the shoulder parts (0.3125 and 0.6875) due to the densification and inward movement of the surrounding soil to fill up the void with the increase in the amplitude of the seismic vibration.

4.6 Seismic-induced lining forces

The evaluation of seismic-induced T, Q, and M is very important to understand the distribution of forces along the tunnel lining,

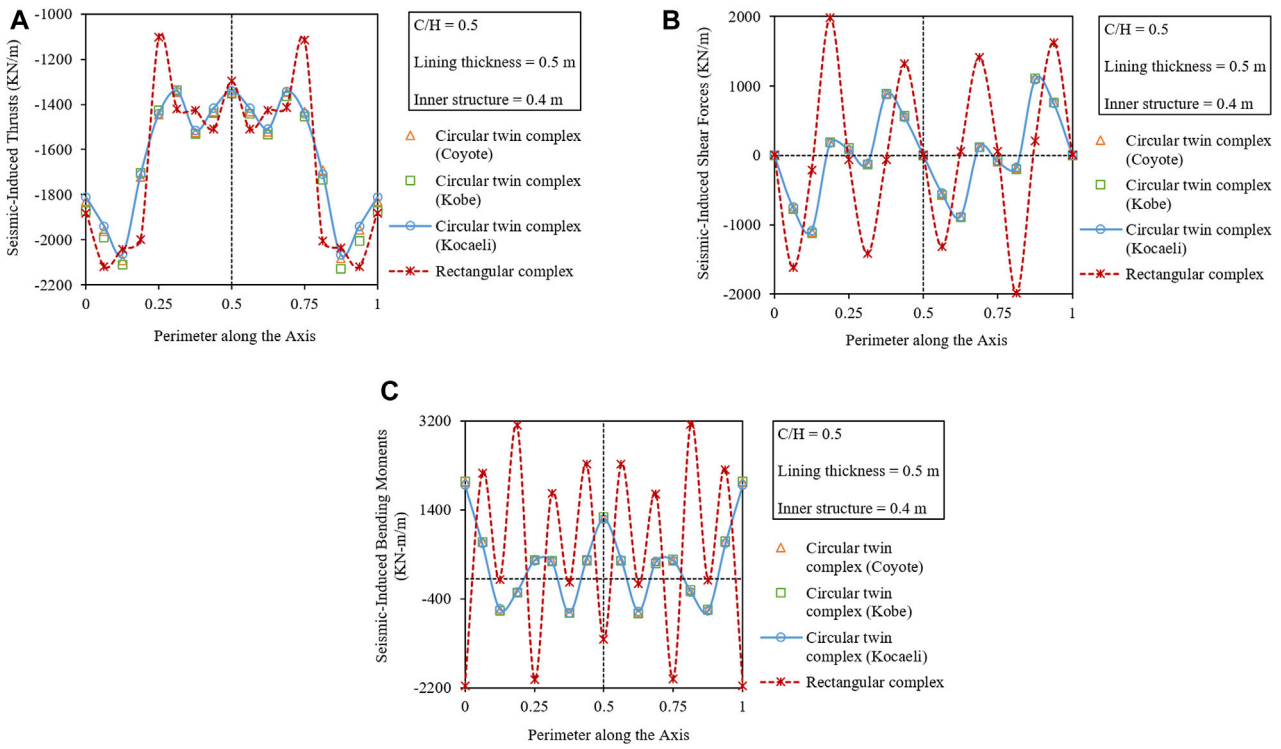

FIGURE 12
Variation in seismic-induced **(A)** thrusts, **(B)** shear forces, and **(C)** bending moments along the perimeter of the circular twin tunnel complex and comparison with the rectangular tunnel complex.

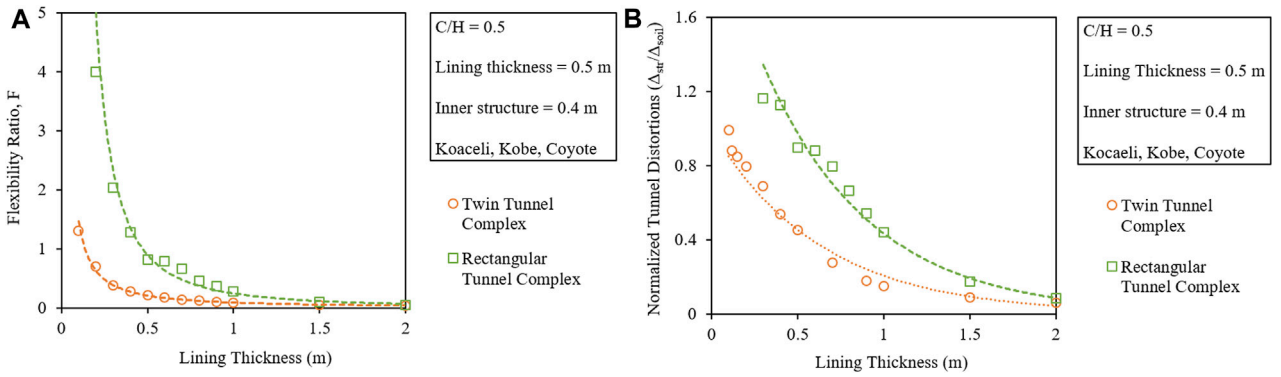

FIGURE 13
Comparison of lining thickness with the **(A)** flexibility ratio. **(B)** Normalized tunnel distortions for circular twin and rectangular tunnel complexes.

which helps in the optimum design of the tunnel structure. To evaluate the forces, the circular twin tunnel complex is subjected to the selected acceleration–time histories while keeping the C/H ratio, the thickness of the lining, and internal connection members constant. The detailed T, Q, and M diagrams can be seen in Figures 11A–C.

Apart from this, the variation in the induced forces along with the tunnel perimeter is also plotted for each of the IMs, which can be seen in Figures 12A–C. The figures show that the critical sections are the invert (0 and 1) and the crown (0.5) which suffer the maximum M, while the knee portions (0.125 and 0.875) are other important sections suffering the maximum T.

4.7 Comparison with the equivalent rectangular tunnel complex

To better understand the seismic performance of the twin tunnel complex, it is compared with the conventional equivalent rectangular tunnel complex (given in Figure 1E).

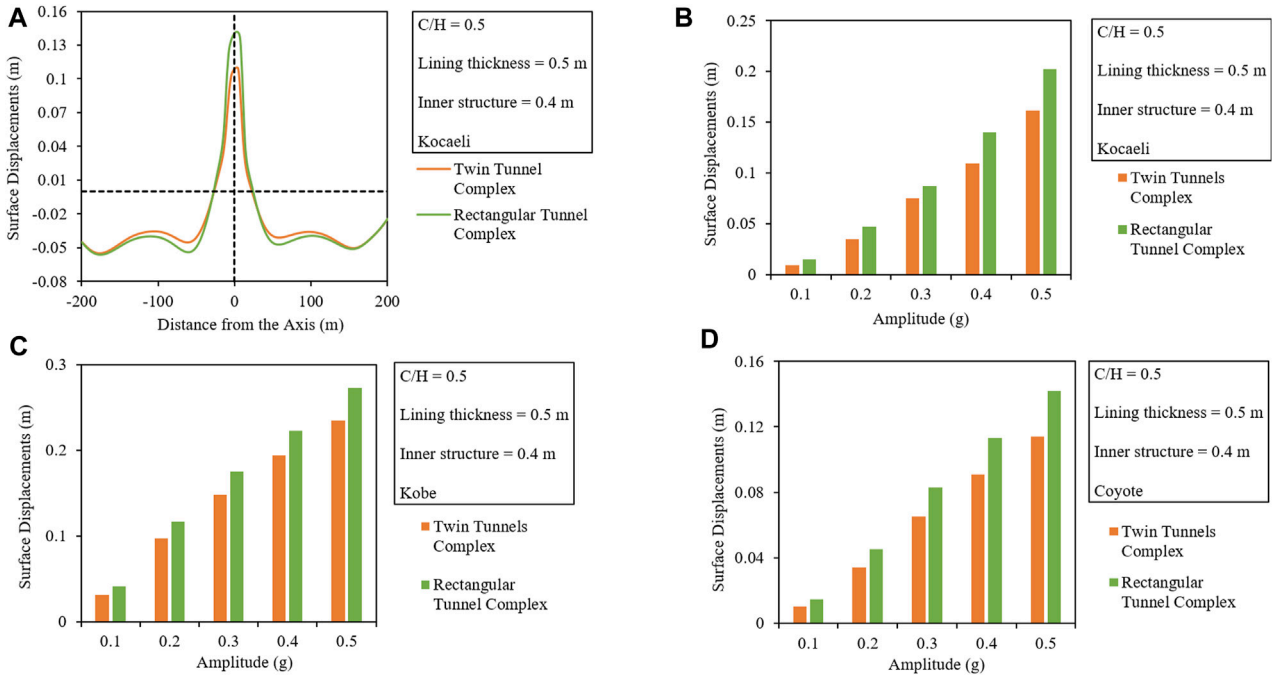

FIGURE 14
Comparison of **(A)** surface displacement troughs along the width and the produced maximum ground displacements with respect to the varying amplitude of **(B)** Kobe, **(C)** Coyote, and **(D)** Kocaeli earthquakes.

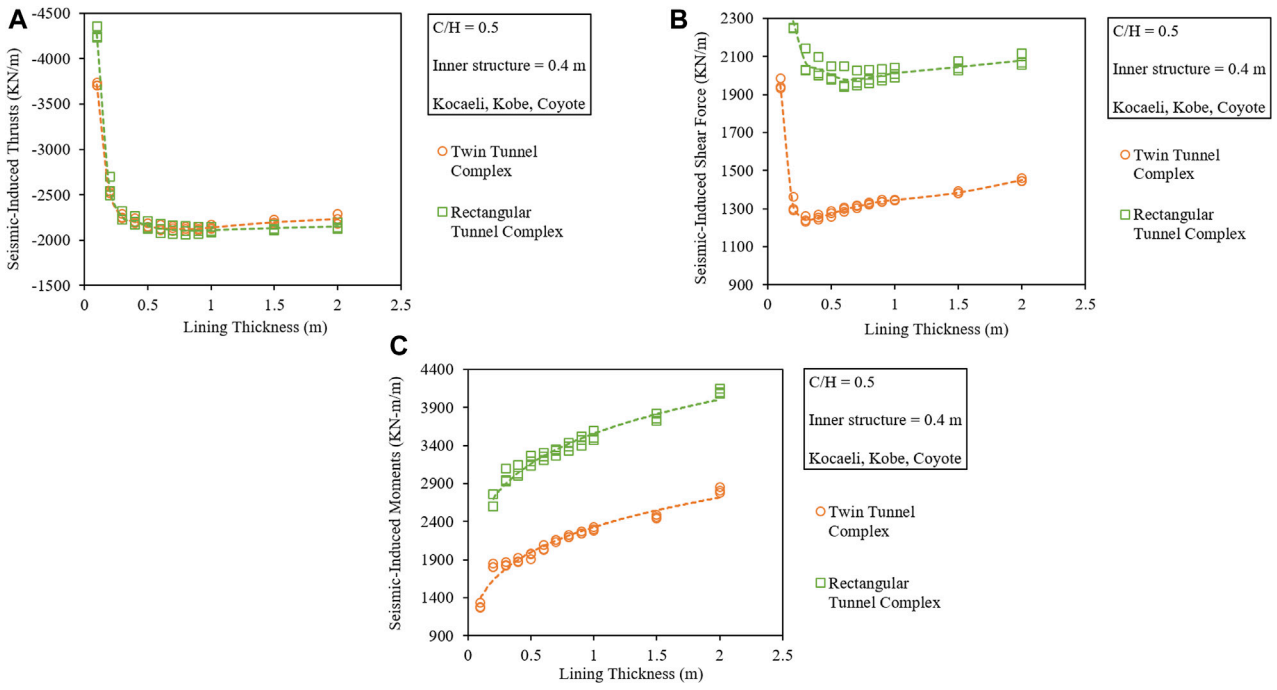

FIGURE 15
Comparison of the seismic-induced **(A)** thrusts, **(B)** shear forces, and **(C)** bending moments with respect to the lining thickness for the circular twin and rectangular tunnel complexes.

4.7.1 Comparison of flexibility

The obtained F and the normalized tunnel distortions with respect to the thickness of the tunnel lining are plotted together for both the tunnel complexes, which can be seen in Figures 13A, B, respectively. All the other affecting parameters, i.e., the C/H ratio, IMs, and the thickness of the internal connecting members, are kept constant.

From the figures, it can be observed that the critical section of the twin tunnel complex (F = 1) has a lining thickness of approximately 0.15–0.2 m, while the rectangular tunnel complex has a lining thickness of approximately 0.45–0.5 m. It means that the same lining thickness would result in a rigid circular twin tunnel complex as well as a flexible rectangular tunnel complex.

4.7.2 Comparison of produced ground displacements

The variation in surface displacement trough along the section width and maximum displacements for both the tunnel complexes are evaluated with respect to the varying amplitude of IMs by keeping the C/H ratio and the thickness of the internal connecting members constant. The obtained plots can be seen in Figures 14A–D. From the figures, it can be noticed that the circular twin tunnel complex results in lesser ground displacements than the equivalent rectangular tunnel complex.

From the comparison, it can be noticed that the twin tunnel is rigid between the two for the given lining thickness and produces approximately 1.3 times lesser displacements than the rectangular tunnel complex.

4.7.3 Comparison of residual dynamic earth pressures

The seismic-induced residual earth pressures are compared for both the tunnel complexes by plotting the variation along with the tunnel perimeter, which can be seen in Figure 10C. From the figure, it can be noticed that having the same lining thickness and other parameters, the circular twin tunnel complex undergoes approximately 1.15 times lesser earth pressures than the rectangular tunnel complex.

4.7.4 Comparison of seismic-induced lining forces

The seismic-induced lining forces, i.e., T, Q, and M, are compared in two different ways. One comparison is made in terms of maximum induced forces with respect to the varying tunnel lining thickness and the second in terms of the variation in induced forces along with the tunnel perimeter which can be seen in Figures 12A–C, 15A–C, respectively.

Figures 15A–C show that having the same C/H ratio and lining thickness, the seismic-induced forces (T, Q, and M) in the twin tunnel complex are lesser between the two complexes. From the variation of seismic-induced forces along with the normalized tunnel perimeter shown in Figures 12A–C, it can be noticed that the rectangular tunnel suffers the maximum seismic-induced forces. Furthermore, it can be noticed that the critical section in the circular twin tunnel complex is the invert (0 and 1) and the knee (0.125 and 0.875) which experience the maximum forces, but in the case of the rectangular tunnel complex, the corners and the joint sections are all critical due to larger induced forces.

Keeping the C/H ratio, the amplitude of IM, the thickness of tunnel lining, and the inner connecting members constant, the T_{max} in a circular twin tunnel complex is approximately 1.03 times lesser than that of the rectangular tunnel complex. The Q_{max} induced in the circular twin complex is approximately 1.81 times lesser than that in the rectangular tunnel complex. The M_{max} induced in the circular twin complex is approximately 1.64 times lesser than that of the rectangular tunnel complex.

5 Limitations

This research is a preliminary study that evaluates and compares the seismic behavior of a novel twin tunnel complex with an equivalent rectangular tunnel complex in 2D. The spatial variation in the longitudinal direction along with the feasibility and practical problems associated with the construction of such a complex shape are ignored while performing this study. Hence, the effect of soil variation, presence of a fault, slope variation, etc., in the longitudinal direction should also be studied using 3D modeling for further evaluation of its seismic performance.

6 Summary and conclusion

Tunnels being an important lifeline structure require an in-depth study when located in an earthquake-prone area to avoid damage during a seismic event. Closely spaced circular twin tunnels combined into a single circular twin tunnel complex result in a novel shape. A detailed numerical study is thus performed on this unconventional tunnel complex shape in the soft soil using three historic major earthquakes to study the effect of lining thickness, embedment depth, and variation in amplitude of seismic vibration on the overall performance. From the obtained results, it is understood that the overall behavior of the tunnel complex depends on both the tunnel lining and the inner connecting members. If the lining thickness is more than the inner structure for F ≤ 0.5, more forces are resisted by the lining than the inner structure. The suffered structural distortions are lesser because the surrounding soil pressure keeps the tunnel complex compact. On the contrary, thinner lining with thicker inner connecting members results in enormous seismic-induced forces in the inner members and hence causes severe distortions. Apart from this, the connection joints of the lining and the inner members are critical sections suffering enormous forces that may result in the collapse of the whole complex and hence need careful consideration during the design. The produced ground heaves, residual dynamic earth pressures, seismic-induced thrusts, shear forces, and bending moments are also compared with those of conventional-shaped rectangular tunnel complex. Based on the study, the following main results are concluded.

1. The increased flexural rigidity of the tunnel lining results in reduced ground heaves while also leading to the increased seismic-induced lining forces.
2. The full-slip interface conditions result in lesser tunnel distortions than the no-slip interface conditions.
3. The increased C/H ratio increases the overall normalized tunnel distortions.

4. The increase in the amplitude of the IM results in an exponential increase of the surface displacements while also leading to a logarithmic increase in the lining forces.
5. The dynamic earth pressures decrease at the invert and crown due to the ground heave and uplift phenomenon but increase at the sides because of the inward soil movement to fill in the void area due to heaving.
6. Keeping the C/H ratio and the amplitude of the IMs constant, the twin tunnel complex behaves rigidly while the rectangular tunnel complex behaves flexibly.
7. The normalized tunnel distortions in the case of a twin tunnel complex are lesser than those in the rectangular tunnel complex.
8. The twin tunnel results in lesser ground heaves and seismic-induced Q and M than the conventional equivalent rectangular tunnel complex. The overall induced T is also minimum in the case of the twin tunnel complex, which makes it a better performer during seismic vibrations.

Data availability statement

The original contributions presented in the study are included in the article/Supplementary Material; further inquiries can be directed to the corresponding author.

Author contributions

AN and HD contributed to the conception. AN contributed to the design of this study, performed numerical analyses, and wrote the main manuscript draft. MK, WA, and SS reviewed and made improvements to the draft. SS, KS, and HD provided useful input and supervision. All authors contributed to the article and approved the submitted version.

Acknowledgments

The authors are thankful to Gent University (Belgium) for providing the facilities, Qilu Institute of Technology (China) to provide the funding for this particular research under the grant "QIT23TP001" and the Higher Education Commission (HEC) of Pakistan to fund this tunneling project under the grant "HRDI-UESTP/UETs Phase 1."

Conflict of interest

The authors declare that the research was conducted in the absence of any commercial or financial relationships that could be construed as a potential conflict of interest.

Publisher's note

References

Abdel-MotaalAhmed, Mohamed, and Mohamed El-Nahhas, FathallaAhmed Tawfik Khiry (2014). Mutual seismic interaction between tunnels and the surrounding granular soil. *HBRC J.* 10 (3), 265–278. doi:10.1016/j.hbrcj.2013.12.006

Adalier, Korhan, Abdoun, Tarek, Dobry, Ricardo, Phillips, Robert, Yang, Di, and Naesgaard, Ernest (2003). Centrifuge modelling for seismic retrofit design of an immersed tube tunnel. *Int. J. Phys. Model. geotechnics* 3 (2), 23–35. doi:10.1680/ijpmg.2003.030203

Anderson, Donald G. (2008). Seismic analysis and design of retaining walls, buried structures, slopes, and embankments. *Transp. Res. Board* 611. doi:10.17226/14189

Azadi, M., Mir, S. M., and Hosseini, Mohammad (2010). Analyses of the effect of seismic behavior of shallow tunnels in liquefiable grounds. *Tunn. Undergr. space Technol.* 25 (5), 543–552. doi:10.1016/j.tust.2010.03.003

Bilotta, Emilio, Lanzano, Giovanni, Madabhushi, S. P. Gopal, and Silvestri, Francesco (2014). A numerical Round Robin on tunnels under seismic actions. *Acta Geotech.* 9 (4), 563–579. doi:10.1007/s11440-014-0330-3

Bobet, A. (2003). Effect of pore water pressure on tunnel support during static and seismic loading. *Tunn. Undergr. Space Technol.* 18 (4), 377–393. doi:10.1016/s0886-7798(03)00008-7

Bobet, Antonio (2010). Drained and undrained response of deep tunnels subjected to far-field shear loading. *Tunn. Undergr. Space Technol.* 25 (1), 21–31. doi:10.1016/j.tust.2009.08.001

Brinkgreve, R. B. J., Swolfs, W. M., Engin, E., Waterman, D., Chesaru, A., Bonnier, P. G., et al. (2010). *PLAXIS 2D 2010 User manual*. Delft, Netherlands: Plaxis bv.

Chang, Dongdong, Travasarou, Thaleia, and Jacob, Chacko "Numerical evaluation of liquefaction-induced uplift for an immersed tunnel," in Proceedings of the 14th world conference on earthquake engineering, Reykjavik, Iceland, June 2008.

Chen, Zhiyi, Shi, Cheng, Li, Tianbin, and Yuan, Yong (2012). Damage characteristics and influence factors of mountain tunnels under strong earthquakes. *Nat. hazards* 61 (2), 387–401. doi:10.1007/s11069-011-9924-3

Chen, Z. Y., and Shen, H. (2014). Dynamic centrifuge tests on isolation mechanism of tunnels subjected to seismic shaking. *Tunn. Undergr. Space Technol.* 42, 67–77. doi:10.1016/j.tust.2014.02.005

Cilingir, Ulas, and Madabhushi, S. P. Gopal (2011c). A model study on the effects of input motion on the seismic behaviour of tunnels. *Soil Dyn. Earthq. Eng.* 31 (3), 452–462. doi:10.1016/j.soildyn.2010.10.004

Cilingir, Ulas, and Madabhushi, S. P. Gopal (2011a). Effect of depth on seismic response of circular tunnels. *Can. Geotechnical J.* 48 (1), 117–127. doi:10.1139/t10-047

Cilingir, Ulas, and Madabhushi, S. P. G. O. P. A. L. (2011b). Effect of depth on the seismic response of square tunnels. *Soils Found.* 51 (3), 449–457. doi:10.3208/sandf.51.449

Code, Euro (2005). *Eurocode 8: Design of structures for earthquake resistance-part 1: General rules, seismic actions and rules for buildings*. Brussels, Belgium: European Committee for Standardization.

Debiasi, E., Gajo, A., and Zonta, D. (2013). On the seismic response of shallow-buried rectangular structures. *Tunn. Undergr. space Technol.* 38, 99–113. doi:10.1016/j.tust.2013.04.011

HashashYoussef, M. A., Hook, J. J., Schmidt, B., John, I., and Yao, C. (2001). Seismic design and analysis of underground structures. *Tunn. Undergr. space Technol.* 16 (4), 247–293. doi:10.1016/s0886-7798(01)00051-7

HashashYoussef, M. A., Karina, Karina, Koutsoftas, Demetrious, and O'Riordan, Nick "Seismic design considerations for underground box structures," in Proceedings of the Earth Retention Conference, Bellevue, Washington, United States, January 2010.

Hoeg, K. A. A. R. E. (1968). Stresses against underground structural cylinders. *J. Soil Mech. Found. Div.*

Huo, H., Bobet, A., Fernández, G., and Ramirez, J. (2005). Load transfer mechanisms between underground structure and surrounding ground: Evaluation of the failure of the daikai station. *J. Geotechnical Geoenvironmental Eng.* 131 (12), 1522–1533. doi:10.1061/(asce)1090-0241(2005)131:12(1522)

KuhlemeyerRoger, L., and Lysmer, J. (1973). Finite element method accuracy for wave propagation problems. *J. Soil Mech. Found. Div* 99, 421–427. doi:10.1061/jsfeaq.0001885

Lanzano, G., Bilotta, E., Russo, G., Silvestri, F., and Madabhushi, S. P. G. "Dynamic centrifuge tests on shallow tunnel models in dry sand," in Proceedings of the VII international conference on physical modelling in geotechnics (ICPMG 2010), Zurich, Switerland, June 2010.

Lanzano, Giovanni (2009).Physical and analytical modelling of tunnels under dynamic loadings PhD Thesis. Naples, Italy: University of Naples Federico II.

Naseem, Ahsan, Kashif, Muhammad, Iqbal, Nouman, Schotte, Ken, and De Backer, Hans (2020). Seismic behavior of triple tunnel complex in soft soil subjected to transverse shaking. *Appl. Sci.* 10 (1), 334. doi:10.3390/app10010334

Naseem, Ahsan, Schotte, Ken, De Pauw, Bart, and De Backer, Hans (2019). Ground settlements due to construction of triplet tunnels with different construction arrangements. *Adv. Civ. Eng.* 2019, 1–18. doi:10.1155/2019/8637837

Owen, G. Norman, and Scholl, Roger E. (1981).*Earthquake engineering of large underground structures* Washington, DC, USA: Bureau of Transportation Statistics.

Park, Kyung-Ho, Tantayopin, Kullachai, Tontavanich, Bituporn, and Owatsiriwong, Adisorn (2009). Analytical solution for seismic-induced ovaling of circular tunnel lining under no-slip interface conditions: A revisit. *Tunn. Undergr. Space Technol.* 24 (2), 231–235. doi:10.1016/j.tust.2008.07.001

Patil, Milind, Choudhury, Deepankar, Ranjith, P. G., and Zhao, Jian (2018). Behavior of shallow tunnel in soft soil under seismic conditions. *Tunn. Undergr. Space Technol.* 82, 30–38. doi:10.1016/j.tust.2018.04.040

Penzien, Joseph (2000). Seismically induced racking of tunnel linings. *Earthq. Eng. Struct. Dyn.* 29 (5), 683–691. doi:10.1002/(sici)1096-9845(200005)29:5<683::aid-eqe932>3.0.co;2-1

Power, M., Rosidi, D., Kaneshiro, J., Gilstrap, S., and Chiou, S. J. (1998). "Summary and evaluation of procedures for the seismic design of tunnels," in *Final report for task* (New York, NY, USA: National Center for Earthquake Engineering Research, Buffalo).

Qiu, Junling, Xie, Yongli, Fan, Haobo, Wang, Zhichao, and Zhang, Yuwei (2017). Centrifuge modelling of twin-tunnelling induced ground movements in loess strata. *Arabian J. Geosciences* 10 (22), 493. doi:10.1007/s12517-017-3297-1

Sadiq, Shamsher, Van Nguyen, Quang, Jung, Hyunil, and Park, Duhee (2019). Effect of flexibility ratio on seismic response of cut-and-cover box tunnel. *Adv. Civ. Eng.* 2019, 1–16. doi:10.1155/2019/4905329

Sandoval, Eimar, and Bobet, Antonio (2017). Effect of frequency and flexibility ratio on the seismic response of deep tunnels. *Undergr. Space* 2 (2), 125–133. doi:10.1016/j.undsp.2017.04.003

Sharma, Sunil, and Judd, William R. (1991). Underground opening damage from earthquakes. *Eng. Geol.* 30 (3-4), 263–276. doi:10.1016/0013-7952(91)90063-q

Tsinidis, Grigorios (2017). Response characteristics of rectangular tunnels in soft soil subjected to transversal ground shaking. *Tunn. Undergr. Space Technol.* 62, 1–22. doi:10.1016/j.tust.2016.11.003

Ulgen, Deniz, Saglam, Selman, and Ozkan, M. Yener (2015). Dynamic response of a flexible rectangular underground structure in sand: Centrifuge modeling. *Bull. Earthq. Eng.* 13 (9), 2547–2566. doi:10.1007/s10518-015-9736-z

Wang, J. N. (1993). *Seismic design of tunnels: A state-of-the-art approach, monograph, monograph 7*. New York, NY, USA: Parsons, Brinckerhoff, Quade and Douglas Inc.

Yang, Dan, Naesgaard, Ernest, Byrne, Peter M., Adalier, Korhan, and Abdoun, Tarek (2004). Numerical model verification and calibration of George Massey Tunnel using centrifuge models. *Can. geotechnical J.* 41 (5), 921–942. doi:10.1139/t04-039

frontiers | Frontiers in Ecology and Evolution

TYPE Original Research
PUBLISHED 25 September 2023
DOI 10.3389/fevo.2023.1256041

OPEN ACCESS

EDITED BY
Liang Cui,
Lakehead University, Canada

REVIEWED BY
Li Tao,
China University of Mining and Technology, China
Sun Lihui,
Hebei Engineering University, China

*CORRESPONDENCE
Aizhong Luo
55192473@qq.com

RECEIVED 10 July 2023
ACCEPTED 15 August 2023
PUBLISHED 25 September 2023

CITATION
Fang J, Luo A, Shao S and Chen C (2023) Progressive failure analysis of soil slopes considering the influences of humidity and loading.
Front. Ecol. Evol. 11:1256041.
doi: 10.3389/fevo.2023.1256041

Progressive failure analysis of soil slopes considering the influences of humidity and loading

Juan Fang[1], Aizhong Luo[1]*, Shengjun Shao[2] and Changlu Chen[1]

[1]School of Civil Engineering and Architecture, Guizhou University of Engineering Science, Bijie, Guizhou, China, [2]Institute of Geotechnical Engineering, Xi'an University of Technology, Xi'an, China

To analyze the progressive failure of structural loess slopes due to changes in humidity and loading, this study analyzes the degrees of influence of these changes on slope failure and their relationships with various structural parameters. According to the analysis, the shear failure of the soil gradually develops with the change of the water content. When the water content reaches a 17%, with the development of shear deformation, the shear zone is formed and finally penetrates the soil body. With the increase of the water content, the total displacement of the slope body gradually develops. When the water content reaches 17%, the total displacement of the slope body changes suddenly. This mutation is consistent with the formation of the shear zone. The sudden change of displacement indicates the penetration of the shear zone and the damage and slippage of the slope. With the increase of the soil moisture of the slope, the strain localization phenomenon occurs, the development of strain localization and shear bands increases, the structural damage increases, and the quantitative structural parameters decrease. The quantitative parameters can therefore be used to evaluate the feasibility and rationality of the progressive failure process of homogeneous structural loess slopes.

KEYWORDS

progressive failure, influence of humidity and load, structural loess, slope, structural parameters

1 Introduction

During infrastructure construction in loess regions, numerous loess foundation and slope engineering problems will inevitably be encountered. The concept of slope progressive failure was first proposed by Terzaghi (1936), who believed that slope failure was caused by the strain softening of the soil mass. Skempton (1964) used the slope progressive failure theory to analyze the stability of a slope, and found that the shear strength of the soil at different positions of the over consolidated cohesive soil slope was asynchronous. According to the concept of progressive failure, the strength of the soil mass does not affect the entire sliding surface simultaneously; only when the shear stress

increases at a certain point and exceeds the soil strength does shear failure occur. With the development of soil deformation, shear failure gradually transfers to adjacent elements, and the asymptotic failure surface gradually expands. Finally, when the sliding thrust of the entire soil mass exceeds the shear strength of the soil screen, the entire slope slides (Lo and Lee, 1973; Troncone, 2005; Conte, 2010). Via research on the shear strength of clay materials, Lu (1986) found that for a slope body composed of strain-softening materials, the shear strength of the local soil on the sliding surface decreases from the peak strength to the residual strength during soil failure. Liu and Wang (1994) proposed an asymptotic failure analysis model of an infinite-plane slope via slope stability analysis. While the analytical model can simulate the asymptotic failure process of the slope very well, the simulation can only be applied to bedding landslides with a planar slope fracture surface. Tan et al. (2000) simulated the process of slope failure from the toe and top of the slope to the middle via a physical similarity model that considered the proportions of fine sand, gypsum, mica powder, and engine oil. Cheng et al. (2000) established a corresponding slope finite element model by introducing the viscoelastic-plastic constitutive relationship, and analyzed the progressive failure of a rock mass with a high slope. Wang (2000) used a new contact element model to simulate the contact friction state on the sliding surface, and carried out the progressive failure process and stability analysis of the slope. Through examples, it was demonstrated that the stability coefficient of the slope while considering progressive failure was 5–10% less than that without the consideration of progressive failure. Zhang and Zhang (2007), Lu et al. (2021), Lu et al. (2022), Xue et al. (2016), and Shen et al. (2016) also analyzed progressive failure according to the characteristics of the soil strain-softening stage.

Loess is a typical structural soil. Due to the existence of the structure, when the initial structural strength is high, the stress-strain relationship curve of the soil usually presents a softened or weakly softened curve. Before the peak value of the softened stress-strain relationship curve, the shear strength gradually develops with the increase of shear strain. After the peak value occurs, the soil structure is gradually destroyed and the shear strain develops. Finally, the regional stability value of the soil strength is the residual strength. Therefore, the sliding failure of loess slopes is a typical asymptotic failure mode.

There have been many theoretical studies on slope progressive failure. However, for loess, a special soil with a strong structure, the gradual failure analysis theory considering the coupling effect of humidification and overload has not been studied. Under the coupling effect of slope overload and possible wetting, the strength and deformation of yellow soil change with the attenuation of the structure. In the present work, reference is made to the structural constitutive models of humidity and loading (Luo et al., 2015a; Luo et al., 2015b; Luo et al., 2016; Luo and Fang, 2018) established based on the understanding of the mechanism of the structural strength and deformation change of loess. By considering the structural evolution and change law of loess slopes under the conditions of overloading and humidification, the distribution laws of the structural parameters and the slip band in the distribution of structural loss are revealed. The stability analysis of loess slopes provides a theoretical basis for reasonable reinforcement measures. Guiding the construction of infrastructure in loess areas and the exploration of a more practical method for the study of the soil structure are of great significance.

2 Moisture distribution and permeability of loess

2.1 Moisture distribution of loess

The existing structural state of natural loess was formed in semi-arid climates and aeolian sediment environments after a long period of geological deposition. The structural connection of loess reflects comprehensive external and internal influences throughout the entire historical formation process. Furthermore, the existing structural state determines the possible change tendency of the loess structure under a new external environment. The structure of loess is composed of structural units, cements, and pores. Due to the unique geological environmental conditions, loess particles are mainly coarse powder accompanied by some large sand particles. Coarse silt is the main skeleton of loess, and fine silt, clay, and detritus are attached to the surface of sandy soil grains. Together with the solution formed by soluble salt and deposited at the contact point of the grains, they form a cementation connection, which strengthens the structural characteristics of loess. Skeleton particles are an important pillar of the loess structural system, and their morphology represents the force transfer performance and deformation properties of loess under external loads. Their connection forms directly affect the structural strength of the loess itself, and their arrangement directly determines the stability of the entire structural system under external loads.

The structural strength of the structural soil largely depends on the composition and corresponding properties of the intergranular cement. For loess, a special structural soil, the main components of intergranular cement are clay minerals and intergranular calcium carbonate. Due to the special activity of finely dispersed clay minerals and their large specific surface area, they more easily aggregate or adsorb on the surface of larger skeleton particles. This is more conducive to the formation of aggregate particles and clay films in loess, which form a special structural system with different structural strengths as the water content changes. These aggregates mainly include non-water-stable aggregates, water-stable aggregates, water-resistant aggregates, and highly-water-resistant aggregates. The main reason for the structural damage change of loess is the existence of a large number of non-water-stable aggregates, which are formed by the cementation of soluble salt and reversible dry adhesive film, and are destroyed when they encounter water; this is also one of the main reasons for the strong water sensitivity of structural loess.

Therefore, the soil humidity is an important indicator of the engineering properties of loess, and its change has serious impacts. Changes in humidity are mainly due to the rise and fall of the groundwater level and absorption and evaporation caused by rainfall. Generally, loess has a very low natural water content. The natural water content of loess on the tableland and beam where the groundwater is deeply buried usually varies from 6% to 10%, and that of loess on a plain terrace varies from 11% to 21% due to groundwater with a

shallow buried depth and high level. In addition, due to the influence of the climate, the moisture content of surface loess varies greatly with the season. In the stratum and buried depth of loess, the change of the moisture content as a humidity indicator will inevitably affect the changes of the compressibility, collapsibility, and shear strength indicators of loess, and will further affect the stability of the loess project site and region. The research of Wang (2008) revealed that under the same slope conditions, the moisture content of a shady slope is higher than that of a sunny slope, but the difference is relatively small after a certain depth range. Moreover, with the increase of the slope of the loess plateau, the water content of the corresponding layers in the soil slope decreases. Furthermore, the seepage generated during rainfall increases with the decrease of the slope.

2.2 Permeability of loess

The factors affecting the permeability of loess include the properties of the soil particles, the shape and grading of the soil particles, the void ratio, the structure, cracks and bedding, according to the research of Xu (2021), Hong et al. (2019), and Liu et al. (2022, 2023). The extant research is far from meeting the needs of engineering practice. Due to spatial constraints, this study does not consider the permeability law of loess, but only describes the general law of loess permeability, which provides the corresponding humidity field for the application of the compression-shear constitutive model under the condition of soil moisture. Previous studies have shown that there are vertical tubular macropores in Q3 loess, which endows the permeability of loess with obvious anisotropy. The vertical permeability is far greater than the horizontal permeability. When loess is soaked and collapses, due to the loss of the structure, the permeability in both directions gradually becomes similar. There is no obvious relationship between the permeability coefficient and the void ratio of loess in the natural state. For loess after disturbance and compaction, the permeability coefficient decreases with the decrease of the void ratio due to the elimination of uneven large pores in the loess. The permeability of Q3 loess is related to its particle composition and structural characteristics, and the permeability of loess in the contact state of coarse particles and overhead is large. During the collapse development of loess, due to the change of the structural state, the permeability coefficient also changes and gradually decreases. In the natural state, the water content of loess is low, and the soil mass is in a three-phase state. When water begins to permeate loess, the permeability coefficient becomes high, gradually decreases with time, and finally approaches stable seepage.

3 Progressive failure of a homogeneous loess slope under humidification

3.1 Numerical model and calculation parameters

In slope stability analysis, the factors that influence the slope stability mainly focus on two aspects, namely (1) the change of the stress or structure state of the slope itself, and (2) the change of the external environment of the slope area, such as excavation, rainfall, overload, etc. In fact, the asymptotic failure of the slope is mainly caused by the following two factors and their coupling effects. First, the internal cause of the progressive instability failure of the slope is the destruction of the internal structure of the slope body and the generation of a plastic failure area under stress conditions, such as humidity and load conditions. The residual energy is fully released, which causes the readjustment of the local stress state of the slope. The elastic region around the plastic region then further develops into a plastic region due to the superposition of residual stress. The soil skeleton structure is further destroyed, and the secondary stable structure is further generated. Second, changes of the hydrogeology and boundary environment of the slope result in the reduction of the mechanical properties of the rock and soil mass within a certain range of the slope, and the local area changes from elastic to plastic. Simultaneously, the stress field adjusts and releases energy, which further expands the plastic failure area. This is also the main reason for the gradual failure of the excavated slope.

Considering the analysis purpose of this study, the change of the stress field of loess slopes caused by excavation and the exertion of the structural strength of slope soil are not considered. Only the asymptotic failure and development mechanism of the slope caused by humidity and load stress after excavation, as well as the exertion characteristics of the strength of the slope soil, are analyzed. Figure 1 presents the model of the slope. The three directions at the bottom are fixed displacement boundary conditions. The displacement in the x-direction is respectively fixed in the two boundary directions, and the displacement in the y-direction is fixed at 1 m.

3.2 Analysis of the calculation results

To analyze the gradual destruction of the homogeneous loess slope caused by the humidification process, the stability of the loess slope caused by the change of the humidity field under the self-weight condition was analyzed. The moisture content was changed from 10% to shear band formation. Figures 2 and 3 present the nephograms of the shear strain increment and total displacement during the progressive failure of a homogeneous self-weight loess slope under the humidification condition. With the change of the moisture content, the shear failure of the soil mass gradually develops. When the moisture content reaches 17%, with the development of shear deformation, the shear band is formed and finally connected. In Figure 4, with the increase of the soil moisture content, the total displacement of the slope gradually develops. When the moisture content reaches a certain value, the total displacement of the slope suddenly changes, which is consistent with the formation of the shear band. With the change of the displacement, the shear band is cut through and the slope produces destructive sliding. When the stress of the slope is concentrated to a certain extent due to the change of the humidity field of the slope, the plastic region first appears at the foot of the mean loess slope and becomes the initial failure point. The analysis shows that due to the strain localization phenomenon at the slope toe, there is strong

10.3389/fevo.2023.1256041

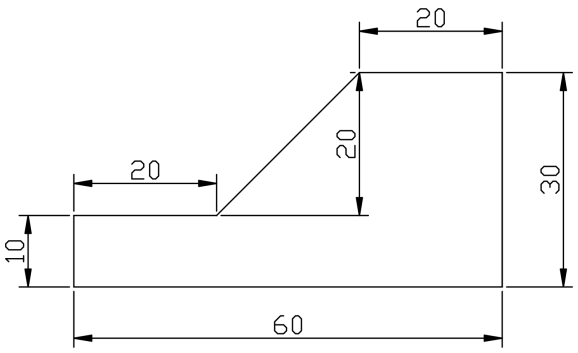

FIGURE 1
The schematic diagram of the model calculation of the slope of unified loess.

stress concentration at this point, at which the local stress concentration exceeds the soil strength of the loess. When the structural strength of the material is high, damage begins and develops, and the plastic deformation also develops simultaneously; thus, a plastic failure zone appears inside the slope. The appearance of the local plastic failure area causes the obvious decrease of the bearing capacity of this area. The stress field of the slope is redistributed, which leads to the destruction of the new primary structure and the generation of a plastic failure area. In this way, during the mutual adjustment and coupling change between the destruction of the primary structure and the generation of the secondary structure, the plastic zone continues to expand until the failure surface and plastic zone are formed. Therefore, it is suggested that the method of "displacement mutation + shear band connection" be used to qualitatively evaluate the stability of loess slopes when determining the slope stability and the position of the slip surface.

Figure 5 presents the evolution process of the structural damage of a homogeneous structural loess slope from near to complete instability. Under certain water content conditions, when the slope is close to the local shear zone, the quantitative structural parameters at the shear band of the slope attenuate relative to other areas of the slope due to the development of shear deformation. Moreover, the attenuation trend of the structural parameters of the stress ratio in the slope is consistent with the development of the shear band caused by the strain localization of the slope. In the past, the strength reduction method was generally used to calculate the safety factor of slope stability in the analysis of progressive slope failure. This method was established based

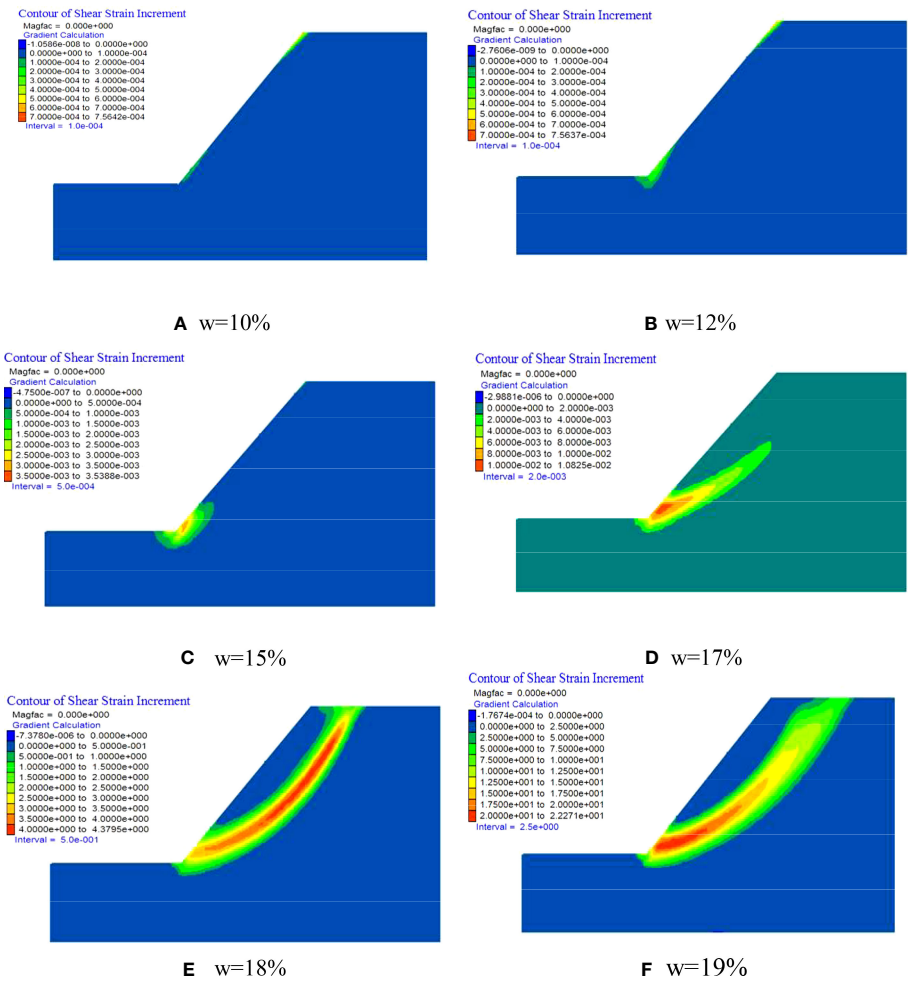

FIGURE 2
The cloud maps of shear strain under different water contents.

10.3389/fevo.2023.1256041

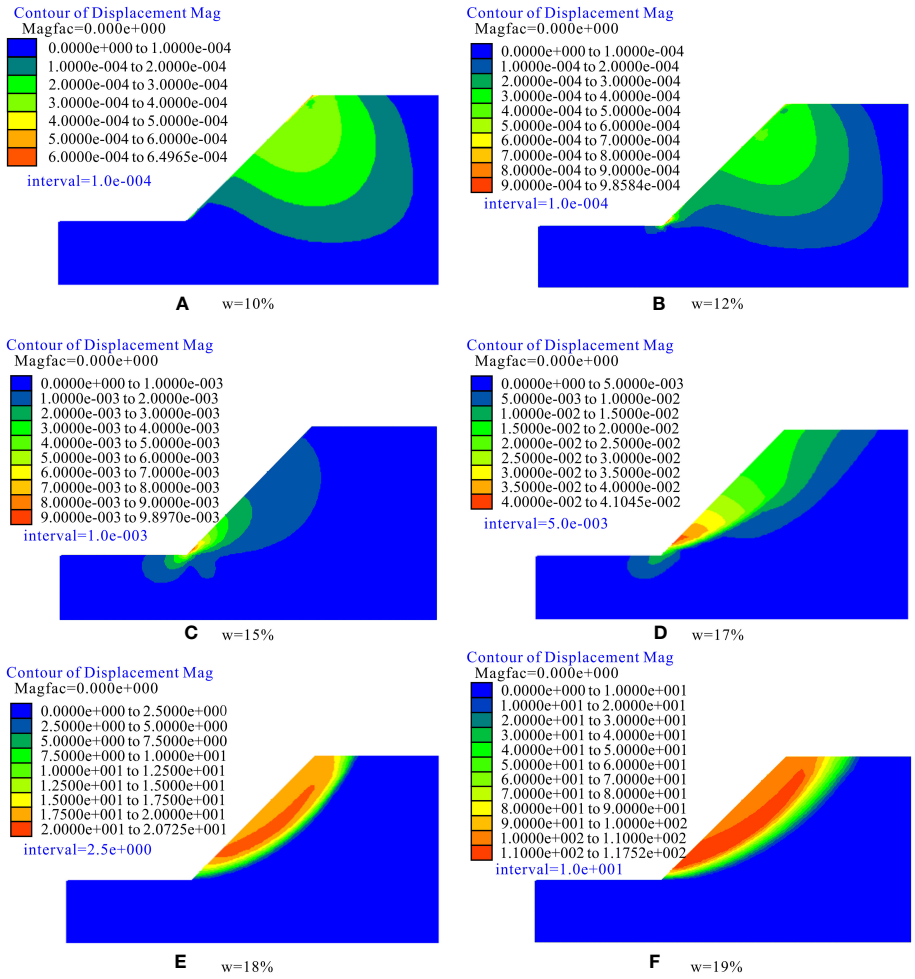

FIGURE 3
The cloud maps of displacement under different water contents.

on the previously mentioned criteria for slope instability. When slope instability occurs, the corresponding reduction factor is specified as the safety factor of the slope. The safety factor defined by this analysis method has no physical significance, nor can its correlation with different soil properties be established. It can be seen that in the stability analysis of homogeneous structural loess slopes, the progressive failure process of the slope is actually the evolution and development process of structural damage; in other words, the development and change of the quantitative structural parameters of the slope can actually be used as some of the instability criteria for the progressive failure analysis. If it is assumed that the quantitative structural parameters of the slope attenuate to a certain extent during the processes of humidification and loading, the slope can be defined as having suffered from instability and failure. At this time, the quantitative structural parameters corresponding to the local shear zone of the slope are consistent with the safety reserve of the slope, i.e., the stability of the homogeneous structural loess slope can be quantitatively evaluated by the quantitative structural parameters of the slope.

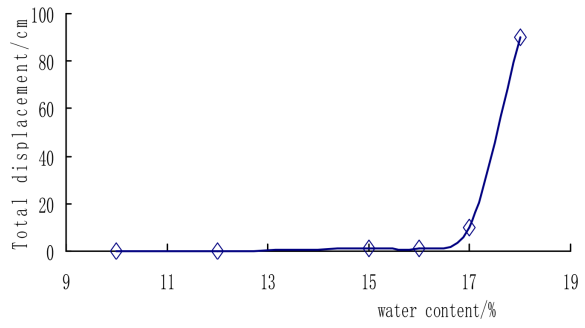

FIGURE 4
The relationship between the total displacement and water content of loess slopes.

4 Progressive failure of a homogeneous loess slope under loading

A homogeneous structural loess slope with an initial moisture content of 0.15 was selected to investigate the progressive failure process of the slope under loading. The load was increased by 20 kPa per section. After the shear band of the slope appeared, the

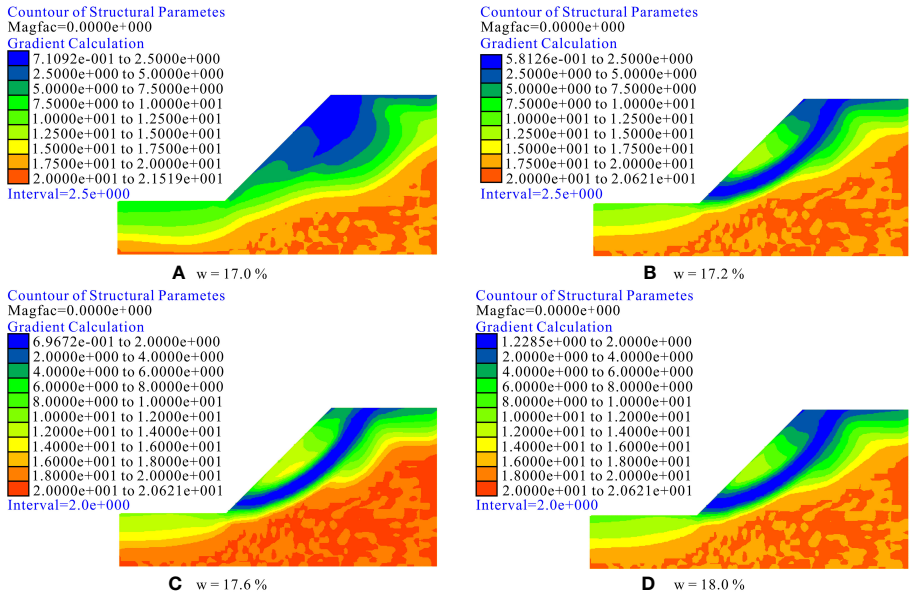

FIGURE 5
The cloud maps of the stress ratio structural parameters under different water contents.

acceleration rate of load application was reduced to investigate the progressive failure evolution process of the slope. The load was uniformly distributed, and the operating distance was 5 m from the slope top.

Figure 6 displays the development and change of the shear strain increment under different top loads under the condition of a 15% water content. The strain increment was found to increase with the increase of the top load of the slope. With the increase of the top load of the slope to 240 kPa, the shear band begins to appear and develop. With its increase to 244 kPa, a shear band forms and runs through the slope. Different from the gradual failure of slopes caused by humidification, the gradual failure of slopes caused by loading begins from the top of the slope, and when the shear band develops to the bottom of the slope, the slope will lose its stability.

Figure 7 shows the development and change process of the total displacement of the slope under the action of the load on the top of

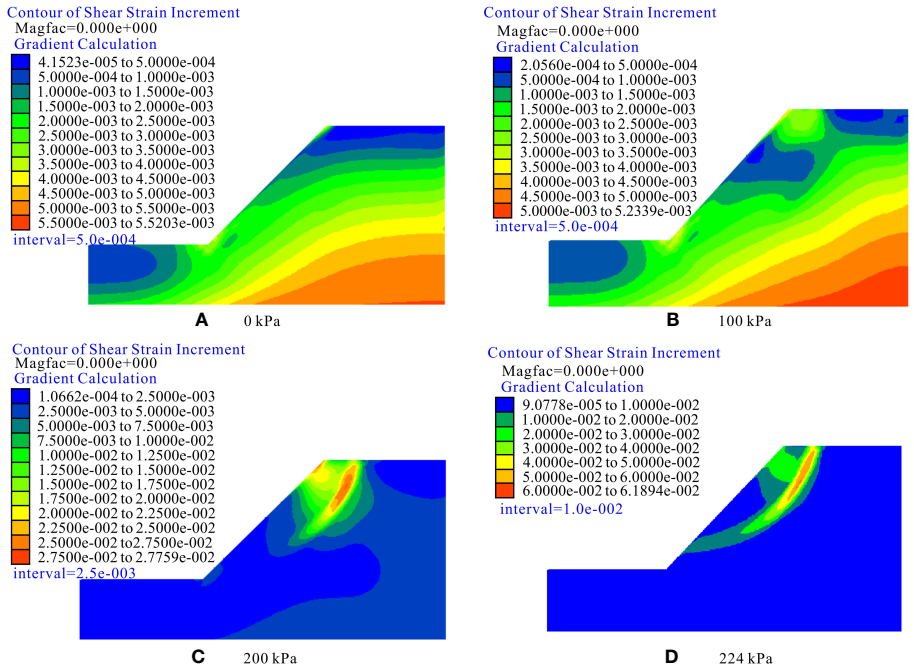

FIGURE 6
The cloud maps of shear strain under different loads.

the slope. The maximum total displacement of the slope was found to first decrease and then increase, and the areas that appear are different before and after the failure. When the load on the top of the slope is low, the total displacement appears at the top of the slope far away from the free surface. When the slope is close to sliding failure, the maximum displacement preferentially moves on the side of the free surface. At this time, the position at which the maximum displacement occurs is consistent with the position on the slope at which sliding instability failure occurs.

Figure 8 exhibits the cloud maps of the structural parameter changes of the progressive failure of the slope under the action of top loading and a water content of 15%. The change law of the structural parameters was found to be basically consistent with the change law and trend of the shear strain increment of the slope body. After the appearance of the slope shear zone, the structural parameters in the shear zone are close to 1. Different from the humidification model findings, the shear band generated by loading has an obvious zonal feature, i.e., there is a typical slip surface during the sliding process. Under the load on the top of the slope, when the whole slope slides, the top of the slope is partially destroyed.

5 Conclusion

It was found that when the water content is 10%, the maximum load on the top of the slope reaches 500 kPa. At this time, the value of slope failure appears at the top of the slope, and there is no continuity of the slip surface throughout the entire slope. With the increase of the water content, the load that the slope top can bear decreases correspondingly, and the slope sliding surface begins to move downward. When the water content reaches 15% and the load on the top of the slope reaches 224 kPa, the sliding surface of slope failure begins to penetrate, but it does not pass the toe of the slope. However, with the further increase of the water content, the load on the top of the slope decreases sharply, and the sliding surface of the slope gradually becomes close to the slope toe. When the water content reaches 17.5%, the slope top slips without any load. The following conclusions can be drawn from the findings:

(1) In previous soil slope stability analysis, it was assumed that the strength of the soil in the assumed sliding surface of the soil slope reaches its peak value simultaneously; in this case, the asymptotic process of slope failure was not considered. The viewpoint that the failure of the slope begins from the slope toe at a certain time and finally develops to the top of the slope to form a slip is one-sided. In theory, the strength of the soil in the slip zone is fully exerted when the slope is subject to sliding failure.

(2) When the water content is 10%, the attenuation of the structural parameters caused by the top loading of the slope mainly occurs at the top of the slope. Moreover, the attenuation of the structural parameters is mainly caused by loading, which exhibits regional characteristics rather than a zonal distribution during humidification. With the increase of the water content, the attenuation of the structural parameters caused by humidification increases and begins to expand in a band to the slope bottom.

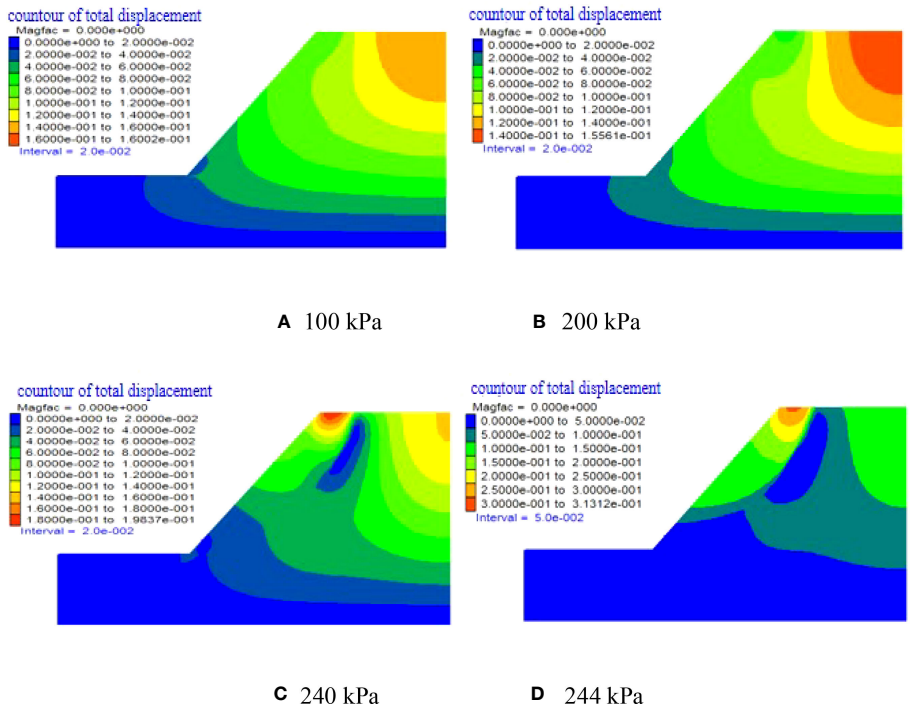

FIGURE 7
The cloud maps of total displacement under different loads.

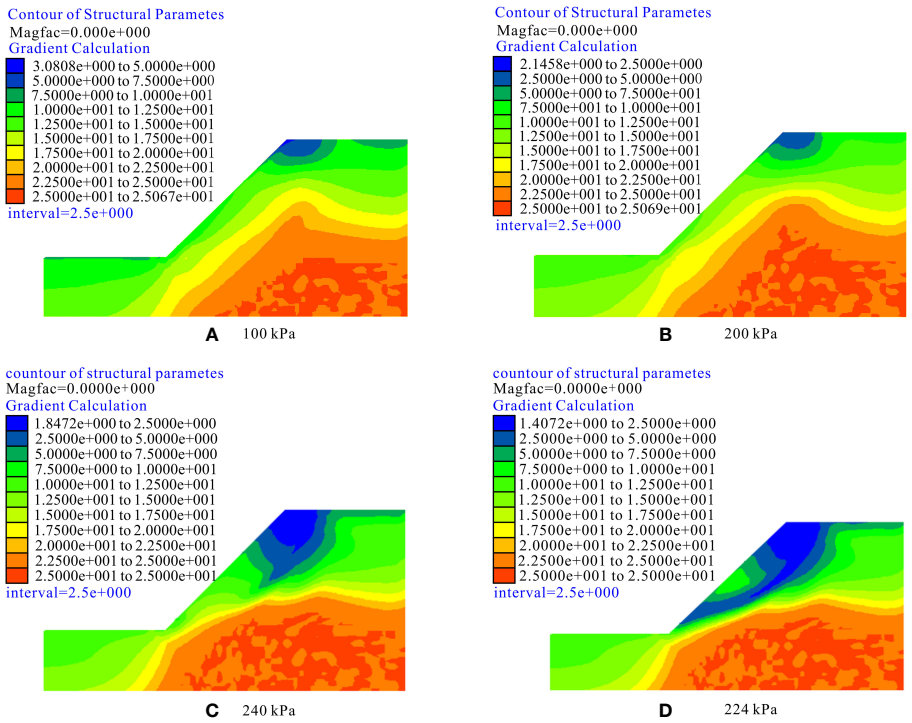

FIGURE 8
The cloud maps of the stress ratio structural parameters under different loads.

(3) Under the action of humidity and loading, the attenuation of the structural parameters becomes increasingly more obvious, and the attenuation band is the slip band corresponding to the shear strain increment; this also shows that the structural parameters can be used as some of the criteria for the progressive failure of structural loess slopes.

(4) For the slope investigated in this study, with the increase of the water content of the slope, the load that the slope top can bear was found to decrease gradually, and the load decreased sharply after the water content reached 17%. This phenomenon provides a certain criterion for the relationship between the magnitude of the slope top surcharge and slope stability in engineering construction.

Data availability statement

The raw data supporting the conclusions of this article will be made available by the authors, without undue reservation.

Author contributions

JF: Formal Analysis, Writing – review & editing, Writing – original draft. AL: Funding acquisition, Writing – original draft, Data curation. SS: Conceptualization, Writing – review & editing. CC: Formal Analysis, Writing – review & editing.

Funding

This study was funded by the Natural Science Foundation of China (No. 50779054), and the Natural Science Foundation Project of Bijie Science and Technology Bureau (Bikelianhezi NO.G [2023] 30, Bikelianhezi NO.G [2023] 55).

Conflict of interest

Author SS is employed by Institute of Geotechnical Engineering, Xi'an University of Technology.

The remaining authors declare that the research was conducted in the absence of any commercial or financial relationships that could be construed as a potential conflict of interest.

Publisher's note

References

Cheng, Q., Hu, H., Hu, G., and Peng, J. (2000). Numerical simulation of viscoelastoplastic finite element for progressive failure of high slope rock mass. *J. Eng. Geology* 8 (1), 25–30.

Conte, E. (2010). Stability analysis of slopes in soils with strain-softening behavior. *Comput. Geotechnics.* 37, 710–722. doi: 10.1016/j.compgeo.2010.04.010

Hong, B, Li, X., Wang, L, and Li, L.-C. (2019). Permeability anisotropy and microstructure of Yan'an Q3 loess. *J. Jilin University (Earth Sci. Edition)* 49 (05), 1389–1397. doi: 10.13278/j.cnki.jjuese.20180156

Liu, N., Li, N., Li, G., Song, Z., and Wang, S. (2022). Method for evaluating the equivalent thermal conductivity of a freezing rock mass containing systematic fractures. *Rock Mechanics Rock Eng.* 55, 7333–7355. doi: 10.1007/s00603-022-03038-9

Liu, N., Li, N., Wang, S., Li, G., and Song, Z. (2023). A fully coupled thermo-hydro-mechanical model for fractured rock masses in cold regions. *Cold Regions Sci. Technol.*, 103707. doi: 10.1016/j.coldregions.2022.103707

Liu, A., and Wang, S. (1994). Progressive Failure Model of planar slope and its application. *J. Eng. Geology* 2 (1), 1–8.

Lo, K. Y., and Lee, C. F. (1973). Stress analysis and slope stability in strain-softening materials. *Geotechnique* 23 (1), 1–11. doi: 10.1680/geot.1973.23.1.1

Lu, Z. (1986). The failure mechanism of soil and its theoretical computations. *Chin. J. Geotechnical Eng.* 1986 (06), 69–74.

Lu, Y., Hu, P., Zhong, Y., Zhang, Y., and Jiang, Y. (2022). Control design based on progressive failure characteristics of slope:taking Budaiying slope in Shiyan city, Hubei province as an example. *Rock Soil Mechanics* 08), 2277–2286. doi: 10.16285/j.rsm.2021.1846

Lu, Y., Zhang, L., Zhang, Y., Li, J., Liu, M., and Zhu, L. (2021). Multi parameter evaluation index of progressive failure of landslide. *Eng. Mechanics* 38 (03), 132–147. doi: 10.6052/j.issn.1000-4750.2020.05.0286

Luo, A., and Fang, J. (2018). Secondary development of wet-loaded structural constitutive models based on FLAC~(3D) loess. *J. Water Resour. Architectural Eng.* 16 (03), 120–125. doi: 10.3969 /j.issn.1672-1144.201803.022

Luo, A., Shao, S., Chen, C., and Fang, J. (2015a). Study on wet load structural constitutive model of loess. *Rock Soil Mechanics* 36 (08), 2209–2215. doi: 10.16285/j.rsm.2015.08.011

Luo, A., Shao, S., Chen, C., and Fang, J. (2016). Numerical realization of wet load structural constitutive model of loess. *J. Yangtze River Sci. Res. Institute* 33 (02), 74–79. doi: 10.11988/ckyyb.20140501

Luo, A., Shao, S., Fang, J., and Chen, C. (2015b). Application of loess wet-loaded structural model in dynamic stability analysis of loess slope. *J. Seismol. Eng.* 37 (03), 816–822+833. doi: 10.3969/j.issn.1000-0844.2015.03.0816

Shen, H., Wang, S., Guo, M., Ding, W., and Yang, C. (2016). A preliminary study of the progressive failure and stability of slope with strain-softening behavior. *Rock Soil Mechanics* 37 (01), 175–184. doi: 10.16285/j.rsm.2016.01.021

Skempton, A. W. (1964). Long term stability of clay slopes. *Geotechnique* 14 (1), 77–101. doi: 10.1680/geot.1964.14.2.77

Tan, W., Wang, J., and Zhou, R. (2000). Study on physical and numerical simulation of progressive failure of rock slope. *Non-ferrous Min. Metallurgy* 16 (3), 5–7.

Terzaghi, K. (1936). "Stability of slopes of natural clay," in *Proceedings of the International Conference on Soil Mechanics and Foundation Engineering*, Graduate School of Engineering, Harvard University, America.Vol. 1, 161–165.

Troncone, A. (2005). Numerical analysis of a landslide in soils with strain softing behavior. *Geotechnique* 55 (8), 585–596. doi: 10.1680/geot.2005.55.8.585

Wang, G. (2000). Progressive failure and stability analysis of slope. *Chin. J. Rock Mechanics Eng.* 19 (1), 29–33.

Wang, T. (2008). Numerical analysis of water field in unsaturated loess subgrade. *Chin. J. Geotechnical Eng.* 30 (1), 41–45.

Xu, P.-p. (2021). *Study on water-soil interaction mechanism of permeability change of remo* (Xi'an: Chang'an University). doi: 10.26976/d.cnki.gchau.2021.000059

Xue, H., Dang, F., Yin, X., Ding, W.-H., and Yang, C.. (2016). Non-proportional correlative reduction finite element method for slope strength parameters. *Math. Problems Eng.*, 10. ID 2725354. doi: 10.1155/2016/2725354

Zhang, G, and Zhang, J.-m. (2007). Stability evaluation of strain-softening slope based on Swedish slice method. *Rock Soil Mechanics* 28 (01), 12–16. doi: 10.16285/j.rsm.2007.01.003

frontiers | Frontiers in Earth Science

TYPE Original Research
PUBLISHED 18 October 2023
DOI 10.3389/feart.2023.1270971

OPEN ACCESS

EDITED BY
Liang Cui,
Lakehead University, Canada

REVIEWED BY
Zhang Yanjie,
Lanzhou Jiaotong University, China
Ping Li,
Northwest University, China

*CORRESPONDENCE
Guohua Deng,
gh_deng@163.com

RECEIVED 01 August 2023
ACCEPTED 09 October 2023
PUBLISHED 18 October 2023

CITATION
Kang J, Deng G, Zhang K and Shao S (2023), Field monitoring of vibration characteristics during advanced ductule installation in sandy cobble stratum. *Front. Earth Sci.* 11:1270971. doi: 10.3389/feart.2023.1270971

Field monitoring of vibration characteristics during advanced ductule installation in sandy cobble stratum

Jiawei Kang[1], Guohua Deng[1,2]*, Kai Zhang[3] and Shengjun Shao[1]

[1]Institute of Geotechnical Engineering, Xi'an University of Technology, Xi'an, China, [2]Xi'an Loess Underground Project Technology Consulting Co., Ltd., Xi'an, China, [3]China Jikan Research Institute of Engineering Investigations and Design, Co., Ltd., Xi'an, China

The sandy cobble stratum presents a high risk for underground tunnel construction due to its low cohesive properties and susceptibility to loosening and falling. The use of Advanced ductule for grouting reinforcement inevitably results in vibrations, and understanding how these vibrations propagate is crucial in selecting tunnel engineering support schemes and responding to accident risks. Based on a bored tunnel under construction in Xi'an, field vibration propagation characteristics testing were carried out for advanced ductile installation. The time-history response and frequency distribution characteristics of the vibration velocity within the tunnel face under sandy cobble stratum conditions were studied, and the law of vibration propagation attenuation within the tunnel face range was obtained. The results showed that: 1) During the conduit drilling process, the tunnel face mainly experienced vertical vibrations, with the horizontal velocity amplitude accounting for only 15%–20% of the vertical velocity amplitude. At a distance of 1.0 m from the conduit, the vertical velocity amplitude reaches 10.602 mm/s, and the vibration energy concentrates mainly in the frequency range of 150–250 Hz. At a distance of 1.5 m from the conduit, the bidirectional vibration velocity significantly attenuates; 2) The vibration characteristics within the tunnel face can be classified into three primary areas: "Loose and Falling" area, "Significant Vibration" area, and "Vibration Attenuation" area. Loose, falling and significant vibrations occurred mainly within a range of about 1.25 m around the conduit. 3) As the diameter of the conduit decreases, the amplitude of vertical vibration velocity decreases by about 20%. By reducing the design diameter of the advanced ductule in a reasonable manner, it is possible to effectively mitigate the impact of vibration caused by the sandy cobble stratum during installation. This can yield a positive impact, curtailing the occurrence of the tunnel's collapse phenomenon and ensuring its stability.

KEYWORDS

bored tunnel, sandy cobble stratum, advance conduit, vibration attenuation characteristics, vibration velocity amplitude

1 Introduction

The sandy cobble stratum is a high risk layer during the construction of underground tunnels, given its loose nature. In the past, collapse accidents occurred frequently during the excavation process of these tunnels, posing a significant danger to the safety of engineering construction. Advanced ductile reinforcement methods are commonly used

due to their cost-effectiveness, uncomplicated construction process, and minimal space requirements. Upon completion of the earthwork excavation in a single cycle of tunnel construction, a grid arch is quickly erected. High-pressure air picks are used to form perforations according to the contour line of the Advanced Ductule layout determined by the design, followed by manual insertion of the ductule, ensuring that the exposed length meets the design specifications. The tail of the ductule is welded to the grid arch to ensure stability and structural integrity. However, during the installation of the advanced ductules, vibrations are inevitably generated, leading to the loosening and collapse of the cohesionless sand and gravel layer. This problem commonly occurs in a variety of engineering practices, with collapse depths and heights ranging from tens of centimeters to several meters. This problem can affect the stability of the face and arch of the tunnel, and in severe cases, lead to a counterproductive effect (Zhou et al., 2018; Liu et al., 2020; Di et al., 2022; Qin et al., 2022; Le et al., 2023). At later stages, this problem can only be solved through a large amount of initial support and grouting behind it, which not only affects the safety of tunnel construction, but also increases investment.

Currently, researchers are placing greater emphasis on major technical issues that arise in tunnel excavation in sandy cobble strata, such as surrounding rock pressure (Zhang et al., 2017; Lin et al., 2021; Zhang et al., 2022), support systems (Li et al., 2020; Cheng et al., 2023), grouting reinforcement (Mei et al., 2021), and deformation control (Zhang et al., 2017; Lin et al., 2021). However, when it comes to construction details, relatively little research has been done. This has resulted in a high proportion of engineering accidents due to inadequate implementation of ideal designs. Therefore, some scholars have proposed the prudent use of advanced ductule in these formations. For example (Wu, 2009), conducted systematic field tests on ductules with different diameters, studying maximum drilling depth, conduit failure, and local collapse under three conventional drilling methods for advanced ducts. A design scheme is recommended for advanced ductules with fine diameters, short lengths, and high frequencies, which is more feasible for construction. At present, the most commonly used installation methods for ductules are high pressure air guide holes, pneumatic picks, or a combination of both. High pressure wind drilling is less disruptive to formation and is suitable for pure sand layers; however, it may not solve the problem of large particle size pebbles in sand and gravel layers. The combination of air pick-up and drilling is currently the most popular method used in sand and gravel layers. However, the jacking of the air pick inevitably causes some disturbance to the sandy cobble layers.

Due to the special mechanical properties of the sandy cobble layer, scholars (Guo et al., 2018; Wu et al., 2022; Fang et al., 2023) have conducted several field vibration propagation attenuation tests on environmental vibration problems induced during shield tunnel excavation in the past. However, there has been no systematic study of vibration effects during bored tunnel construction. However, the vibration effect during the formation of ductules in sand and gravel underground tunnels exists objectively, leading to frequent local tunnel collapse accidents. This paper intends to select a tunnel under construction in Xi'an to conduct *in-situ* vibration monitoring tests, analyze the propagation law of vibration during the drilling process of advanced ductules, and provide a basis for addressing the collapse risk of sand and gravel layers during tunnel implementation.

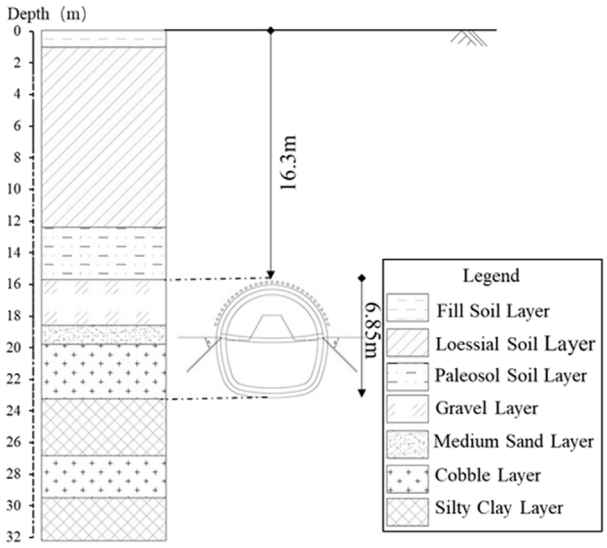

FIGURE 1
Geological profile of the test section.

2 Experimental procedure

2.1 Geological overview of the test site

This vibration monitoring test is located in Baqiao District, Xi'an City, Shaanxi Province. This tunnel is carried out using the "bending tunneling method", with an advanced length of 3–5 m on the upper step and a spacing of 0.5 m between the grid arches. The length of excavation per step is consistent with the grid arch space.

Figure 1 shows the geological profile of the test section. The soil layer in the tunnel body is mainly composed of alluvial-proluvial silty clay, sand, and middle pleistocene alluvial gravel. The observed long-term phreatic water level was found to be 25.5 m below the ground surface and below the tunnel base. At the top of the tunnel arch, there is a layer of sand and gravel, that is, about 2 m thick. The soil layer within the tunnel body mainly consists of round gravel, pebbles, and medium sand. Inside the tunnel base, the soil layer is mainly composed of silty clay.

Figure 2 shows the particle size distribution curve of the characteristic soil layer at the test section location. The pebble layers on the experimental site appear to have an uneven distribution, with the original rock being mainly composed of granite particles ranging in size from 3 to 7 cm, and the maximum size being 12 cm. About 28% of the particles are larger than 10 cm, including a mix of gravel sand and round gravel, along with some clay filling. The gradation of cobble layer is also uneven, with the original rock mostly consisting of granite particles ranging in size from 0.2 to 2 cm, and a maximum size of 3 cm. In this layer, moderate amounts of gravel, sand, and pebbles are present, along with some clay filling. As for the medium sand layer, it has an uneven quality, with granite being the predominant rock type.

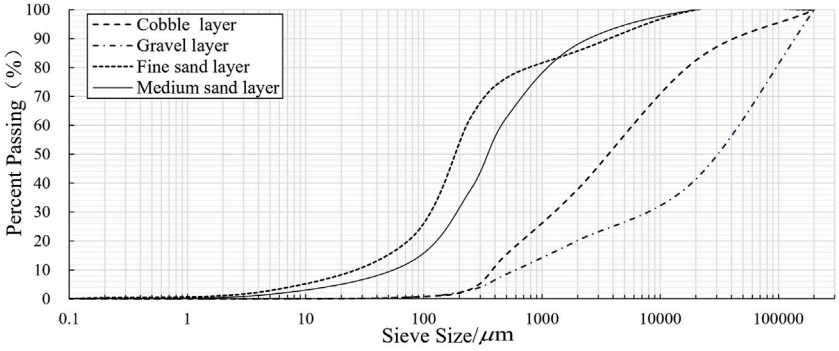

FIGURE 2
Particle size distribution curve of characteristic soil layers at the test section.

FIGURE 3
Schematic diagram of using small conduits and installation methods in the experiment.

The main mineral components of this layer are feldspar and quartz, along with moderate amounts of gravel sand, round gravel, and some clay filling.

2.2 Advanced ductule and installation methods for testing

Taking into account factors such as tunnel operating space, advanced ductile processing and manufacturing capabilities, and slurry diffusion requirements, two sets of ductile diameters and three kinds of lengths of ductile material were prepared for the test. The advanced ductules is produced using φ 32/φ 42 mm steel ductules, which are segmented into lengths of 1.5, 2.0, and 3.0 m. One end is made into a conical shape 300 mm long and sealed using a hot melt machine, as shown in Figure 3A). A joint is provided at the end of the conduit, which is directly connected to the high pressure pneumatic pick. Use a high-pressure impact force to place the leading ductules inside the sand layer, as shown in Figure 3B).

2.3 Test conditions and monitoring points layout

Supplementary Table S1 presents the experimental conditions for this study, detailing the advanced ductile test. The test was

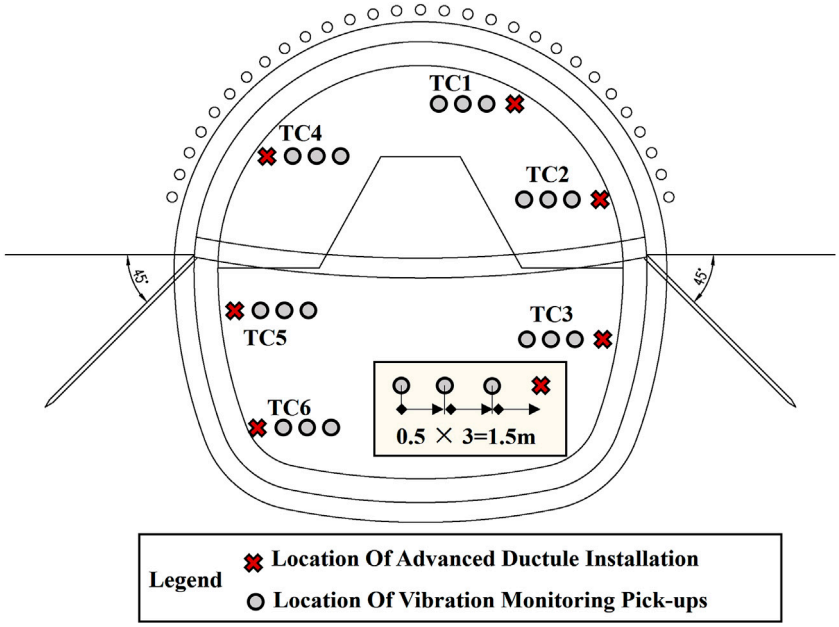

FIGURE 4
Layout of vibration test monitoring points and schematic diagram of implementation points for each working condition.

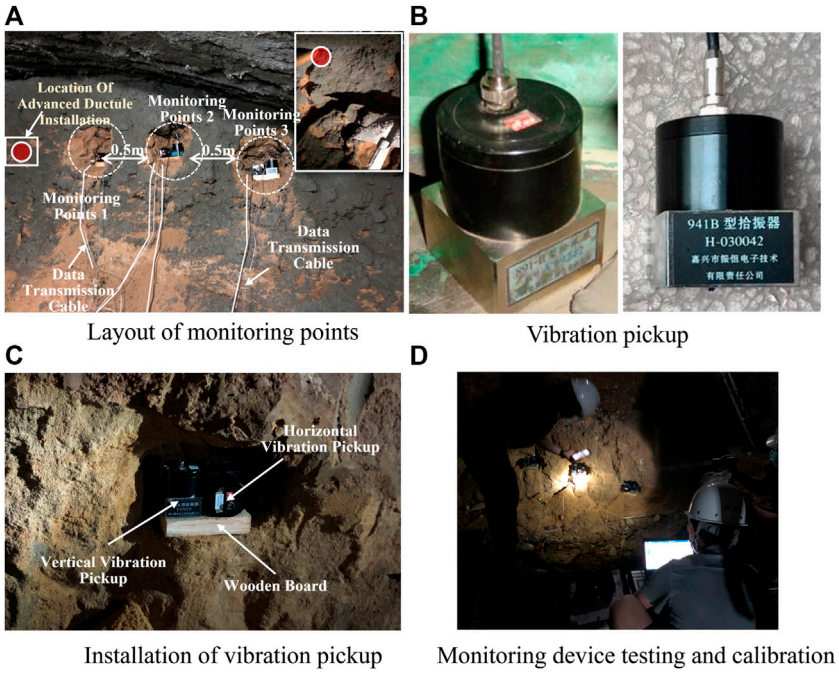

FIGURE 5
Schematic diagram of the arrangement, installation, and calibration of vibration pickup measuring points.

performed under different specifications of ductules, powered by high pressure pneumatic picks. In the event of encountering large diameter pebble layers during installation, and if they cannot be easily driven through, the installation angle of the conduit will be adjusted accordingly. If the conduit cannot be adjusted, the vibration test will be terminated. Once the test is complete, the actual location of the advance conduit into the soil will be marked. The conduit will be pulled out from the inside of the formation, and the length of the conduit will be recorded. In addition, the condition of the conduit body and the characteristics of the sealing section will be observed.

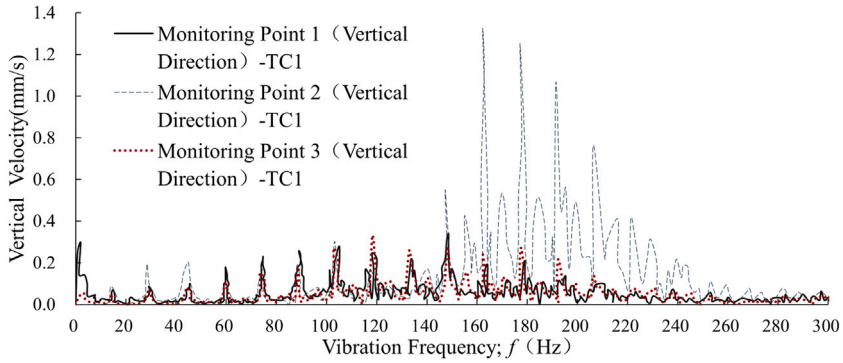

FIGURE 6
Vertical velocity frequency distribution characteristics at each vibration monitoring point during TC1 installation.

To monitor vibration levels during the installation of advanced ductule, three sets of vibration monitoring points are installed around the installation site with a horizontal separation of 0.5 m between each point. These monitoring points are located along the tunnel face and empty surface as shown in Figure 4, with both horizontal and vertical vibration pick-ups installed at each point. The purpose of recording the horizontal and vertical components of vibration in real time at each monitoring point is to analyze the attenuation and propagation of vibration in the surrounding sand and gravel layer within a radius of 1.5 m of the conduit installation.

Figure 5A shows the layout of field vibration monitoring points. The vibration pickup uses 891-II and 941-B speed sensors, which offer ranges of 0.3 and 1.4 m/s, respectively. The frequency response range of the sensors is 0.17–100 Hz. The vibration data acquisition instrument used herein is a dynamic signal acquisition analyzer with a model INV3060A, as shown in Figure 5B. Before installing the vibration pick-up, a pit is hand-dug at the tunnel face, and a wooden board is placed horizontally as a support platform. The vibration pickup is placed above the wood panel to ensure accurate recording of the direction of the vibration component, as shown in Figure 5C. The data collection system is then connected. To verify the correct installation and accurate data transmission, we check the stability of each monitoring point and any changes in the data. If no significant fluctuations or anomalies are observed, we consider the vibration pickup properly connected and the data transmission line accurately established, as shown in Figure 5D.

3 Analyses of field measurements

3.1 Actual installation depth and ductules body characteristics

Supplementary Table S1 summarizes the actual penetration depth of the conduit across each test condition. There are large diameter pebble layers distributed within the range of conduit installation, which cannot be fully penetrated. During the installation process, the angle is difficult to adjust and cannot avoid the pebble body. Finally, the conduit is continuously installed for about 3 min before terminating the test.

During the installation of the advanced ductules, sand and gravel were loose and fell above the actual installation position and within the free range of the side wall. It can be observed that the structure of the conduit body is basically intact, and the sealing section has undergone severe deformation and damage.

3.2 Characteristics of vibration propagation

Figure 6; Figure 7; Figure 8; Figure 9 shows vertical and horizontal velocity response curves and velocity spectrum characteristics at each vibration monitoring point during TC1 installation.

During the implementation of the advanced ductule, the maximum vertical peak velocity was observed at a distance of 1.0 m from the conduit installation point, specifically at monitoring point 2, reaching a velocity of 10.602 mm/s. The vibration energy of the ductules was mainly concentrated in a frequency range of 150–250 Hz. At a distance of 1.5 m from the installation point (monitoring points 3), the vertical peak velocity is reduced to 3.906 mm/s, with most of the vibration energy distributed in the frequency range of 50–150 Hz. Similarly, at Monitoring Point 1, located 0.5 m from the installation point, the vertical peak velocity was found to be 5.077 mm/s, which fell between velocities recorded at Monitoring Points 2 and 3. The dominant vibration frequency at this point was similar to that observed at Monitoring Point 3, but with a reduction in vibration energy compared to Monitoring Point 2.

Combined with the field implementation process, the reason for this law of attenuation of vibration velocity is that within the range of vibration monitoring points 1–2, the vibration energy caused by the installation of advanced ductules dissipated in the form of loose and falling surrounding sand and gravel, thereby reducing the vibration velocity test value.

Compared to vertical vibration, horizontal vibration during installation ductules has a narrow range of numerical values. At a distance of 1.0 m from the installation point (monitoring points 2), the horizontal vibration velocity reaches its maximum, with a velocity amplitude of 2.054 mm/s. This amplitude is 20% of the vertical velocity amplitude at the same monitoring points. At monitoring points 3, located 1.5 m from the installation point,

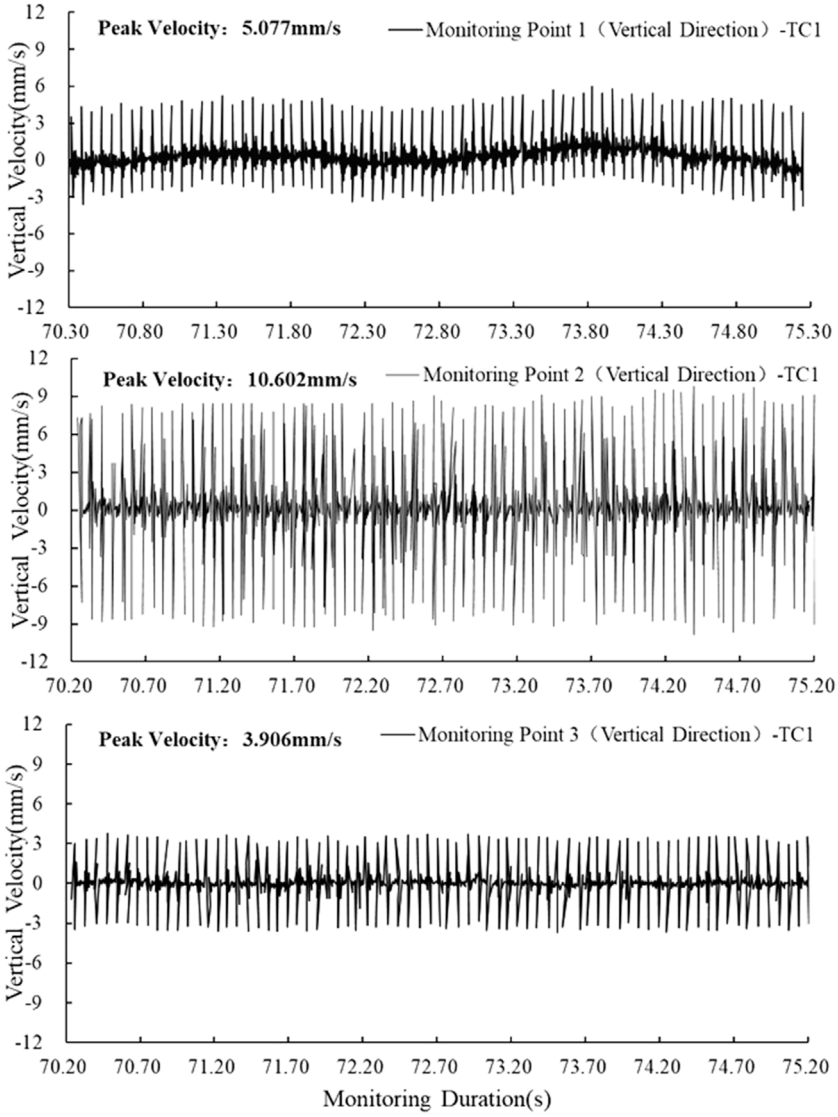

FIGURE 7
Vertical velocity time-history curve at each vibration monitoring point during TC1 installation.

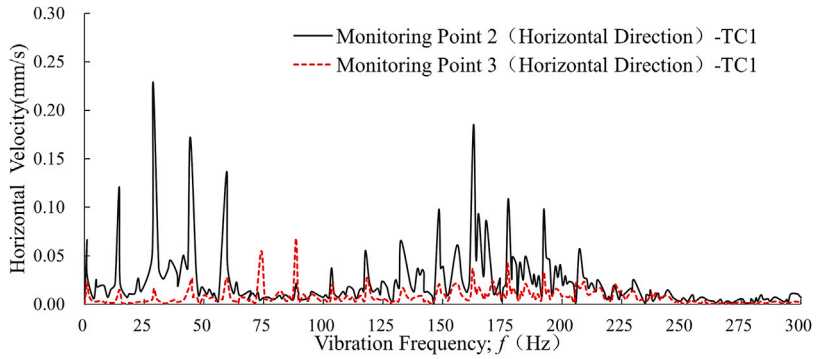

FIGURE 8
Horizontal velocity frequency distribution characteristics at each vibration monitoring point during TC1 installation.

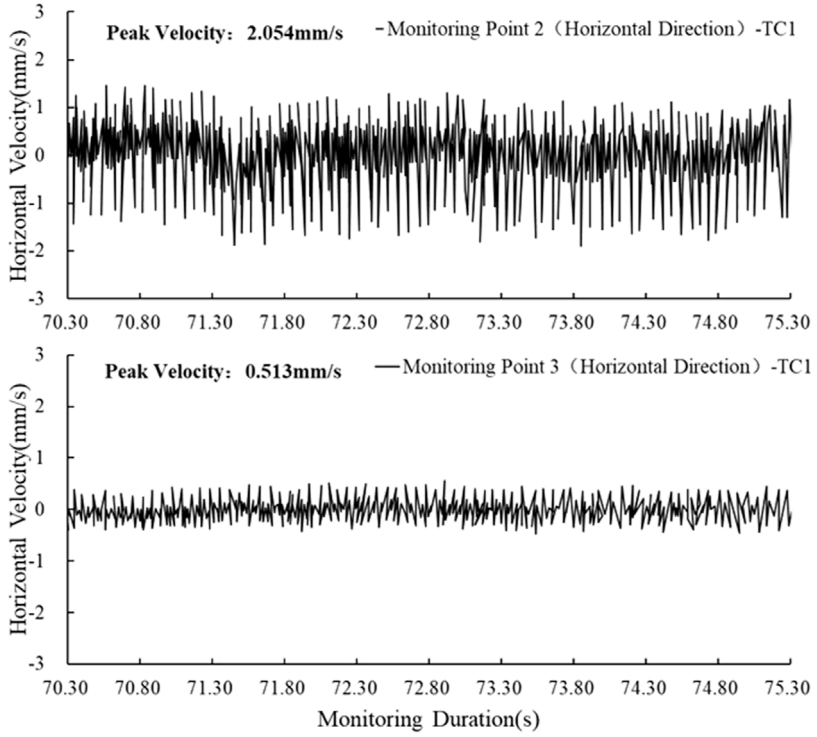

FIGURE 9
Horizontal velocity time-history response curves at each vibration monitoring point during TC1 installation.

the horizontal velocity amplitude is 0.513 mm/s, which accounts for 15% of the vertical velocity amplitude. These findings suggest that horizontal vibration is less impactful than vertical vibration during the installation of advanced ductule.

The vibration energy of the ductules is mainly concentrated in the frequency bands 0–50 and 125–200 Hz at a distance of 1.0 m from its installation position (monitoring points 2). At a distance of 1.5 m from the ductile installation position (monitoring points 3), horizontal vibration energy is distributed over a wide frequency range of 50–250 Hz, and its velocity amplitude significantly decreases. This test result correlates with the law of vertical velocity attenuation.

3.3 The Influence of ductules diameter on the vibration characteristics

Figures 10, 11 shows the vertical and horizontal velocity spectrum characteristics and velocity time history curve of vibration monitoring points 2 under two different conduit diameter conditions (TC1 and TC4).

During the installation of ductules of different ductules diameters, the sand and gravel layers at the installation site exhibited similar spectral distribution characteristics. Vibration energy was observed to be mainly vertical, with the majority of its frequency concentrated between 150 and 250 Hz. Meanwhile, horizontal vibration energy was found to be mainly distributed in two frequency bands, at 0–50 and 125–200 Hz.

Reducing the diameter of the duct leads to a decrease in its vibration energy. In the frequency range of 150–250 Hz, when the conduit diameter is reduced from φ 42 to φ 32 mm, the corresponding vertical vibration velocity decreases from 1.31 to 0.80 mm/s. The maximum vertical velocity amplitude also decreases from 10.602 to 8.165 mm/s with a reduction ratio of 20%. Horizontal vibration spectrum characteristics remain similar under both conditions with maximum horizontal velocity amplitudes of 2.436 and 2.054 mm/s respectively. These values are within a relative range.

4 Discussion

4.1 Vibration law of ductules installation

During the installation of advanced ductules, the vibration effect caused by the interaction between the structure of the conduit body and the sand and gravel layer of the tunnel, as well as the diffusion and attenuation law within the face range of the tunnel, are prominent problems in identifying the range of loose and collapsed sand and gravel bodies, optimizing support measures for concealed excavation tunnels, and responding to engineering risks.

Figure 12 shows the propagation attenuation characteristics within the tunnel face range. The main statistical objects are velocity amplitudes at each monitoring point under two types of advanced ductile diameter conditions.

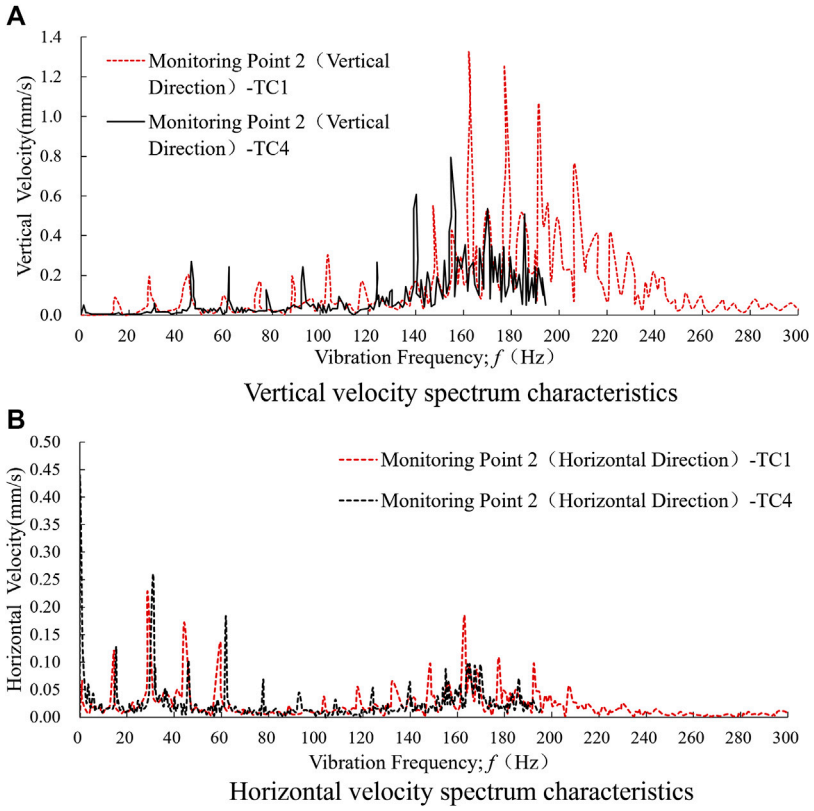

FIGURE 10
Velocity frequency distribution characteristics of vibration monitoring points 2 under two different conduit diameter conditions (TC1 and TC4).

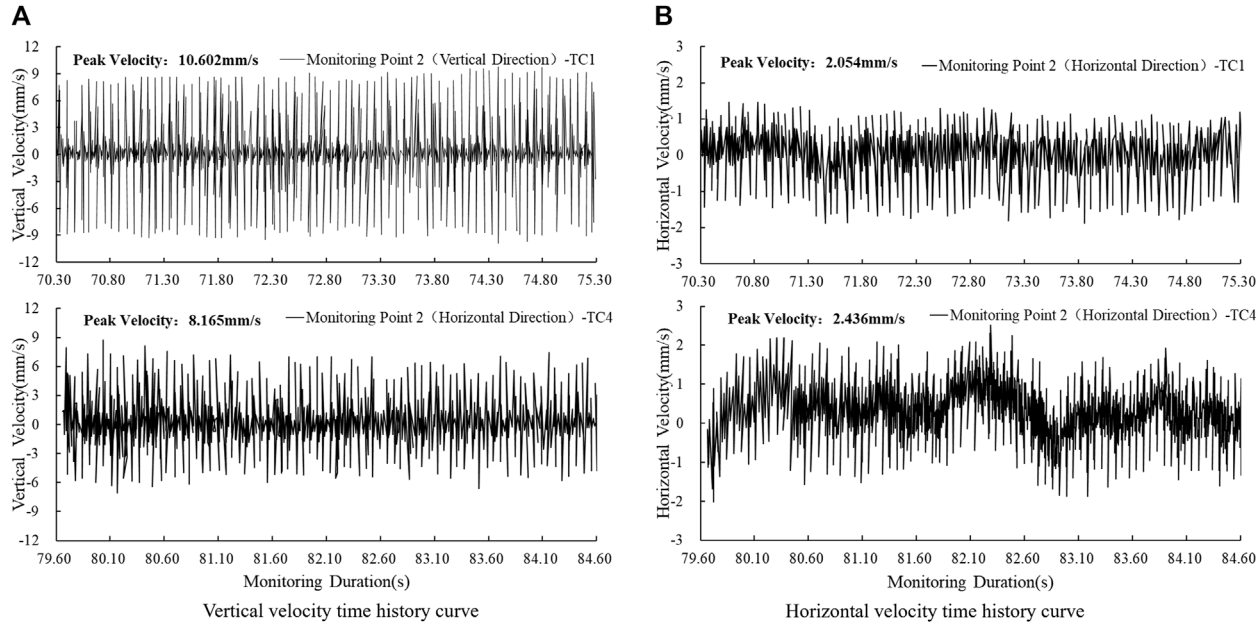

FIGURE 11
Velocity time-history curve of vibration monitoring points 2 under two different conduit diameter conditions (TC1 and TC4).

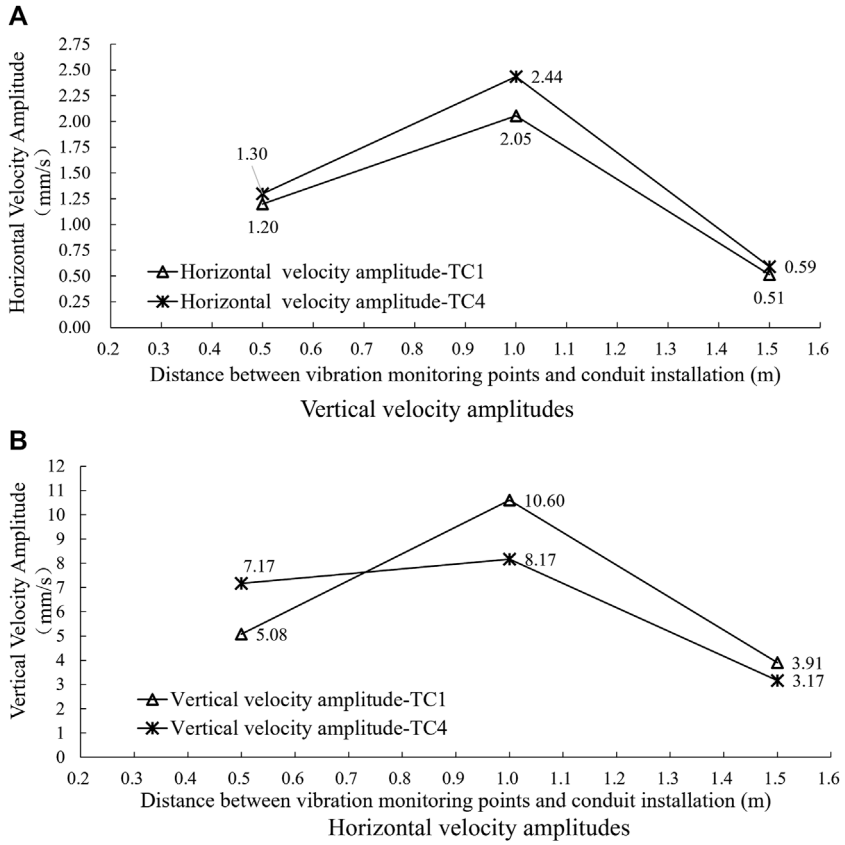

FIGURE 12
Characteristics of velocity amplitude attenuation within the range of the palm during the installation of advanced ductule.

During the installation of advanced ductule, the vertical and horizontal velocity amplitudes within the tunnel face exhibit similar patterns of diffusion attenuation. This is because sand and gravel in the range of 25–75 cm around the location of the advanced ductile installation undergo "loose and fall", leading to the dissipation of vibration energy. From the test results, it was observed that the amplitude of the vibration velocity has a numerical range. The maximum amplitude of the vertical and horizontal vibration velocity was found to occur at a distance of 1.0 m from the installation position of the ductules (monitoring points 2).

The vibration velocity within the tunnel face decreases significantly as the distance from the installation position of the conduit increases. For example, when comparing Measurement Point 3 with Point 2, there is an attenuation of 50%–60% in its vibration speed. Further, it was observed that as the diameter of the conduit decreases (from φ 42 to φ 32 mm), the amplitude of the bidirectional velocity reduces by about 20% at a distance of 1.0 m (monitoring points 2) from the installation position of the ductules.

To summarize, during the advanced ductile installation process, the range of vibration disturbance within the tunnel face is mainly concentrated within 1.5 m of the installation location in the sandy cobble stratum. Based on the vibration response characteristics obtained from this field monitoring, the center position of adjacent measurement points is used as the regional boundary, the disturbance propagation attenuation characteristics of the sand and gravel layer are classified into three areas: "Loose and Falling" area, "Significant Vibration" area, and "Vibration Attenuation" area. Figure 13 shows the specific division diagram. These findings provide a better understanding of the dynamic characteristics of the advanced ductile installation process and can be used to improve future operation and maintenance practices.

4.2 Suggestions for engineering measures

By conducting field monitoring vibration characteristics during advanced ductule installation in sandy cobble stratum, the vibration propagation characteristics and attenuation laws within the tunnel face range during the process of using high pressure pneumatic picks for jacking were presented. In order to effectively control the engineering risks of sandy cobble stratum, the following engineering measures and suggestions are proposed:

(1) It is recommended to carefully consider the advanced ductules grouting reinforcement scheme during the design process of the support scheme for the sandy cobble stratum underground excavation tunnel; It is recommended to prioritize the use of low vibration drilling methods such as high-pressure air drilling,

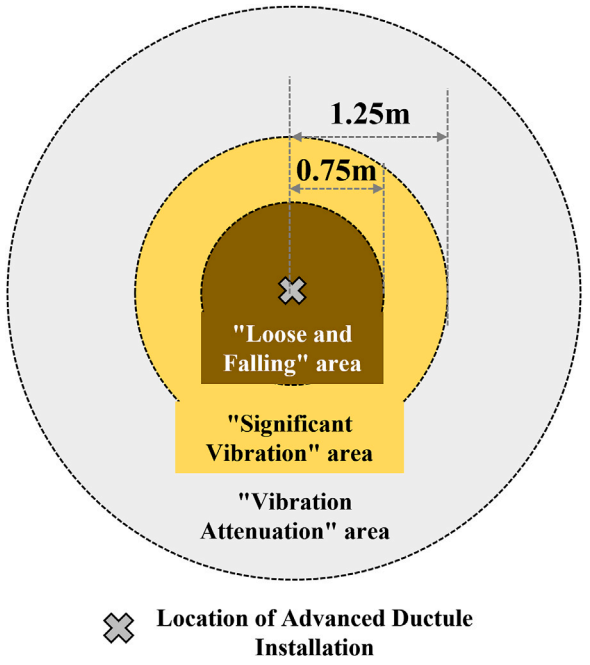

FIGURE 13
Schematic diagram of disturbance area division for advance ductule installation in sandy cobble stratum.

and the use of high-pressure air picks for direct jacking is only recommended as an auxiliary measure.

(2) If it is necessary to use it, it is recommended to minimize the diameter and length of the conduit as much as possible to reduce the risk of loosening, falling, or even collapse of the sandy cobble layer caused by disturbance during installation; It is recommended to take cover protection measures for the sand and gravel layer within 1.25 m around the advance conduit;

(3) Before the excavation of bored tunnels, it is necessary to thoroughly investigate the particle size distribution characteristics of sandy cobble layer, and evaluate the feasibility of the advanced ductules installation plan; ensure welding quality, improve the strength of the conduit mouth, and ensure the success rate of the first installation of the advanced ductules.

5 Conclusion

In this article, a series of research work was carried out on the time-history response law and velocity spectrum distribution characteristics of vibration velocity in the face of the tunnel by conducting field vibration propagation characteristics testing tests for advanced ductules installation under sandy cobble stratum. The vibration energy diffusion and attenuation law during the advanced ductules installation process was obtained. It has certain reference significance for optimizing the design of excavation support schemes for underground tunnels under such geological conditions. The main conclusions are as follows:

(1) During the design and construction process of underground excavation tunnels in sandy cobble stratum, the drilling plan of advanced ductule should be reasonably matched with the characteristics of the strata. If not properly selected, significant vibration effects will occur, leading to the risk of loosening, falling blocks, and even collapse of the surrounding sandy cobble stratum.

(2) During the installation of advanced ductule, when encountering a large diameter pebble layer, the vibration velocity within the tunnel face area increases significantly, mainly in the vertical direction, with a horizontal velocity amplitude of about 15%–20% of the vertical direction. Before tunnel excavation, the stability of the sandy cobble stratum under vibration should be evaluated according to the specific geological conditions of the site.

(3) During the installation of advanced ductule, the vibration propagation characteristics within the tunnel face can be divided into three main areas: “Loose and Falling” area, “Significant Vibration” area, and “Vibration Attenuation” area. During the excavation and support process of bored tunnels, effective protective measures should be taken to control the loosening and falling of sand and gravel layers within the range of 0–0.75 m around the advance conduit. Sand and gravel layer in the range of 0.75–1.25 m around have a large amplitude of vibration velocity. During the excavation and support process of underground tunnels, it is necessary to minimize the disturbance to the strata within the area. If necessary, reinforcement measures can be taken to maintain the stability of the tunnel face;

(4) Based on the vibration monitoring results under different conduit diameter conditions, it is recommended to reasonably reduce the design diameter of the advanced ductules during the bored tunnel construction process, which has beneficial effects on suppressing the collapse of sandy cobble stratum and maintaining the stability of the tunnel face.

Data availability statement

The original contributions presented in the study are included in the article/Supplementary Material, further inquiries can be directed to the corresponding author.

Author contributions

JK: Writing–original draft, Formal Analysis, Visualization. GD: Conceptualization, Funding acquisition, Writing–review and editing. KZ: Investigation, Visualization, Writing–review and editing. SS: Supervision, Writing–review and editing.

Funding

The author(s) declare financial support was received for the research, authorship, and/or publication of this article. This

work was financially supported by the National Natural Science Foundation of China (Grant No. 52178355) and the Natural Science Basic Research Program of Shaanxi (2022JM-216).

Conflict of interest

Author GD is employed by Xi'an Loess Underground Project Technology Consulting Co., Ltd. Author KZ is employed by China Jikan Research Institute of Engineering Investigations and Design, Co., Ltd.

The remaining authors declare that the research was conducted in the absence of any commercial or financial relationships that could be construed as a potential conflict of interest.

Publisher's note

Supplementary material

The Supplementary Material for this article can be found online at: https://www.frontiersin.org/articles/10.3389/feart.2023.1270971/full#supplementary-material

References

Cheng, C., Jia, P., Ni, P., Wang, Y., Zhao, W., Guan, Y., et al. (2023). Upper bound analysis of longitudinally inclined EPB shield tunnel face stability in dense sand strata. *Transp. Geotech.* 41, 101031. doi:10.1016/j.trgeo.2023.101031

DI, Q., Li, P., Zhang, M., and Cui, X. (2022). Investigation of progressive settlement of sandy cobble strata for shield tunnels with different burial depths. *Eng. Fail. Anal.* 141, 106708. doi:10.1016/j.engfailanal.2022.106708

Fang, Y., Li, X., Hao, S., Liu, H., Yang, Y., and Guo, Y. (2023). Failure analysis of slurry TBM discharge pipe in complex strata combined with wear and vibration characteristics. *Eng. Fail. Anal.* 150, 107307. doi:10.1016/j.engfailanal.2023.107307

Guo, F., Tao, L., Kong, H., Ma, H., Zhang, L., and Zhang, X. (2018). Analysis of propagation and attenuation of vibration induced by shield tunneling in Lanzhou Sandy Cobble layer. *Rock Soil Mech.* 39, 7. doi:10.16285/j.rsm.2016.2820

LE, B. T., Nguyen, T. T. T., Divall, S., and Davies, M. C. R. (2023). A study on large volume losses induced by EBPM tunnelling in sandy soils. *Tunn. Undergr. Space Technol.* 132, 104847. doi:10.1016/j.tust.2022.104847

Li, P., Zou, H., Wang, F., and Xiong, H. (2020). An analytical mechanism of limit support pressure on cutting face for deep tunnels in the sand. *Comput. Geotechnics* 119, 103372. doi:10.1016/j.compgeo.2019.103372

Lin, Q., Lu, D., Lei, C., Tian, Y., Gong, Q., and DU, X. (2021). Model test study on the stability of cobble strata during shield under-crossing. *Tunn. Undergr. Space Technol.*, 110. doi:10.1016/j.tust.2020.103807

Liu, T., Xie, Y., Feng, Z., Luo, Y., Wang, K., and Xu, W. (2020). Better understanding the failure modes of tunnels excavated in the boulder-cobble mixed strata by distinct element method. *Eng. Fail. Anal.* 116, 104712. doi:10.1016/j.engfailanal.2020.104712

Mei, Y., Zhang, X., Nong, X., and Fu, L. (2021). Experimental study of the comprehensive technology of grouting and suspension under an operating railway in the cobble stratum. *Transp. Geotech.* 30, 100612. doi:10.1016/j.trgeo.2021.100612

Qin, Y., Lai, J., Gao, G., Yang, T., Zan, W., Feng, Z., et al. (2022). Failure analysis and countermeasures of a tunnel constructed in loose granular stratum by shallow tunnelling method. *Eng. Fail. Anal.* 141, 106667. doi:10.1016/j.engfailanal.2022.106667

Wu, J.-B. (2009). Test and research on Pore-Forming Techniques on ductule large particle sandy cobble stratum. *Archit. Technol.* 40, 3. doi:10.3969/j.issn.1000-4726.2009.11.020

Wu, K., Zheng, Y., Li, S., Sun, J., Han, Y., and Hao, D. (2022). Vibration response law of existing buildings affected by subway tunnel boring machine excavation. *Tunn. Undergr. Space Technol.*, 120. doi:10.1016/j.tust.2021.104318

Zhang, M., Dai, Z., Zhang, X., Javadi, A. A., Wang, C., Zhang, L., et al. (2022). Epidemiological survey and genetic characterization of type 3 vaccine-derived poliovirus isolated from a patient with four doses of inactivated polio vaccine in Henan Province, China. *Tunn. Undergr. Space Technol.* 11, 124. doi:10.1186/s40249-022-01028-1

Zhang, Z., Zhang, M., Jiang, Y., Bai, Q., and Zhao, Q. (2017). Analytical prediction for ground movements and liner internal forces induced by shallow tunnels considering non-uniform convergence pattern and ground-liner interaction mechanism. *Soils Found.* 57, 211–226. doi:10.1016/j.sandf.2017.03.004

Zhou, X.-P., Huang, X.-C., Liu, P.-F., and Li, T.-F. (2018). A probabilistic method to analyze collapse failure of shallow rectangular tunnels. *Tunn. Undergr. Space Technol.* 82, 9–19. doi:10.1016/j.tust.2018.07.029

Frontiers in Earth Science

Investigates the processes operating within the major spheres of our planet

Advances our understanding across the earth sciences, providing a theoretical background for better use of our planet's resources and equipping us to face major environmental challenges.

Discover the latest Research Topics

See more →

Frontiers

Avenue du Tribunal-Fédéral 34
1005 Lausanne, Switzerland
frontiersin.org

Contact us

+41 (0)21 510 17 00
frontiersin.org/about/contact